Thèse n° 9882

Measuring the electron energy distribution in tokamak plasmas from polarized electron cyclotron radiation

Présentée le 24 mars 2023

Faculté des sciences de base
SPC - Physique du Tokamak TCV
Programme doctoral en physique

pour l'obtention du grade de Docteur ès Sciences

par

Arsène Stéphane TEMA BIWOLE

Acceptée sur proposition du jury

Prof. F. Courbin, président du jury
Prof. A. Fasoli, Dr L. Porte, directeurs de thèse
Dr D. Farina, rapporteuse
Prof. R. Vann , rapporteur
Dr J. Decker, rapporteur

École
polytechnique
fédérale
de Lausanne

2023

Résumé

Dans cette thèse de doctorat, il a s'agit d'utiliser une technique prometteuse, qui n'avait plus été réussie sur un tokamak depuis plusieurs décennies, pour la mésure des électrons dit rapides sur TCV. La technique exploite l'ECE Vertical pour discriminer plus aisément le rayonnement en fonction de l'énergie des électrons. Les premières tentatives d'utilisation de l'ECE Vertical au début des années 1980 avaient néanmoins révélé une limitation majeure : celle de la réfraction de la ligne de visée de l'antenne ECE dans le plasma. La réfraction, qui s'empire avec la densité des électrons, dévie la ligne de visée de l'antenne et permet la détection du rayonnement de fond du tokamak après de multiples réflexions.

L'antenne ECE Vertical, conçue et installée sur TCV, produit un faisceau de col maximal 3 cm pour des mesures dans l'intervalle de fréquences de 78 à 148 GHz. Des simulations numériques préliminaires, effectuées pour déterminer l'ampleur de la réfraction, contraignaient la densité maximale d'opération à $n_{\mathrm{e}} < 1 \times 10^{19}\mathrm{m}^{-3}$. Ce résultat réduisait drastiquement le champ d'action du système de mesure jusqu'à ce qu'une découverte tout à fait anodyne vienne changer la donne. En réalité, la réfraction pose un problème uniquement si le rayonnement de fond a son origine dans le plasma. En ce qui concerne TCV, ce rayonnement tire son origine essentiellement de la composante X2 de l'ECE. Une combinaison adéquate du champ magnétique (qui varie sur TCV de 0.9 à 1.5 T) et des fréquences de mesure permet de maintenir l'origine de ce rayonnement loin du plasma, réduisant entièrement l'intensité du rayonnement de fond. Cette observation qui a déchainé le potentiel de l'ECE Vertical sur TCV a aussi permis d'exploiter le plasma, sur environ 70 décharges ohmiques, pour calibrer le système de mesure. La calibration se base sur le calcul de l'intensité du rayonnement X3 dans des conditions de faible épaisseur optique, et est validée par le rayonnement de corps noir, toujours en provenance du plasma.

C'est donc avec un système de mesure calibré, et une plus grande marge d'opération, qu'il a été possible de mesurer le rayonnement des électrons rapides appartement à des distributions non-Maxwelliennes. Ces mesures des rayonnements polarisés X et O ont été accomplies au cours des scenarios ECCD et runaway à très haute résolution temporelle, de l'ordre de $\sim 10\mu s$.

Dans les scenarios ECCD, la grande flexibilité de la puissance ECH sur TCV a été exploitée, parfois en variant en plein tir les angles du lanceur pour faire conduire le courant à des électrons de plus en plus énergétiques. Pour les runaways, les mesures ont été reaslisées au cours des scenarios simples, à haut courant plasma ($I_{\mathrm{p}} \sim 200$ kA) et densités en dessous de $1 \times 10^{19}\mathrm{m}^{-3}$.

Des mesures particulièrement interessantes avec les runaways ont été réalisées avec MGI, ou en présence de l'ECCD. Une observation de la réduction de l'émission des runaways en présence de l'ECCD a pu être accomplie avec l'ECE Vertical, en conformité avec d'autres systèmes de mesure. Dans ce travail de doctorat, une claire identification du rayonnement des électrons rapides a donc pu être réalisée et des approches pour la reconstruction de la fonction de distribution ont été tentées. Les reconstructions montrent une augmentation de l'énergie dans les directions parallèle ou perpendiculaire pour les différents scenarios. Concernant les runaways, la reconstruction de la distribution a permis l'observation d'une queue, relativement plate, dans la distribution en energie des électrons, en accord avec les attentes théoriques.

Mots clefs : energie, fusion nucléaire, tokamak, plasma, distributions non-maxwelliennes, electrons rapides, emission cyclotronique electronique, micro-ondes, réfraction, rayonnement de fond, radiometrie.

Abstract

In this doctoral thesis, a promising technique has been used for the measurement of non-thermal electrons in TCV. The technique employs a Vertical viewing ECE to more easily discriminate the radiation according to the energy of the electrons. Successful measurements using the Vertical ECE were achieved, for the last time on a tokamak, several decades ago. That is due, among other reasons, to a major limitation that emerged from the early attempts in the 1980s: that of the refraction of the line of sight of the ECE antenna in the plasma. The refraction, which increases with electron density, shifts the antenna's line of sight and allows the detection of the tokamak's background radiation via multiple wall reflections.

The Vertical ECE antenna, designed and installed on TCV, produces a beam of maximum waist size ~ 3 cm, for measurements in the frequency range from 78 to 148 GHz. Early simulations, to determine the extent of the refraction issue on TCV, constrained the maximum operational density to $n_{\mathrm{e}} < 1 \times 10^{19}\mathrm{m}^{-3}$. This result drastically reduced the operational window of the diagnostic until an innocent discovery came in to change the game. In reality, refraction causes trouble only if the background radiation originates within the plasma. As far as TCV is concerned, the background radiation originates essentially from the X2 component of the ECE. A suitable combination of magnetic field (which varies on TCV from 0.9 to 1.5 T) and measured frequencies allows to keep the origin of the background radiation away from the plasma, thus reducing, almost entirely, the level of background radiation. This observation, which unleashed the potential of the Vertical ECE on TCV, also made it possible to exploit the plasma itself, in approximately 70 ohmic discharges, for the calibration of the diagnostic. The calibration is based on the calculation of the X3 radiation intensity under the conditions of low optical thickness, and is validated against the plasma black-body radiation.

It is therefore with a calibrated diagnostic system, and a relaxed window of operation, that we have been able to measure the radiation from non-thermal electrons in some generated non-Maxwellian distributions. These measurements of X and O polarizations were achieved in ECCD and runaway electron scenarios at very high temporal resolution, in the order of $\sim 10\mu s$.

In ECCD scenarios, the great flexibility of the ECH power on TCV has been exploited, sometimes by varying the ECH launcher angles in full firing to allow increasingly energetic electrons to drive the current. For the runaways, the measurements were carried out during simple scenarios, at high plasma current ($I_{\mathrm{p}} \sim 200$ kA) and densities below $1 \times 10^{19}\mathrm{m}^{-3}$. Particularly interesting

were the measurements of runaways with MGI, or in the presence of ECCD. In agreement with other diagnostics, the Vertical ECE has allowed the observation of a reduction of the runaway emission intensity in the presence of ECCD.
In this doctoral thesis, a clear identification of the emission from non-thermal electrons could thus be achieved and attempts were made to reconstruct their energy distribution. The reconstruction shows enhancements in the parallel or perpendicular direction for the different scenarios. Concerning the runaways, the reconstruction has allowed the observation of a flat tail in the energy distribution of the electrons, in line with theoretical expectations.

Key words: energy, nuclear fusion, tokamak, plasma, non-maxwellian distributions, non-thermal electrons, electron cyclotron emission, microwaves, refraction, background radiation, radiometry.

Contents

1 Introduction

1.1 Tokamak: the most successful experimental device for fusion

"It's not often that a scientist gets a chance to work on a project that will change the world", says Mike Forrest, commenting on the journey he made to the Soviet Union to witness the "biggest ever breakthrough in the quest for fusion" . That was in 1968, 10 years after the declassification of fusion research. A team of British scientists went on to measure the record temperature of over 10 millions degrees, 1 keV, achieved in the T3 tokamak at the Kurchatov Institute in Moscow [1]. The word tokamak, Russian acronym for *toroidal chamber with magnetic coils* [2], was resounding, for the first time, across the fusion community. The performance of the T3 tokamak impressed the world and tokamaks were, forthwith, adopted for many fusion experiments. An increasing number of scientists joined the field, dazzled by the promises of fusion energy and the progress being made. The efforts aimed at a net energy gain from the tokamak fusion reactors. In that spirit, larger tokamaks were built over the years, with remarkable advancements, by comparing to fields of particle accelerators or information technology [3]. Hence, the progress in tokamak reactors reached the pinnacle in 1997 on the *Joint European Torus*, JET, by setting the record of the highest fusion gain ever achieved in an experimental device [4]. The JET tokamak paved the way to a much larger tokamak, now under construction, planned to achieve an even higher fusion gain. The device is named ITER, initially for *International Thermonuclear Experimental Reactor*, now simply for the Latin word *the way*, as ITER is the way to the long-sought fusion energy, the "machine that will realize our dream", quoting Dr. Bernard Bigot[I].
The efforts being made towards ITER for fusion energy are complemented by research on other fusion experiments. Those other experiments are the ones that have survived over the years, as well as those relying on innovative approaches to fusion energy. The field is booming, as it should be, and it continues to offer several research opportunities. The opportunities include, inevitably, research on plasma, the most common state of matter in the universe, trapped in fusion reactors.

[I] Dr. Bernard Bigot, Director General of ITER from 2015 to 2022

1.2 Plasma: the most common state of matter, trapped in tokamaks

In the fusion reactors, natural or artificial, matter is in the state of plasma. In fact, the part of the Universe we know is primarily made of plasma, the state in which nuclei and electrons are set free. In tokamaks, the plasma is confined by magnetic fields, which constrain the motion of the charged particles. Better understanding of tokamak plasmas relies on measurements of plasma parameters for validation of the theories and the numerical simulations. The measurements exploit the large spectral range of electromagnetic radiation coming from the plasma. The radiation originates from several mechanisms, either passive or externally induced. An example of passive radiation from the plasma are the X-rays emitted when an electron slows down on the heavier plasma particles: the Bremsstrahlung radiation. The emitted photon can be used to obtain quantitative information on the electron energy. The plasma emission that is of interest for this research is the so-called Electron Cyclotron Emission, ECE. To avoid any confusion, we recall that in the tokamak jargon, the cyclotron emission refers to the spontaneous emission associated to the cyclotron motion around the confining magnetic field. In the same jargon, the synchroton emission is the ultra-relativistic limit of the cyclotron emission previously defined, with the electron motion either mainly along the confining field or around it. The ECE has been used for several decades now as a well-established tool for electron temperature measurements in tokamak plasmas [5]. The measurement of the electron temperature hinges on the assumption that the electrons are distributed in energy space according to a Maxwellian distribution. In reality, in part due to the peculiarity of collisional phenomena in hot plasmas, the electron energy distribution in tokamak plasmas departs, quite often, from the Maxwellian distribution. This happens when some electrons are somehow accelerated to higher velocities, in numbers exceeding those of a Maxwellian distribution. Those electrons are called non-thermal electrons and are central to this research work. The study of non-thermal electrons has been a very interesting area of research since almost the beginning of the fusion effort, due the important role they play in various areas of tokamak physics. Non-thermal electrons in tokamaks appear sometimes as a disease, other times as a cure. They are, as an example, at the core of the runaway electron phenomenon. In fact, during tokamak plasma discharges, when the collisional drag on an electron by a Maxwellian background is taken over by an accelerating force such as an electric field, the electron "runs away", meaning that it continuously gains energy. The runaway electrons constitute a serious disease in tokamaks and are of great concern, as they can attain very high energies, up to tens of MeV. It is very much feared that in ITER, events such as plasma disruptions, leading to a loss of plasma confinement, could open up to the acceleration of runaway electrons by the residual electric field of the tokamak. In those catastrophic scenarios, runaway electron beams would reach currents of millions of Ampere, capable of melting the wall of the machine. The mitigation of the effects of runaway electrons, after a plasma disruption, is of high priority for ITER [6, 7].

The presence of non-thermal electrons is also relevant in tokamaks in various other scenarios. For example when the plasma is heated with Neutral Beam Heating, NBH, or when the current sustaining the plasma is provided by Lower Hybrid Current Drive, LHCD, or Electron Cyclotron Current Drive, ECCD. The idea behind ECCD was originally to launch waves in a direction

such that the energy given to the electrons by the wave accelerates them in the appropriate direction to sustain the plasma current [8]. Later on, it was understood that the primary mechanism for current drive is either anisotropic resistivity due to asymmetric perpendicular heating (Fisch-Boozer current) or asymmetric trapping (Ohkawa current) [9, 10] . In both mechanisms the wave-particle interaction acts through electron cyclotron resonance, also responsible for the ECE radiation. The ECCD technique can thus use waves to select electrons moving in the current-carrying direction and place them in a collisionless regime while imparting no parallel momentum. In that case, the rest of the particles will relax back to a Maxwellian distribution while the collisionless particles will still carry their original momentum. The role of non-thermal electrons in ECCD, in LHCD as well, was hence brought to the fore in the late seventies, in the first days of Radio Frequency driven currents in tokamak plasmas [11]. This time around, non-thermal electrons are the cure, not the disease. In both cases, it is important to be able to diagnose non-thermal electrons in tokamak plasmas, their production rate and dynamics, for a better understanding of the physical mechanisms in which they are involved. The goal of characterizing non-thermal electron distributions represents, even to this day, a very challenging investigation in tokamak plasmas. The goal is being addressed following different paths, such as the one presented in this research work, wich exploits the ECE radiation emitted by the plasma.

1.3 The electron distribution from cyclotron emission : a challenging investigation

Reconstructing the details of the electron distribution from the cyclotron emission is challenging. That is because the electron cyclotron emission is a macroscopic manifestation of processes that occur at the microscopic scale, involving the electron distribution. It is very well established in the literature how to obtain the ECE spectrum from the electron distribution. Challenging is to solve the inverse problem, that of obtaining the distribution from the ECE spectrum. The complexity arises from the spectrum itself, which is determined both by the density of (fast) electrons in phase space and the gradient of the magnetic field along the ECE line of sight. Electrons at different energies, with different velocity components with respect to the magnetic field, located at different locations along the line of sight, can satisfy the resonance condition and contribute to the ECE radiation. In addition, the ECE total radiation is not straightforwardly the sum of the single emissions. In fact, each emitting electron can absorb the radiation emitted by another electron in its neighborhood. It is the complicated convolution of the physical and the energy space contained in the ECE spectrum which makes it difficult to invert. Efforts to ease the inversion are made by constraining the regions in the physical and energy space which contribute to the radiation. This has been achieved in this thesis work, using an ECE configuration that views a constant magnetic field region in the plasma, a Vertical ECE.

1.4 Organization of this thesis

This general introduction is followed by the Chapter 2: **TCV and the non-thermal electrons**. In that chapter, we present TCV, the experimental device on which the research has been carried out. The chapter will touch upon the equipment that has supported this work.

In Chapter 3: **Theory of the Vertical ECE**, we review the theoretical background for electron distribution studies using electron cyclotron emission. The advantages of the vertical line of sight over the horizontal ones will be illuminated. The chapter will also afford a leap into the history of Vertical ECE studies in tokamaks.

The Chapter 4: **The Vertical ECE of TCV** will move from theory to present the diagnostic system on the tokamak. The design and performance of key components of the diagnostic will be presented, so as the conditions for operation, to which a particular attention will be dedicated.

In Chapter 5: **Calibration**, we describe the novel technique used to calibrate the diagnostic. The technique demonstrates the possibility of using the plasma itself as the calibration source for ECE diagnostics, at arbitrary line of sight and optical depth.

The results from the measurements of non-thermal electron distributions will be summarized in Chapter 6: **Experimental results**. The measurements were taken during Electron Cyclotron Current Drive and runaway electron experiments on TCV. In addition, an hybrid scenario combining both the calibration and the measurement of non-thermal electrons will be unveiled.

Chapter 7: **Reconstruction of the electron distribution**, finally, will open the discussion on the reconstruction of the electron energy distribution from the experimental measurements. Examples of reconstructed distributions will be shown.

The main achievements of this thesis, together with an outlook, will be discussed in Chapter 8: **Conclusion**.

2 TCV and the non-thermal electrons

2.1 The Tokamak

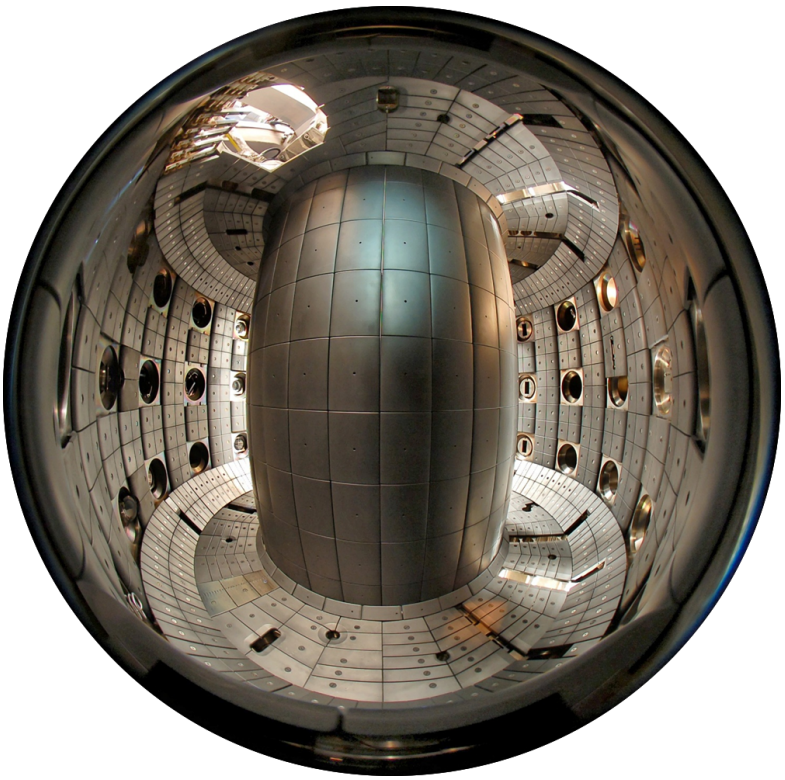

Figure 2.1: Inside TCV, the Tokamak à Configuration Variable. © *Swiss Plasma Center*.

TCV [12, 15, 16, 17, 18, 19, 20, 21, 22, 13, 14], the *Tokamak à Configuration Variable*, is the main experimental facility at the Swiss Plasma Center of EPFL. It is a medium-sized tokamak of major radius $R_0 = 0.88$ m, and minor radius $a = 0.25$ m. TCV is thus ~ 0.5 m wide and ~ 1.5 m high, making its vessel relatively elongated in shape, see TCV pictured in Figure 2.1. The elongation of TCV allows the realization of elongated plasma shapes in the vessel, also thanks to the set

of 16, independently powered, poloidal field coils. A wide variety of plasma shapes has been achieved on TCV. Those shapes include highly elongated plasmas and plasmas with negative triangularity explored for plasma confinement studies [23, 24, 25] and, even for studies of the effect of plasma shaping on runaway electron beam formation [26]. The shaping capability of TCV also allows studies of various, sometimes exotic, divertor configurations for heat exhaust purposes [27]. Recently, work performed on the TCV tokamak in collaboration with Google DeepMind has exploited the flexibility of TCV to demonstrate the control of the plasma position with artificial intelligence [28]. TCV is equipped, as well, with a set of 16 toroidal copper field coils which allows tokamak operations at a central magnetic field ~ 0.9 T $< B_0 < 1.54$ T. The ohmic heating of TCV plasmas is achieved with toroidal plasma currents up to $\sim$ 1 MA. The auxiliary heating system includes two Neutral Beam Injector systems, NBI and an Electron Cyclotron Resonance Heating/Current Drive, ECRH/ECCD system. In ~ 30 years of operations, TCV has been equipped with a large variety of diagnostic systems for various kinds of plasma measurements.
This chapter presents the heating and diagnostic systems on the TCV tokamak that are relevant for non-thermal electron studies.

2.2 Creating the fast electrons

2.2.1 The heating systems

The ECRH/ECCD system on TCV

TCV has a very powerful and flexible ECRH/ECCD system [29], composed of two gyrotrons at 82.7 GHz and nominal power ~ 680 kW, three gyrotrons at 118 GHz with nominal power ~ 480 kW and two dual frequency gyrotrons of nominal power ~ 1000 kW for heating either at 84 GHz or 126 GHz. That is, the total ECRH power installed on TCV is ~ 4800 kW for a machine volume of ~ 4 m^3. The polarization of the electromagnetic wave injected by the gyrotrons is usually selected to be the X-mode as this leads to better power absorption [30, 31]. The gyrotrons heat the plasma electrons by cyclotron resonance at either the second (X2) or the third (X3) harmonic of the cyclotron frequency. The gyrotrons are connected to launchers, which direct the beam into the plasma, and which are located on top ports, equatorial and upper-lateral ports as can be seen in Figure 2.2.
Current drive is achieved by imparting a parallel component, with respect to the plasma magnetic field, to the ECH wave vector. The ECCD experiments on TCV exploit the (X2) gyrotrons, in general combined to a launcher in an equatorial port of the machine. The schematic of one of the launcher is shown in Figure 2.3. In general, the location of the beam power deposition along the radial coordinate is controlled by the chosen value of the magnetic field. The toroidal and poloidal directions of the beam (in the reference frame of the plasma) are controlled by the launcher angles, the so-called toroidal angle, ϕ_{L}, and poloidal angle, θ_{L}. The launcher poloidal angle θ_{L} can be varied during discharges, for example to vary the toroidal direction of the injected beam in the plasma. The toroidal angle ϕ_{L} on the other hand can only be varied in between discharges.

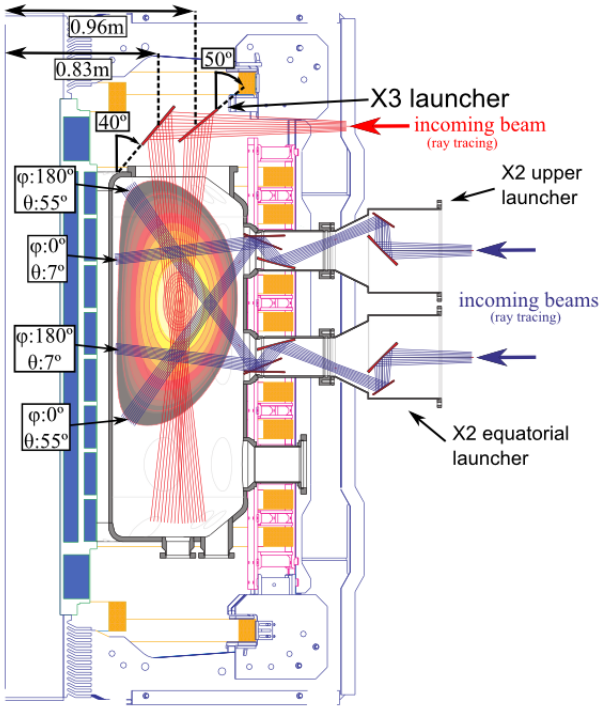

Figure 2.2: Drawing of a poloidal cross section of TCV with the ECRH ports.

The TCV ECRH/ECCD system is well suited for the creation of non-thermal electrons. The flexible use of the powerful system in various ECCD configurations allows the study of non-thermal electrons, which are created in the tail of the distribution for current drive.

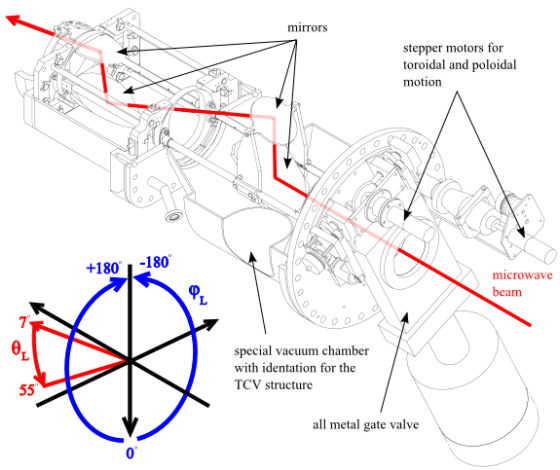

Figure 2.3: Drawing of an ECRH launcher with the gyrotron wave trajectory and the launcher degrees of freedom, θ_L and ϕ_L illustrated.

Neutral Beam Heating

The Neutral Beam Heating on TCV uses the two systems NBI-1 and NBI-2 [32, 33]. The NBI-1 injects deuterium atoms at a maximum energy of ~ 28 keV, for a beam power up to ~ 1300 kW. The NBI-2 injects hydrogen atoms of energies $\sim 50 - 60$ keV, with corresponding maximum power ~ 1000 kW. Once injected in the plasma, the neutrals are ionized and exchange their energy with both ions and electrons via Coulomb collisions. The heating of the electrons with NBH, which is of interest for our topic, happens in general at higher beam energy. At a certain critical energy the heating rate is similar for ions and electrons. When the beam energy is higher than the critical energy, the NBH power is transferred mostly to the electrons and in the opposite case, it is the ions that are mainly heated. An expression for the critical energy, E_{kc}, from [34] can be written as:

$$E_{\mathrm{kc}} = \left(\frac{3\sqrt{\pi}}{4}\right)^{2/3}\left(\frac{m_{\mathrm{ion}}}{m_{\mathrm{e}}}\right)^{1/3}\frac{m_{\mathrm{beam}}}{m_{\mathrm{ion}}}T_{\mathrm{e}} = 14.8\frac{A_{\mathrm{beam}}}{A_{\mathrm{ion}}^{2/3}}T_{\mathrm{e}}. \tag{2.1}$$

Calculation of the the critical energy with TCV parameters, using Equation 2.1 yields values of $E_{\mathrm{c}} \sim 9$ keV for deuterium injection and $E_{\mathrm{c}} \sim 4.5$ keV for hydrogen injection. The values are below the maximum values of beam energies of both NBI-1 and NBI-2. In a NBH injection with beam energy higher than the critical energy, it is likely that the beam will first heat the electrons. Then, the beam energy will decrease with collision up to the critical energy. As the beam continues through the plasma and loses energy until below the critical energy, the ions will then heated by the beam.

2.2.2 Runaway electrons on TCV

TCV is well poised for runaway electron studies. On TCV, control of the runaway beam position and real time control of loop voltage can be achieved. Moreover, the ECH system on TCV allows real time control of the location of the ECCD power deposition, useful to study, for example, the interaction of the runaway beam with Neoclassical Tearing modes (NTMs). Runaway electrons of energies from tens of keV to tens of MeV can be created on TCV. Runaways are created in low density discharges at relatively high plasma current, in the order of hundreds of kA. on TCV, the RE seed generation can happen at a peak density below $0.5 \times 10^{19}\mathrm{m}^{-3}$. In general, runaway electrons are generated when the collisional drag due to the friction force is insufficient to balance the acceleration of the electrons by the electric field . The electrons, in that case are more and more accelerated and run away. Two quantities are often used to assess the possibility of runaway electron formation: the Dreicer electric field E_{D}, and the critical electric field, E_{C}. The quantities E_{C} and E_{D} can be expressed as [35]:

$$E_{\mathrm{D}} = \frac{e^3 n_{\mathrm{e}} \log \Lambda}{4\pi\epsilon_0^2 T_{\mathrm{e}}} \quad ; \quad E_{\mathrm{C}} = \frac{e^3 n_{\mathrm{e}} \log \Lambda}{4\pi\epsilon_0^2 m_{\mathrm{e}} c^2} \tag{2.2}$$

where $\ln\Lambda$ is the Coulomb logarithm. The Dreicer field is a reference parameter for runaway electron formation, which scales like the slide-away threshold. The critical field is the value of electric field that allows a particle moving close to the speed of light to run away. That is, no runaway generation can occur at toroidal electric field below the critical field. On TCV, runaway electron seeds are generated at low density for electric field values $E/E_{\mathrm{C}} \sim 40$ and $E/E_{\mathrm{D}} \sim 6\%$. TCV is also equipped with a Massive Gas Injection system for disruption runaway studies. The System can inject large amounts of gas in the plasma including Deuterium, Helium, Neon, Argon, Krypton and Xenon. The gas is injected to induce a plasma disruption and, subsequently, a runaway electron beam. A remarkable work, reported in Reference [26] has exploited the MGI system to demonstrate on TCV the full conversion, from ohmic to runaway electron driven current. More experiments and theoretical work are to be done in the field on runaway electron studies, which has become of huge interest for the fusion community in the recent years. On TCV, runaway studies and fast electron studies in general rely on a large spectrum of diagnostic techniques, some well-established and others under development.

2.3 Diagnosing non-thermal electron distributions

We present in this section the TCV diagnostics, which can be used for non-thermal electron studies. The diagnostics are subdivided by the kind of radiation that is exploited.

2.3.1 X ray diagnostics

TCV is equipped with an in-vessel (HXRS) [36] and an ex-vessel (PMTX) Hard-X-Ray diagnostic. Both diagnostics provide, directly, quantitative information on the photons energy. The (HXRS) diagnostic can measure photon energies in the range $20 - 200$ keV and the (PMTX) can detect photons of energy above 150 keV. The detected photons are the result of Bremsstrahlung radiation from the slowing down of the fast electrons in the tokamak. The photon energies that are detected thus represent a lower limit of the electron energies. Those diagnostics are often used to verify if runaway electrons, above a certain energy, have been created during a plasma discharge. More quantitative information on the fast electrons require in principle some modeling efforts. A Hard-X-Ray Spectrometer is currently under development on TCV. The new diagnostic will have an improved sensitivity and energy resolution to photons with energies above ~ 300 keV. Here again modelling will be required to invert the measurement to obtain direct information on the non-thermal electrons energy.

2.3.2 Synchroton radiation diagnostics

A real-time multi-spectral imaging system (MANTIS) is used on TCV for runaway experiments [37]. The diagnostic provides synchroton images in flat-top conditions. The runaway energies, pitch-angles and spatial distributions can be reconstructed for the most energetic part of the distribution using the diagnostic [38, 39].

The Infrared Cameras, (IR) cameras, can also be used as a synchroton diagnostic during runaway electron beam studies on TCV. The IR cameras, by measuring the tiles temperature, can provide estimates of the heat flux reaching the targets.

2.3.3 VUV/UV/Vis and NIR spectroscopy

The Divertor Spectroscopy System (DSS) [40], composed of a vertical and a horizontal system, is used for RE beam studies on TCV. The diagnostic measures line emission from Hydrogen, Helium and Neon I, II and III. The ratio of the line intensities of the Neon species can provide qualitative information on the plasma temperature. The line emission from helium is used to assess the impurity content in the plasma.

2.3.4 Electron cyclotron emission diagnostics

The Electron Cyclotron Emission (ECE) diagnostic has been part of the non-thermal electron studies on TCV for about 20 years now. The ECE suite on TCV is composed of two horizontal ECE systems with antennas located at the low field side (LFS ECE) and at the high field side (HFS ECE) [41]. The diagnostics measure, with high time resolution, the cyclotron radiation from the plasma electrons. In general, the ECE is very sensitive to the presence of a population of non-thermal electrons. However, with a horizontal line of sight, it is often complicated to obtain quantitative information on the non-thermal population. This is because the radiation from a non-thermal electron that has reached the antenna cannot be attributed straightforwardly to a radial location in the plasma. That comes as a consequence of a difficulty in the determination of the energy of the non-thermal electrons. Results of non-thermal electrons measurement using the (HFS ECE) on TCV have been reported in Reference [42]. In those studies, the assumption of a bi-maxwellian electron distribution was used in order to match the measured intensity of the radiation.
This is where the Vertical ECE diagnostic comes in, with a great potential to complement the existing diagnostic for non-thermal electron studies. The Vertical ECE, unlike the horizontal ECE systems, would ideally not have the ambiguity on the radial location of non-thermal emission. Unlike the X-ray diagnostics which provide the photon energy, the Vertical ECE can provide information, directly on the energies of the non-thermal electrons. In addition, The Vertical ECE has the potential to resolve the lower energies of the distribution. The diagnostic can be very useful for non-thermal electrons created during ECCD or for runaway electrons of energies in the order of a few hundreds of keV. The theory of the Vertical ECE diagnostic, its potential, and its application on previous tokamaks will be presented in Chapter 3. Next are presented the tools that have been used to support this thesis research.

2.4 Tool kit for this research

2.4.1 The soft equipment

The code SPECE

The code SPECE [43] has been an essential tool for this research work. SPECE originated from the ECRH/ECCD beam tracing code GRAY [44] and was developed as a support tool for the oblique ECE diagnostic on JET [45]. The main features of SPECE include the equation of radiation transfer solved in general tokamak equilibrium, the geometric optics approximation and cold plasma dispersion for the wave propagation. The code calculates the EC emission in a relativistic description for Maxwellian and multi-Maxwellian distribution functions. The code can be used for arbitrary line of sight, and effects such as the antenna polarization and finite beam-width are included in SPECE. The ECE localization and spatial resolution are quantified in SPECE, where an attempt to include wall effects is performed through a simplified model for multiple wall reflections, generalising an approach proposed by Costley in [46]. Prior to using SPECE as a synthetic diagnostic for Vertical ECE, SPECE was used to simulate the LFS ECE radiation temperature. The satisfying result of the simulation is shown in Figure 2.4.

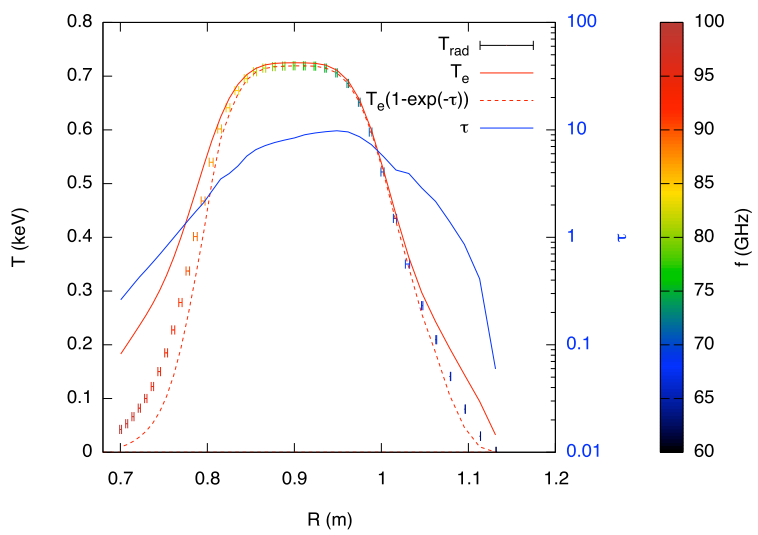

Figure 2.4: SPECE used in a LFS ECE configuration on TCV: In the tokamak center, the simulated radiation temperature, T_{rad}, coincides with the local electron temperature, T_{e}, as expected in optically thick thermal plasmas.

It is important to note that SPECE has been used for this research, mainly for simulations involving Maxwellian electron distributions. In fact, the model for non-Maxwellian distribution implemented in SPECE is a superposition of Maxwellian distributions drifting along the magnetic field. The distribution function $F(\psi, \vec{u})$, from the simplified model can be explicitly

written as [47]:

$$F(\psi, \overrightarrow{u}) = \Big(1-\xi(\psi)\Big) F_{M,T_b}(|\overrightarrow{u}|)+\xi(\psi)\sum_{i=1}^{N} F_{M,T_{tail}}(|\overrightarrow{u}-\overrightarrow{u_{0,i}}|)\ , \xi(\psi) = \xi_0 \exp\left[-\frac{(\psi-\psi_0)^2}{2\Delta\psi^2}\right] \tag{2.3}$$

here ψ labels each of the magnetic surfaces, $\overrightarrow{u}$ indicates the electron velocity vector, T_b and T_{tail} respectively the bulk and tail temperature. ξ is defined as the ratio of tail electron density to the bulk electron density. The model of the drifting Maxwellians implemented in SPECE is perhaps one of the current limitation of the code. In fact, a more generalized model for the distribution would be better suited for studies of non-Maxwellian distributions created during runaway electrons and ECCD scenarios. This has motivated the initiation of the development of another code on TCV, which could use the modelled electron distribution function from kinetic codes to predict the ECE spectra. SPECE has however been particularly useful for ECE simulations of thermal plasmas, which is relevant for calibration and interpretation of the diagnostic data.

LUKE

The 3-Dimensional bounce-averaged Fokker-Planck code LUKE [48] is used for the calculation of the electron distribution function. To calculate the distribution, LUKE solves the equation

$$\frac{\partial F}{\partial t} = C(F) + Q^{\mathrm{RF}}(F) + E(F) + T(F), \tag{2.4}$$

where C is the collision operator, Q^{RF} the RF wave operator. E and T are respectively the ohmic and radial transport operators. The RF wave operator uses the embedded ray-tracing code C3PO for the calculation of the wave propagation in the plasma. Simulation of the electron distribution with LUKE serves as theoretical support for the experimental investigation of the distribution function, using the Vertical ECE diagnostic. In Figure 2.5 a framework combining LUKE simulations and Vertical ECE measurement is sketched.

SOFT

The Synchrotron-detecting Orbit Following Toolkit (SOFT),is a synthetic diagnostic primarily developed for the study of bremsstrahlung and synchrotron radiation from fast electrons, but with some capabilities of simulating cyclotron emission as well [49]. As a synthetic ECE diagnostic, SOFT is used to predict the cyclotron radiation from an ensemble of electrons, with distribution obtained from a kinetic calculation (e.g. LUKE). SOFT does not include the ECE antenna modelling nor any interaction of the ECE wave with the plasma. SOFT is therefore applicable in the limit of a transparent plasma and only for qualitative evaluation of ratios of emissions at given harmonics and polarizations.

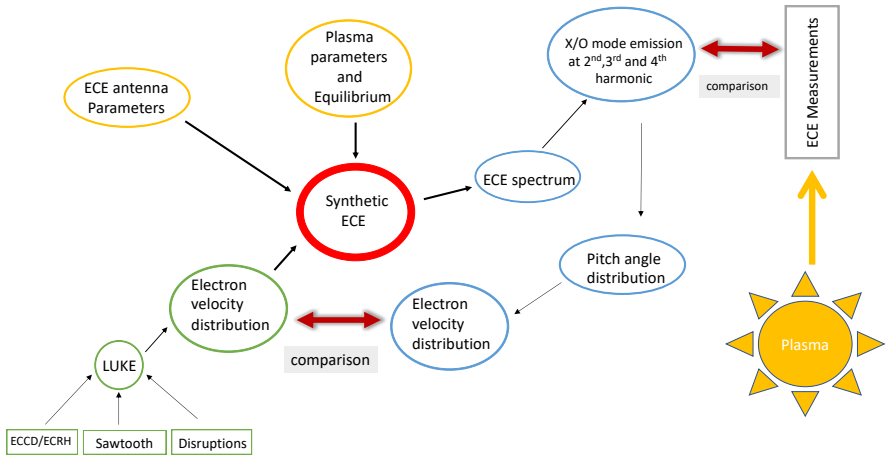

Figure 2.5: Combining LUKE simulations and Vertical ECE measurement for electron distribution function studies.

3 Theory of Vertical ECE

3.1 Introduction

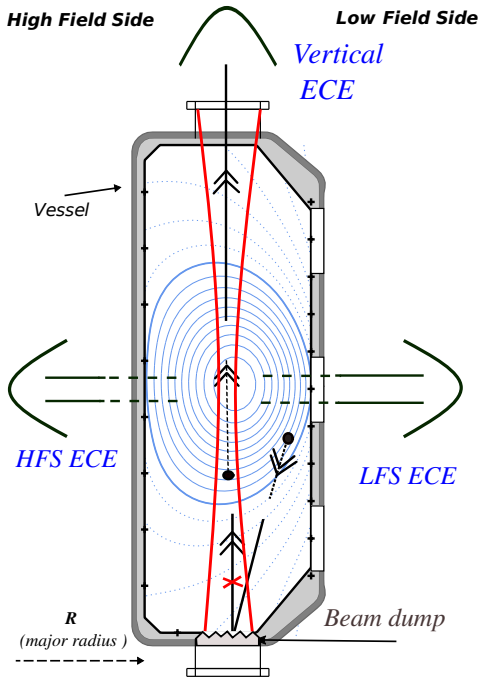

Figure 3.1: Illustration of ECE configurations on TCV.

ECE has been used with success over the years, to diagnose plasma parameters such as the electron temperature and its fluctuations. For non-thermal distribution studies, a Vertical ECE configuration has come into play since it can overcome some of the limitations of the horizontally viewing ECE. With horizontal lines of sight, the radiation from a non-thermal electron can originate in different regions along the line of sight, depending on the energy of the electron. This issue can be avoided if the line of sight is vertical. In the case of a vertical line of sight, the ECE spectrum broadening due to the magnetic field gradient can be reduced, allowing a more direct determination of the electron energies. Those are some of the reasons

why in the 1980s and 1990s, works performed by Luce on PLT [8], Kato and Hutchinson on ALCATOR [50], Giruzzi on TORE SUPRA [51, 52, 53], focused on a Vertical ECE configuration for the characterization of non-thermal electrons. While the advantages of the Vertical ECE approach were promising, the configuration also came with its own limitations. In fact, in the Vertical ECE configuration, the emission from a non-thermal electron can compete, at the same frequency with thermal radiation from different regions in the plasma. This happens if the line of sight is not isolated from wall reflected radiation. We will refer to this issue as the background radiation issue. To cope with background radiation, the recommendations that emerged from the early applications of Vertical ECE were to use retro-reflectors or microwave beam dumps at the termination of the line of sight, as illustrated in Figure 3.1. These solutions, which are required to limit the background pollution, are useful when the refraction in the plasma does not shift the line of sight out out of the dump or retro-reflector. With the isolation of the line of sight, it can be needed, additionally to constraint either the density or the frequencies in order to limit the effect of refraction. In the early 1990s, Vertical ECE studies on DIII-D were, as a matter of fact, limited to the higher frequencies to mitigate the effects of plasma refraction [54]. Higher frequencies meaning higher harmonics, the Vertical ECE diagnostic on DIII-D had to deal with the severe harmonic overlap characterizing the higher harmonic region of the ECE spectrum. This chapter provides some theoretical concepts in order to enlighten the merits and the limitations of the Vertical ECE.

3.2 Vertical ECE resonance

The literature provides detailed derivations of the general ECE resonance condition, see References [55] and [56]. In this section, we only summarize the steps to derive the vertical ECE resonance condition.
We start from the motion of an electron in a static magnetic field $\overrightarrow{B}$, which is governed by the equation

$$\frac{\mathrm{d}}{\mathrm{dt}}(\gamma m_{\mathrm{e0}}\overrightarrow{v_{\mathrm{e}}}) = -e(\overrightarrow{v_{\mathrm{e}}} \times \overrightarrow{B}), \tag{3.1}$$

where m_{e0} is the electron rest mass, e the absolute value of the electron charge; v_{e} the electron velocity and $\gamma = (1 - \frac{v_{\mathrm{e}}^2}{c^2})^{-1/2}$ is the relativistic factor . Taking the geometry as in Reference [55] with the magnetic field along the z−direction (x− and y−directions perpendicular to $\overrightarrow{B}$), Equation 3.1 can be solved for the electron displacement, $\overrightarrow{\rho}$

$$\overrightarrow{\rho} = \hat{x}\frac{\beta_\perp}{\omega_{\mathrm{ece}}}\sin(\omega_{\mathrm{ece}}t) - \hat{y}\frac{\beta_\perp}{\omega_{\mathrm{ece}}}\sin(\omega_{\mathrm{ece}}t) + \hat{z}\beta_{||}t \tag{3.2}$$

and for and the normalized electron velocity, $\overrightarrow{\beta} = \overrightarrow{v_{\mathrm{e}}}/c$

$$\overrightarrow{\beta} = \hat{x}\beta_\perp\cos(\omega_{\mathrm{ece}}t) + \hat{y}\beta_\perp\sin(\omega_{\mathrm{ece}}t) + \hat{z}\beta_{||} \tag{3.3}$$

with $\omega_{\mathrm{ece}} = eB/m_{\mathrm{e0}}$, the orbital frequency of the electron, also known as the fundamental electron cyclotron frequency. ω_{ece} should not be mistaken to the relativistically downshifted cyclotron frequency, $\omega_{\mathrm{ecr}} = \omega_{\mathrm{ece}}/\gamma = eB/m_{\mathrm{e}}$, as $m_{\mathrm{e}} = \gamma m_{\mathrm{e0}}$. $\beta_{\parallel}$ and $\beta_{\perp}$ represent respectively the components of the electron velocity parallel, and perpendicular to the magnetic field. The Lorentz force causes the spiral motion of the electron around the magnetic field, as found in Equation 3.2. Knowing the electron motion and acceleration, it is possible to calculate the differential power, emitted by a single electron, per unit frequency, and per unit solid angle:

$$\frac{\mathrm{d}^2P}{\mathrm{d}\Omega_{\mathrm{s}}\mathrm{d}\omega} = \frac{e^2\omega^2}{8\pi^2\epsilon_0 c}\sum_{n=1}^{\infty}\left\{\left(\frac{\cos\Theta-\beta_{\parallel}}{\sin\Theta}\right)^2 J_n^2\left(\beta_{\perp}\frac{\omega}{\omega_{\mathrm{ecr}}}\sin\Theta\right)+\beta_{\perp}^2 J_n'^2\left(\beta_{\perp}\frac{\omega}{\omega_{\mathrm{ecr}}}\sin\Theta\right)\right\} \times\frac{\delta[(1-\beta_{\parallel}\cos\Theta)\omega-n\omega_{\mathrm{ecr}}]}{1-\beta_{\parallel}\cos\Theta}. \tag{3.4}$$

Equation 3.4 is also known as the Schott-Trubnikov formula (see References [57, 56, 55] for a detailed derivation). In Equation 3.4, n is the harmonic number, J_n is the nth order bessel function of the first kind and J_n' its derivative with respect to the argument, $\beta_{\perp}\frac{\omega}{\omega_{\mathrm{ecr}}}\sin\Theta$. The angle Θ is the angle of observation, measured with respect to the direction of the magnetic field. In the case of perpendicular observation, as we assume for vertical ECE, Equation 3.4 simplifies to

$$\frac{\mathrm{d}^2P}{\mathrm{d}\Omega_{\mathrm{s}}\mathrm{d}\omega} = \frac{e^2\omega^2}{8\pi^2\epsilon_0 c}\sum_{n=1}^{\infty}\left\{\beta_{\parallel}^2 J_n^2(\beta_{\perp}\frac{\omega}{\omega_{\mathrm{ecr}}})+\beta_{\perp}^2 J_n'^2\left(\beta_{\perp}\frac{\omega}{\omega_{\mathrm{ecr}}}\right)\right\}\times\delta[\omega-n\omega_{\mathrm{ecr}}]. \tag{3.5}$$

The δ function in Equation 3.5 represents the resonance condition. The ECE power is radiated if

$$\omega = n\omega_{\mathrm{ecr}} = n\frac{eB}{\gamma m_{\mathrm{eo}}}. \tag{3.6}$$

In tokamak geometry, the magnetic field depends on the major radius, R, as $B \sim 1/R$. The electron cyclotron emission frequency in perpendicular propagation is then proportional to

$$\omega \sim \frac{n}{\gamma R}. \tag{3.7}$$

From Equation 3.7 we note that, for a fixed harmonic n, there exist multiple combinations of energy γ, and location R, satisfying the resonance condition. This has been anticipated in Section 3.1 as a limitation of horizontally viewing ECE. Assuming a constant major radius along the Vertical ECE line of sight, one finds from Equation 3.7 that the ECE frequency depends solely on the harmonic number and on the electron energy. If the radiation can be assigned to a single harmonic, the energy broadening would then be the only responsible for the frequency broadening, allowing a direct determination of the electron energy from the radiation frequency.

More generally, the resonance condition from Equation 3.4 can be written as

$$\omega = \frac{ne}{m_{\mathrm{eo}}}\frac{B}{\gamma[1-\beta_{\parallel}\cos\Theta]}. \tag{3.8}$$

From Equation 3.8, three broadening mechanisms of the frequency can be identified. The broadening from the relativistic mass increase through γ, previously discussed. The broadening from the Doppler effect via the term $[1 - \beta_{\|} \cos \Theta]$ and from the magnetic field (B) broadening. In an experimental configuration, all three broadening mechanisms will be present since the line of sight of the antenna cannot be infinitely narrow. The finite size of the antenna pattern in the radial and toroidal directions will introduce respectively, the magnetic field and Doppler broadening. Those broadening mechanisms should be evaluated to assess the energy resolution of the Vertical ECE diagnostic.

3.3 The harmonic overlap

The previous section showed, using the Vertical ECE resonance, the possibility of directly determining of the electron energy from the radiation frequency of electron cyclotron emission. The condition is that the ECE should come from a fixed harmonic. From Equation 3.7, we note that the higher the harmonic number, the higher the electron energy emitting at a fixed frequency. We calculate the maximum energy to avoid harmonic overlap between the harmonics n and $n+1$, as

$$E_{\max} = \frac{m_{\text{eo}} c^2}{n} \sim \frac{511\text{keV}}{n}. \tag{3.9}$$

Equation 3.9 shows how severe is harmonic overlap at higher harmonics, compared to the lower ones. That is due to the decreasing ratio of consecutive harmonic frequencies, with increasing harmonic number. The maximum energy that can be measured without harmonic overlap, and the ratio of harmonic frequencies, Ω_{n+1}/Ω_n are plotted in Figure 3.2. Measurements below the fundamental frequency push the energy boundary for harmonic overlap above ~ 511 keV. This energy boundary is below ~ 100 keV already from the 5th harmonic.

3.4 Background radiation

In order to assign an electron energy to a radiation measured at a given frequency, we need to be sure that the radiation originated within the vertical chord. That is, the vertical line of sight needs to be isolated at its termination on the tokamak wall. If the chord is not isolated, radiation originating out of the vertical chord can reach the Vertical ECE antenna after multiple reflections off the wall. A crude assessment of the magnitude of this issue, as it has been done in Reference [50], is considering the tokamak vessel as a back-body cavity. The relationship between a single chord integrated intensity I_{sc}, and the intensity out of the cavity hole, I_{cav} is given by

$$I_{\text{cav}} = \frac{I_{\text{sc}}}{1 - R_{\text{wall}}}, \tag{3.10}$$

with R_{wall} being the reflectivity of of the cavity wall. Taking the reflectivity to be ~ 0.99 , the single chord intensity will be masked by the intensity from multiple reflections out of the cavity,

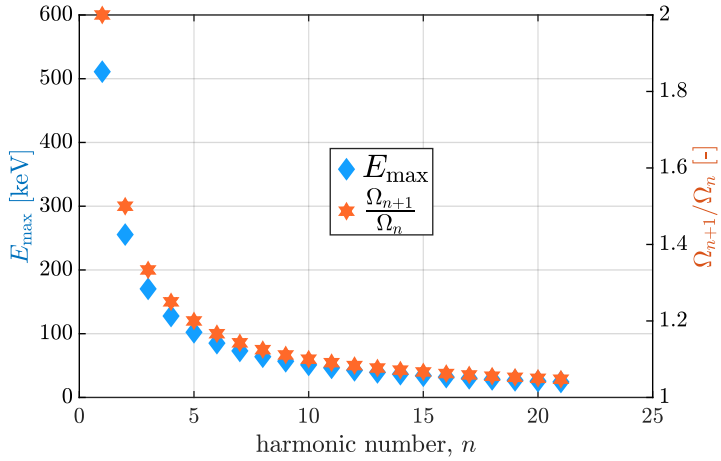

Figure 3.2: Maximum energy for harmonic overlap and ratio of the harmonic frequencies.

$I_{\text{cav}} \sim 100\ I_{\text{sc}}$. To have a single chord intensity, $I_{\text{sc}} \sim 10\ I_{\text{cav}}$, the reflectivity at the opposite side of the cavity hole should be $R_{\text{wall}} \sim 0.01$. Thus the isolation of a vertical chord would require for example a microwave absorber of the lowest possible reflectivity. A more rigorous calculation, estimating the emission intensity from an assumed non-Maxwellian electron distribution and comparing it to the black-body intensity at a given temperature and frequency gives more or less the same result on the required value of reflectivity.

3.5 The Cyclotron radiation from single electrons

We use Equation 3.5 from Section 3.2 to express the radiation intensity from single particles. The equation is composed of two terms. The terms are associated with the radiation with electric field parallel and perpendicular to the static magnetic field. In general, we refer to the two radiations as the O-mode and the X-mode radiation respectively. The emissivity for the O-mode is

$$\eta_{\text{O}} = \frac{e^2\omega^2}{8\pi^2\epsilon_0 c}\sum_{n=1}^{\infty}\beta_{\parallel}^2 J_n^2(n\beta_{\perp})\delta[\omega - n\omega_{\text{ecr}}], \tag{3.11}$$

and that of the X-mode,

$$\eta_{\text{X}} = \frac{e^2\omega^2}{8\pi^2\epsilon_0 c}\sum_{n=1}^{\infty}\beta_{\perp}^2 J_n'^2(n\beta_{\perp})\delta[\omega - n\omega_{\text{ecr}}]. \tag{3.12}$$

It is interesting to note that the X-mode emissivity has no dependence on the electron parallel velocity. The O-mode emissivity contrary-wise is sensitive to the parallel velocity of the emitting electron, which is of great importance for electron distribution analysis. A small argument

expansion of the bessel functions in Equations 3.11 and 3.12 yields

$$\frac{\eta_{\mathrm{X}}}{\eta_{\mathrm{O}}} \approx \frac{1}{\beta_{\parallel}^{2}}. \tag{3.13}$$

We call θ_{p}, the angle between the electron velocity and the magnetic field vectors, also known as the pitch angle,

$$\theta_{\mathrm{p}} = \tan^{-1}\left(\frac{\beta_{\perp}}{\beta_{\parallel}}\right), \tag{3.14}$$

such that $\theta_{\mathrm{p}} = 90°$ in a pure gyromotion of the electron. The O-mode and X-mode emissivities computed for selected values of pitch angles are shown in Figures 3.3b, 3.3a and 3.5 . The calculation of the emissivity was performed for a value of $\omega/\omega_{\mathrm{ece}} \sim 2.7$. Since the frequency is fixed, the ratio of the harmonic number to the electron energy is also fixed. At fixed frequency, the higher the electron energy, the higher would be the harmonic contributing to the the radiation. From the calculation it can be seen how the values of the emissivities, for both modes, depend strongly on the pitch angle. The O-mode emissivity peaks at a value of pitch angle $\theta_{\mathrm{p}} \sim 65°$ and the X-mode peaks at $\theta_{\mathrm{p}} = 90°$. The results of single particle emissivity suggest that, with a Vertical ECE chord, the emission will be dominated in general by high pitch angle electrons present in the plasma. That is provided there is no strong anisotropy, like in the case of highly energetic runaway electrons for example, whose motion is strongly enhanced in the parallel direction. The Figure 3.4 shows the emissivity in both polarizations, calculated for selected values

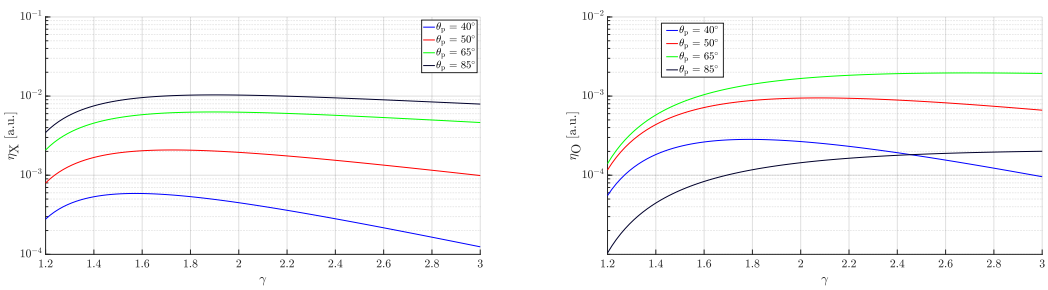

(a) X-mode

(b) O-mode

Figure 3.3: Emissivity as a function of energy for selected values of pitch angle.

energy as a function pitch angle. The general behaviour from the curve consolidates the fact that the X-mode emissivity peak at at high pitch angle, while the O-mode near about $\sim 65°$. In the case of O-mode, the intensity values increase with increasing energy (γ). The X-mode case is interesting, as it shows the highest values of emissivity around $\gamma = 1.8 - 2$. In both cases, the lowest values of single particle emissivities are seen for a value of $\gamma \sim 1.2$ regardless of the pitch angle value.

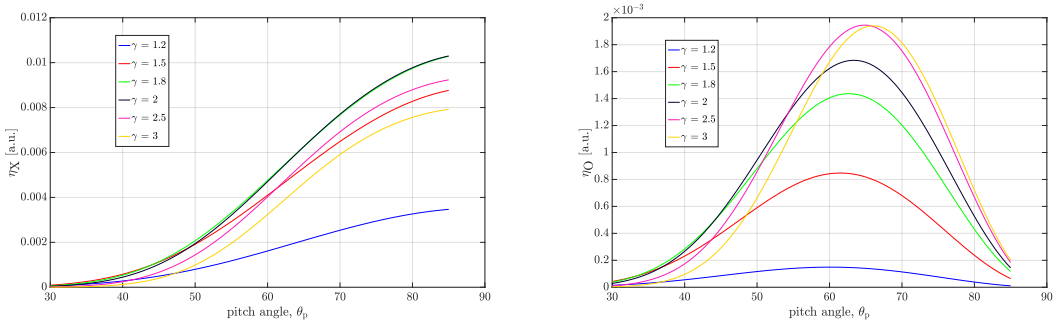

(a) X-mode

(b) O-mode

Figure 3.4: Emissivity as a function of pitch angle for selected values of energy.

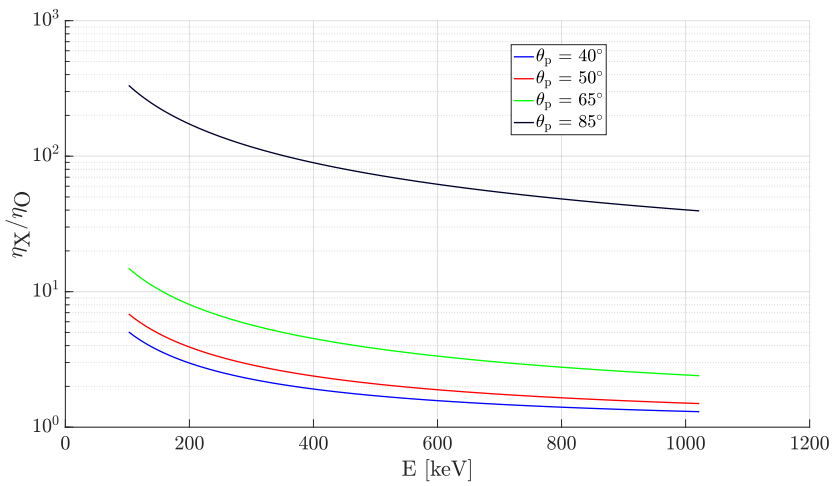

Figure 3.5: Ratio of X-mode to O-mode emissivity as a function of energy.

3.6 The Electron distribution

The purpose of this section is to illustrate a method to infer the electron energy distribution from Vertical ECE data. The method assumes that the total intensity is simply the sum of the individual contributions, thus neglecting collectives effects in the plasma.

We can write the emission from an ensemble of particles, with distribution in momentum $\overrightarrow{p}$ as

$$j = \int \eta F(\overrightarrow{p}) \mathrm{d}\overrightarrow{p}. \tag{3.15}$$

In theory, the emissivity j of the ensemble of electrons should be integrated along the vertical chord to obtain the Vertical ECE intensity. Assuming j is the line-averaged intensity measured by the Vertical ECE, Equation 3.15 needs to be inverted to obtain the electron distribution,

$F(\overrightarrow{p})$. Examples of distributions that can be inferred from the inversion of Equation 3.15 will be shown in the following subsection. We note that in Equation 3.15 the single particle emissivity η can be that of the X-mode , η_{X}, that of the O-mode η_{O} or that of harmonics of the X- and O-modes. The emissivity η and the intensity j can thus be associated with different harmonics and polarizations, with the same electron distribution. That is, the inversion of the ECE spectrum needs independent measurements at different polarizations or harmonics in order obtain a fitting of the energy distribution.

3.6.1 A delta distribution

The inversion technique relying on a delta distribution, a simplifying model, was proposed in Reference [8]. In the technique, the distribution $F(\overrightarrow{p})$ is rewritten as $F(p, y)$, with $y = \cos(\theta_{\mathrm{p}})$. The distribution $F(p, y)$ is taken as the delta distribution normalized as

$$F(p, y) = \frac{n_{\mathrm{fast}}}{2\pi p_0^2}\delta(p - p_0)\delta(y - y_0), \tag{3.16}$$

where n_{fast} is the density of the electrons with momentum p and pitch angle y_0. The delta-type distribution assumes that the electrons of density n_{fast}, all have momentum p_0 and pitch angle y_0. The first assumption is actually plausible in experimental conditions with minimized harmonic overlap and background pollution. In those conditions, the intensity measured at a given frequency corresponds to a given energy. The assumption of all electrons at the same pitch angle is a much stronger assumption. That is, the objective of the technique is that of presenting the regions of the pitch angle space which contribute the most to the measurement. y_0 can be seen as an emission weighted pitch angle. Using the distribution of Equation 3.16 in Equation 3.15, with the expression of the emissivities in Equations 3.11 and 3.12, we obtain after integration, the expression of the X-mode intensity,

$$j_{\mathrm{X}} = \frac{e^2\omega}{8\pi^2\epsilon_0 c} n_{\mathrm{fast}} p_0 (1 - y_0^2) J_n'^2\left(np_0\sqrt{1 - y_0^2}\right) \tag{3.17}$$

and that of the O-mode intensity,

$$j_{\mathrm{O}} = \frac{e^2\omega}{8\pi^2\epsilon_0 c} n_{\mathrm{fast}} p_0 y_0^2 J_n^2\left(np_0\sqrt{1 - y_0^2}\right) \tag{3.18}$$

The weighted pitch angle y_0 can be determined from the ratio $j_{\mathrm{X}}/j_{\mathrm{O}}$ which is a monotonic function of of y_0. The quantity n_{fast}, can then be obtained from a single polarization intensity using one of the Equations 3.17 or 3.18. We note that the assumption regarding the pitch angle distribution is close to reality in some experimental scenarios. The runaway electrons in tokamak plasmas are accelerated mainly in the parallel direction. The fact that $\beta_{\parallel} \gg \beta_{\perp}$ for all the runaway in an energetic runaway beam makes it that the detected radiation in that case can truly be assigned to a narrow region in the pitch angle space. If in those scenarios, the extent of the harmonic overlap is also reduced, the Vertical ECE diagnostic can provide important

information on the line averaged distribution of the electrons.

3.7 Further consideration on the theory of Vertical ECE

Regarding the lack of parallel asymmetry

A limitation of the vertical viewing ECE, just as any perpendicular ECE measurement, is the lack of information on the asymmetry in the direction parallel to the magnetic field. This limitation is relevant for the analysis of asymmetric distributions, which can be found in runaway electron discharges.

Regarding the finite density effects

To neglect collective effects in the treatment, the assumption of tenuous plasma is made. Tenuous plasmas are plasmas in which the inequality $\omega \gg \omega_{\mathrm{pe}}$ holds. Depending on the plasma density and the harmonic number, the inequality can no longer hold and collective plasma effects should be taken into account. In those cases, the plasma refractive index can differ appreciably from unity. Plasma scenarios for low density runaway experiments allow the assumption of tenuous plasma even at the low harmonics. As an example, in a low density discharge at peak density $\sim 0.5 \times 10^{19}\mathrm{m}^{-3}$, we can have $\omega \sim 6\ \omega_{\mathrm{pe}}$ for the third harmonic emission. At higher densities, for an ECCD discharge at, say, peak density $\sim 2.5 \times 10^{19}\mathrm{m}^{-3}$, the result for the same harmonic would be $\omega \sim 2\ \omega_{\mathrm{pe}}$. The density effects, when the assumption of tenuous plasma does not hold, should be included in the calculation of the emissivity in Equation 3.15.
The integral of Equation 3.15, considering the finite density effects, can be written [50] in X-mode as

$$j_{\mathrm{X}} = \frac{e^2\omega^2}{8\pi^2\epsilon_0 c}\frac{N_r^2}{N_{\mathrm{X}}}\int (N_{\mathrm{X}} K J_n \gamma + p_\perp J_n')^2 \frac{1}{\gamma^2}\delta[\omega - n\omega_{\mathrm{ecr}}]F(\overrightarrow{p})\mathrm{d}\overrightarrow{p} \tag{3.19}$$

and in O-mode

$$j_{\mathrm{X}} = \frac{e^2\omega^2}{8\pi^2\epsilon_0 c}\frac{N_r^2}{N_{\mathrm{O}}}\int (p_\parallel J_n)^2 \frac{1}{\gamma^2}\delta[\omega - n\omega_{\mathrm{ecr}}]F(\overrightarrow{p})\mathrm{d}\overrightarrow{p}. \tag{3.20}$$

The additional terms in Equations 3.19 and 3.20 are the ray refractive index N_r and the X- and O-mode refractive indices, N_{X} and N_{O}, which in this case differ from unity. We note in the modified X-mode emission coefficient a factor K, which reduces to zero when density effects are neglected. An expression of the factor K is given (see Reference [50] again) by [50]

$$K \equiv \frac{\omega_{\mathrm{pe}}^2\omega_{\mathrm{ece}}\omega}{(\omega^2 - \omega_{\mathrm{pe}}^2) - \omega_{\mathrm{ece}}^2\omega^2}, \tag{3.21}$$

where $\omega_{\mathrm{pe}}^2 = \frac{n_{\mathrm{e}}e^2}{m_e 0\epsilon_0}$ is the plasma electron frequency. An expression for the ray refractive index

at arbitrary angle Θ, taken from the Reference [58] is

$$N_{\mathrm{r}}^2 = \left| N_{\mathrm{X/O}}^2 \sin\Theta \frac{\left[1+\left(\frac{1}{N_{\mathrm{X/O}}}\frac{\partial N_{\mathrm{X/O}}}{\partial\Theta}\right)^2\right]^{1/2}}{\frac{\partial}{\partial\Theta}\left(\frac{\cos\Theta+\left(\frac{1}{N_{\mathrm{X/O}}}\frac{\partial N_{\mathrm{X/O}}}{\partial\Theta}\right)\sin\Theta}{\left[1+\left(\frac{1}{N_{\mathrm{X/O}}}\frac{\partial N_{\mathrm{X/O}}}{\partial\Theta}\right)^2\right]^{1/2}}\right)} \right| . \tag{3.22}$$

The X- and O-mode refractive indices, N_{X} and N_{O} can be obtained directly from the Appleton-Hartree cold plasma dispersion relation [59]. The corrections in the emission coefficient are then of three essential types. The first type is the enhancement of the emission coefficient by the term $N_r^2/N_{\mathrm{X/O}}$. The others are the K factor, to be included in the integral of the X-mode coefficient, and the change in the Bessel argument, induced by the change in the k vector, due to the finite density effects.

3.8 Summary

In theory, details of non-thermal electron distributions can be inferred from Vertical ECE measurements. The measurement along a vertical chord in the plasma reduces the broadening due to the magnetic field and allows direct determination of the electron energy. That is provided the effects of harmonic overlap and background radiation are prevented or mitigated. Single particle calculation allow quantitative assessment of the radiation that will be measured in experiments. In general, measurements at multiple polarizations at the lower harmonics can yield information on the electron pitch angle distribution at given energies. Example of distribution function that can be obtained have been shown with analytic derivation of the electron density in phase space. The derivation neglected the re-absorption of the emission in the plasma, taking for granted that we are in a tenuous plasma limit.
The Vertical ECE appear to be well poised for measurements of runaway electrons in low density plasmas. In those plasma scenarios, the assumption of tenuous plasma can hold, so as the assumption of an average pitch angle for all the electrons. A delta distribution, as the one presented, can provide interesting insights on the runaway electron distribution. Further, the plasma density in runaway electron can be low enough to limit the effects of refraction, thus allowing a good control of the multiply reflected radiation. In low density runaway scenarios, the issue of harmonic overlap can also be avoided, measuring low energy runaway electrons, so called startup runaways. The distribution that will be found, will however be a line average distribution, blind to the parallel asymmetry since the determined pitch angle would be, $y_0 = \cos(\theta_{\mathrm{p0}}) = \cos(-\theta_{\mathrm{p0}})$. However, for runaways it is not such a limitation since the sign of θ_{p} can be readily obtained from the sign of the electric field.

In ECCD scenarios, more modest energies can be attained by electrons, in principle. For the ECCD wave absorption, the electron density should necessarily be high and collective effects might be important. Types of distributions, other than delta distributions can be more appropriate for ECCD electron distributions.

4 The Vertical ECE of TCV

The previous chapter on the theory of Vertical ECE raised a red flag on the background radiation, which should be prevented to ease the interpretation of Vertical ECE measurements. Acknowledging recommendations from previous studies on Alcator C [50], PLT[8] and DIII-D [54], TCV was first of all, equipped with a viewing dump to prevent background pollution [60]. The design and performance of the viewing dump will be presented in this chapter, in Section 4.3, preceded by the description of the radiometer for the Vertical ECE in Section 4.1. Section 4.2 is dedicated to describing the optical arrangement of the antenna which, terminating on the dump, produces a vertical line of sight with finite dimensions in the horizontal plane. Section 4.4 is a study of the plasma conditions required for Vertical ECE measurements with the available components of the diagnostic. The study leads to a window of plasma operations that can guarantee measurements of non-thermal emission from an isolated vertical region of the plasma, without harmonic overlap. Subsequently the estimation of the energies and energy resolution observable by the system will be presented. These estimations, presented in Section 4.5 will conclude the chapter.

4.1 Radiometry for the Vertical ECE

4.1.1 Overview

The detection systems for ECE diagnostics can be divided into two main categories: quasi-optical instruments and guided-wave instruments. Quasi-optical instruments such as spectrometers and Michelson interferometers are used to cover a large spectral range at the expenses of a good spectral and temporal resolution. Guided wave techniques, such as heterodyne radiometers, in the other hand, are often used for frequency ranges below $\sim 250\,\mathrm{GHz}$. The heterodyne radiometers can offer high temporal and spectral resolution together with a good sensitivity in a moderate bandwidth. The frequency range for ECE measurements depends on the specific application and on the strength of the magnetic field, which determines the fundamental cyclotron frequency ($\Omega_{\mathrm{ece}}\ [\mathrm{GHz}] \propto 28nB$) . Electron temperature measurements in tokamaks are often performed at the first two harmonics of the cyclotron frequency. In a low field machine

such as TCV ($0.9\ \mathrm{T} < B_0 < 1.54\ \mathrm{T}$), ECE measurements have been achieved in the past for frequencies up to ~ 110 GHz. That is why heterodyne radiometers have historically been part of the ECE detection system on TCV, either for the HFS ECE [61] or the LFS ECE [62]. A detection system that includes heterodyne radiometers was naturally chosen for Vertical ECE measurements. This solution allows us to probe non-thermal ECE in the low harmonic region of the spectrum, and to re-use some of the components from the existing ECE systems on TCV. Figure 4.1 shows a block diagram of the Vertical ECE detection system. The Radio Frequency (RF) radiation from the plasma, typically in the frequency range $30 - 200$ GHz, travels in the transmission line to reach the microwave components of the detection system. The microwave components include a set of notch filters in the front face to protect the system against the ECRH power which may reflect off the vessel to reach the transmission line. A variable power attenuator can be used in series to fine-tune the intensity of the incoming power. This is for practical importance as the ECE intensity depends on the plasma scenario and can greatly vary with the presence of non-thermal electrons. A 3 dB directional coupler shares the filtered RF power into the different branches of the heterodyne receiver.

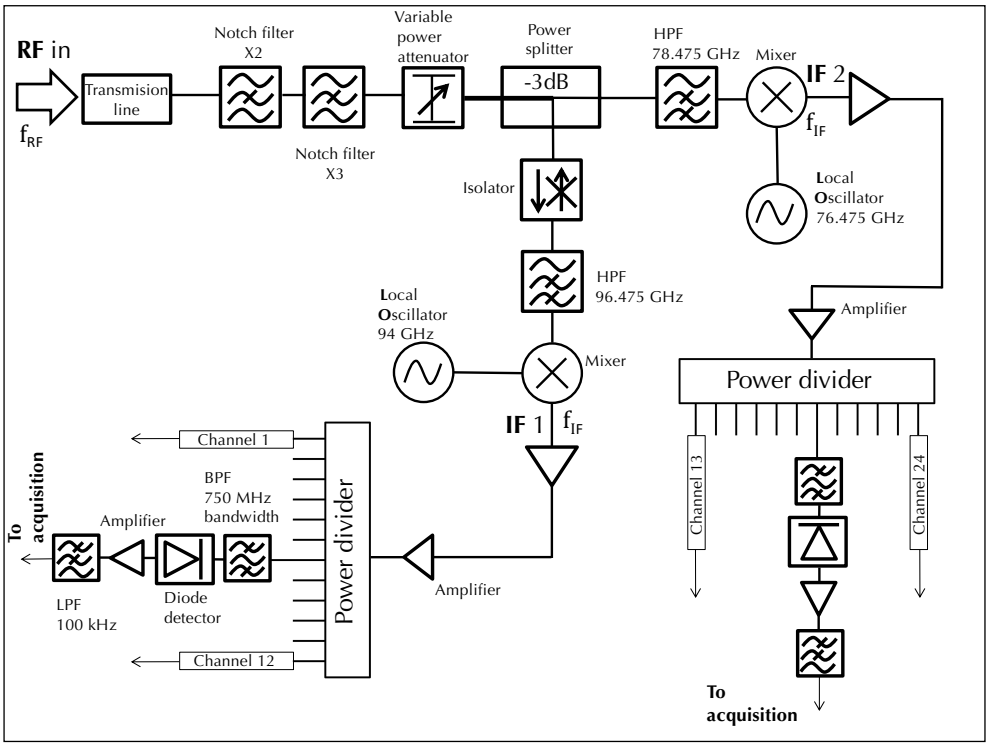

Figure 4.1: An overview of the detection system for the Vertical ECE.

The heterodyne receiver then processes the radiation up to the acquisition in three main stages; the RF stage, the Intermediate Frequency (IF) stage, and the video stage. The summarized stages are shown in Figure 4.2. The RF stage is where the frequency of the incoming radiation is shifted to a lower frequency for further processing. The need to downshift the incoming RF frequency

has historically been motivated by the technological constraints, that will be interesting to follow in this era when higher field tokamaks are being built.

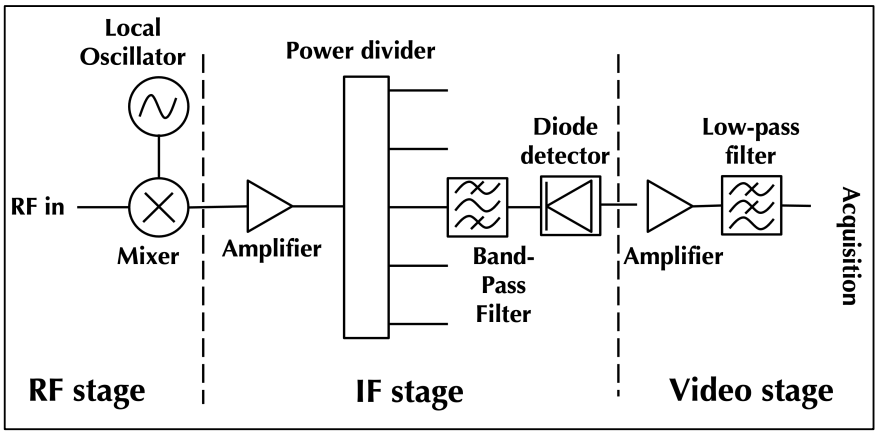

Figure 4.2: The main stages of an heterodyne receiver.

In the RF stage, the frequency conversion happens in the mixer, the most important component of the heterodyne receiver. The mixing element is a diode with a non-linear I/V characteristic. This can be modelled as a two port device with one port for the RF input signal at frequency f_{RF} and a IF frequency output port at frequency f_{IF}. In addition, a LO port connected to a local oscillator feeds the mixer with a signal at frequency f_{LO}. The relationship between the frequencies in the mixer is such that:

$$f_{\mathrm{IF}} = |m f_{\mathrm{RF}} - n f_{\mathrm{LO}}| \quad \text{with } m,n = 1,2,3,...$$

The cases with $m,n > 1$ are the ones in which the mixing process involves the harmonics of the RF and the LO frequencies. The harmonics are generated when the input signals drive the I/V characteristic of the diode into its nonlinear regime. The case of interest for our detection system is when $f_{\mathrm{IF}} = f_{\mathrm{RF}} - f_{\mathrm{LO}}$. In such case, when an incoming RF signal with bandwidth $BW_{\mathrm{RF}} = [f_{\mathrm{RF2}} - f_{\mathrm{RF1}}]$ is processed in the mixer with a fixed LO frequency, the resulting IF bandwidth is $BW_{\mathrm{IF}} = [(f_{\mathrm{RF2}} - f_{\mathrm{LO}}) - (f_{\mathrm{RF1}} - f_{\mathrm{LO}})]$. Since most of the components in the IF frequency range are built for the range $2 - 20$ GHz, the use of a single LO at fixed frequency would limit the detected RF frequency band to about 18 GHz. That is why the detection system of Figure 4.1 features 2 mixers and 2 different LO frequencies, to cover an RF frequency band of about 36 GHz in a single radiometer. High pass filters are used before the mixing elements to ensure that only the frequencies above each LO frequency can reach the mixer. It is also common to have an isolator in higher frequencies circuit. That is to avoid, in the low frequency circuit, the detection of some frequencies coming from the LO in the high frequency circuit. The IF stage after the mixing elements is identical for both circuits. In the IF stage, the signals are amplified and fed into a power divider and split in 12 frequency bands with the help of band pass filters (BPF), wide ~ 750 MHz. Each frequency band constitutes a channel, whose RF frequency band is determined by the IF filter bandwidth. The filtered signals are rectified in the diode detector and further processed in the video stage. In the so-called video stage the signals are amplified

and low-pass filtered down to 100 kHz for the acquisition.

4.1.2 Data acquisition

To digitize the data, the diagnostic relies on high performance acquisition cards of the model ACQ42ELF from the company *D-TACQ Solutions Ltd* in Scotland, UK. The model is a 32 channel simultaneous sampling digitizer with 16 bit resolution and sample rate of 200 kHz per channel. The 200 kHz sample rate allows measurements with time resolution in the order of 10 μs . The 16 bit resolution of the digitizer allows 2^{16} discrete voltage levels, that is equivalent to 0.3 mV resolution for signals of amplitude ± 10 V. The acquisition module has 3 acquisition cards mounted for a total of 96 channels available for the radiometers.

4.1.3 The radiometers

Introduction

A set of 4 heterodyne radiometers, pictured in Figure 4.3, were made available for the detection system of the Vertical ECE diagnostic. Their 42 channels are connected to the DTACQ acquisition board. We designed and assembled one of the radiometers, a heterodyne receiver with two mixing units previously shown in the diagram of Figure 4.1. The radiometer covers with 24 channels the frequency range $78 - 114$ GHz . The other radiometers, 6 channels each, were received from *Forschungszentrum Julich GmbH*. One of them can be switched between 2 LO frequencies to cover the range $89 - 104$ GHz or $133 - 148$ GHz. The other two span the frequencies $104 - 114$ GHz and $125 - 130$ GHz. The radiometers are used according to the experimental needs. The flexibility of the system is the reason for the versatile set of microwave components included in the detection system. Those components are directional couplers, curved or straight waveguides, variable power attenuators etc. We refer to these components collectively as the front-end of the radiometers. The properties of each component of the radiometers and the front-end influences the overall performance of the detection system, justifying the need to characterize each individual component. A full, detailed characterization of the components of the radiometer $78 - 114$ GHz can be found in [63]. The following subsections present the methods that we have used, and a summary on the main component properties and their influence on the overall performance.

Characterization of the components: The method

A Keysight Portable vector Network Analyser (PNA) is used for the characterization of the components. The PNA measures the phase and amplitude of a signal passing through a Device Under Test (DUT). The DUT is characterized in terms of the Scattering parameters (S-parameters) measured in decibels (dB). A S-paramater, S_{mn} , describes the gain or loss in power (measured in decibel -milliwatts, dBm) between port m and port n. For a two ports device, with an input port (port 1) and an output port (port 2), the incident power on the ports (a_1,a_2) are related to

Figure 4.3: The set of radiometers used for Vertical ECE measurements.

the reflected power (b_1, b_2) via the relation:

$$\begin{bmatrix} b_1 \\ b_2 \end{bmatrix} = \begin{bmatrix} S_{11} & S_{12} \\ S_{21} & S_{22} \end{bmatrix} \begin{bmatrix} a_1 \\ a_2 \end{bmatrix}$$

where S_{11} is the input port reflection coefficient, S_{21} the reverse gain, S_{12} the forward gain and S_{22} the output port reflection coefficient. The parameter S_{21} is of particular interest for component characterization as it represents power gain or power loss of a signal through the tested device in the direction of propagation. The PNA itself is limited to frequencies up to ~ 43.5 GHz, so there is need for extension modules to cover RF frequencies during tests. We used extension modules WR-10 $(75 - 110)$ GHz and WR-6 $(110 - 170)$ GHz, connected to the PNA via coaxial cables to to extend the frequency range for the measurements. The coaxial cables from the module to the PNA were also characterized to assess their power loss. We used the continuous wave (CW) signal generator from the PNA to simulate radiating power into the DUT. The input port of the DUT receives RF radiation from the CW source via the transmitter extension module and the output port transmits the signal to the receiver extension module, which relays the signal back to the PNA. The extension modules had to be calibrated each time before the characterization of a DUT.

Characterization of the Front-end components

The front-end components were characterized using the PNA and the extension heads. The S_{21} parameter of each component, treated as a two port device, is measured with the radiation circulating in the proper direction and a RF power attenuator protecting the receiving port. The input port of the DUT receives RF radiation from the CW source via the transmitter extension

module and the output port transmits the signal to the receiver module which relays the signal back to the PNA. The S_{21} of the Notch filters for gyrotron protection (Band stop filters) exhibited a low insertion losses (~ 2 dB) across the extension heads frequency band, and about 70 dB of attenuation in the $80 - 85$ GHz band. The variable power attenuators were characterized using a similar setup. The power for each opening step of the attenuator was recorded to produce the curve of the attenuator opening versus the power reduction . The variable power attenuators exhibited a maximum power reduction of 40 dB. For the flexible use of the set of radiometers, customized waveguides (curved or straight) were fabricated and the power loss in the waveguide was measured to be compared to the theoretical ones. The theoretical loss of 2 dBm /m for rectangular WR-10 waveguides was measured with straight waveguide, while curved waveguides exhibit higher power loss. A 3 dB directional coupler from *SAGE millimeter Inc* shares the incoming RF input power into the two circuits of the heterodyne receiver. A directional coupler can also be used to share the RF input power between different radiometers. The directional couplers are W bands, three port waveguides delivering a 3dB nominal coupling level and a 30 dB minimum directivity across the full band $75 - 110$ GHz. They have predicted low insertion losses, about 1 dB, and high directivity $(30 - 40)$ dB. Each output port of the directional couplers was measured independently with the RF power from the PNA in the input port. The measured insertion loss was higher than expected in each of the two output ports of the directional coupler. The transmittivity in the output ports of the directional couplers varied from -6 dB to -5 dB across the WR-10 band . The low power losses in the other components, such as vertical to horizontal transitions, waveguide bends, were also measured.

Characterization of the components in the RF stage

The power isolator which guarantee no power exchange between the mixers of the radiometer $78 - 114$ GHz was also measured. The transceiver module of the extension heads was used to transmit the power in the isolator in both direction. in the normal direction, the insertion loss was measured to be very low and the in the opposite direction a transmission down to -70 dB was measured, confirming that the power from the high frequency branch could not pollute the low frequency branch. The two mixers and the two local oscillators in the RF stage were manufactured by the millimetre wave division of *ELVA-1*. The mixers are broadband balanced mixers, with $6 - 12$ dB insertion loss, up to 40 dB balance, and deliver up to 22 GHz IF frequencies. They require ~ 10 mW of LO power and are based on a GA-As diode technology. The local oscillators deliver input signals at the fixed frequencies 76.475 GHz and 94.475 GHz with ~ 10 MHz frequency accuracy. They are made from stabilised diode oscillators and deliver up to 50 mW power output. The test of the mixing unit was achieved by sending via the transceiver module RF power at fixed frequency to the RF port of the mixer. The LO was fed with the appropriate voltage and connected to the LO port of the mixer while the IF port of the mixer was directly connected to the PNA via and IF cable. The reason for this is that IF frequency ranges can be directly detected in the PNA. The PNA then, in spectrum analyser mode could detect the incoming IF frequency. the peaks in the PNA spectrum at the expected IF frequency only confirmed the proper mixing of the frequency. The amplitude of the IF helped evaluating the insertion loss in the mixer. A sweep

in the RF frequency at the RF port of the mixer resulted in a sweep of the IF frequency peaks in the spectrum. The detected IF frequency confirmed the fixed frequency of the local oscillators. the RF section of the radiometer $78 - 114$ GHz is pictured in Figure 4.4a.

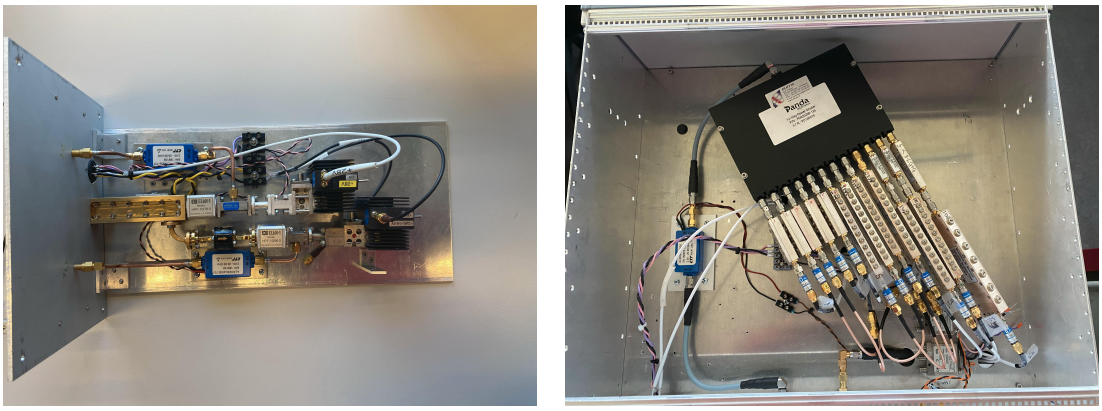

(a) RF stage (b) IF stage

Figure 4.4: The RF stage and one side of the IF stage of the $78 - 114$ GHz radiometer.

Characterization of the components in the IF stage

The RF spectral information in the IF stage is obtained by means of the IF filters connected to power dividers, which receive signal from the IF port of the mixers. The characterization of the components in the IF section is achieved with the input power directly from the PNA to the tested device, and the output power from the tested device back to the PNA. Low loss coaxial cables are used to transport the power, and power attenuators are used to protect the PNA from excessive power that can damage it. The 12 ways power divider (see Figure 4.4b) was tested by sending IF power at fixed frequency and measuring the transmittivty in each of the 12 output port of the divider. The insertion loss in the power divider was high, yet uniform across the output ports. The gains of the IF amplifier were readily measured, sending power in the proper direction of the amplifier and connecting the output port to the PNA. Amplification gains of up ~ 40 dB were measured, using power attenuators to protect the PNA. It is important to note that the PNA dynamic range spans from -30 dBm to 4 dBm. A 40 dB amplification of the minimal PNA power would lead to a power of 10 dBm in the receiving port of the PNA, which could potentially damage the PNA. A set of 10 dB power attenuators, independently characterized, were used to limit the power at the receiving port of the PNA. The ~ 750 MHz bandpass IF filters, connected to the 12 power dividers are built to work in the range $1 - 22$ GHz. To improve the frequency selectivity, some filters were coupled in series (see Figure 4.4b). The band pass frequencies of the IF filters and the insertion losses were measured by sweeping the input power across the full PNA frequency band and by measuring the response from the output port of the filter or the couple of filters. Low values of insertion losses where measured to be approximately $1 - 2$ dB, with the band selectivity of the filters close to 750 MHz. The IF filters frequency band (f_{IF}) and the local

Frequencies (GHz), Radiometer 78 − 114 GHz						
Channel #	IF	Bandwidth	LO	RF	LO	RF
Channel 1	18.875	0.75	94.470	113.345	76.475	95.350
Channel 2	17.375	0.75	94.470	111.845	76.475	93.850
Channel 3	15.875	0.75	94.470	110.345	76.475	92.350
Channel 4	14.375	0.75	94.470	108.845	76.475	90.850
Channel 5	12.875	0.75	94.470	107.345	76.475	89.350
Channel 6	11.375	0.75	94.470	105.845	76.475	87.850
Channel 7	9.875	0.75	94.470	104.345	76.475	86.350
Channel 8	8.375	0.75	94.470	102.845	76.475	84.850
Channel 9	6.875	0.75	94.470	101.345	76.475	93.350
Channel 10	5.375	0.75	94.470	99.845	76.475	81.850
Channel 11	3.875	0.75	94.470	98.345	76.475	80.350
Channel 12	2.375	0.75	94.470	96.845	76.475	78.850
Channel 13	3.125	0.75	76.475	79.600	94.470	97.595
Channel 14	4.625	0.75	76.475	81.100	94.470	99.095
Channel 15	6.125	0.75	76.475	82.600	94.470	100.595
Channel 16	7.625	0.75	76.475	84.100	94.470	102.095
Channel 17	9.125	0.75	76.475	85.600	94.470	103.595
Channel 18	10.625	0.75	76.475	87.100	94.470	105.095
Channel 19	12.125	0.75	76.475	88.600	94.470	106.595
Channel 20	13.625	0.75	76.475	90.100	94.470	108.095
Channel 21	15.125	0.75	76.475	91.600	94.470	109.595
Channel 22	16.625	0.75	76.475	93.100	94.470	111.095
Channel 23	18.125	0.75	76.475	94.600	94.470	112.595
Channel 24	19.625	0.75	76.475	96.100	94.470	114.095

Table 4.1: Frequency mapping for the radiometer 78 − 114 GHz.

oscillator frequencies determine the corresponding RF frequency band detected by the receiver via the relation $f_{\mathrm{RF}} = f_{\mathrm{IF}} + f_{\mathrm{LO}}$. In conventional ECE measurements with a horizontal line of sight, the bandwidth of the IF filters determines the spatial resolution of the diagnostic. For Vertical ECE, the bandwidth influences the resolution in energy as will be discussed in Section 4.5.

With the characterization of each IF filter in the radiometer 78 − 114 GHz, the RF frequency detected in each channel was easily determined. The IF outputs from the two mixers can be connected to one or the other power divider in the IF stage. The two different configurations allow two sets of RF frequencies in the channels. That is because the IF filters connected to the power dividers do not have exactly the same band pass frequencies. Table 4.1 summarises the frequencies in the radiometer 78 − 114 in the two configurations. The set of Schottky diodes that convert the IF signal into a DC voltage for amplification and filtering in the video stage can also be seen in Figure 4.4b. Schottky diodes were chosen for their high frequency capabilities and their high sensitivity. the DC voltage generated by the diodes can be easily related to the

power of the radiation they receive, which is itself proportional to the power emanating from the plasma. To determine the I/V characteristic of the diodes, each diode is connected via a coaxial cable to the CW source of the PNA, which generates a signal at the IF frequency of each channel. The diode output is connected to a digital voltmeter. The combination of power from PNA and attenuation from the attenuators allowed a power scan from -50 dBm up to 0 dBm, in steps of 2 dBm for each diode. The detected voltage gives the I/V characteristic of the diodes. From the response of the diodes, exponential curves for each diode could be fitted, relating the incoming power to the voltage across the diode.

Frequency mapping of the other radiometers

The other heterodyne receivers used for this research work on the same principles as the one we built and characterized. However, the characteristics of the IF filters used for those radiometers were not available and the very compact design of the radiometers made it difficult to extract the components and measure their properties. For those radiometers, the PNA and the transceiver module were connected to the RF input of the radiometers. The DC voltage from the video stage of those radiometers were then read in a voltmeter for each of the channel (see Figure 4.5). The PNA frequency was continuously swept to identify the central frequency and the bandwidth of each channel. The frequency band was measured to be approximately 500 MHz. The frequencies of the radiometers that have been determined indirectly are summarized in Table 4.2.

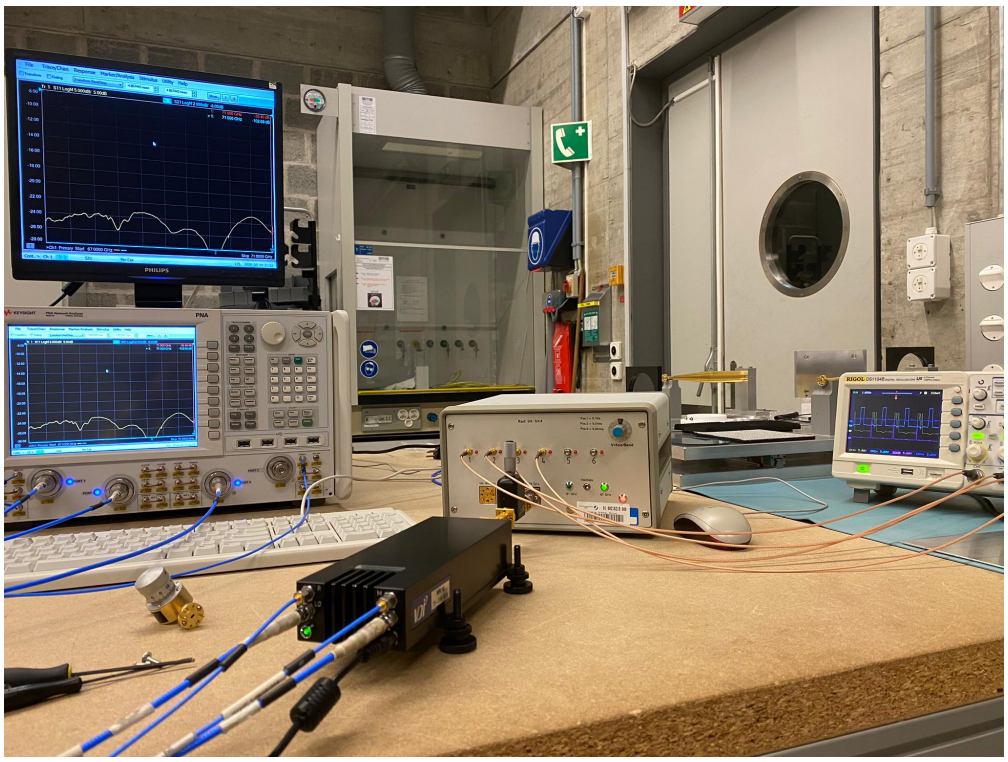

Figure 4.5: Setup for a radiometer channel mapping.

Frequencies (GHz)					
Radiometer 89 − 104 GHz			Radiometer 133 − 148 GHz		
Channel #	Bandwidth	RF	channel #	Bandwidth	RF
Channel 1	0.5	89	channel 1	0.5	133
Channel 2	0.5	92	channel 2	0.5	136
Channel 3	0.5	95	channel 3	0.5	139
Channel 4	0.5	98	channel 4	0.5	142
Channel 5	0.5	101	channel 5	0.5	145
Channel 6	0.5	104	channel 6	0.5	148
Radiometer 104 − 114 GHz			Radiometer 125 − 130 GHz		
Channel #	Bandwidth	RF	channel #	Bandwidth	RF
Channel 1	0.5	104.80	channel 1	0.5	125
Channel 2	0.5	106.50	channel 2	0.5	126
Channel 3	0.5	107.95	channel 4	0.5	127
Channel 2	0.5	109.75	channel 4	0.5	128
Channel 2	0.5	111.25	channel 5	0.5	129
Channel 6	0.5	113.10	channel 6	0.5	130

Table 4.2: Measured frequencies of the radiometers.

Frequency coverage

The overall frequency coverage of the detection system is summarized in Figure 4.6. The figure also shows the frequencies used by gyrotrons to heat the TCV plasma. The overlap of some of the radiometers frequencies allows simultaneous measurements at those frequencies in different radiometers.

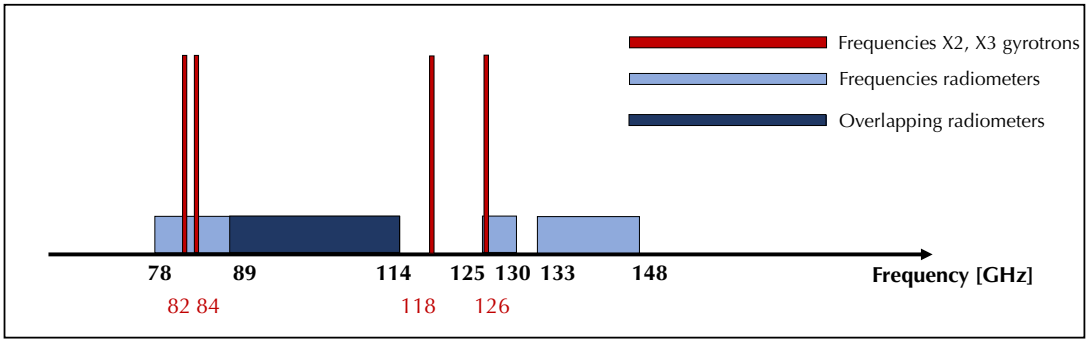

Figure 4.6: Frequency coverage of the radiometers.

Temporal resolution and sensitivity

The Low Pass Filter (LPF) in the video stage of the detection system determines the time resolution of the diagnostic and influences its signal to noise ratio. In general, the minimum detectable power from the plasma in a frequency band Δf increases with B_V, the frequency band of the

video LPF according to the relation [64]:

$$T_{min} = T_{sys}\sqrt{\frac{2B_V}{\Delta f}}. \tag{4.1}$$

Here T_{min} is the minimum detectable power and T_{sys} the noise of the system in units of a temperature. The video band, B_V, in the one hand influences the signal to noise ratio. In the other hand, higher values of B_V increase the time resolution of the diagnostic, allowing it to track fast changes in the plasma. High time resolution, with B_V of the order of megahertz, is relevant for some ECE applications such as temperature fluctuations measurements. In our case, a value of B_V equal to 100 kHz is enough for Vertical ECE studies, as it allows good sensitivity of the receiver and a time resolution of $\sim 10^{-5}$ s.

4.1.4 Protection from the gyrotrons

The ECRH heating system on TCV was presented in Chapter 2. The gyrotrons deliver power at the second harmonic (X2) and the third harmonic (X3) of the fundamental cyclotron frequency. The frequencies of the waves that are sent into the plasma are $f_{X2} = 82.7$ GHz and $f_{X2} = 84$ GHz for the (X2) gyrotrons. The frequencies for the (X3) gyrotrons are $f_{X3} = 118$ GHz and $f_{X3} = 126$ GHz. The (X2) frequencies are well stabilised and change at the most by ~ 100 MHz. The risk for the Vertical ECE detection system is that the gyrotron power reflects off the vessel, reaches the detection system and destroys the components of the radiometer. Some components of the detection system such as the mixers can withstand at most ~ 15 mW of input power. The discussion on the eventual harm of the gyrotrons on the detection system can be split into two scenarios. The first is considering that the total 4500 kW gyrotron power in TCV is uniformly distributed on the vessel surface $\sim 18\ \mathrm{m}^2$ (4500kW is an overestimate of the power, as it is the sum of the powers at the gyrotron window). The incident power in the transmission line would be

$$P_{inc} = \frac{4.5 \times 10^6 \mathrm{W}}{18\mathrm{m}^2}\lambda^2, \tag{4.2}$$

where λ^2 replaces the effective area of the detection system. Considering a value of $\lambda^2 \sim 1\times10^{-5}\ \mathrm{m}^2$, we find and incident power of $P_{inc} \simeq 3$ W, which would require a power attenuation of about 25 dB in the transmission line in order to protect the mixer. An even worse scenario for the detection system is the case when the gyrotron power is not uniformly distributed in the vessel but is received in the transmission line with good directivity after a few reflections off the vessel. In that case, considering a gyrotron beam size of ~ 5 cm in diameter at the launcher, after a few reflections off the vessel the beam would travel approximately 10 m. The size of the gyrotron beam of wavelength 3 mm and waist size 30 mm after 10 m would be approximately 320 mm. The incident power of a 500 kW gyrotron wave, passing through the vessel window

($\sim$ 100 mm radius), can be calculated as

$$P_{inc} = 5 \times 10^5 \frac{100^2}{320^2} = 50 \text{ kW}. \tag{4.3}$$

This power would destroy the detection system, unless the gyrotron wave undergoes a power attenuation of ~ 65 dB along the transmission line. We will discuss the strategies to avoid the destructive effects of gyrotron power on the system components, but it is important to first make some precision on the methods we just used to assess the gyrotron power. First we have assumed that the power of the wave from the gyrotron does not change after each reflection off the vessel. This in practice is too pessimistic, as the vessel tiles reflection is not perfect. With a value of the reflection coefficient on the tiles of 0.95, the power of a 500 kW gyrotron wave would be, after 10 reflections of the order of $0.95^{10} \times 500$ kW $\simeq 300$ kW. We have also assumed that the reflected wave can fill entirely the vessel window to reach the transmission line, and we have not accounted for a power distribution in the beam of the gyrotron after the reflections. The order of magnitude is however consistent and the assessment is valid for higher power gyrotrons as well (dual frequency gyrotrons have 1000 kW of nominal power). To protect the detection system against the gyrotron power, two main techniques are used:

1. Redundancy of band stop filters, power attenuators and directional couplers along the line of sight. We use band stop filters (notch filters), characterized in the previous subsection to protect the system . These filters attenuate the power at the specific gyrotrons frequencies. The attenuation of the filters can go down to -70 dB, see Figure 4.7. The variable power attenuators reduce the power at all frequencies across their band by up to 40 dB. The directional couplers in the front end of the radiometer reduce the power by an additional 3 dB.

2. The other tactic to protect the system is a trip on the gyrotron whenever the power at the diagnostic window reaches a certain value. This method stops the gyrotrons during TCV shots in which a certain power level is measured at the window of the Vertical ECE diagnostic. In general a very low value is set to trip the gyrotron and the reaction time of the trip is relatively fast.

4.1.5 Dynamic range

This subsection discusses the assessment of the dynamic range of our detection system. The assessment is made from the waveguides transporting the radiation from the antenna to the detection system up to the video stage of the radiometers. We include in the assessment only the insertion losses of the components that are necessary for the detection system. Those losses are :

- 0.1 dB losses in the circular, oversized waveguide connecting the antenna to the radiometer

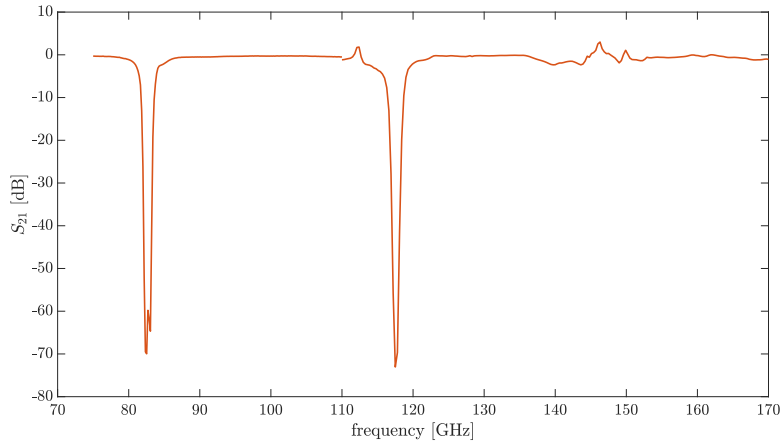

Figure 4.7: Band stop filters transmittivity.

front-end. They are two waveguides connected in parallel approximately 5 meters long. The losses in the waveguide are estimated as in [61].

- 0.5 dB attenuation from the transition circular (0.165 inch diameter) to rectangular WR−10.
- 8 dB attenuation from the insertion losses of the notch filters.
- 5 dB attenuation from from the 3dB directional coupler.
- 14 dB attenuation from the Mixer, high pass filter and isolator.
- 14.4 dB attenuation from the 12 way power divider and IF band pass filter

The sum of the losses of the components in the detection system is then ~ 42 dB. Two power amplifiers in the IF stage ensure a total power gain of 60 dB. The Schottky diodes response to the input power is typically in the order of 1500 mV/mW. In the video stage, the signal is amplified by ~ 1000 before the acquisition. Ideally the power at the diode should be of the order of a few μW to allow the acquisition of signals of a few volts. What is for interest now is to understand how much should be the losses in the antenna in order to have of $\sim 1\ \mu$W at the diode. For this estimation we consider a thermal plasma radiating like a black-body at temperature $T_e = 1$ keV. The total power emanating from the plasma in the frequency band $\Delta f = 750$ MHz is

$$P_{\mathrm{BW}} = \Delta f T_e. \tag{4.4}$$

The power P_{BW} is found to be 12 μW (-39 dBm).The power balance at the diode without losses in the antenna is then -39 dBm $+$ (60 dB -42 dB) $= -21$ dBm. In conclusion, in order to have a signal power of -30 dBm (1 μW) at the diode, the power losses in the antenna system should

then be close to a value of ~ 10 dB.
The description of the Vertical ECE antenna follows in the next section of this chapter.

4.2 The Vertical ECE antenna

4.2.1 Layout

The optical arrangement of the Vertical ECE antenna is designed to produce a line of sight in the tokamak with minimal radial extent. The antenna exploits a top port of 20 cm in diameter on top of which an ellipsoidal mirror of focal length ~ 61 cm is fastened. The aperture of the top port is at 163.4 cm from the the machine floor and the center of the mirror is at ~ 101 cm of the vessel mid-plane. The mirror is made out of copper while the window at the port is in sapphire implying its optical opacity. Sapphire was chosen for the diagnostic window in order to take advantage of its low microwave reflectivity. However, the opacity of the window makes it difficult to check, for the purposes of an alignment, the trajectory in the vessel of a visible light reflecting off the mirror. This constraints the alignment of the mirror with visible light to be performed only during openings of the machine. The radiation from the plasma, after the focusing mirror, is collected in an oversized corrugated waveguide of 63.5 mm in diameter. The waveguide aperture is positioned ~ 72 cm from the mirror center to transport the plasma radiation to a quasi optical telescope. The telescope was manufactured by the company *Thomas Keating Ltd* in the United Kingdom. It is equipped with a wire grid polarizer, broadband scalar horns and focusing mirrors. The wire grid polarizer separates the incoming beam into two polarizations, each of which is collected in a horn and fed in the transmission lines for the detection. Figure 4.8 and Figure 4.9 show the drawing of the antenna for the Vertical ECE on TCV.

The antenna beam pattern was designed, following a series of deductive steps imposed by the practical constraints of the tokamak . The design starts with our desired waist size and desired waist location in the plasma, which are the imposed initial conditions. The idea is to have the beam centered at the port major radius $R = 88$ cm, with radial size at the mid-plane of the vessel as small as possible. The height of the beam waist is desired at a vessel height near $Z \simeq 20$ cm to have the beam waist near the plasma for the majority of TCV experiments. The desired waist size and position in the vessel is however constrained by the aperture of the top port and the height of the mirror, centered in $R = 88$ cm. The achievable spot size and location allow the calculation of the beam parameters at the floor of the machine and at the mirror, as the beam mirrors itself in $Z \simeq 20$ cm. The beam parameters on the mirror are used to calculate the distance from the HE11 waveguide aperture to the mirror. This is done with the constraint on the internal diameter of the waveguide, as the beam from the mirror should have the waist at the aperture of the HE11 waveguide. The beam parameters from the plasma to the mirror and from the mirror to the waveguide are then used to calculate the parameters of the focusing mirror: the size, focal length, depth, radius of curvature and ellipticity. The design of the mirror is refined optimising the size of the beam in the toroidal direction to have a stigmatic beam in both radial and toroidal directions. The next subsections will be dedicated the antenna beam size in the plasma, a fundamental parameter for Vertical ECE measurements, and to the wave polarizations measurements. The antenna, from design, favours free propagation of the electromagnetic radiation or propagation in low losses waveguides to limit the attenuation of the radiation

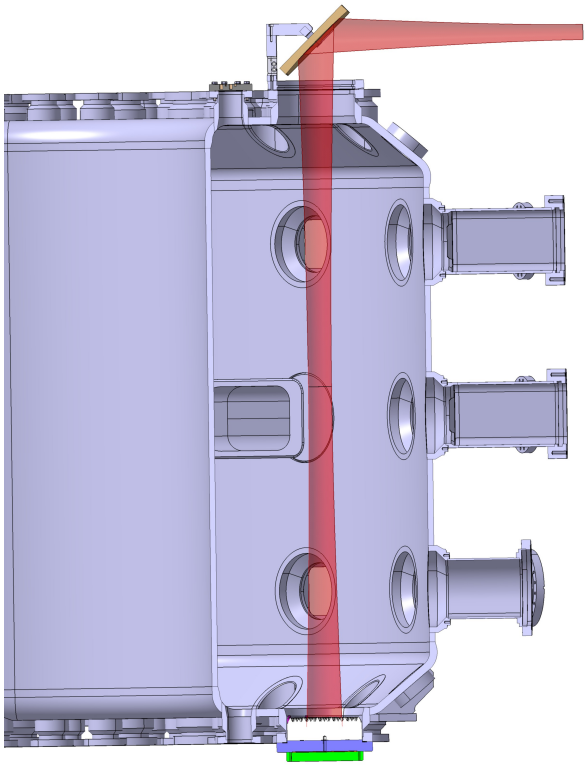

Figure 4.8: Layout of the Vertical ECE antenna beam pattern in the vessel.

from the plasma. The antenna system is aligned during TCV openings by means of an optical laser irradiating from one of the horns of the telescope. The stability of the alignment is in general under discussion due, among others, to the mechanical vibrations of the vessel. The misalignment of the line of sight can however be tracked during plasma experiments and physics results can be deduced even if the line of sight has departed from the vertical direction.

4.2.2 The antenna beam size

The beam size from design

The effective size of the antenna beam is an important parameter for the diagnostic, as it influences the energy resolution and the conditions for non-thermal emission measurements. The design method of the antenna has been presented in the previous subsection. Here we assess the beam size effectively produced by the antenna. Figure 4.10 recalls the design parameters for radiation at 100 GHz of frequency. The size of the beam is defined by the extent of the $1/e^2$ intensity level in the assumed Gaussian beam. The designed beam waist is large 3 cm in radius and is located $\sim$ 20 cm above the vessel mid-plane, i.e. 81 cm away from the mirror and 95 cm from the machine floor. The size of the beam is 4 cm on the mirror and 5 cm on the floor. Accord-

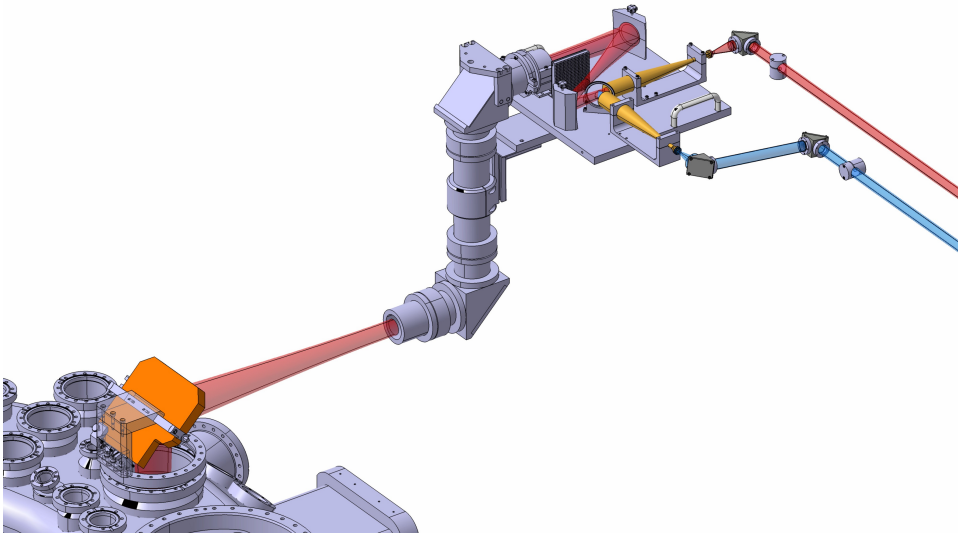

Figure 4.9: Layout of the Vertical ECE antenna beam pattern out of the vessel.

ing to the design, the mirror produces a beam waist of 4 cm at the position of the waveguide at 72 cm from the mirror in the direction towards the detection system. The beam divergence in vacuum is calculated to be $\approx \arctan \frac{10-6}{2\times 95} = 2.14°$. The designed beam is thus well collimated along the 176 cm path from the mirror to the machine floor.

The beam size from direct measurement of the antenna pattern

The size of the antenna pattern was measured. The components of the Vertical ECE antenna were removed from the machine for this purpose and installed in the low power laboratory of the *Swiss Plasma Center*. For the measurements we used the telescope, the HE11 waveguide and the ellipsoidal mirror, rotated, to produce the beam along the horizontal direction (see Figure 4.11).

The beam is produced along the horizontal direction for practical reasons only, the size of the beam should not be affected by the mirror rotation. The horizontal and vertical axes of the beam in our setup are equivalent, respectively, to the radial and toroidal axes of the beam produced in the vessel. For the beam measurement, the transceiver module of the PNA was connected to a horn on the telescope irradiating the system with 6 dBm power at a fixed frequency. The receiver module was used to measure the amplitude of the electric field of the beam . A small rectangular waveguide was attached to the receiver's test port to allow the module to be recessed and screened with absorber, improving the quality of the measurement. A robot scanning the vertical and horizontal direction with fine steps was used to to allow the receiver module to scan the beam area. As a test, the beam size was measured before the reflection off the mirror, at the aperture of the HE11 waveguide. The results are shown in Figure 4.12, the measurement suggests a stigmatic beam with size approximately 2.8 cm in both horizontal and vertical directions. A

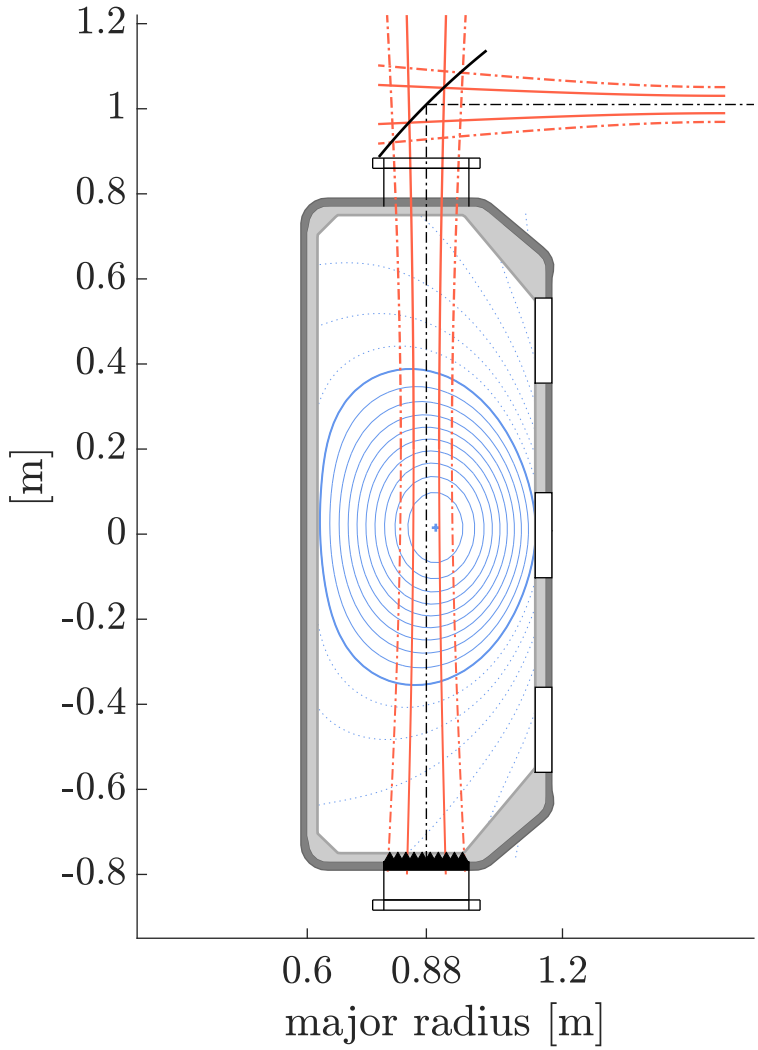

Figure 4.10: The designed beam of the Vertical ECE antenna pattern for radiation at 100 GHz.

measurement of the size of the beam reflected off the mirror was attempted. The receiver module was positioned ~ 50 cm from the mirror center. The beam size at this location would correspond to the size of the beam at ~ 50 above the vessel midplane. The measured beam shown in Figure 4.12 suggests a Gaussian beam of size ~ 2.3 cm for a frequency of 100 GHz. On the same Figure, a superposition of a theoretical Gaussian beam of the same size suggests that the beam produced by the antenna can be assumed Gaussian at ~ 50 cm from the mirror. It can be concluded that in vacuum, the radial extent of the antenna beam at 100 GHz is ~ 2.3 cm at ~ 30 cm above the waist position . Since the beam is assumed to be stigmatic, the toroidal extent of the beam can be considered to be approximately equal to the radial size. The measured beam sizes are thus consistent with the designed beam.

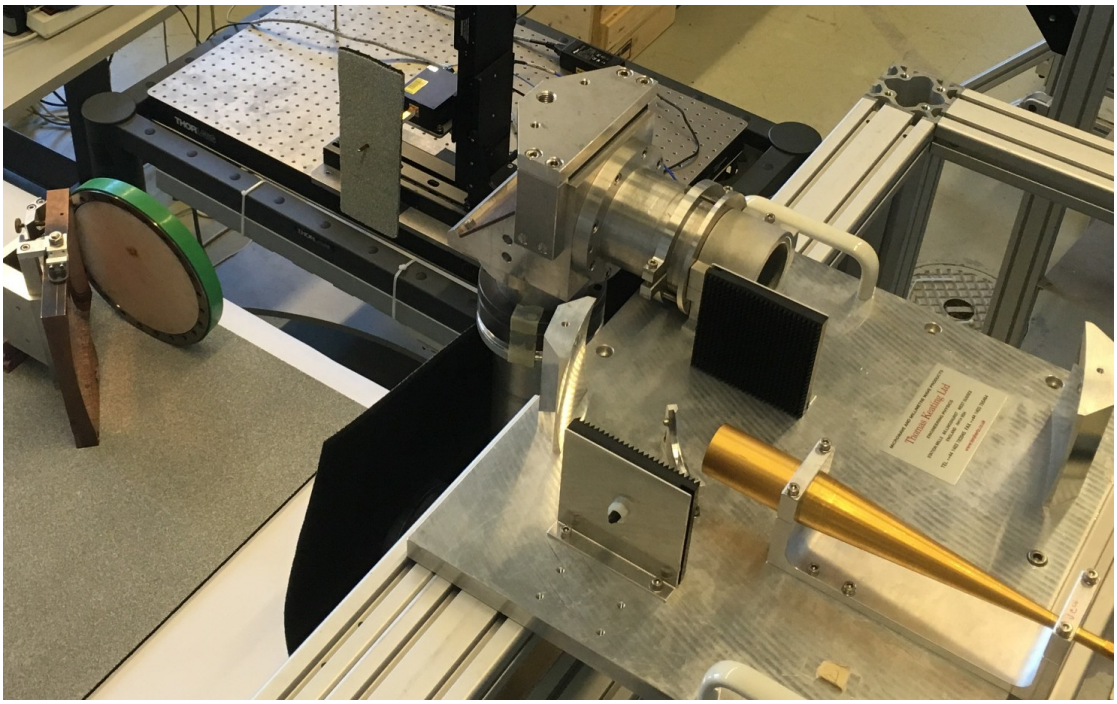

Figure 4.11: Experimental setup for the measurement of the beam size produced by the Vertical ECE antenna.

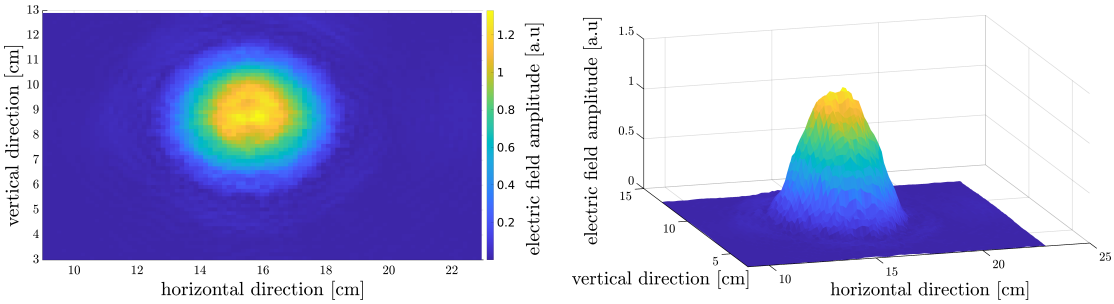

Figure 4.12: Result of the beam size measurement at the aperture of the HE11 waveguide.

The beam size from experimental plasma discharges

Another approach, using experimental plasma discharges to infer, approximately, the magnitude of the beam size was also attempted. The idea is as follows: during a plasma discharge, the magnetic field is ramped up or down such that the resonance location at one of the harmonics of the fundamental cyclotron frequency crosses the antenna line of sight. When the resonant frequency within the line of sight corresponds to a frequency of the radiometers, the time trace on that frequency channel during the field ramp carries information on the beam size. In fact, the time the resonance spends within the line of sight is mainly due to the radial extent of the

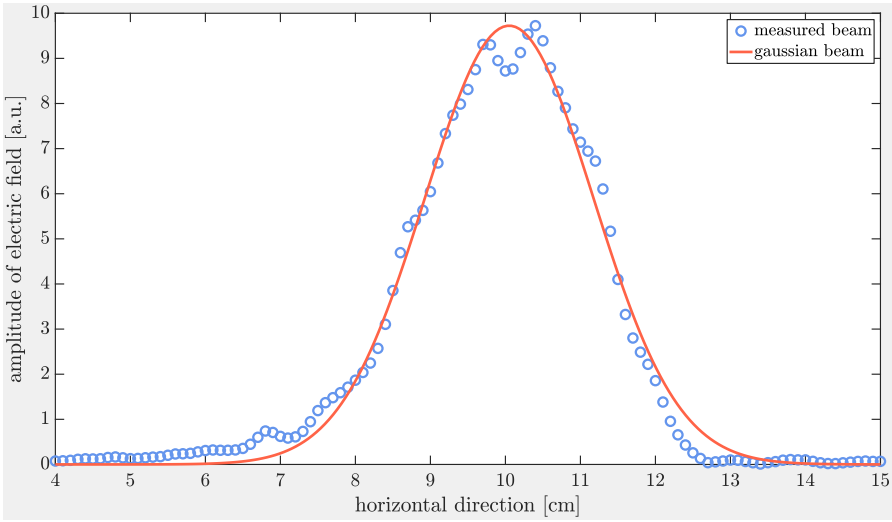

Figure 4.13: Measured beam size versus Gaussian beam size.

antenna beam pattern . It is possible in our case to infer the size of the beam from the time trace on each channel only because the size of the antenna pattern is supposedly much larger than the size of the resonant emission layer. If the size of the emission layer were to be larger than the beam size, the signal time trace would carry the information on the width of the emission layer instead. These concepts will be discussed thoroughly in Chapter 5 discussing the calibration of the diagnostic. For the present analysis, a set of plasma discharges with magnetic field ramps has been considered. The time interval for the resonance crossing each channel is used to infer the corresponding change in the magnetic field as shown in Figure 4.14. From the change in magnetic field, the radial extent of the beam pattern is readily obtained via the equivalence $\Delta_R = \frac{n|e|}{2\pi m_{eo}} \Delta_B$, where n is the harmonic number. The time interval in the signal trace around the peak was limited to the extent of the $1/e^2$ intensity level to ensure that the reconstructed beam size is within the $1/e^2$ intensity level. Note that the beam size that is inferred is the size of an antenna pattern undergoing interaction with the plasma (not the size in vacuum). Consequently, the average size deduced by this method represents an upper limit of the antenna beam size in vacuum.

The result obtained for a few plasma discharges are shown in Figure 4.15. The radial extent, Δ_R, is the width of the beam that has been inferred and thus represents the beam diameter. The analysis was performed at frequencies close to 100 GHz to ease the comparison with the other approaches. An average size of the beam diameter close to ~ 6 cm could be inferred, which is consistent with the expectations. The deviation of some of the points from the average is due to the refraction of the beam in the plasma. Concerning the location along the vertical axis of the beam, this approach cannot give a precise answer, even though the beam size is likely not the beam waist. The detection of the resonance occurs when the optical depth of the plasma is high enough. The optical depth scales mainly with the temperature in the chosen frequency range. There are then good reasons to believe that the inferred beam size is the beam size near the

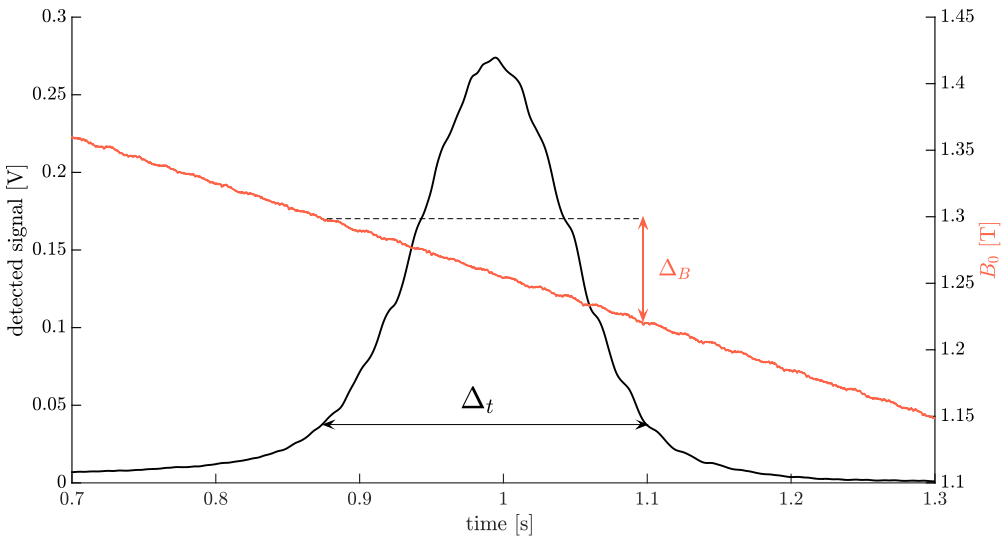

Figure 4.14: Response of a channel of the detection system to a magnetic field ramp. The time interval delimits the drop by $1/e^2$ in the signal intensity.

center of the plasma in these experiments, which was at $Z = 0$, 20 cm below the waist height.

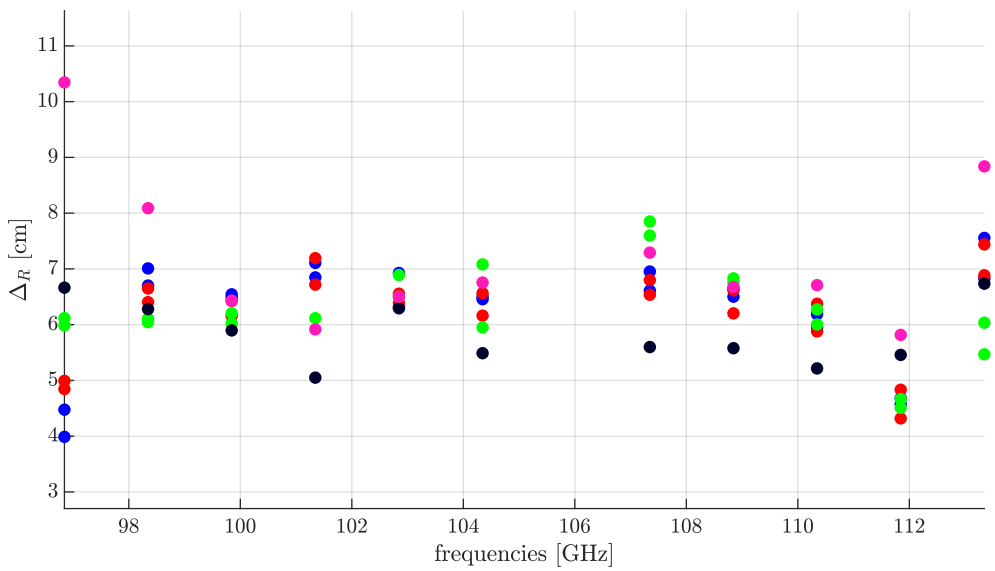

Figure 4.15: Radial extent of the antenna beam deduced from experimental plasma discharges with magnetic field ramp.

4.2.3 Tracking the wave polarization

The Vertical ECE is designed to measure for each frequency the eXtraordinary (X) and the Ordinary (O) polarizations of the radiation. The wave polarization is calculated for a cold plasma in the Appleton-Hartree/Stix framework. For a perpendicular upward propagation ($\vec{k} \perp \vec{B}$), the electric field of the O-mode of a gyrating electron oscillates along the local magnetic field. The electric field of the X-mode describes an elliptic orbit in the plane perpendicular to the local magnetic field. Given that the propagation is perpendicular to the magnetic field, the X-mode has both longitudinal and transverse components. This can happen only because the wave propagates in the plasma. The orientation of the electric field that is considered in the measurements is that at the last closed flux surface, shown in Figure 4.16.The electric field of the O-mode is aligned with $\vec{B}$ and that of the X-mode is perpendicular to $\vec{B}$ and $\vec{k}$. In a hypothetical case of a magnetic field with just the toroidal component, the electric field of the O-mode would be aligned in the toroidal direction and that of the X-mode in the radial direction. In that case the polarizations at the wire grid in the telescope (Figure 4.17) would be vertical and horizontal for the X- and O-mode respectively, assuming the polarization had not changed during the reflections on the antenna components. The wire grid reflects the polarization that has its electric field parallel to its fibers and lets through the polarization with electric field perpendicular. For Vertical ECE experiments, the precise direction of the magnetic field vector is calculated accounting for the poloidal and toroidal components. The direction of the electric field vectors for the O- and X-mode is inferred, propagated through the mirror using ECPOL [65], and separated at the wire grid. The poloidal component of the magnetic field shifts the ideal polarizations (vertical and horizontal) by a few degrees typically. It is very important to avoid cross polarization at the grid by fixing a precise angle. This is because the ratio in a typical thermal plasma of the X- to the O- mode intensities is of the order of 10^2. A scrambling of the X- with the O- mode of just 1% would completely shadow the original O-mode emission from the plasma.

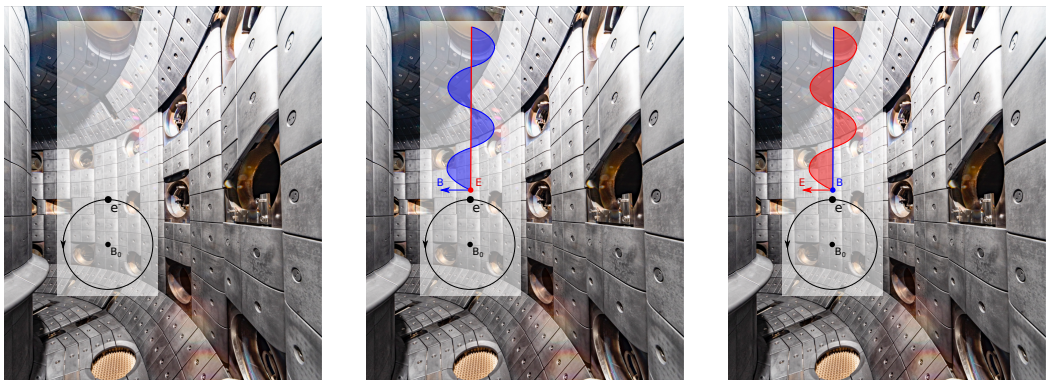

(a) Cyclotron motion of an electron (b) Ordinary polarization (c) eXtraordinary polarization

Figure 4.16: The Ordinary and extraordinary polarizations in the TCV vessel.

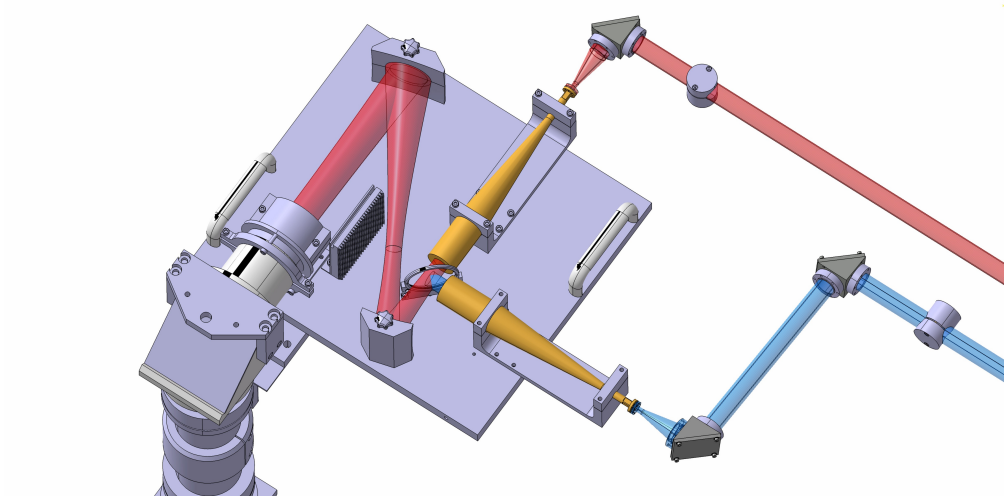

Figure 4.17: Splitting of the beam into X- and O- modes at the wire grid polarizer on the telescope.

4.3 The Viewing dump

This section presents the design and performance of our custom-made viewing dump. The dump is made of MACOR, a machinable glass-ceramic, to fulfill the requirements of high electromagnetic absorption and compatibility with the tokamak high temperature and high vacuum environment. Glass-ceramics were accidentally discovered at Corning Inc in the early fifties [66] and later measurements of MACOR properties reported values of absorption coefficient α to vary between $0.08 < \alpha(\mathrm{mm}^{-1}) < 0.15$ [67]. These values of absorption coefficient, evaluated at the frequency range relevant to our measurements, increase with frequency and are at least an order of magnitude higher than the values for common low loss ceramics. MACOR is in appearance a white, porcelain-like material that is easily machinable, see [68]. It has a continuous operating temperature of $800\,^{\circ}$C, a peak temperature of $1000\,^{\circ}$C and can be considered to withstand high heat fluxes. The MACOR does not outgas in vacuum environments and is strong, non-porous, radiation resistant and therefore a good candidate material for a viewing dump in a plasma confinement device.

4.3.1 Design

The preferred viewing dump shapes are triangular grooves, array of horns or pyramid arrays. Those shapes increase the absorption of the incident wave by geometric means, inducing multiple reflections or by varying the wave refractive index. Straight grooves which are the easiest to fabricate have absorption properties that strongly depend on the relative orientation of the dump. In fact, dumps featuring straight grooves exhibit high reflectivity (low absorption) for wave polarization parallel to the grooves. The TCV dump in Figure 4.18 is an array of pyramids which is difficult to manufacture but does not have a preferential orientation. The dimensions of a pyramid are $10\times10\times\sim11.6$mm and the angle between faces of adjacent pyramids is $45\,^{\circ}$ (see

Figure 4.19) resulting in ~ 4 reflections for a normally incident ray on the MACOR, enhancing the absorption. The size of the pyramids was chosen to be approximately 1 cm, based on the optical thickness of MACOR. The diameter of the dump instead is constrained by the available space on TCV. The size of the dump is a key parameter that will later turn out to be important in understanding the conditions for Vertical ECE measurements on TCV.

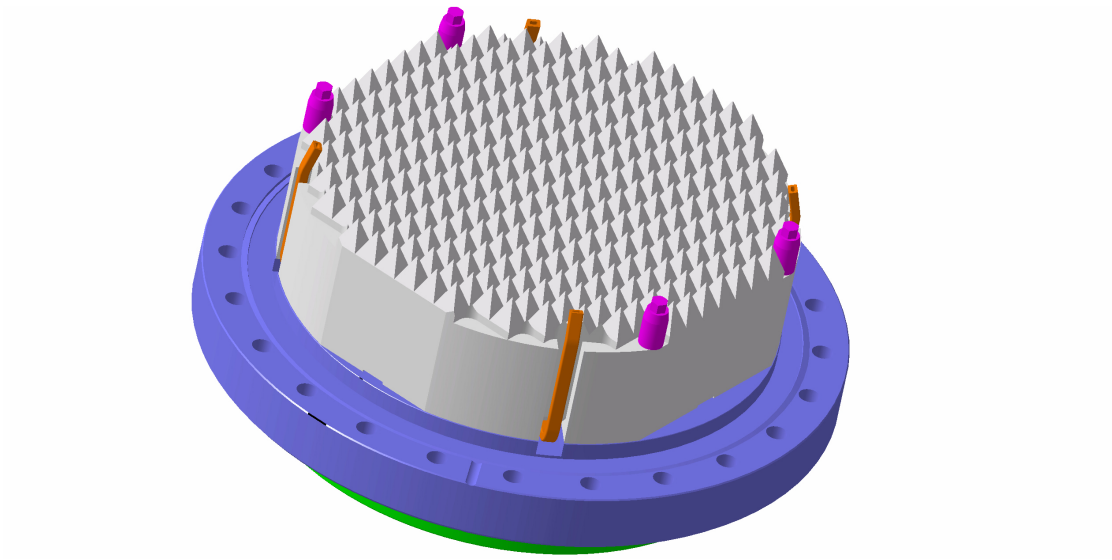

Figure 4.18: TCV viewing dump design: arrays of pyramids with 90° rotational symmetry.

The dump on TCV

On TCV, a bottom port of 20 cm in diameter hosts the 16 cm large viewing dump, see Figure 4.20. The port hosting the dump is centered at major radius R $\sim$ 0.88 m and faces a similar size port at the top of the machine which, at his turn, should host the Vertical ECE antenna, (Figure 4.21). After the first installation on TCV, the dump was damaged by a mishandling of ~ 500 kW power from the microwave heating system. The damage can be understood given the high absorption coefficient, low thermal conductivity and low toughness of MACOR. The dump was replaced with an identical copy in 2012 and had since been exposed to irradiation from the plasma itself. During routine operation on TCV, the dump is irradiated without risk by the plasma, receiving microwave power of the order of $\sim 10^{-4}$ W. We focus our attention on the potential impact on the dump of direct heat and particle flux from the scrape off layer plasma, i.e the plasma outside the last closed flux surface (LCFS). Direct interaction between the dump and the plasma can be relevant only in the diverted configuration (Figure 4.22b) with the divertor leg at the radial position of the dump. The other configuration, limited (Figure 4.22a), allows only minimal interaction between the plasma and the vessel ground. In diverted configurations, the direct exposure of the dump to the plasma also depends on the angle of incidence of the grazing magnetic field lines. A minimum angle of incidence of 13° would be necessary for direct heat deposition along the magnetic field lines. This value is unpractical on TCV, as the combination of the magnetic field generated by the plasma current and the one externally generated from

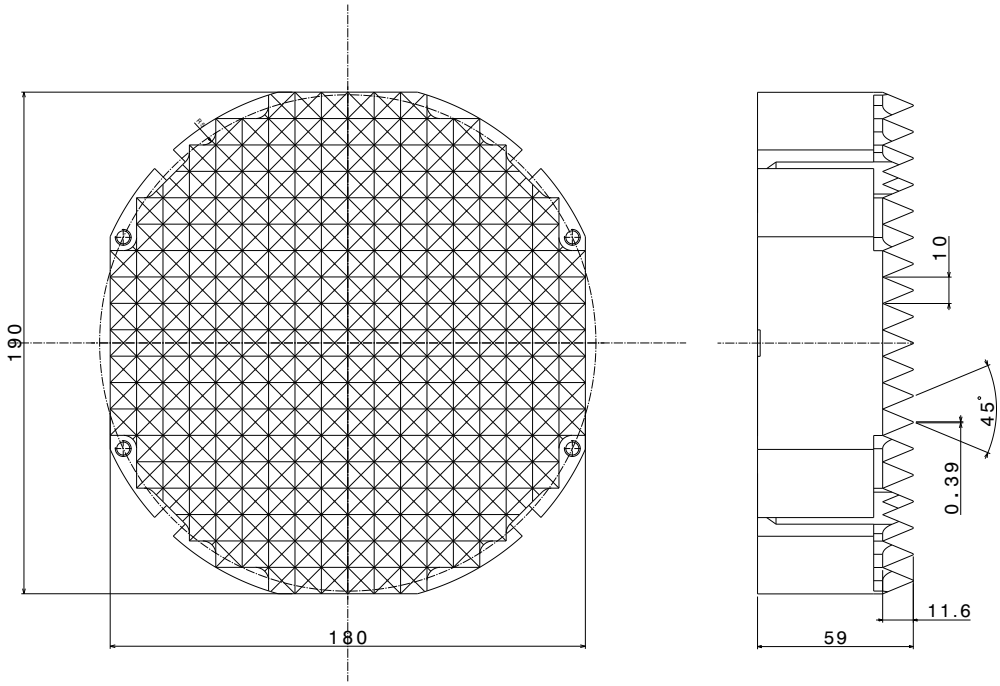

Figure 4.19: Drawing of the viewing dump with detailed design parameters.

poloidal and toroidal coils leads to field lines with an incident angle on the dump of at most $\sim 8°$. In this worst case scenario, a few MW/m^2, are deposited at ~ 1.7 cm above the dump pyramids, as shown in Figure 4.23.

The fact that the dump is not in the path of TCV magnetic field lines is reassuring not only for the dump safety but for the plasma operations, as well. No impurity transport from the dump to the plasma can occur along the field lines. Possible impurities on the dump arise essentially from carbon deposition, which explains the dark coating on top of the pyramids, as it can be seen in Figure 4.24. The deposition originates from cross-field transport of carbon ions sputtered from graphite tiles in the machine and travelling mostly along the field lines; the preferential deposition of carbon on the dump betrays the preferred field helicity of TCV experiments. It may also be possible that carbon deposition on the dump arises from (electrically) neutral carbon atoms and molecules that can be deposited in regions hidden from direct exposure to the magnetic field lines [69]. This latter mechanism is however less important than cross field transport of carbon ions. The presence of carbon coating on the viewing dump justifies the assessment of its performance after years of exposure in the tokamak, to make sure its properties have not been adversely altered.

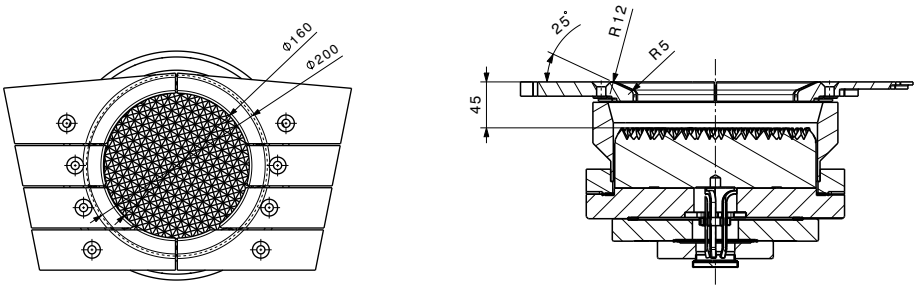

(a) Top view (b) Side view

Figure 4.20: Viewing dump fitting in port B02A 2 on TCV.

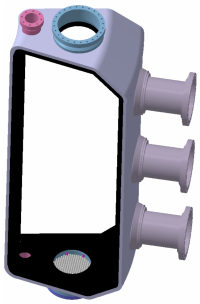

Figure 4.21: The ports hosting the viewing dump and the TCV antenna on TCV.

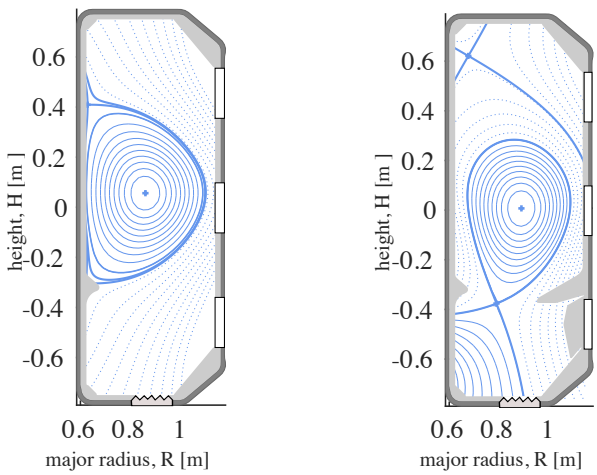

Figure 4.22: Examples of magnetic equilibria on TCV in limited configuration (a) and diverted configuration (b). The LCFS and the divertor legs are in bold lines.

4.3.2 Performance

The performance of the dump is characterized in terms of its capacity to absorb electromagnetic radiation in the millimeter range with wavelength $1.75 < \lambda$ (mm) < 4. The wavelength window

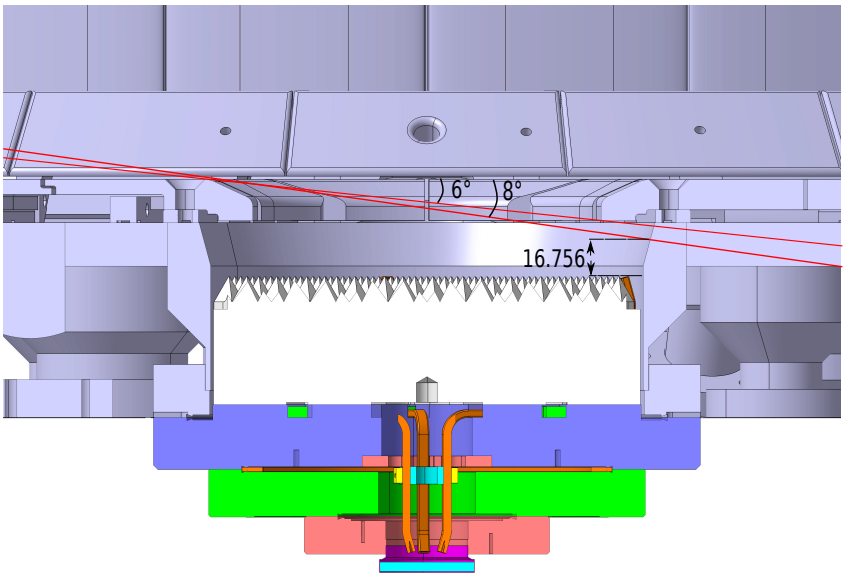

Figure 4.23: The pyramids of the dump are 45 mm below the floor, with an incidence angle of 8° which is a limit value on TCV, the heat and particles are deposited ~ 16.7 mm above the dump pyramids.

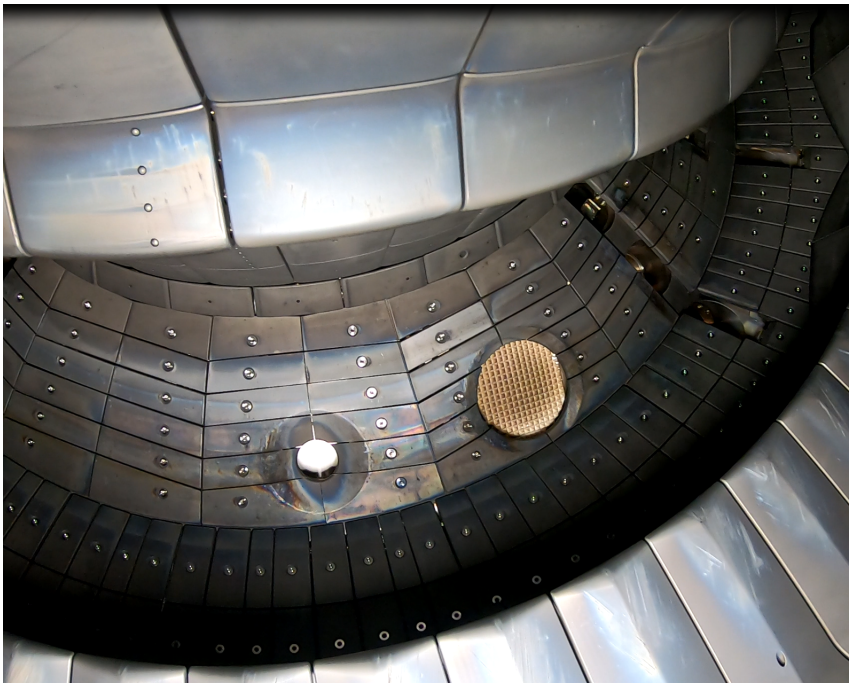

Figure 4.24: Viewing dump in the TCV vessel, exposed to carbon deposition.

covers the planned frequencies for Vertical ECE measurements on TCV $(75 < f\ (\mathrm{GHz}) < 170)$. The absorbing properties of the dump are assessed by measuring its reflectivity both on-axis i.e the

reflection of a wave with normal incidence on the plane of the dump, and off-axis i.e the reflection in the normal direction of a wave incident with different angle with respect to the normal direction. On-axis reflectivity is the parameter to look for when assessing the contribution to the detected radiation of emission that originated within the line of sight before reflection on the dump. Off-axis reflectivity in the other hand, is the key parameter to assess the dump capability to prevent radiation originating outside the line of sight from entering the detection system, as illustrated in Figure 4.25.

The measurement of the dump performance took place prior to the installation of the dump on TCV and 12 years later during this PhD thesis.

Performance prior to installation on TCV

The dump was measured at CNR-IFP (now CNR-ISTP) in Milan in 2007 prior to installation in TCV [70]. The measurements were performed using with an AB Millimetre $8 - 350$ Vector Network Analyzer equipped with WR-10 heads. The measured parameters are expressed in terms of the scattering matrix, the term 11 (S_{11}) and the term 21 (S_{21}) for respectively the reflectivity and the transmitivity. Transmittivity, on- and off-axis reflectivities were measured with the rows of the pyramids parallel and inclined at $45°$ with respect to the incident polarization. Off-axis reflectivity was also measured for polarizations parallel and perpendicular to the plane of incidence. Measurements were achieved using antennas irradiating directly the viewing dump. The distance from the antenna to the dump was chosen to minimize the sensitivity to individual pyramids and to dump edge effects. As a result, on- and off-axis reflectivities were always lower than approx -25 dB and -35 dB respectively. On-axis reflectivity measurements were limited by noise and incomplete removal of systematics due to the poor match of the antennas available at the time, so the results should be viewed as an upper limit. The transmittivity instead was always lower than approximately -27 dB.

Performance after years of exposure in TCV: measurement of the dump reflectivity, with the dump removed from the machine.

The dump reflectivity was first measured removed from the machine, with two different optical setups. Both setups used the Keysight Performance Network Analyzer (PNA) of type PNA N5224A from 10 MHz to 43.5 GHz available at the SPC. The native frequency range of the PNA was extended above the 43.5 GHz limit using modules of Virginia Diodes Inc (VDI) extension heads. The heads included a transceiver/receiver module (TX/RX) and a only receiver module (RX). The on-axis reflectivity of the dump was readily measured with the TX/RX module in reflectometry mode, while the off-axis reflectivity was measured using both modules with the RX modules fixed on axis, and the TX/RX modules scanning different angles around the normal direction.

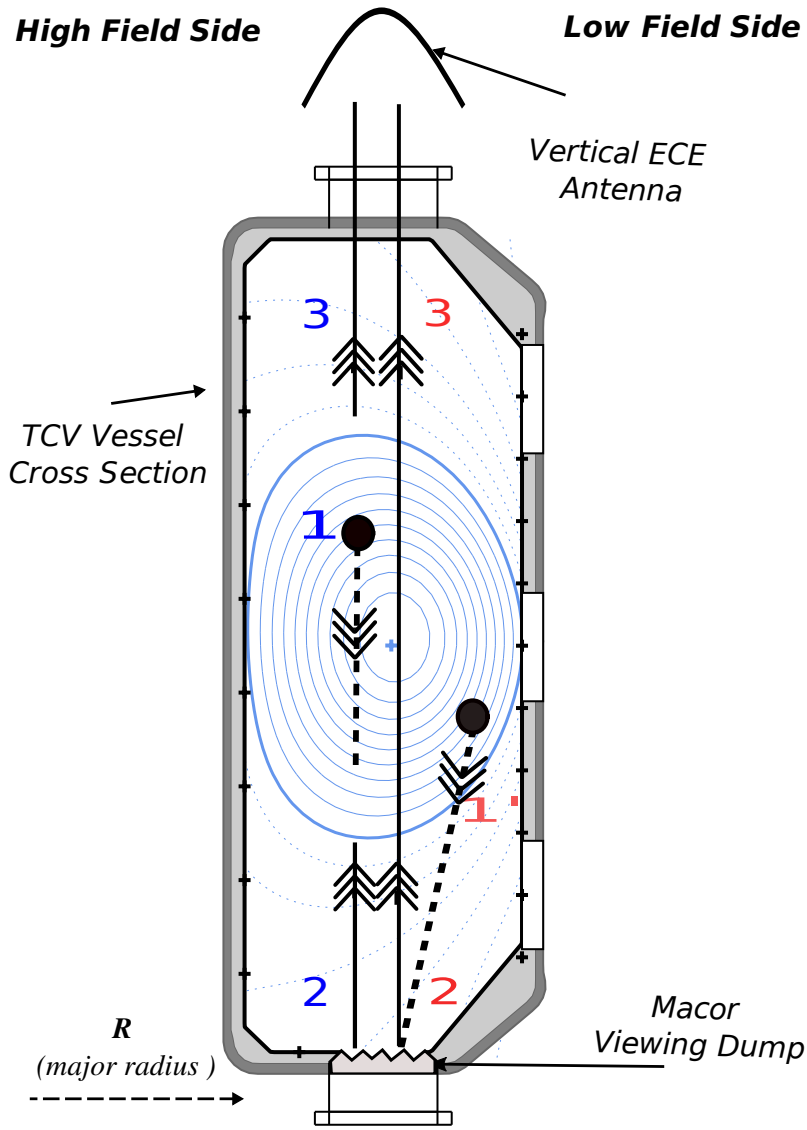

Figure 4.25: TCV cross section with a representation of the MACOR viewing dump and the antenna for Vertical ECE. The radiation reaching the antenna may originate from a region out of the line of sight, in the Low Field Side, following the path 1'-2-3. This is the unwanted radiation for which the assessment of the off-axis reflectivity of the dump is needed. The path path 1-2-3 is instead taken by radiation that originates within the vertical line of sight.

One of the optical setups included the use of horn antennas for measurements in the frequency range 70 to 110 GHz, see Figure 4.26a. For the on-axis reflectivity, a smooth-walled circular horn of aperture ~ 1.63 cm was attached to the TX/RX module to produce a beam of diameter ~ 1.23 cm at the antenna aperture. A Teflon lens (index of refraction ~ 1.4 [71]) was positioned at ~ 15 cm from the horn, obtaining a beam waist of $\sim$4.9 cm for a wave at 70 GHz (waist at ~ 43 cm from the lens) and a beam waist of ~ 3 cm for a wave at 110 GHz (waist at ~ 27 cm from the lens). The beam size was computed using Gaussian beam optics [72]. The diameter of the beam

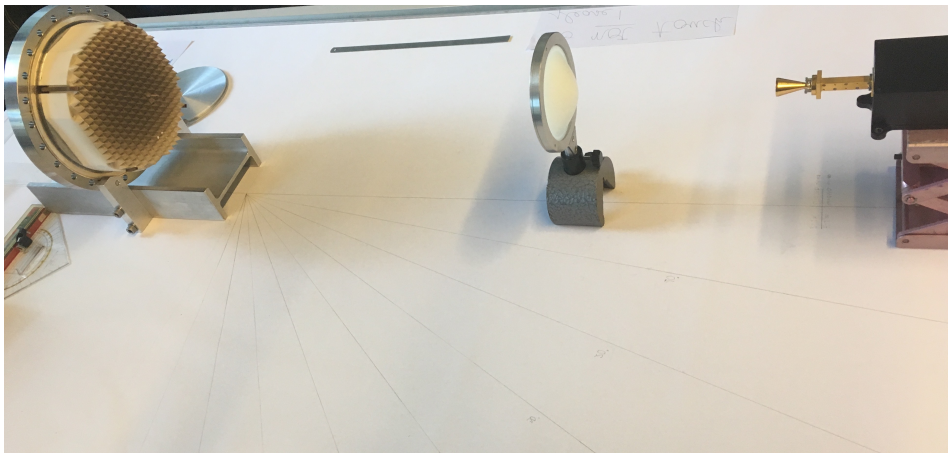

(a)

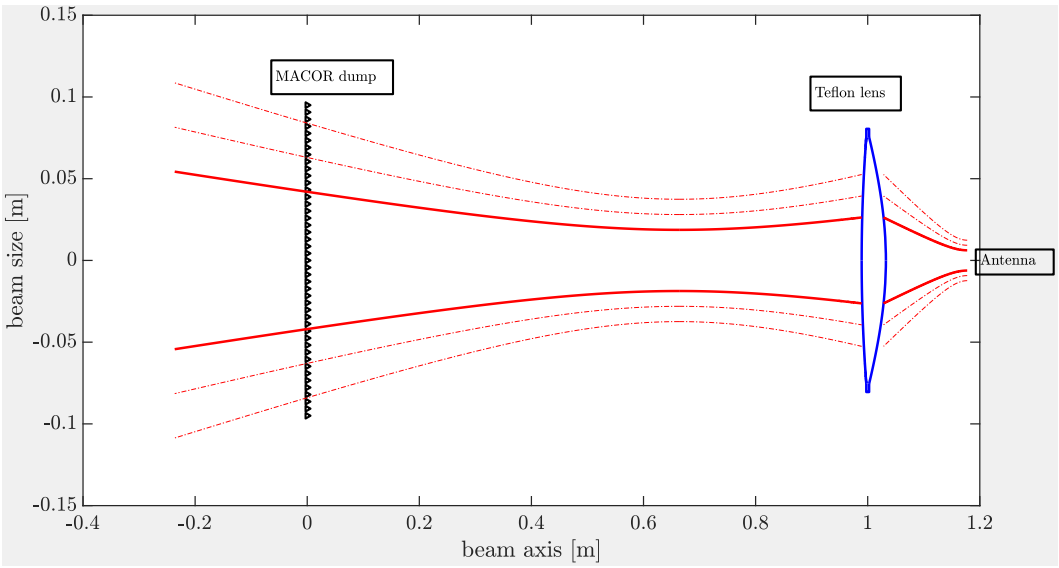

(b)

Figure 4.26: Experimental setup for dump on-axis reflectivity measurement with horn antenna and focusing Teflon lens (4.26a). The pattern of a 90 GHz beam has been computed using Gaussian beam optics applied to our experimental setup (4.26b). The bold line correspond to the beam size at which the field amplitude falls to $1/e^2$ relative to its on-axis value, w_0 ($1/e^2$ power width). The dashed lines correspond respectively to $1.5w_0$ (98% power width) and $2w_0$ (99.97 % power width).

calculated at the dump, ~ 1 m away from the lens (Figure 4.26b), varied from ~ 8 cm at 70 GHz to ~ 8.6 cm at 110 GHz. Stray environmental reflections were suppressed using Eccosorb as absorbing material; the measured reflectivity of the Eccosorb was below -15 dB in our frequency range. The pieces of Eccosorb that are not shown in the figure were spread all around the antenna.

The off-axis reflectivity of the dump was also measured, this time keeping the receiver in front

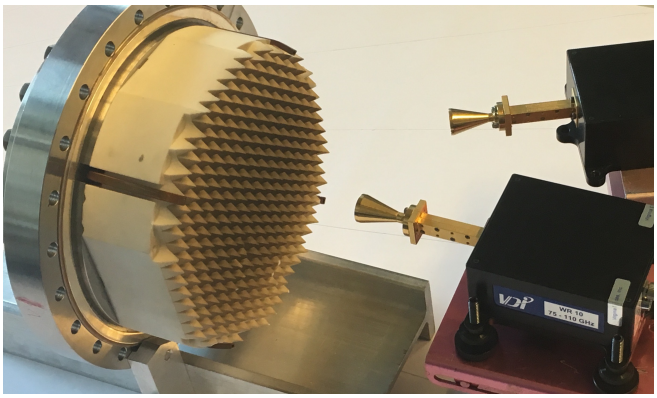

Figure 4.27: Picture of the setup for off-axis reflectivity.

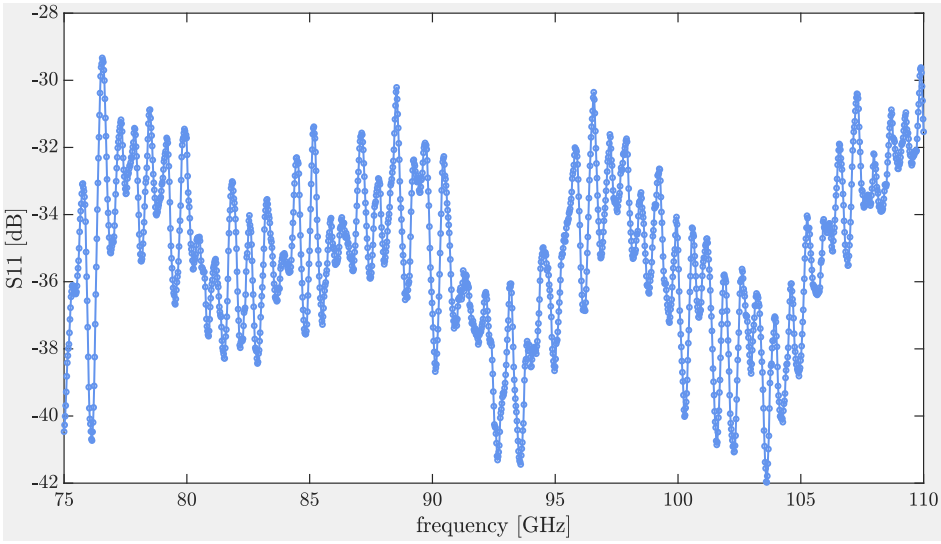

Figure 4.28: Result of the dump on-axis reflectivity measurement.

of the dump and moving the transceiver (Figure 4.27). It was difficult in this case to focus the beam and the resulting values of reflectivity were much lower than the ones measured on-axis and shown in Figure 4.28.

Another measurement of the dump was performed in frequency range $110 - 170$ GHz using the free-space quasioptical table pictured in Figure 4.29. The table is equipped with corrugated horn antennas in the WR-6.5 and WR-4 bands which produce axially symmetric beams with low side lobe. For the reflectivity measurement of the dump, the table was calibrated using as perfect reflector an Aluminium plate. The result for dump reflectivity on the optical table is shown in Figure 4.30. The same Aluminium plate was used for S_{11} normalization for all the measurements.

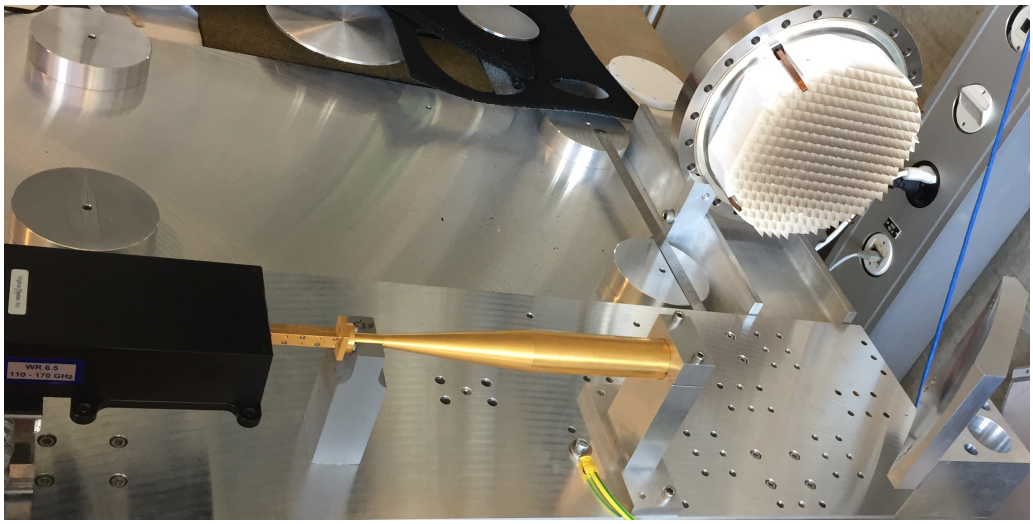

Figure 4.29: Optical table setup for S_{11} measurement.

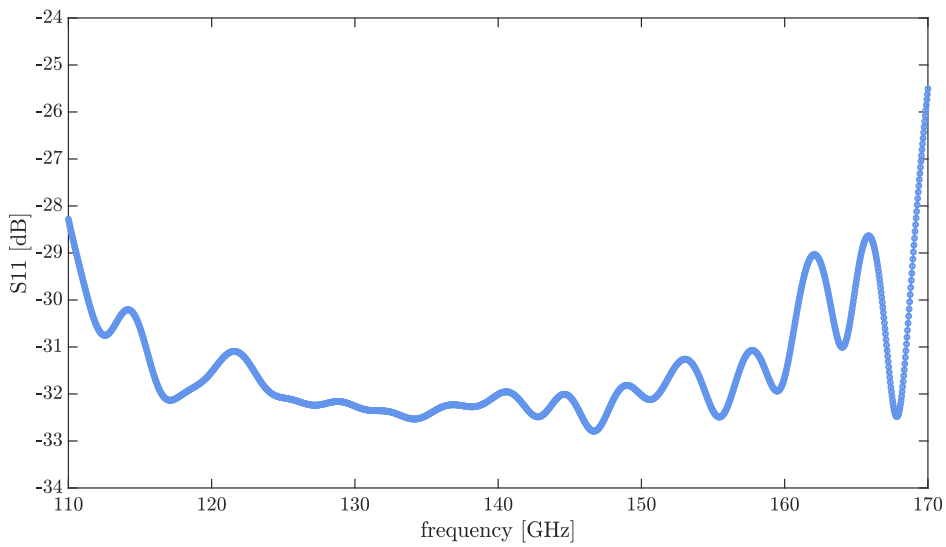

Figure 4.30: Result of the dump reflectivity measurement on the optical table.

Performance after years of exposure in TCV: measurement of the dump reflectivity, with the dump in the machine.

A last attempt to measure the dump properties was achieved with the dump at its port location at the bottom of the tokamak ($\sim$ 1.5 m from the top) . For this measurement, we used the vertical ECE antenna at the top port facing the dump. The details of the antenna and the optics of the diagnostic have been presented in Section 4.2. This reflectivity measurement helped to check the alignment between the dump and the Vertical ECE antenna. Multiple reflections occurred along the path from the antenna to the dump, complicating the measurement. One reflection certainly occurred at the window on the top port. Other reflections originated in waveguides and other metallic spots around the window and the dump. To remove the pervasive reflections

shadowing the dump reflectivity, the plate of Aluminium was installed to cover the dump and, by time of flight we isolated the reflection arising exactly at the position of the plate (time gating). We used that value for the calibration and then removed the plate of Aluminium and repeated the process with the dump instead.
The result for this measurement is shown in Figure 4.31. The reflectivity at the lower frequencies is unexpectedly low compared to the one at higher frequencies. An explanation is that the radiation at low frequencies are diffused in the machine chamber and does not reach back the antenna. The broader radiation pattern at lower frequencies could explain the significant loss of signal. This hypothesis cannot be confirmed on the basis of what has been done in this work, but we note that, what sets the upper limit of the reflectivity as seen by the VECE are the values at higher frequencies. The values of reflectivity at higher frequencies, which come close to -20 dB, also include the reflection at the metallic frame around the dump previously shown on Figure 4.24.

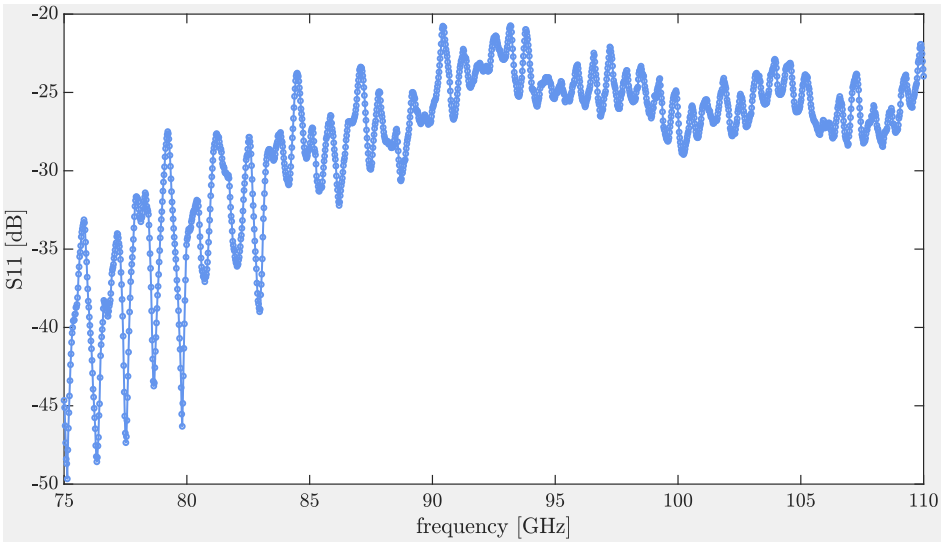

Figure 4.31: Result of the dump reflectivity measurement on TCV.

Conclusion on the performance of the dump

Measurements of the dump properties, prior to the installation on TCV resulted in an average (over frequency) of off-axis reflectivity below -35 dB (Figure 4.32) and on-axis reflectivity around -30 dB. The on-axis reflectivity of the dump measured in 2019 after years of exposure in the tokamak has an average value around -31 dB in the $110 - 170$ GHz range (Figure 4.30), and around -35 dB in the $70 - 110$ GHz range. It is important to mention that these results were obtained with an uncalibrated PNA, taking the ratio of reflectivity measured on a metallic plate, instead of using a free-space PNA calibration including all the discontinuities up to the antenna as done in e.g. [73],[74],[75]. The measurements therefore overestimate the dump reflectivity. Nonetheless, the measurements performed in 2019 are fully compatible with the first measurement of the dump properties prior to its installation (see Figure 4.33). This shows beyond doubts that the dump performance has not been significantly affected by the plasma.

The reflectivity of the dump then can be considered to lie below a value of -30 dB. This result in practice means that the dump reflects $\sim 0.1\,\%$ (or alternatively that it absorbs $\sim 99.9\,\%$) of an incident wave power.

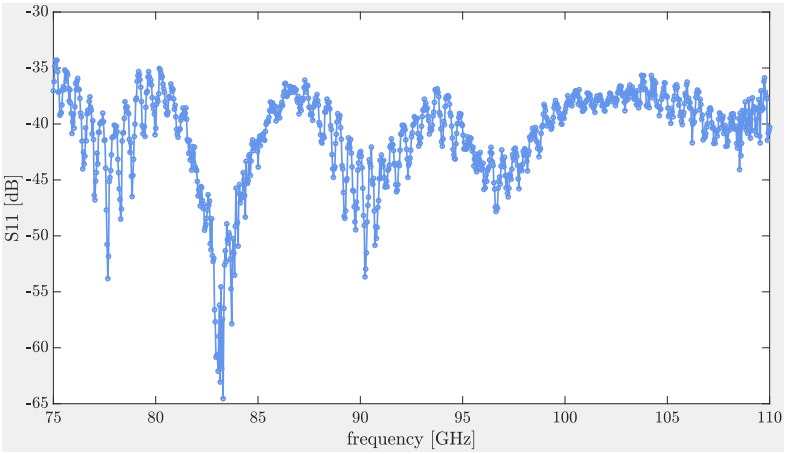

Figure 4.32: A Result of off-axis reflectivity of the dump as measured in 2007 with the TX/RX module at 30° from the axis of the dump.

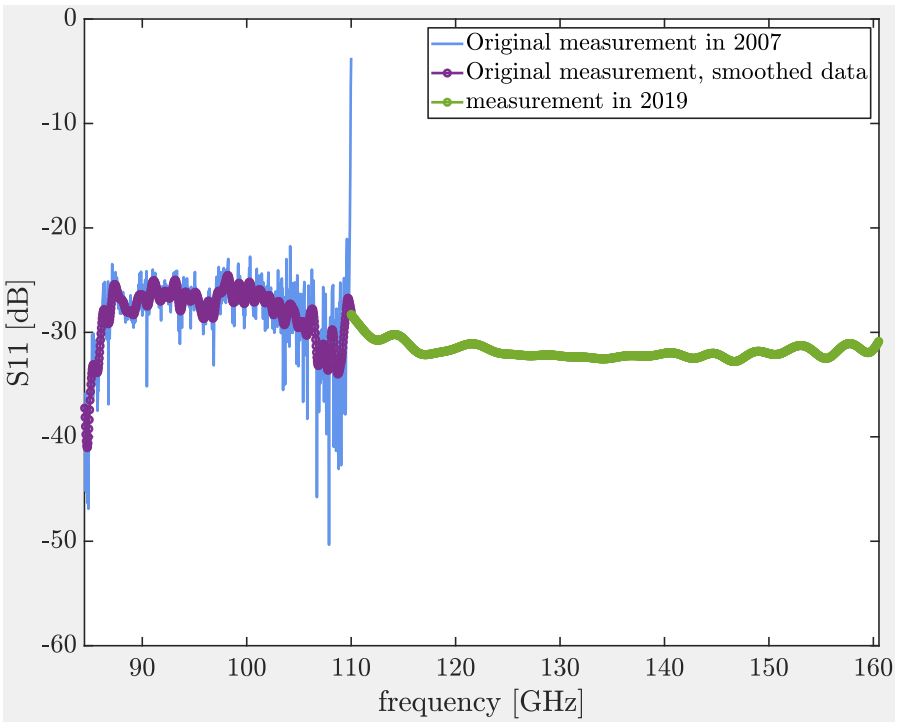

Figure 4.33: Comparison of the measured reflectivity, the S_{11} parameter, before exposition in the tokamak (original measurement in 2017) and after years of exposition (measurement in 2019).

Now that the dump performance has been assessed it is interesting to understand if the presence of a greatly performing viewing dump guarantees the elimination of the tokamak background radiation. For sure some plasma parameters should play a role to allow the dump to fulfill this mission. The next section will clarify the plasma conditions that are needed for the dump to be necessary in Vertical ECE experiments.

4.4 Plasma conditions for Vertical ECE measurements

Some conditions, in terms of plasma parameters, are required for Vertical ECE measurements. The conditions are required such that the detected radiation originates within an isolated vertical volume in the tokamak. From design, the antenna pattern is vertical and terminates on the viewing dump. Multiple reflected radiation to reach the antenna line of sight, reaches first the highly absorbing viewing dump. However, during plasma discharges the refraction in the plasma shifts the antenna pattern which may now miss the viewing dump. The conditions we are looking for in this subsection are the conditions which minimize the beam refraction in the plasma. It may seem from this preliminary consideration that we take for granted that the radiation originating within the line of sight will reach the detection system in any case. We should indeed also avoid the cut-off of the waves originating within the line of sight. We discuss first the conditions to avoid the cut-off, which must be less severe than those to minimize the beam refraction in the plasma. We start the analysis by recalling the the expressions of the refractive indices for the X- and O- polarizations. The expressions are derived within the cold plasma wave theory for perpendicular wave propagation [76, 77],

$$N_{\mathrm{O}}^2 = 1 - \left(\frac{\omega_{\mathrm{pe}}}{\omega}\right)^2, \tag{4.5}$$

$$N_{\mathrm{X}}^2 = 1 - \left(\frac{\omega_{\mathrm{pe}}}{\omega_{\mathrm{ece}}}\right)^2 \frac{\omega^2 - \omega_{\mathrm{pe}}^2}{\omega^2 - \omega_{\mathrm{ece}}^2 - \omega_{\mathrm{pe}}^2}, \tag{4.6}$$

with $\omega_{\mathrm{ece}} = \frac{eB}{m_{eo}}$ the cyclotron frequency, $\omega_{\mathrm{pe}} = \sqrt{\frac{ne^2}{m\epsilon_0}}$ the plasma frequency and ω the wave frequency. The wave cut-off occurs when the refractive index vanishes $(N^2 = 0)$, the wavelength of the wave becomes infinite and the wave energy is reflected. Imposing the cut-off conditions in Equations 4.5 and 4.6 provides the expressions, as a function of the frequency, of the density at which the X and O-mode waves will be in cut-off:

$$n_{\mathrm{O,cut-off}} = \frac{m_e \epsilon_0 \omega^2}{e^2}, \tag{4.7}$$

$$n_{\mathrm{X,cut-off}} = \frac{m_e \epsilon_0 [\omega^2 - \omega\omega_{\mathrm{ece}}]}{e^2}. \tag{4.8}$$

The cut-off density for the O-mode (Equation 4.7) depends solely on the wave frequency, while the cut-off density for the X-mode (Equation 4.8) also decreases with the magnetic field via the cyclotron frequency. A plot of the cut-off densities is shown in Figure 4.34. The cut-off densities for the X-mode have been computed at the highest possible value of the magnetic field within the Vertical ECE line of sight, ~ 1.54 T, to obtain the lowest densities in the plasma needed for the X-mode cut-off. As shown in Figure 4.34, an electron density of at least $\sim 7.94 \times 10^{19}$

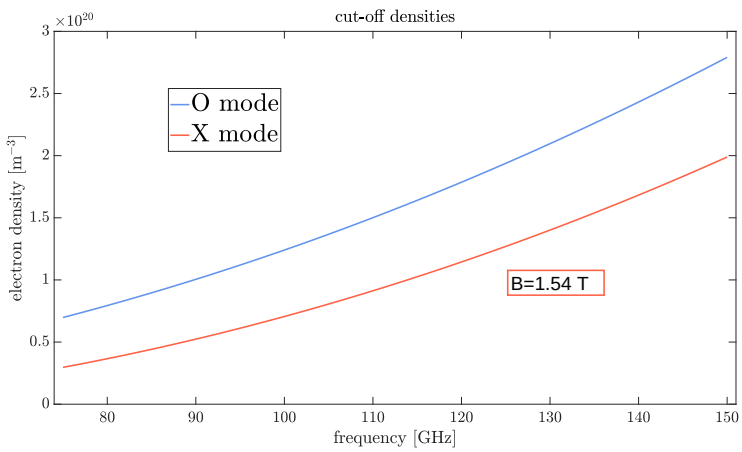

Figure 4.34: Cut-off densities for the X and the O-mode in the frequency range of the Vertical ECE. The cut-off densities for the X-mode are computed at 1.54 T.

m^{-3} in O-mode and $\sim 3.67 \times 10^{19}\ \mathrm{m}^{-3}$ in X-mode are needed to have a wave at 80 GHz in cut-off . The density limit is lower in the extraordinary mode, yet still higher that the typical densities that can be used for Vertical ECE measurements. It is interesting to mention that most of the vertical ECE experiments will use the X2 gyrotrons to create non-thermal electrons and that the X2 gyrotrons operate at a frequency close to 80 GHz. That means we would anyway be constrained in those experiments to stay below the cut-off density limit for X mode to ensure that the gyrotron wave itself does not enter in cut-off. Many of the other plasma experiments for Vertical ECE require lower densities. We can thus, in general, consider that the wave cut-off of both polarizations is avoided during Vertical ECE measurements.
The evaluation of the plasma conditions needed to minimize the beam refraction in the plasma is another story, requiring the simulation of the beam propagation in the tokamak.

4.4.1 Refraction of the beam pattern in the plasma

Simulation method

The antenna beam pattern is simulated using the code SPECE [43] already introduced in Chapter 2. The ray-tracing code mimics the antenna pattern with a set of rays and models their propagation in the vessel. In reality, only the propagation in the plasma is actually modelled, and that is because effects such as the wave diffraction are not included in ray-tracing approaches. The rays propagate in a straight line in the vacuum and cannot curve to produce the beam waist at the design spot near the vessel mid-plane. For our analysis, this limitation does not have a great influence as we are only attempting to have a window of electron density that certainly minimizes the effect of the beam refraction in the plasma. But in general, the ray tracing approximation, or

the geometrical optics approximation, has validity when the wavelength of the waves is much shorter than the characteristic length of variation of the background quantities. If the length of variation of the background magnetic field and density is

$$L \sim |\nabla \log n_{\mathrm{e}}|^{-1} \sim B|\nabla \overrightarrow{B}|^{-1}, \tag{4.9}$$

then the ray tracing approach has validity when the inequality $kL \gg 1$ holds, with k being the wavenumber [78]. In most of the cases of our interest, we can consider that geometric approach is appropriate. That being said, minimizing the refraction means finding a window of of plasma parameters that allows the antenna beam intensity to mainly fall within the viewing dump after its interaction in the plasma. To compensate for the missing diffraction effect, the beam size used for the simulation is a bit larger that the waist size, ~ 5 cm. As input, the simulation needs the plasma equilibrium, the electron density and temperature as a function of ψ, the normalized toroidal flux. Figure 4.35 shows the results of the modelling for a wave at 80 GHz in the O-mode and X-mode for different electron densities, and Figure 4.36 for a wave at 150 GHz. The simulations were performed with the same plasma equilibrium. The input electron density at each ψ was multiplied by the same factor to obtain the different values of line averaged density, to isolate the only effect of the density on the refraction. Of course there was no need to modify the input temperature as it has no effect on the beam refraction.

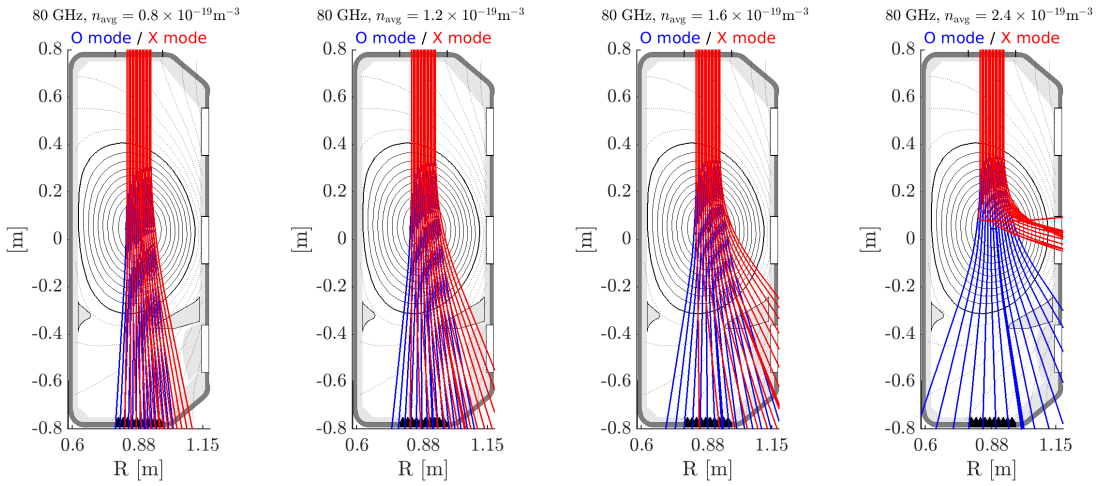

(a) (b) (c) (d)

Figure 4.35: Simulation of rays trajectories for a wave at 80 GHz with scan of the line averaged density from 0.8×10^{-19} m^{-3} (4.35a) to 2.4×10^{-19} m^{-3} (4.35d).

The general considerations we can draw from the Figures 4.35 and 4.36 are actually as expected: the refraction effect is worst at the lower frequencies and at higher densities. The dependence of the beam refraction on the frequency was already clear from the expression of the indices of refraction in Equations 4.5 and 4.6. The refractive indices for both polarizations increase asymptotically with the frequency. By looking at the same equations, it is also with no surprise that the refraction effect is worst for the X-mode, since its index of refraction is always lower

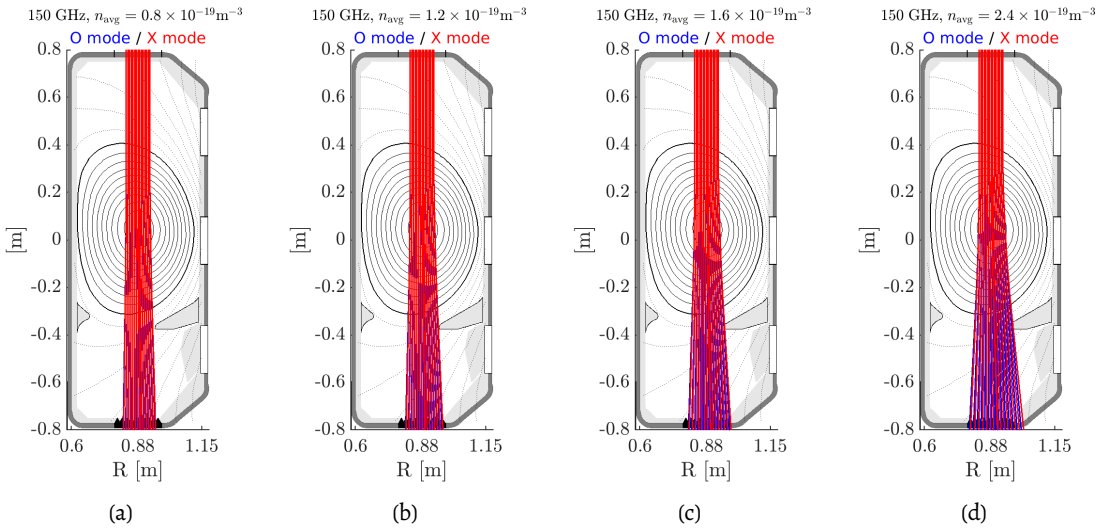

Figure 4.36: Simulation rays trajectories for a wave at 150 GHz with scan of the line averaged density from 0.8×10^{-19} m^{-3} (4.35a) to 2.4×10^{-19} m^{-3} (4.35d).

than that of the O-mode. In the simulation of the wave at 80 GHz, the most explicit effect is that of the density on the beam refraction. It is really the density gradient that drive the change in the refractive index and thus induces the beam refraction. By multiplying the densities at each Ψ by a constant factor and keeping the magnetic equilibrium frozen, the density gradient was also increased. The consequence is the increased effect of refraction on the beam at higher densities. The Figure 4.35d is actually interesting as it shows the refraction of the O-mode and the cut-off of the X-mode beams. That simulation was done with a line averaged density of 2.4×10^{-19} m^{-3} . With this value, the maximum density near the center of the plasma reaches 3.7×10^{-19} m^{-3}, very close to the density limit needed for the X-mode cut-off at 80 GHz, as we previously found. The cut-off limit , as expected, is higher for the O-mode and for the higher frequencies. This is an important consideration, which means that during Vertical ECE experiments, we will certainly hit the limit for the beam refraction before the limit of the wave cut-off. We should logically only focus on minimizing the antenna beam refraction in the plasma. For that we need to infer quantitative information from the refraction simulation, we need to obtain numbers on the density limit for refraction using the SPECE simulations.

The approach we use is made of a few steps. First we find an optimal number of rays to mimic the antenna pattern. We chose in our case 105 rays. They are distributed in 13 concentric circles on which 8 rays are equally spaced, plus of course the central ray at the center of the antenna beam. The set of rays is propagated through the plasma and the trajectory for each ray is computed and recorded at the height of the viewing dump to quantify the effect of refraction in the plasma. The ray distribution at the antenna and at the dump height can be seen in Figure 4.37. The rays are weighted such that the intensity in the beam forms a Gaussian beam pattern with a $1/e^2$ power level wide 10 cm in diameter.

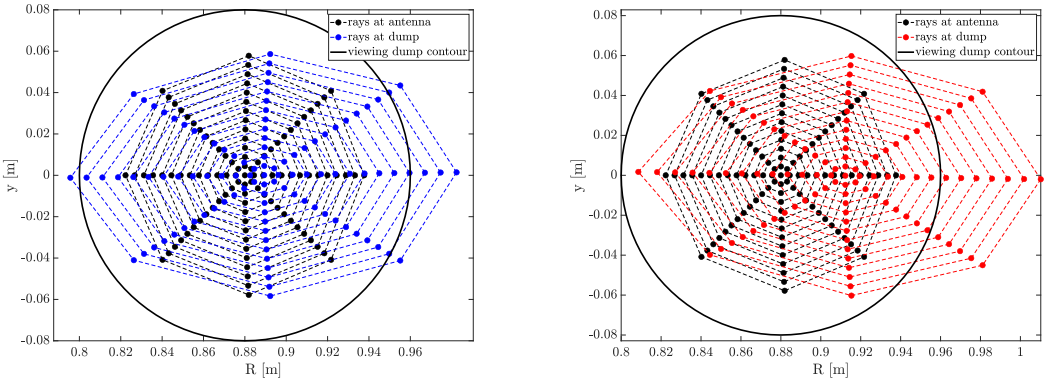

(a) O-mode

(b) X mode

Figure 4.37: Top view of the ray distribution at the dump and at the antenna for the two polarizations at frequency 80 GHz and line averaged density of $0.4\ \mathrm{m}^{-3}$.

The radial and toroidal distributions of the rays at the dump height is shown in Figure 4.38. The rays are shifted mainly in the radial direction and the situation is, again, worst for the X-mode. It is interesting to look at the ray distribution along the toroidal direction in Figures 4.38a and 4.38d. For both modes there is very little shift in the toroidal direction. That is due to the density gradient which is almost constant along the toroidal direction.

The second step of the approach is to reconstruct the beam intensity distribution at the dump height. This relies on the assumption that the beam, after its interaction in the plasma, conserves its Gaussian distribution. Assumption that was verified in previous studies on TCV plasmas [79]. In the extreme cases, when the beam does not reach the dump height we consider that the beam power at the dump is null. In cases when the beam reaches the floor of the machine, its intensity is distributed according to a Gaussian distribution around the central ray as shown in Figure 4.39.

When the beam intensity distribution at the dump height is found, a straightforward calculation is done to infer the fraction of that beam intensity falling within the dump diameter. The intersection of the dump diameter and the beam intensity distribution is also schematically shown in Figures 4.39a, 4.39b.

This analysis is repeated for a set of frequencies. In theory the density limit is the density at each frequency for which a considerable fraction of the beam intensity does not fall within the dump diameter. The Figure 4.40 shows that this limit in the X-mode is reached already at a low line averaged density at 80 GHz. This will have important consequences on the diagnostic operation.

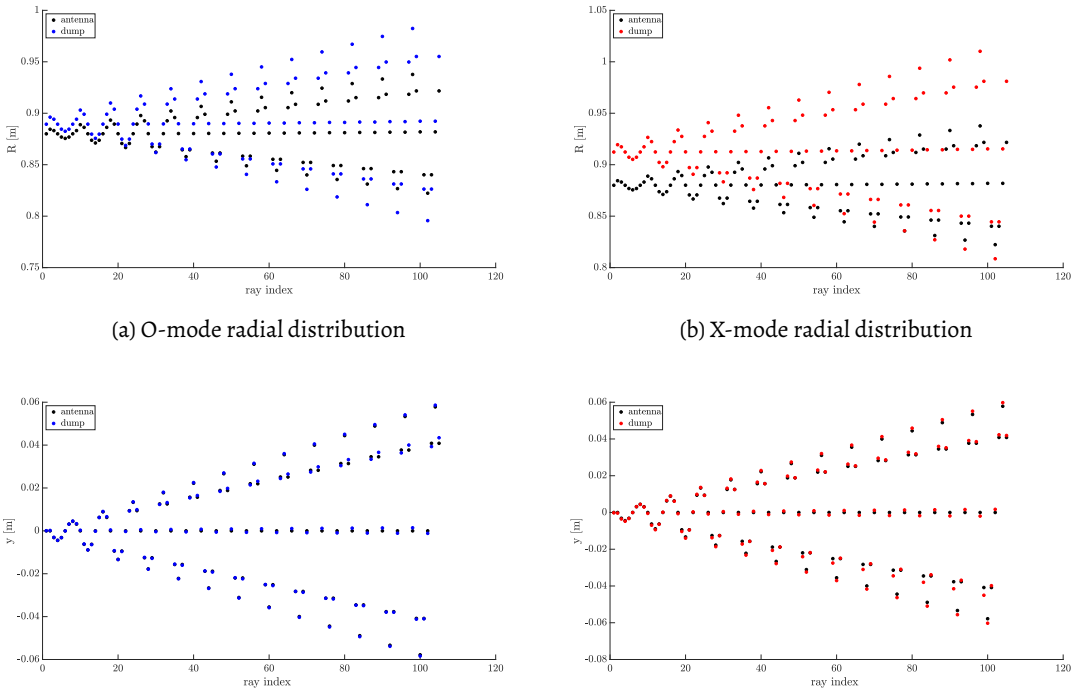

(a) O-mode radial distribution

(b) X-mode radial distribution

(c) O-mode toroidal distribution

(d) X-mode toroidal distribution

Figure 4.38: Radial (4.38a, 4.38b) and toroidal (4.38c, 4.38d) distribution of the rays at the antenna and at the dump height for the two polarizations at frequency 80 GHz and line averaged density of $0.4\,\mathrm{m}^{-3}$.

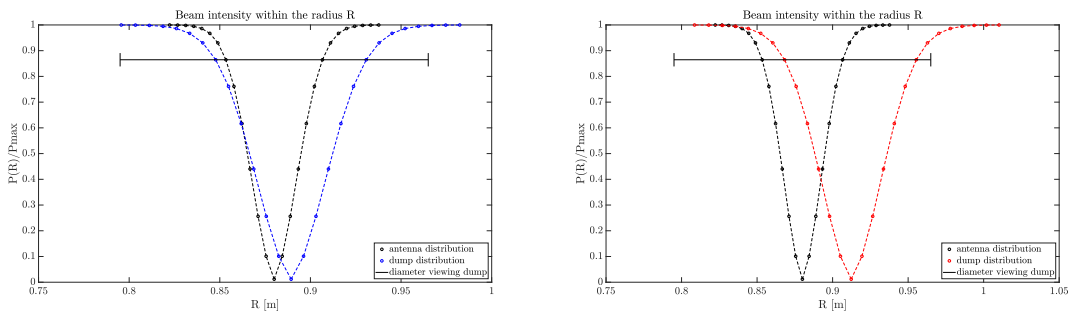

(a) O-mode

(b) X-mode

Figure 4.39: Beam intensity distribution at the dump and at the antenna for the two polarizations at frequency 80 GHz and line averaged density of $0.4\,\mathrm{m}^{-3}$.

Simulation consequences

The simple analysis we have performed has allow us to estimate the fraction of the beam intensity which falls out of the dump as a function of discrete values of the electron density in the plasma. The result shown in Figure 4.41 refers to the X-polarization only, for which the density limit is

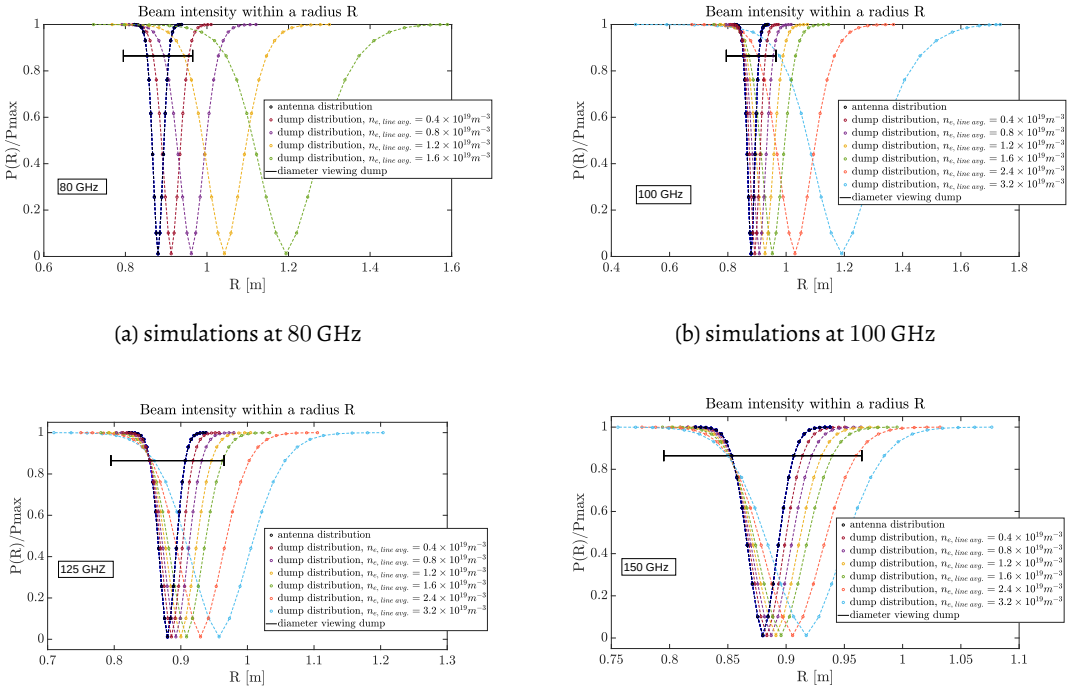

(a) simulations at 80 GHz

(b) simulations at 100 GHz

(c) simulations at 125 GHz

(d) simulations at 150 GHz

Figure 4.40: Beam intensity distribution at the dump and at the antenna for the X mode at different frequencies and different line averaged densities of electrons in the plasma.

the most constraining. At high frequencies (e.g. 150 GHz), the antenna beam intensity falls quasi-entirely within the viewing dump until we reach a line averaged density of 2.4×10^{-19} m^{-3}, corresponding to a maximum density in the plasma of 3.7×10^{-19} m^{-3}. The density limit at this frequency is practical, allowing operation of the Vertical ECE diagnostic in most plasma conditions. The situation at low frequencies instead is essentially unpractical. The refraction constrains Vertical ECE measurements to be achieved in plasmas with line averaged densities $\sim 0.4 \times 10^{-19}$ m^{-3} corresponding to a maximum density in the plasma of $\sim 0.6 \times 10^{-19}$ m^{-3}. At a line density of $\sim 0.8 \times 10^{-19}$ m^{-3} (maximum density $\sim 1.2 \times 10^{-19}$ m^{-3}), half the beam intensity at 80 GHz would already miss the dump. This sets the maximum density for refraction to a stringent value, below $\sim 1 \times 10^{-19}$ m^{-3}. With this constraint, the window of operation of the Vertical ECE is drastically limited and something needs to be done.

4.4.2 Mitigating the antenna beam refraction in the plasma

In an attempt to reduce the effect of the antenna beam refraction for the Vertical ECE diagnostic, we have considered three possible solutions:

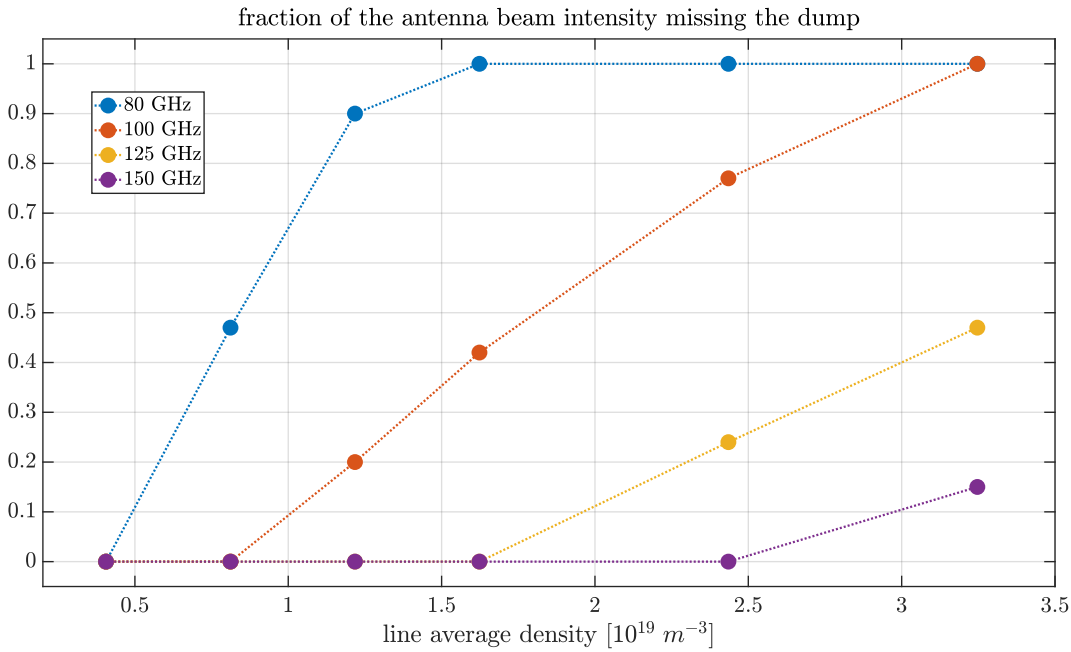

Figure 4.41: Density threshold for refraction at different frequencies calculated with the same plasma equilibrium.

Pushing the density limit by adjusting the experimental parameters

Some experimental parameters can be tuned to limit the refraction of the antenna beam. We have previously seen that refraction is worst in the X-mode. One solution could be to favor the measurement of the ordinary polarization only for Vertical ECE studies. Even if this solution could help pushing the refraction boundaries, it will limit the information we gain with the diagnostic. Measurements of both polarizations are necessary to have more independent measurements at the same frequency. Discharge parameters such as the triangularity, the plasma height in the vessel and the magnetic field can be optimized to reduce the refraction. A lower magnetic field reduces the refraction in the plasma by decreasing the cyclotron frequency in Equation 4.6. Choosing 0.9 T, the lowest magnetic field achievable on TCV for Vertical ECE experiments can increase the threshold density for refraction. This solution should however limit the use of the X2 gyrotron for heating as it puts the cold resonance location out of the machine. The solution also shifts upward the harmonics that we measure in our frequency range. Changing the plasma height in the vessel could have an influence, although marginal on the fraction of the beam intensity that falls within the dump after the refraction in the plasma. This is because the beam travels essentially straight in vacuum. If the plasma is formed very close to the viewing dump at the floor of the vessel, reducing the distance between the the viewing dump ant the plasma, the fraction of the beam falling out of the dump will be reduced. The

antenna beam in this condition would be subject, in vacuum, to the natural beam divergence only and would remain collimated until its interaction with the plasma near the bottom of the machine. The proximity of the plasma to the dump would then allow a significant fraction of the beam to fall within the dump, even if the refraction in the plasma was considerable. This solution will however not be tried for Vertical ECE measurements for practical reasons. A more practical solution instead is keeping the plasma at a height near the mid-plane of the machine and modifying its shape. Modifying the triangularity of the plasma, for example, could modify the density gradient in the region of interaction of the beam and the plasma. Some of these solutions are illustrated in Figure 4.42.

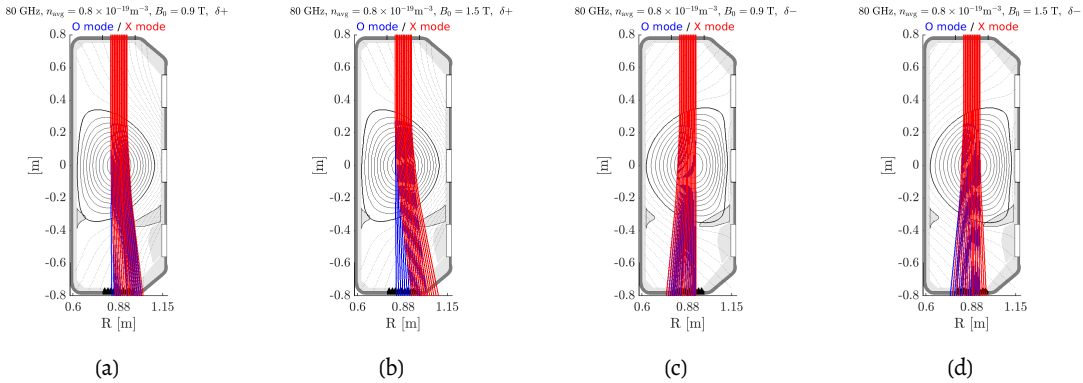

Figure 4.42: Rays trajectories simulation for a wave at 80 GHz at fixed line averaged density $0.8 \times 10^{-19}\ \mathrm{m}^{-3}$ to illustrate the effect on refraction of the magnetic field and the plasma shape.

Working at low densities to minimize refraction

The solutions proposed previously to increase the density limit for refraction are not practical for Vertical ECE measurements. Here we discuss the possibilities of Vertical ECE measurements constrained by a severe density limit. A plasma with a maximum density in the center of $\sim 1. \times 10^{-19}\ \mathrm{m}^{-3}$, would allow the antenna beam pattern to fully fall within the dump. At that density, the viewing dump, would absorb the background radiation resulting from multiple wall reflections in the vessel. That density limit reduces the diagnostic applicability to only low density ohmic discharges for example for runaway electron studies. In runaway electron discharges, the background radiation for which the dump should be useful is actually not as relevant. In fact, the runaway discharges, due to their low electron densities have their thermal radiation, contained within low levels, levels much lower than the non-thermal emission from the highly energetic electrons in the tail of the distribution.

Magnetic field variation

The issue of the refraction of the antenna beam in the plasma should not be dissociated from the multiple wall reflection of radiation in the tokamak. When the antenna beam pattern is shifted out of the viewing dump, the risk for the diagnostic is the contamination of the non-thermal emission by the background radiation via multiple wall reflections. The measured radiation in that case is a combination, difficult to disassemble, of the background radiation and the non-thermal radiation. The modelling of multiple wall reflections, in order to assess its contribution to the detected radiation has been attempted over the years in some ECE studies, see References [46] and [80] for example. The difficulties in using a reflection model to separate the various contributions lie in the complicated geometry of the vessel tiles, the wave diffraction on the tiles apertures and the change of polarization of the wave at each reflection. In this paragraph, we present an approach that goes around both the modelling of multiple wall reflections and the operation of the diagnostic at a highly constrained electron density. This approach focuses on the question: what if the antenna beam pattern is refracted out the dump and the diagnostic, still, does not peak up the background radiation? To provide an answer to this question we should first focus on the origin of the background radiation. It is a thermal radiation competing at the same frequency with the non-thermal emission originating within the diagnostic line of sight. In theory, the thermal background can originate exclusively in the discrete radial locations of the cold resonances of the contributing harmonics. The radial location, $R_{n\mathrm{ece}}$, of the cold resonance at an harmonic n, of a given frequency $\omega_{n\mathrm{ece}}$, is a function of the only central magnetic field in the machine, B_0 . An expression is given from the resonance condition in tokamak by the equation

$$R_{n\mathrm{ece}} = \frac{neB_0R_0}{2\pi m_e\omega_{n\mathrm{ece}}}, \tag{4.10}$$

here $R_0 = 0.88$ m is the major radius of the tokamak. From Equation 4.10, an expression relating the radial distance between the cold resonances of two consecutive harmonics $n, n+1$ can be written as

$$R_{(n+1)\mathrm{ece}} = \frac{1}{n+1}R_{n\mathrm{ece}}. \tag{4.11}$$

What we would like to assess is the maximum number of harmonics that can contribute to the background radiation. For that we need the radial distance between the harmonics of a given frequency, which follows directly from Equation 4.11 as:

$$\Delta R_{n+1,n} = \frac{1}{n} R_{n\text{ece}} \ , \quad \Delta R_{n+2,n} = \frac{2}{n} R_{n\text{ece}} \ , \ldots \tag{4.12}$$

Calculations using Equation 4.12 with TCV parameters suggest that $\Delta R_{n+1,n}$ is in any case smaller that the minor radius a of the machine and that $\Delta R_{n+2,n}$ is in any case larger than a. This means that only two consecutive harmonics can, in theory, participate to the background radiation on TCV. Considering the magnetic fields and our frequency range on TCV, there is actually no possibility for the cold resonance of the first harmonic to be located in the vessel. The higher harmonics, which are optically thick for the extraordinary polarization, are the ones that can contribute to the background radiation. This is an interesting point: the background radiation that can be measured by the refracted antenna beam originates on TCV essentially as an X-mode emission from a known location that depends on the magnetic field only.

The magnetic field determines for a given frequency band the location of the resonances of the thermal X-mode emission. Depending on the field value, the two contributing harmonics within the vessel can be X2 and X3 (see Figure 4.45a) or X3 and X4 (Figure 4.45b) for example. Let's consider the case of Figure 4.45a when the X2 and the X3 harmonics are the ones contributing to the background radiation. In that case, the Vertical ECE antenna is set up to measure the down-shifted third harmonic emission from the non-thermal electrons, and in the vessel are present the X2 and X3 cold resonances. It is of great interest to determine the relative contributions of X2 and X3 to the background radiation. Actually, the X2 emission that reaches the black-body level literally dominates over the X3 (X2/X3 $\gg 1$) , and the background radiation can be considered to have essentially originated from the X2 emission. Experimental validations of the large X2/X3 ratio will be presented and used in the next chapter to calibrate the diagnostic. As a theoretical support, we show in Figure 4.43 the ratio of the black-body intensity (X2) to the X3 intensity as a function of the plasma optical depth. In a plasma with an electron temperature $T_e \sim 1$ keV and density, $n_e \sim 1 \times 10^{19}\ \mathrm{m}^{-3}$ the ratio X2/X3 reaches values close to ~ 20. Since both the X2 and X3 emissions undergo wall reflections in the same conditions, and the scrambling on the tiles does not depend on the harmonic number, we conclude that the ratio of the multiply reflected radiation ($\mathrm{X2_{refl}/X3_{refl}}$) is of the same order of the ratio X2/X3 of the single pass intensities. It is important to note that the X3 optical depth scales like $n_e T_e^2$, so the ratio X2/X3 decreases with increasing electron temperature. Calculations at temperatures ~ 4 keV yield a ratio X2/X3 still high enough to neglect the X3 contribution to the background radiation on TCV. Moreover, neglecting the X3 contribution necessary means neglecting higher harmonics contribution.
At this point of the discussion we have two important pieces of information: (1) the background radiation originates as a thermal radiation in specific locations in the plasma and (2) the thermal radiation dominating the background radiation was an X2 emission at its origin.

Based on this, it now appears obvious that a way to avoid multiple wall reflection is to simply keep the X2 cold resonance radius out of the machine. We can then relax the constraint on the electron density and allow for antenna beam refraction, which cannot be detrimental for the

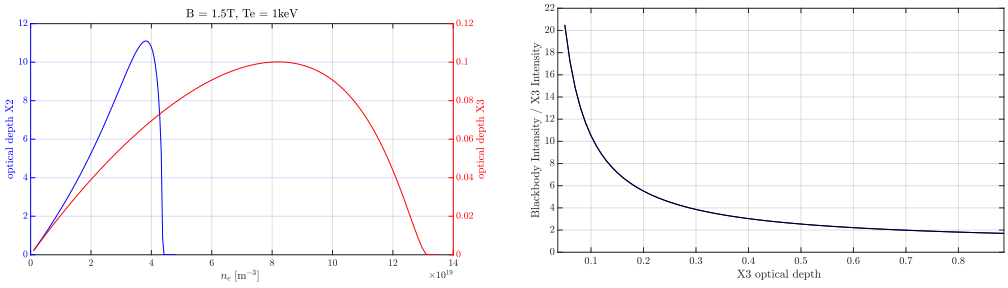

(a) (b)

Figure 4.43: Optical depth of the X2 and X3 calculated at a temperature of 1 keV 4.43a and ratio of the X2/X3 intensity as a function of the X3 optical depth.

measurement if the the background radiation does not originate within the machine. Figure 4.44 illustrates the situation on TCV. The X2 cold resonance location (major radius) increases with B_0 and decreases with the frequency as of Equation 4.10. When that major radius increases (decreases), the resonance is shifted towards the LFS (HFS) of the machine. When B_0 is lowered down to $\sim$ 1 T, all the frequencies that we measure have their X2 cold resonance out of the machine, in the HFS. Increasing B_0 allows the frequencies from 78 GHz to progressively have their X2 in the machine, up to the maximum $B_0 \sim 1.5$ T where all frequencies below $\sim$ 117 GHz have their X2 in the machine. Figure 4.44 provides another information: all the frequencies above $\sim$ 117 GHz will always have their X2 resonance out of the machine, and in that sense will never encounter the issue of background contamination from multiple wall reflection on TCV.

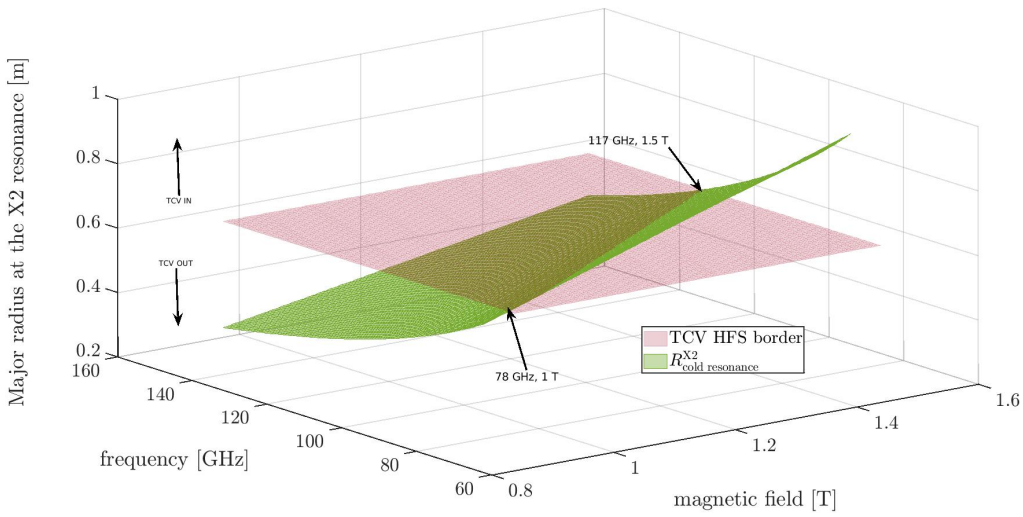

Figure 4.44: Major radius of the X2 cold resonances in the Vertical ECE frequency range, computed for all magnetic field achievable on TCV.

In Subsection 4.4.1 we found moderate density constraint at high frequencies. In this paragraph we find that those frequencies are also free from the issue of multiple wall reflections on TCV. The only constraint at frequencies above ~ 120 GHz would be the cut-off density, which is above $10 \times 10^{-19}\ \mathrm{m}^{-3}$ in X-mode. From Figure 4.44 it is also clear, that by decreasing the field, we could get rid of the multiple wall reflection issue for all the frequencies of our system. This solution will have a limitation related to the heating system during ECH experiments. In fact, the frequencies of the X2 gyrotrons are around 82 and 84 GHz. By decreasing the magnetic field, we shift the absorption location of the heating power towards the HFS with the consequences of possible shine through. From this, we conclude that the optimal window for Vertical ECE operations is the window that allows all the frequencies to have their X2 out of the machine, while allowing the X2 resonance location of the gyrotron frequencies close to the center of the machine. With the available radiometers, the frequencies above ~ 117 GHz are, based on this analysis, free from the thermal background radiation issue. At those frequencies, the Vertical ECE diagnostic can even be operated **without a viewing dump**. Most of the frequencies of the available radiometers are between ~ 78 GHz and 114 GHz as seen in Section 4.1. For those frequencies, a fine tuning of the experimental parameters such as magnetic field, electron density, etc. will be needed to obtain clean measurements at those frequencies too. In a design of a future radiometer for Vertical ECE on TCV, the frequency range between $120 - 170$ GHz should be privileged as it allows clean measurements of the non-thermal X4/O4 and X3/O3 emission with very little constraints on the experimental parameters. That is provided a good calibration of the system can be achieved at those frequencies. The calibration will be discussed in the next chapter, after the section on the energies measured by the diagnostic.

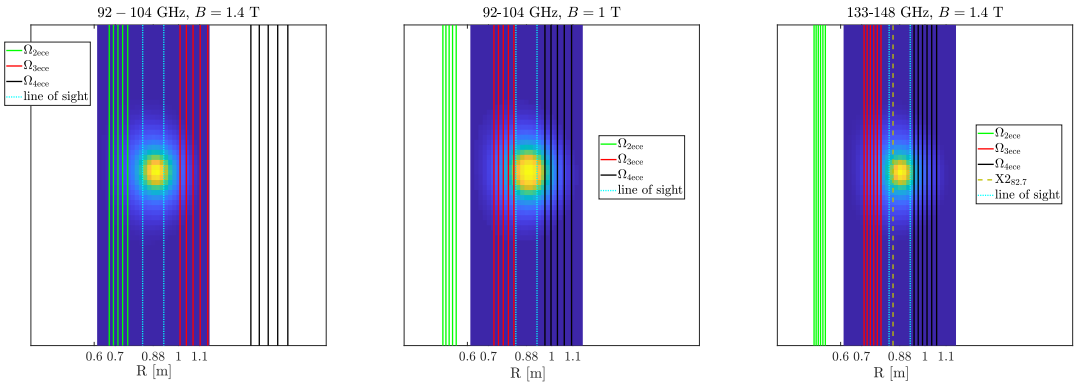

(a) (b) (c)

Figure 4.45: Illustration of the radial location of the harmonics contributing to the background radiation for selected frequencies. The emission layers which are not shown for simplicity lie at the high field side of each of the vertical line representing the the cold resonances major radii. The line of sight is also schematically drawn to represent the vertical region from which direct emission originates. In Figure 4.45a, the X2 harmonic, essential contributor to the background radiation is present in the vessel. In this situation, multiple wall reflection of the original X2 emission can pollute the downshifted third harmonic emission in the frequency band $92 - 104$ GHz if the line of sight is refracted out of the dump. In Figure 4.45b the field is lowered to keep the X2 thermal emission out of the machine, in the frequency band $92 - 104$ GHz. This is a condition for a clean operation of the diagnostic where density constraints can be relaxed and the viewing dump removed from the machine. The only issue: the gyrotrons cannot heat the plasma at the second harmonic at this field value. In 4.45c is shown a good compromise. The field value allows the gyrotrons to heat the plasma near its center, the X2 resonance location of the gyrotron frequency even lies within the line of sight. The diagnostic can measure the downshifted fourth harmonic emission from non-thermal electrons in the frequency band $133 - 148$ GHz. The measurement can be achieved, again, without need for a viewing dump and with a relaxed density constraint related only to the wave cut-off.

4.5 Energies and resolution

4.5.1 Energy range

We have now reached the point where we can estimate the energies that the Vertical ECE diagnostic can measure in our frequency range, $78 - 148$ GHz. For the calculation of the energies, we assume that the detected radiation is a direct emission originating within the diagnostic line of sight, and that harmonic overlap is minimized. With those assumptions, Equation 3.6 in Chapter 3 can be used to calculate the kinetic energy of the electrons whose emission is detected. Figure 4.46 shows the result of the calculated energies in a map where the values of energies at the field value of 1.4 are highlighted.

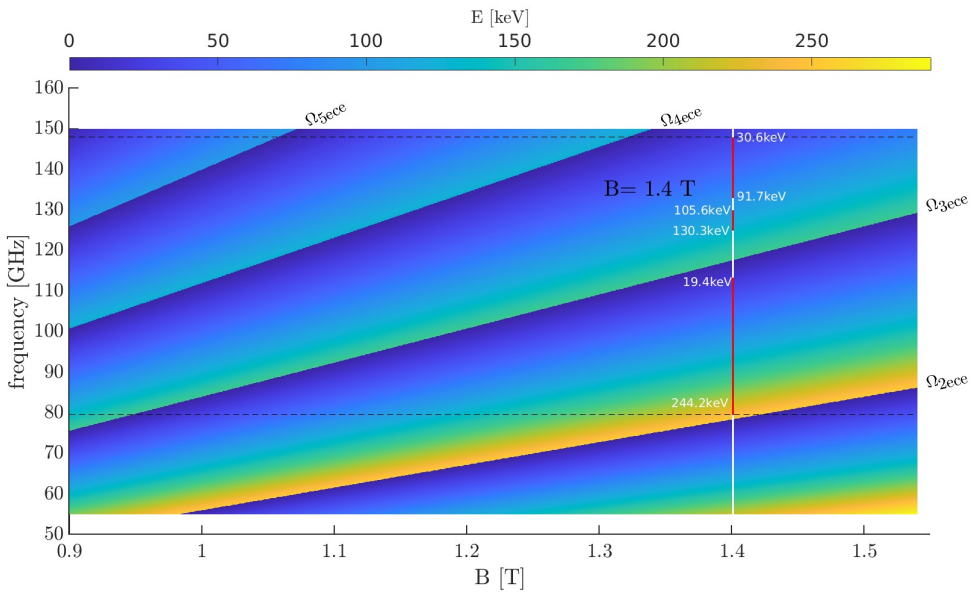

Figure 4.46: Map of the energies measured by the Vertical ECE on TCV in the absence of harmonic overlap.

The measurements at the available frequencies can in theory span from the downshifted second harmonic (Ω_{2ece}) to the downshifted sixth harmonic (Ω_{6ece}). The energy measured by a frequency is determined by the frequency difference between that frequency and the frequency of the upward harmonic of the fundamental cyclotron frequency. That distance depends only on the value of the magnetic field. Changing the value of the field allows each frequency to probe a different region of the phase space. This situation is equivalent, in the physical space, to the antenna which is fixed vertical and and the cold resonance of the harmonic of the measured frequency that is shifted in the radial direction by a change of the magnetic field. The diagnostic can only measure downshifted emission from the harmonics at the lower field side of the line of sight. At a given frequency, the energy measured will be higher if the line of sight is far from the the cold resonance of the harmonic. Likewise, lower energies are measured if the line of sight is closer to the cold resonance of the harmonic - where the bulk electrons of the emission layer

emit. The system can then measure energies up to ~ 250 keV without harmonic overlap, at ~ 80 GHz from radiation emitted at the downshifted third harmonic, as illustrated in Figure 4.46.

4.5.2 Energy resolution

The approach to calculate the energies in the previous subsection assumed that the line of sight is vertical and infinitesimally narrow. Also, we have assumed that the instruments can measure an infinitesimal narrow frequency band around the considered frequencies. We introduce the experimental considerations studied in Sections 4.1 and 4.2 for the calculation of the actual energy resolution of the real diagnostic. We start the calculation recalling Equation 3.7 from Chapter 3. The relativistic factor γ, of a resonant electron in the absence of harmonic overlap is proportional to

$$\gamma \propto \frac{B}{f}. \tag{4.13}$$

The energy resolution (broadening of γ) is determined by the broadening in both the magnetic field and the measured frequency. The antenna pattern, which is ~ 6 cm wide in the plasma center, introduces a γ broadening

$$\frac{\delta\gamma}{\gamma}|_{\text{beam}} = \frac{\delta B}{B} = \frac{\delta R}{R} \simeq \frac{6\text{ cm}}{88\text{ cm}} \sim 7\% \tag{4.14}$$

while the radial aperture of the antenna causes a broadening of the magnetic field, the toroidal aperture of the same size leads to a frequency uncertainty due to the Doppler effect. The Doppler effect can shift the frequency of the resonant electrons travelling along the magnetic field as

$$\frac{\delta f}{f} = \beta_{\|}\sin\Delta\theta \tag{4.15}$$

To estimate the Doppler broadening in the worst case scenario, we take the opening angle of the antenna pattern as $\Delta\theta$, the maximum deviation of the viewing angle from perpendicular. Also, we consider the parallel velocity of the resonant electron to be the velocity associated to the maximum energy that we can measure

$$\beta_{\|} = \sqrt{1 - \frac{1}{(1+\frac{E_{\text{max}}}{m_{\text{e0}}c^2})^2}} = \sqrt{1 - \frac{1}{(1+\frac{250\text{ keV}}{511\text{ keV}})^2}} \simeq 0.7 \tag{4.16}$$

We can then estimate the maximum uncertainty on γ due to the Doppler effect as:

$$\frac{\delta\gamma}{\gamma}|_{\text{doppler}} = 0.7 \times \sin\frac{6\text{ cm}}{101\text{ cm}} \sim 4\% \tag{4.17}$$

The radiometer introduces a frequency broadening due to the 750 MHz bandwidth around each measured frequency. The corresponding γ broadening, evaluated at 78 GHz, is equal is equal to :

$$\frac{\delta\gamma}{\gamma}|_{\text{instrument}} = \frac{\delta\omega}{\omega} \simeq \frac{0.75\text{ GHz}}{78\text{ GHz}} \sim 1\%. \tag{4.18}$$

The poloidal magnetic field, which is not constant along the vertical direction in the vessel, introduces a broadening of at most:

$$\frac{\delta\gamma}{\gamma}|_{\text{poloidal}} = \frac{\delta B}{B} \sim 1\% \tag{4.19}$$

We end up with a total uncertainty on the relativistic factor

$$\frac{\delta\gamma}{\gamma} = \frac{\delta\gamma}{\gamma}|_{\text{beam}} + \frac{\delta\gamma}{\gamma}|_{\text{doppler}} + \frac{\delta\gamma}{\gamma}|_{\text{instrument}} + \frac{\delta\gamma}{\gamma}|_{\text{poloidal}} \simeq 13\% \tag{4.20}$$

This resolution in the relativistic factor is calculated for the worst cases and we should not assume it is constant across the whole frequency range. In fact, the antenna beam pattern depends on the frequency and is narrower at high frequencies. We expect up to 5% lower resolution for the higher frequencies, also because the instrumental broadening decreases further with frequency. We use an average $\frac{\delta\gamma}{\gamma} = 10\%$ to illustrate the effect on the energy resolution of the broadening of the relativistic factor. The energy resolution $\frac{\delta \mathrm{E}}{\mathrm{E}}$ can be expressed, in terms of $\frac{\delta\gamma}{\gamma}$ by manipulating the expression of the relativistic kinetic energy, $\mathrm{E} = (\gamma - 1)\mathrm{mc}^2$ as:

$$\frac{\delta \mathrm{E}}{\mathrm{E}} = \frac{\delta\gamma}{\gamma}(1 + \frac{\mathrm{mc}^2}{\mathrm{E}}) \tag{4.21}$$

Equation 4.21 is important as it shows that the energy resolution, in the first order, is better (decreases) for the higher energy. An estimation of $\frac{\delta\gamma}{\gamma}$ for each frequency should however be performed for a rigorous estimation of the energy resolution. A calculation of the energy

resolution with a constant $\frac{\delta\gamma}{\gamma} = 10\%$ is shown in Figure 4.47. As expected, the performance of the system in our energy range is not ideal. Improvements of the energy resolution is however possible via the factor $\frac{\delta\gamma}{\gamma}$ which depends on the frequency and which is directly proportional to $\frac{\delta E}{E}$. A solution could be to use the higher frequencies to measure the lower energies where the resolution needs to be improved.

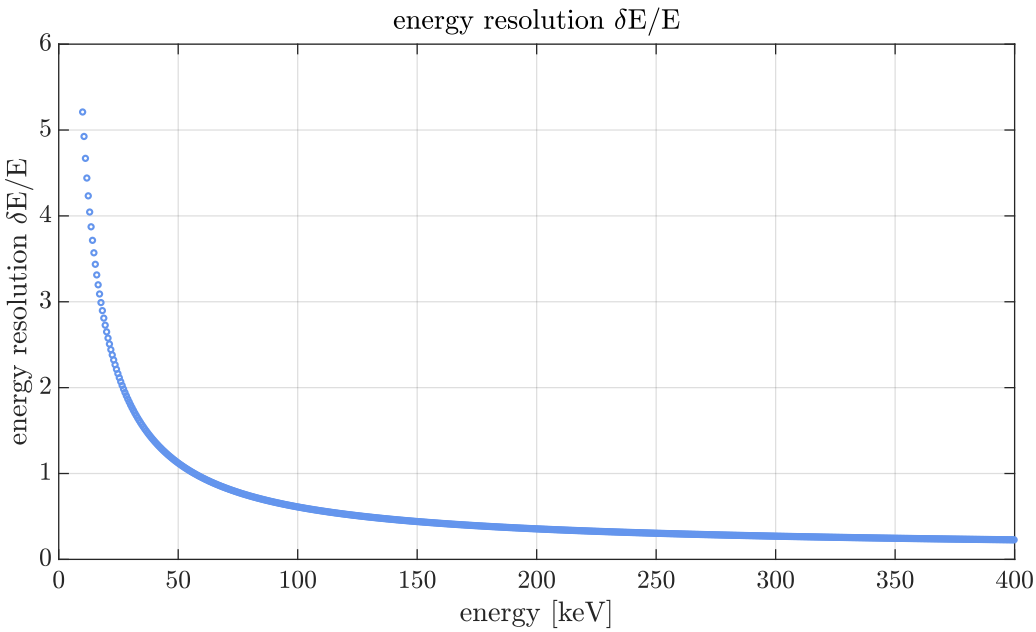

Figure 4.47: Energy resolution of the Vertical ECE diagnostic calculated with a constant $\frac{\delta\gamma}{\gamma} = 10\%$.

5 Calibration

5.1 Introduction

The calibration of the Vertical ECE diagnostic on TCV is described in this chapter. The novel technique that we have used for the calibration deserves a dedicated chapter since the approach may be of interest for ECE diagnostic applications in the future. In 50 years of ECE diagnostics, the calibration of the measurement systems has, in general, been considered as a challenging task for the experimenters. The challenge being that of determining, with the highest accuracy, the spectral response of the measurement system to a given radiation power. Two approaches have been traditionally retained for ECE calibration: (1) the use of sources of known characteristics as substitutes for the plasma and (2) the cross-calibration on a different, absolutely calibrated instrument. In the former approach, hot and (or) cold sources are placed within the vacuum chamber to irradiate the ECE antenna. The approach has been used since the seventies in the vast majority of ECE systems in magnetic confinement devices [46, 5]. A strong limitation of the approach is the necessity to be performed in vessel during an opening of the tokamak. The response of the system that is found during a hot/cold source calibration is used for several months, years even, until another calibration can be performed. This limitation has opened the question on the stability of the calibration with respect to changes in the experimental conditions, which may occur on a daily basis.

The latter calibration approach exploits the absolute calibration of a different instrument on the same tokamak to obtain the response function of an ECE system. The ECE system can be cross-calibrated on another ECE system, as in JET [81], inheriting all the uncertainties from the absolute calibration, or can be cross-calibrated on a different diagnostic which measures the same plasma parameters, such as Thomson scattering diagnostic. The cross-calibration on Thomson scattering is interesting in tokamaks featuring a reliable and accurate Thomson scattering systems. This calibration method has an advantage from the stability point of view but relies on the strong assumption that both diagnostics measure the (same) bulk electron temperature. For ECE diagnostics, the measurement of the electron temperature requires that the plasma is optically thick and that the electron distribution is Maxwellian. When those

conditions are met, cross-calibration of ECE systems on Thomson scattering can be used, with good success, as it has been done over the years on TCV [42, 82, 83]. For the Vertical ECE diagnostic of TCV, a cross-calibration on Thomson scattering could not have been adopted for two main reasons. The first reason is that, even in an optically thick plasma, the radiation intensity measured with a vertical line of sight cannot be associated straightforwardly to a local electron temperature since the ECE resonance is not localized in the vertical direction. The second reason for which a new approach for calibration has been studied, is the fact that the plasma will hardly be optically thick for frequencies above ~ 86 GHz if the line of sight of the diagnostic is vertical. For those frequencies, an accurate estimation of the radiation intensity needs to be performed if the plasma emission is used for the calibration. We present in the next sections the technique that has been developed for the calibration of the Vertical ECE in the context of this thesis. The main idea is to not use external sources to substitute the plasma, but the plasma itself to enhance the stability of the calibration. Moreover, the requisites for the use of this calibration method are not limited to horizontal lines of sight nor optically thick conditions, which is the novelty in the approach.

5.2 Theoretical background

It is useful to review the theoretical basis underlying the calibration of ECE systems, using the emission from the plasma. The intensity of the plasma radiation reaching the ECE antenna, I_ω, can be calculated, as in Reference [58], starting from the radiative transfer equation

$$N_r^2 \frac{d}{ds}\left(\frac{I_\omega}{N_r^2}\right) = j_\omega - \alpha_\omega I_\omega. \tag{5.1}$$

The transfer equation assumes that the trajectory of the electromagnetic radiation is described by means of rays. The coordinate s measures the ray path whereas N_r is the ray refractive index. The subscript ω in the radiation intensity recalls that the intensity is a spectral radiance. The absorption coefficient, α_ω, represents the rate of absorption of the radiation per unit path length, and j_ω is defined as the emission coefficient. In lossless media, Equation 5.1 translates to

$$\frac{d}{ds}\left(\frac{I_\omega}{N_r^2}\right) = 0. \tag{5.2}$$

In that case, I_ω/N_r^2 is constant along the ray path. In the particular case of vacuum, $N_r = 1$, I_ω is constant and does not depend on the distance from the antenna.
We introduce the source function

$$S_\omega = \frac{1}{N_r^2}\frac{j_\omega}{\alpha_\omega} \tag{5.3}$$

and the optical depth τ, which we define such that:

$$d\tau = -\alpha_\omega ds. \tag{5.4}$$

The radiation transfer equation 5.1 can then be rewritten as:

$$\frac{d}{d\tau}\left(\frac{I_\omega}{N_r^2}\right) = \frac{I_\omega}{N_r^2} - S_\omega. \tag{5.5}$$

We solve equation 5.5 in the geometry illustrated in Figure 5.1. We calculate the intensity leaving the plasma $I_\omega(A)$ (which replaces the intensity at the antenna), accounting for the total optical depth of the plasma and the incident radiation intensity in the plasma $I_\omega(B) = I_\omega^{\text{inc}}$. The integration of Equation 5.5 across the ray trajectory in the plasma yields:

$$\frac{I_\omega(A)}{N_r^2(A)}e^{-\tau_A} = \frac{I_\omega(B)}{N_r^2(B)}e^{-\tau_B} + \int_{\tau_A}^{\tau_B} S_\omega(\tau)e^{-\tau}d\tau \tag{5.6}$$

We consider $\tau_A = 0$, $N_r(A) = N_r(B) = 1$ as A and B are incident and emergent points to the plasma. We also take $\tau_B = \tau_0$ as the total optical depth of the plasma. Equation 5.6 simplifies to

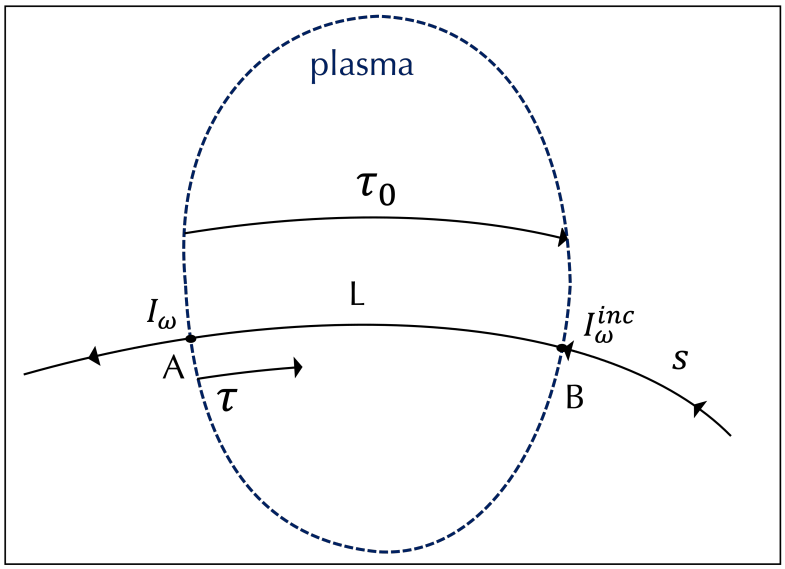

Figure 5.1: Schematics for the radiative transfer equation.

the form

$$I_\omega = I_\omega^{\text{inc}} e^{-\tau_0} + \int_0^{\tau_0} S_\omega(\tau) e^{-\tau} d\tau. \tag{5.7}$$

The first term in Equation 5.7 represents the contribution of the incident radiation to the intensity at the antenna. It is interesting to note that this contribution vanishes out in case of no incident radiation, $I_\omega^{\text{inc}} = 0$, or high optical depth $\tau \gg 1$. An optically thick plasma absorbs the incident radiation, including that of wall reflections in tokamaks. In case of optically thin plasmas, $\tau < 1$, an estimation of the contribution from multiple wall reflection is needed to assess I_ω. That contribution can be neglected if the line of sight avoids radiation from multiple wall reflections, as discussed in the previous chapter.

We proceed by calculating the integrand in Equation 5.7. For that we need an expression for the terms defining the source function in Equation 5.3. Both the absorption and the emission coefficient can, in reality, be written in terms η_ω, the single particle differential emissivity as in Reference [58],

$$j_\omega = \int \eta_\omega(\overrightarrow{p'}) f(\overrightarrow{p'}) \overrightarrow{dp'}, \tag{5.8}$$

$$\alpha_\omega = \frac{8\pi^3 c^2}{N_r^2 \hbar \omega^3} \int \eta_\omega(\overrightarrow{p'}) \Big[- f(\overrightarrow{p'}) + f(\overrightarrow{p}) \Big] \overrightarrow{dp'} \tag{5.9}$$

where $\hbar$ is the Planck constant. j_ω and α_ω are scalar quantities which can be evaluated locally on

the ray trajectory. The source function is then transformed as

$$S_\omega = \frac{1}{N_r^2}\frac{j_\omega}{\alpha_\omega} = \frac{\hbar\omega^3}{8\pi^3c^2}\frac{\int \eta_\omega(\overrightarrow{p'})f(\overrightarrow{p'})}{\int \eta_\omega(\overrightarrow{p'})[-f(\overrightarrow{p'})+f(\overrightarrow{p})]d\overrightarrow{p'}}. \tag{5.10}$$

Equation 5.10 is in reality just a form of the Kirchoff's law for anisotropic, non-thermal plasmas. In the particular case of a Maxwellian plasma, it can be shown that the ratio of the integrals in that equation becomes $(e^{\hbar\omega/T}-1)^{-1}$, where T is the temperature of the radiating particles. The source function in the Rayleigh-Jeans approximation, valid for $\hbar\omega/T \ll 1$, has the simplified form

$$S_\omega = \frac{\omega^2 T}{8\pi^3c^2}. \tag{5.11}$$

The form of the source function obtained in 5.11 equals the expression of the black-body emission at a temperature T and frequency ω. Two comments can be made accordingly:

- If the distribution of particles is not Maxwellian, the integrals in Equation 5.10 should be computed and a quantity T_{rad}, can be defined such that

  $$S_\omega = \frac{\omega^2 T_{\mathrm{rad}}}{8\pi^3c^2}. \tag{5.12}$$

  The quantity T_{rad} is usually named as the radiative temperature, to be distinguished from the true particles temperature.

- If, instead the distribution of particle is Maxwellian, the case of interest for the calibration, the source function equals the black-body emission at the temperature of the radiating particles. Equation 5.7 becomes

  $$I_\omega = I_\omega^{\mathrm{inc}}e^{-\tau_0} + \frac{\omega^2 T}{8\pi^3c^2}[1-e^{-\tau_0}]. \tag{5.13}$$

The solution of the radiative transfer equation, given by the expression in Equation 5.13, will now be used to discuss some aspects regarding the calibration of the ECE system. If the distribution of the particles can be asssumed Maxwellian and the plasma is at the same time also optically thick, $\tau_0 \gg 1$, the radiation intensity at the antenna reduces to

$$I_\omega = \frac{\omega^2 T}{8\pi^3c^2}. \tag{5.14}$$

In that case the plasma emits as a black-body at the temperature of the resonant particles. A conversion of the radiation intensity in units of a temperature is often made by defining the quantity T_A, the antenna temperature as

$$T_A = \frac{8\pi^3c^2}{\omega^2}I_\omega, \tag{5.15}$$

with the aim to emphasize that the intensity of the radiation detected at the antenna, in units of a temperature, is truly a local electron temperature in the plasma. In those conditions straight cross-calibration against the Thomson scattering diagnostic can be made to obtain absolutely calibrated measurement of the temperature. In optically thin conditions, as it will mostly be the case in Vertical ECE calibrations, the concept of antenna temperature will not be relevant any-longer and the intensity I_ω would need to be accurately estimated. We take advantage of the definition of the optical depth in Equation 5.4 to express I_ω in a more suitable form for optically thin conditions,

$$I_\omega = I_\omega^{\text{inc}} e^{-\tau_0} + \frac{\omega^2}{8\pi^3 c^2} \int_0^L T(s)\ \alpha_\omega(s)\ e^{-\tau(s)}\ ds. \tag{5.16}$$

As to Equation 5.16, the calculation of the intensity at the antenna is achieved by calculating the absorption of the radiation along the rays path that mimics the antenna pattern. Once that is done, the integral in the equation can be computed, as the total optical depth in the first term of the equation. The theory of ECE emission and absorption in plasmas can be considered to be very well established. The pioneers of the field have proposed throughout the years formulas that have been extensively used and validated, especially in the frame of the Electron Cyclotron Resonance Heating [84, 76]. This means that the challenges in this approach for calibration are rather in the modelling of the experiment. As a matter of fact, each term in Equation 5.16 hides an challenge. In the second term of the equation, the challenge is to use the sophisticated ECE formulas to compute, in the experimental conditions, the radiation absorption with satisfactory accuracy. In the first term of the equation the challenge is that of avoiding, during the calibration, the incident radiation from multiple wall reflections in order to minimize the uncertainties in the calculations.

5.3 Experiment

5.3.1 The plan

The primary idea to calibrate the Vertical ECE diagnostic is to use the plasma emission from ohmic-only discharges. This is to minimize the generation of non-thermal electrons so that the electron distribution can be taken as Maxwellian. During the discharge, the magnetic field can be varied to better identify the radiation features. The magnetic field variation also allows the ECE resonances to move in different channels in our vertical configuration. This is useful for multiple channels calibration within the same plasma discharge. It is however not necessary to vary the plasma current together with the magnetic field to keep the magnetic equilibrium nearly constant. That is because the absolute calibration of the channels just requires the calculation of the radiation intensity with the given plasma parameters. Plasma emission and field variation had been used in the past to try and improve the relative calibration of the Michelson inferferometer on JET [85]. The approach, that was proposed by Bindsley and Barlett in the late 1980s was not meant for the absolute calibration of the diagnostic. They had assumed that the errors in the absolute calibration of their instrument were fixed in frequencies. So a variation of the toroidal magnetic field would have allowed the ECE spectrum to traverse the calibration errors by traversing the frequencies. Their technique was useful only in the regards of improving the relative stability of the calibration and that was provided the plasma was optically thick and the magnetic equilibrium frozen during the field variation. Our idea for the calibration is really to absolutely calibrate each channel, independently of the others, by calculating the radiation intensity in each channel.

5.3.2 The execution

Measurements were taken during calibration experiments with the set of available radiometers. In general, the radiometers are connected to the transmission line transporting the X- polarized radiation. To illustrate the method, we describe the measurement shown in Figure 5.2, taken from the discharge $\#67946$, with the radiometer $104 - 114$ GHz. The magnetic field is ramped down from ~ 1.4 T to ~ 1 T and up again, while the plasma current remains nearly constant. Peaks are observed, consecutively in each channel during the field ramps. The peaks are symmetric and separated by a time interval in which the signal intensity is at the noise level of the radiometer. The signal level outside the peaks is lower than the peaks level. We observe approximately the same signal level for the peaks during the ramp down and the ramp up of the field. The intensity outside the peaks is higher for the lowest frequencies in the first flat-top of of field. In the second flat-top, at the end of the discharge, the lower level of the signal can be correlated to the drop in the temperature and plasma current.

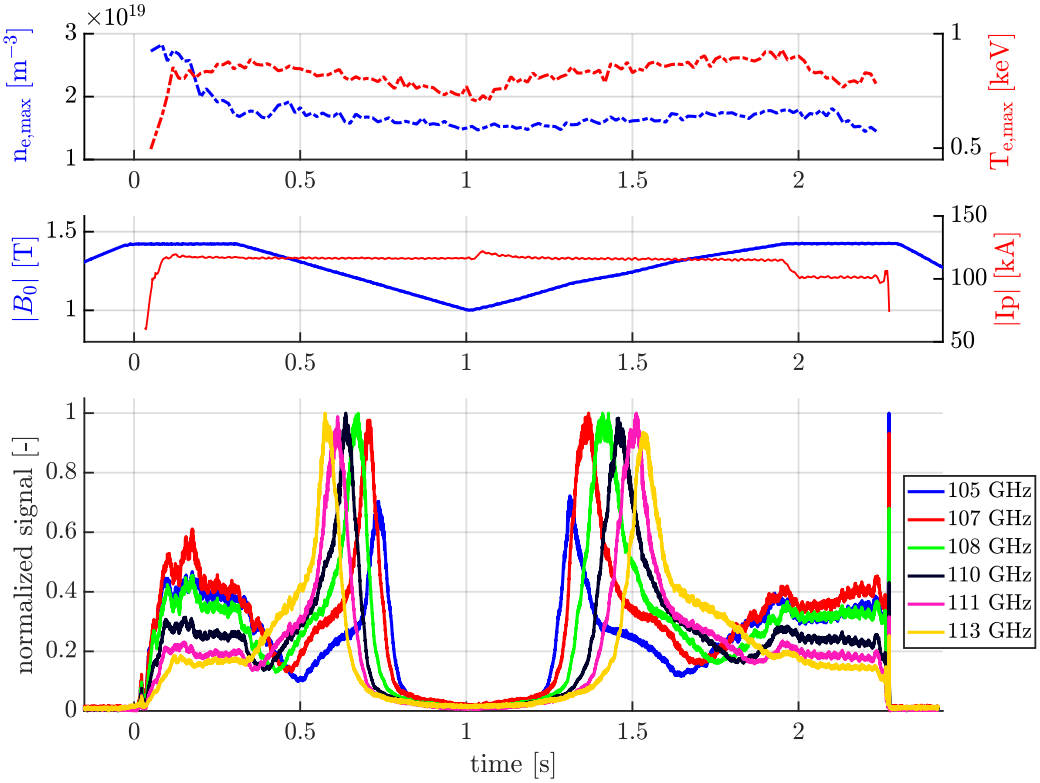

Figure 5.2: Measurement with the radiometer $104 - 114$ GHz during the calibration discharge #67946 with two field ramps and flat plasma current.

5.3.3 Route to the calibration

The route to the calibration is identified observing the measurements, at various frequencies during magnetic field ramps. The measurements from the radiometer $104 - 114$ GHz for the discharge #67946 shows X-mode radiation detected both from single pass emission and from multiple wall reflections. The Figure 5.3 shows, for the frequency 108 GHz, two peaks than can be associated to the single pass emission at the third harmonic. The multiply reflected radiation, which originated as an X3 emission is buried in the noise in between the two peaks. The radiation from multiple wall reflections, which originated as an X2 emission is the one observed out of the peaks. An interesting other example is the measurement at a lower frequency shown in Figure 5.4. The measurement, which is taken at frequency 81 GHz, features in addition a single pass, second harmonic radiation when the magnetic field intensity reaches its highest value.

By decoding the features of the measured signals, we can conclude that the diagnostic detects both reflected radiation and single pass radiation during the field ramps. The reflected X2 radiation largely dominates the background radiation, as from theoretical predictions. The drop of intensity to the noise level following the detection of the single pass X3 radiation confirms the absence of the background radiation originating as an X3 emission. These observations suggest a clear path to the calibration of the diagnostic using the plasma emission. The path consists of

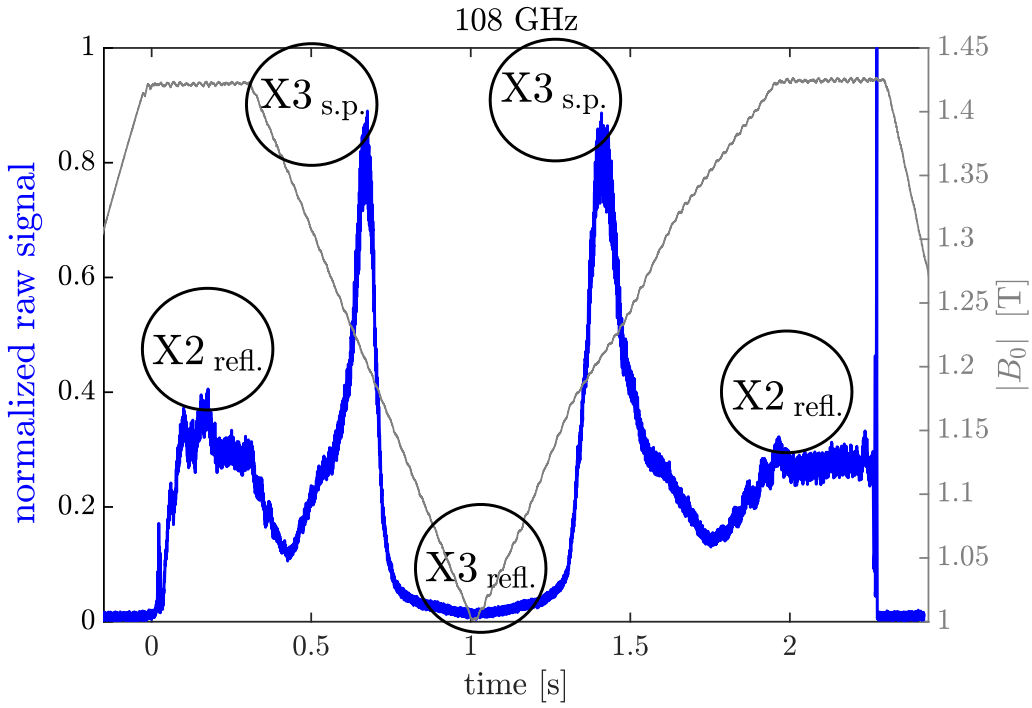

Figure 5.3: Decoding the features of the signal at 108 GHz from the radiometer $104 - 114$ GHz during the calibration shot #67946.

modelling the single pass X3 emission which can in general be detected by the radiometer. We notice that the lowest frequencies of the radiometer can, in a single discharge, detect the single pass emission from both X2 and X3 (Figure 5.4). The single pass X2 emission, which is optically thick reaches the black-body level and can be used to validate the modelling of the single pass X3, detected within the same discharge.

Before moving to the calculation of the single pass X3 radiation, we should however make sure that the peaks associated to X3 are single pass emission only, which is of great importance for the calibration. We are certain that the reflected X2 radiation cannot pollute the single pass X3 emission because the cold resonance of the X2 lies out of the plasma when that of the X3 traverses the line of sight. We need to address the possibility for the X3 single pass emission to be polluted by the reflected X3 emission. That is done assuming that during the calibration discharges, the line of sight of the diagnostic misses the dump due to refraction or misalignment of the line of sight. If the line of sight terminates on the tiles of the vessel, how can we be sure that the single pass X3 radiation, directed towards the tile does not reflect off the tile to add up to the single pass emission directed towards the antenna ? It is interesting to observe that when the X3 peak has crossed the line of sight, during the ramp down of the field, the signal level drops to the noise level of the radiometer (Figure 5.2). If the X3 reflected radiation, which should be seen after the X3 peak is negligible, it actually means that it should be neglected, as well, in the radiation detected at the X3 peaks. We consider that the X3 peaks observed are single pass emissions, precisely because the reflected X3 is below the noise level of the radiometer. If

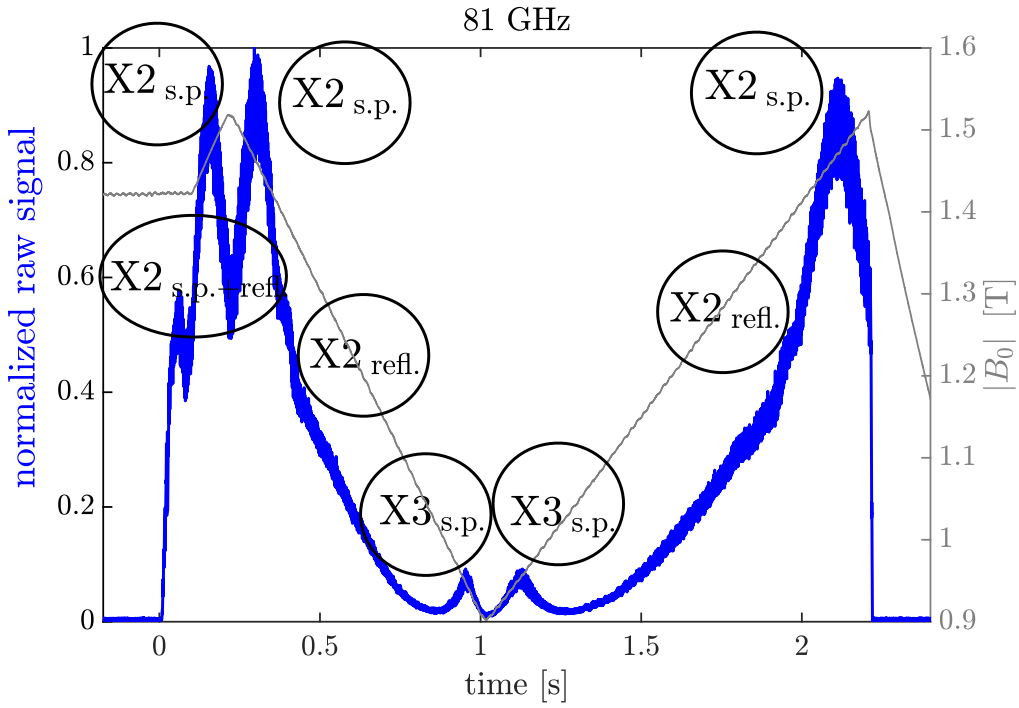

Figure 5.4: Decoding the features of the signal at 81 GHz from the radiometer $78 - 114$ GHz during the calibration shot #75023.

the X3 radiation originates in or out of sight, it actually does not change much; in both cases the reflected X3 which gets back to the antenna is drastically reduced at the reflection off the vessel tiles. The reflected X2 radiation gets away with that just because the single pass X2 radiation is much higher, nearly ~ 20 times higher in TCV conditions. The importance of the question that has just been addressed can be illustrated by a simple reflection model. The model shows how to include the incident radiation from the reflection off the tiles in the calculation of the X3 peaks. For that we consider the two parameters r and p representing the reflection coefficient and the coefficient for the polarization scrambling of a wave reflecting off the vessel tiles. The intensity of the radiation from a single reflection off the tiles, as illustrated in Figure 5.5, can be written for the X- and O- polarizations as:

$$\begin{cases} I_{\mathrm{O}}^{\mathrm{out}} = r(1-p)I_{\mathrm{O}}^{\mathrm{in}} + rpI_{\mathrm{X}}^{\mathrm{in}} \\ I_{\mathrm{X}}^{\mathrm{out}} = rpI_{\mathrm{O}}^{\mathrm{in}} + r(1-p)I_{\mathrm{X}}^{\mathrm{in}} \end{cases}$$

In our case, assuming that the incident radiation on the tiles is the single pass emission and that the single pass emission from the O-mode is negligible, Equation 5.3.3 simplifies to

$$\begin{cases} I_{\mathrm{O}}^{\mathrm{out}} = rpI_{\mathrm{X}}^{\mathrm{s.p.}} \\ I_{\mathrm{X}}^{\mathrm{out}} = r(1-p)I_{\mathrm{X}}^{\mathrm{in}} \end{cases}$$

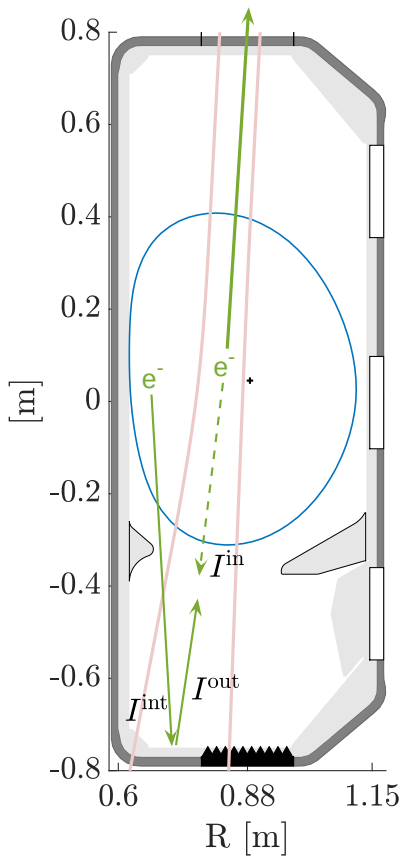

Figure 5.5: Illustration for the estimation of the radiation that can reach the antenna after reflection off the tiles. The two situations when the radiation originates in and out of sight are shown.

It is thus possible, in theory, to include the contribution of wall reflections in the calculation of the optically intensities for calibration purposes. The example of a single wall reflection is illustrated by the Equation 5.3.3. What is needed is to account for the optical depth along the trajectory taken by the reflected radiation to reach the antenna (see again Equation 5.16). It is an advantage that observed X3 peak in our cases is a single pass emission only, that ensures the possibility of a much more accurate calibration. Calibration which will be freed from the uncertainties on the parameters r and p describing the tiles of the vessel. That been said, we conclude this section addressing another interesting pending question.

Which role does the viewing dump play in the calibration?

The examples that have been discussed so far have shown, in general, a high level of background radiation associated to the multiply reflected X2 emission. That radiation is not cleaned up

by the viewing dump since the electron density exceeds the density limit which minimise wall reflections. Attempts to reduce the density, in order to have the line of sight within the dump were tried and rapidly abandoned. Lowering the density down to $\sim 1 \times 10^{-19}\mathrm{m}^{-3}$ in our ohmic discharges in order to minimize refraction can lead to the generation of runaway electrons. Since the experiments are designed to also minimise the population of non-thermal electrons, it was a necessity to have the calibration shots at relatively high densities. Moreover, the X2 reflected radiation, essential contributor to the background radiation, does not create any pollution when the the single pass X3 culminates in the signal. It is thus not necessary to work at a constrained density for calibration discharges since refraction will not have significant consequences. An even stronger information, as a conclusion, is that the dump is not necessary during the calibration. This has been confirmed by experiments performed with and without dump. The X3 peak radiation, on which the radiometers are calibrated, can be considered to be single pass emission only, regardless of the level of refraction. Leaning on the code SPECE, we will present in the next section the calculation of the X3 single pass radiation that we have measured during the experiments. We stress that only that calculation is needed for the calibration of the plasma discharge.

5.4 Calibrating

This section explains how the peak intensity observed during the experiments is modelled and how it is used to obtain the calibration factor for each frequency. We recall that the radiation is measured in units of Volts in each bandwidth around the central frequencies of the radiometers. The modelling will provide an estimate of the power, in units of Watts that is detected in each bandwidth, such that the equivalence between the detected voltage and the incoming power can be made. The power from the modelling will be the power leaving the plasma. That will ensure that all the components from antenna to the radiometers are included in the calibration. The antenna pattern is modelled by a set of rays for the calculation of the single pass intensity. The simulated intensity will be the spectral intensity I_ω, previously seen in Section 5.2. The spectral intensity is in units of $\mathrm{Watts/Hz/sterad/m^2}$. Integration over the bandwidth frequencies, effective area of the antenna and solid angle will be performed in order to obtain the bandwidth power from the calculated spectral intensity.

5.4.1 The difficulties in the modelling

When using substitutes to the plasma to calibrate ECE system, one needs to make sure that the calibration source fills entirely the antenna pattern. It is important to understand if that condition is met when using the plasma itself as the source. Of course the question is not whether or not the whole plasma fills the antenna pattern; what is relevant for the calibration is the size of the emitting layer in the plasma. The relative sizes of the emitting layer and the antenna pattern will naturally have an impact on the calibration approach. It is a general principle that a medium that emits radiation also absorbs radiation at the same frequency. For the estimation of the emission layer of the ECE single pass emission in the plasma, we calculate the profile of the absorption coefficient for the X-mode wave propagating perpendicular to the magnetic field, following the treatment in Reference [84]. Analytical expressions for the radial extent absorption coefficients for the second and third harmonic can be written, in the tenuous plasma limit $\omega_p \ll 2\omega_{\mathrm{ece}}$ as

$$\alpha_\omega^{X2} \approx \frac{16}{15}\frac{\pi^{3/2} n_e |e|}{B_{\mathrm{res},2}}\frac{2R}{R_{\mathrm{res},2}}\left[\mu\left(\frac{R_{\mathrm{res},2}}{R}-1\right)\right]^{5/2} e^{-\mu\left(\frac{R_{\mathrm{res},2}}{R}-1\right)}, \tag{5.17}$$

$$\alpha_\omega^{X3} \approx \frac{324}{315}\frac{\pi^{3/2} n_e |e|}{B_{\mathrm{res},3}}\frac{3R}{\mu R_{\mathrm{res},3}}\left[\mu\left(\frac{R_{\mathrm{res},3}}{R}-1\right)\right]^{7/2} e^{-\mu\left(\frac{R_{\mathrm{res},3}}{R}-1\right)}. \tag{5.18}$$

The expressions for the absorption coefficient in Equations 5.17 and 5.18 are expressed in cgs units and the term μ stands for is the normalized electron temperature, $\mu = \frac{mc^2}{kT} = \frac{c}{v_t} \sim \frac{511\mathrm{keV}}{kT}$. B_{res} and R_{res} are respectively the magnetic field and the major radius at the resonance.

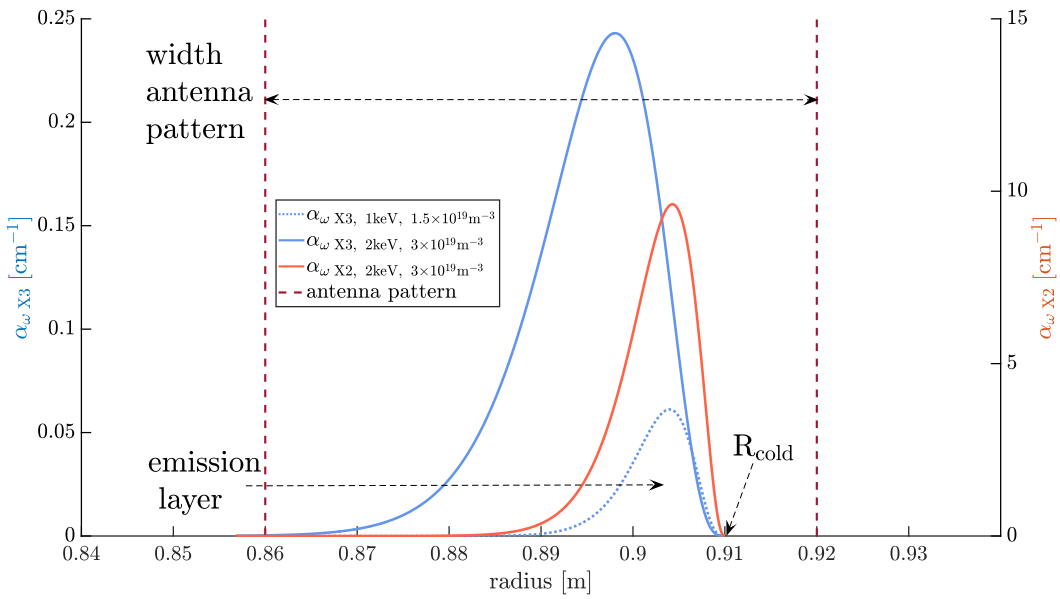

Figure 5.6: Layers of the electron cyclotron emission for various plasma parameters.

A plot of the absorption coefficient is shown in Figure 5.6. As can be seen, the X3 emission layer for a temperature of 1 keV and a density of $1.5 \times 10^{-19}\mathrm{m}^{-3}$, typical calibration parameters, is much narrower that the antenna beam pattern. The layer is $\sim$ 2 cm wide while the beam pattern is about $\sim$ 6 cm wide. Even though typical temperature on TCV during ohmic discharges are below $\sim$ 1 keV, estimations of the radial extent of the emission layer were made for a temperature of 2 keV for X2 and X3. Since the layer grows with increasing temperature, the calculation was to obtain a confirmation that the emission layer will in any case be much smaller than the beam pattern and that the modelling of the intensity should be performed accordingly. The main impact in the modelling will be in synthetic antenna mimicked by means of rays. It is clear that a single ray cannot be used for the modelling. It is interesting to note that the issue related to the width of the emission layer is a typical issue that will not be significant in a configuration with a horizontal line of sight. That is because a single ray propagated along a horizontal direction towards the emission layer will in general not miss the layer. Launching rays from the top instead, is more complicated in this case as some of the rays mimicking the antenna pattern will actually miss the emission layer, which forces the optimization of the number of rays. The optimization of the rays number and other parameters for the modelling follow in the next subsection.

5.4.2 Optimizing the parameters of the synthetic diagnostic

To illustrate the optimization process, we exploit the measurement at 108 GHz during the shot #67946 shown in Figures 5.2 and 5.3. A few parameters need to be optimized to obtain the most accurate prediction of the peak radiation from the plasma. For the modelling, we first need to

find:

The appropriate line of sight

This is the first step of the optimization, and the shot #67946 was chosen in purpose to illustrate the importance of this step. That is because the thermal resonances for the frequencies $104 - 114$ GHz during the discharge did not occur at the expected values of magnetic field. In that case, either the frequencies of the radiometer are not correct or the line of sight is not exactly vertical as from design. Verification have been made with the radiometer $78 - 114$ GHz whose frequencies are well identified. It appeared that the line of sight was shifted towards the HFS of the machine. This explains why the thermal resonances occurred during the ramp down at lower than predicted values of magnetic field.

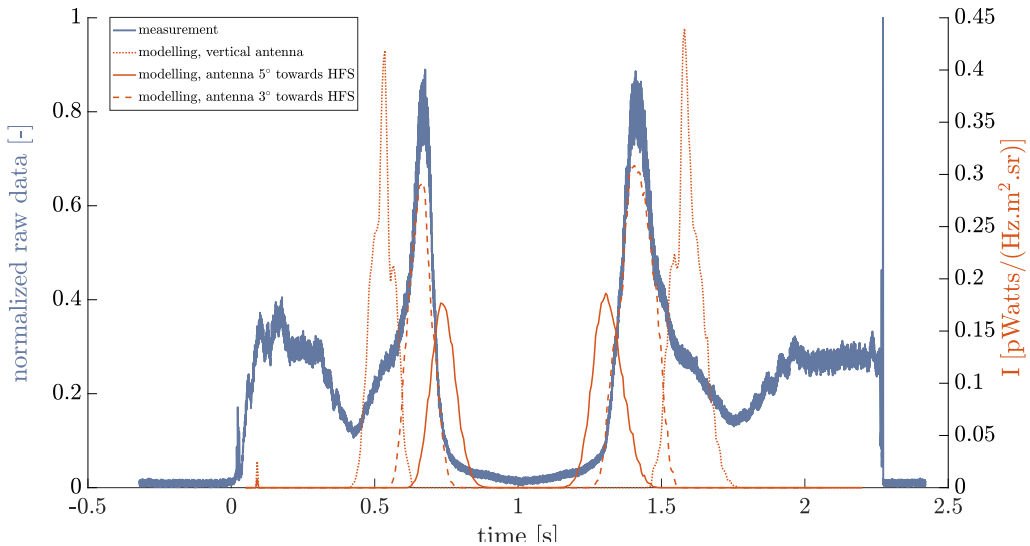

Figure 5.7: Scan of the angle with respect to the vertical for the identification of the right orientation of the line of sight during the experiment.

Figure 5.7 shows how, an inclination of the line of sight by 3° towards the HFS allows the modelling to be in phase with the experimental measurement. The modelled intensity is the mean spectral intensity in the considered frequency band.

The right beam size

The beam size for the synthetic diagnostic should in principle be the size of the antenna beam that has been designed and validated by the measurement. However, it is important to look for the beam waist for the synthetic diagnostic (synthetic antenna) matching the measurement. The match is done on the temporal extent of the single pass radiation at the peak. In other words, the wider the measured peak is over time, the larger is the actual beam size. This optimization is

relevant also because in the ray approach we could not include diffraction. The modelled beam pattern is assumed to have a constant size in vacuum and we should find the optimal size to reproduce the measurement. In Figure 5.8 we can see that a waist radius of $\sim$ 3 cm matches best the measurement.

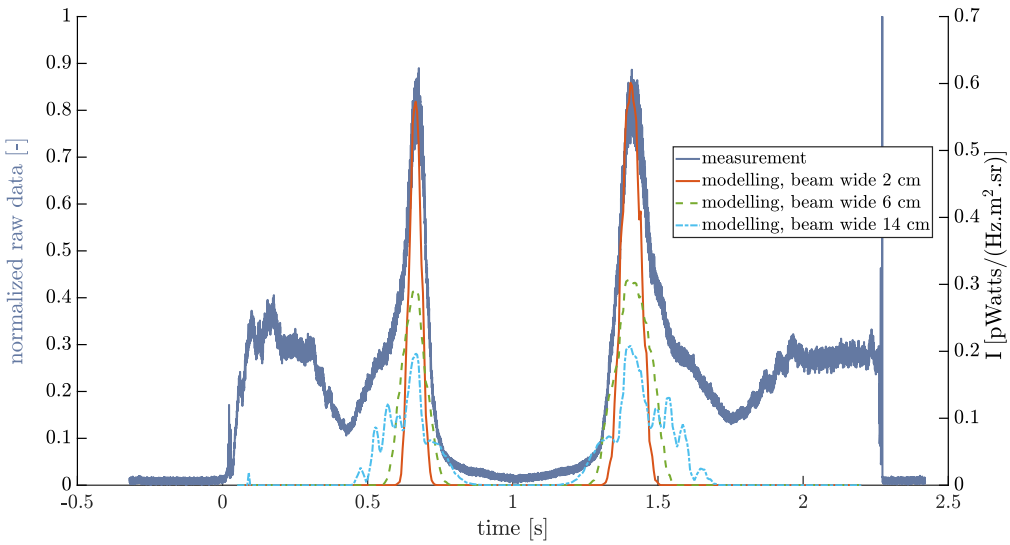

Figure 5.8: Scan of the beam size for the synthetic antenna the identification of the best match with the experimental measurements.

The optimal number of rays

Once the beam size is optimized, we can then proceed to the optimization of the number of rays needed for the synthetic antenna. The question on the number of rays has been raised already at the beginning of the section. For the modelling, SPECE distributes the rays in n_{rad} concentric circles on which n_{ang} rays are equally spaced. A scan in the total number of rays $n_{\text{rad}} \times n_{\text{ang}}$ is shown in Figure 5.9. The mean spectral intensity during the peaks converges from a total number of rays equal to 24. The modelling has thus adopted a ray configuration consisting of 5 concentric circles on each of which 8 rays are equally spaced. It is interesting to comment on a configuration with a single ray, which largely overestimate the spectral intensity. That is due to the width of the emission layer as previously discussed. With a single ray, the average intensity in the antenna pattern is biased because regions of the beam that do not interact with the emission layer are not taken into account.

The best time resolution

The modelling of the plasma intensity works at follows: a density profile, a temperature profile and a plasma equilibrium are given to the synthetic diagnostic for the calculation of the relevant

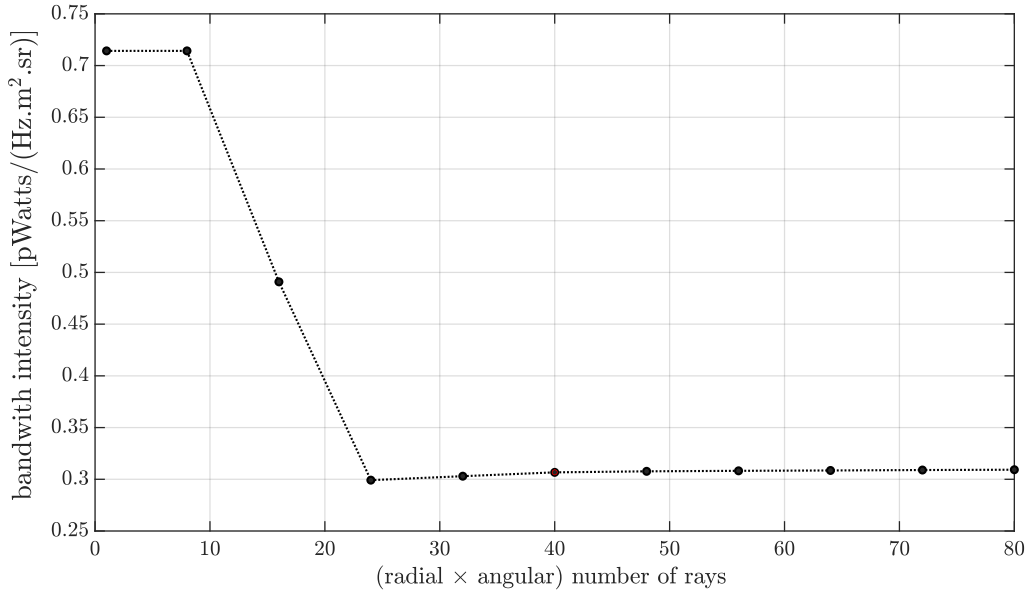

Figure 5.9: Scan of the ray number for the synthetic antenna.

quantities. This means that to compute the plasma intensity for a whole shot, the plasma parameters should be given to the synthetic diagnostic repetitively with a given time resolution. Here we address the optimal time resolution needed for a convergence of the bandwidth power. The bandwidth power is the integral of the spectral intensity, whose calculation will be discussed in the next section. Figure 5.10 shows the scan in the time steps for the synthetic diagnostic. The convergence is reached for a time step smaller than $\sim 5 \times 10^{-3}$ s. The time resolution adopted for the synthetic diagnostic is faster than the Thomson scattering resolution ($\sim 10^{-2}$s) at which the profiles of the electron density and temperature are measured. This is the reason why the measured Thomson data are further processed, through smoothing and interpolation before the use in the synthetic diagnostic. The effect of the data processing on the calibration uncertainties will be discussed later in this chapter.

The frequency step in a channel bandwidth

A last optimization to be performed is the optimization of the frequency step in the synthetic bandwidth. In Chapter 4 were presented the characterization of the radiometers which showed that each channel was ~ 750 MHz wide around the central frequency. For the calculation of the power in the bandwidth, the synthetic diagnostic computes the spectral intensity for discrete values of frequencies in the bandwidth. The values are used to calculate the integral of the spectral intensities over the bandwidth frequencies. Later it will be clear why the simplest approach, using the discretization of the bandwidth in the two extreme frequencies is not the best option for our calculation. For now, a scan in the frequency step is shown in Figure 5.11. A discretization

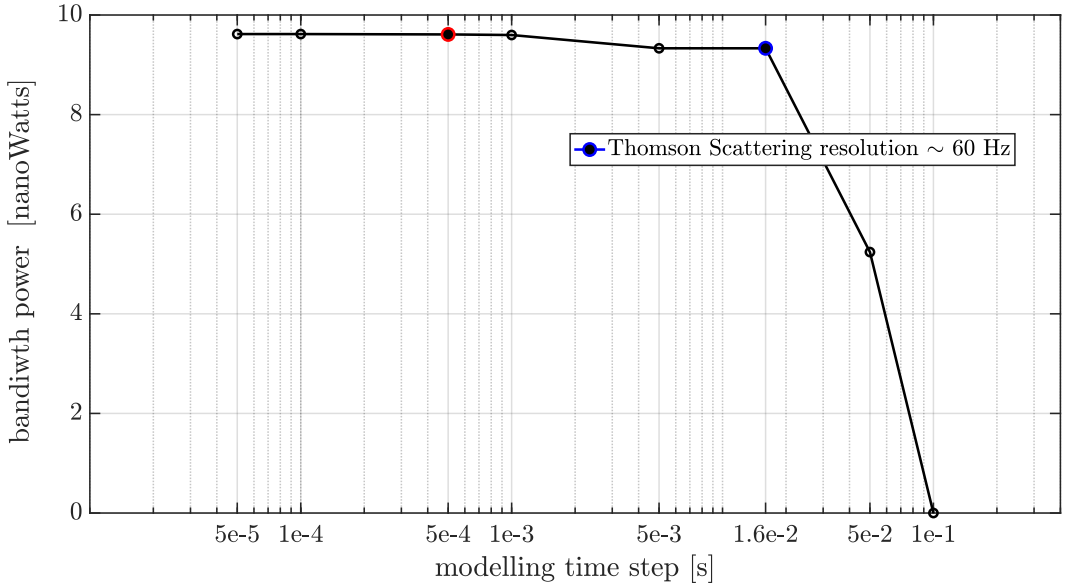

Figure 5.10: Scan of the time resolution of the synthetic diagnostic.

of the bandwidth with at least 15 frequencies ($\delta_f = 53$ MHz) is necessary to obtain a convergent bandwidth power.

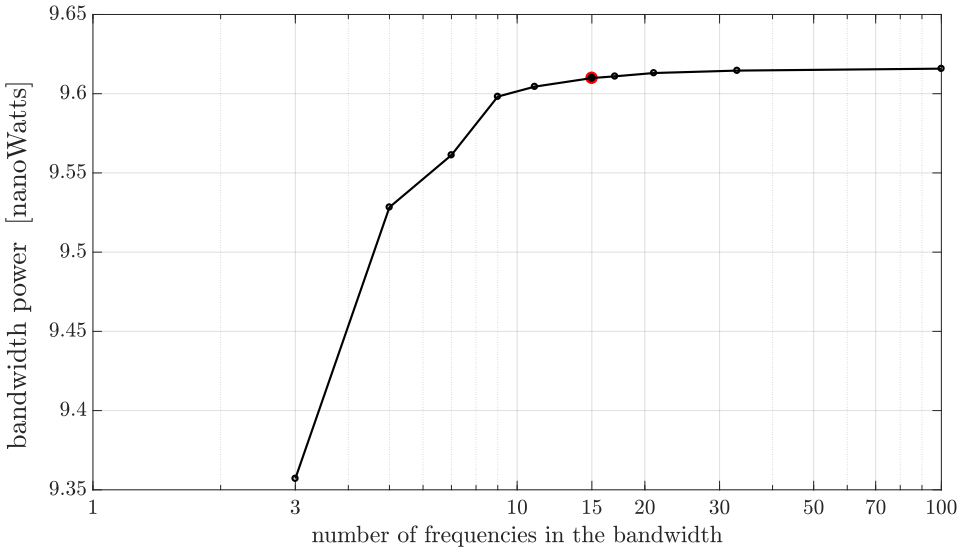

Figure 5.11: Scan of the frequency step in the synthetic bandwidth.

5.4.3 The experiments modelled

This subsection presents the modelling of the single pass radiation for the selected case. The modelled intensity is the mean spectral intensity in the bandwidth. The spectral intensity for each frequency is the X-mode intensity, averaged over all the rays mimicking the Gaussian antenna pattern. In Figure 5.12 is shown the result of the modelling at frequency 108 GHz during the discharge #67946. The result of the modelling shows a good qualitative agreement between the modelling of the single pass radiation and the measurement. The modelling well predicts the temporal extent of the peak radiation at the ramp up and ramp down of the field.The difference in the temporal width is due to the ramp velocity which is different for the two phases, as was shown in Figures 5.2 and 5.3. The slower is the ramp, the larger is the width of the peak in time. The modelling, as expected does not capture the trend of the background radiation from multiple wall reflections out of the peak. This result is expected as the model estimates only the single pass radiation, which is sufficient for the full calibration of the discharge.

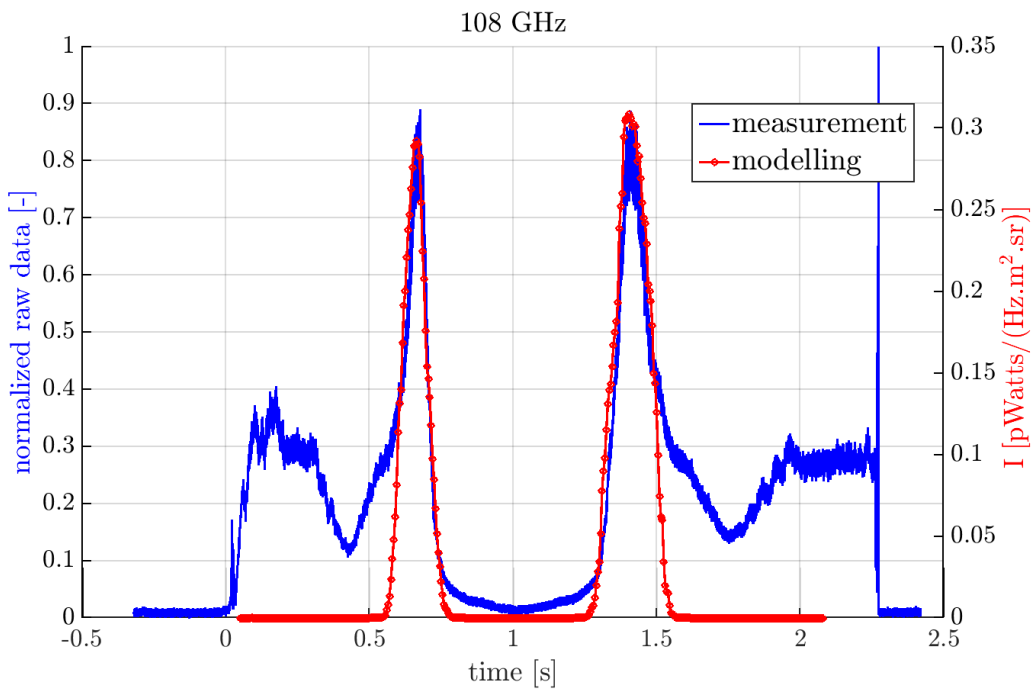

Figure 5.12: Modelling of the spectral intensity for the shot #67946 at frequency 108 GHz.

The low frequencies of the diagnostic, as already discussed, can measure both the X2 and the X3 single pass radiation depending on the field value. The discharges #75022 and #75023 presented in the Figures 5.13 and 5.14 are examples of a measurement with the detection of both single pass emissions. The trends of the observed X2 and X3 single pass emissions are qualitatively captured by the modelling. The fast field ramps, up and down, at the beginning of the discharge #72023 (the ramps are shown on Figure 5.4) allow the observation of the different intensity levels for the X2 single pass radiation on Figure 5.14. The modelling of the spectral intensity for the discharge #75023 is also shown on Figure 5.14. The model captures, qualitatively

the X2 level change at the beginning of the discharge during the fast ramps. The fact that the modelling predicts a lower X2 peak during the ramp down, contrarily to measurement is due to refraction effects and will be discussed later while discussing the uncertainties of the calibration. For the discharge #75022 on Figure 5.13, the modelling captures the flat trend of the X2 single radiation towards the end of the discharge. The model also exhibits a drop in intensity at the beginning of the discharge consistently with the measured signal. Drop which is caused by a drop in the electron temperature.

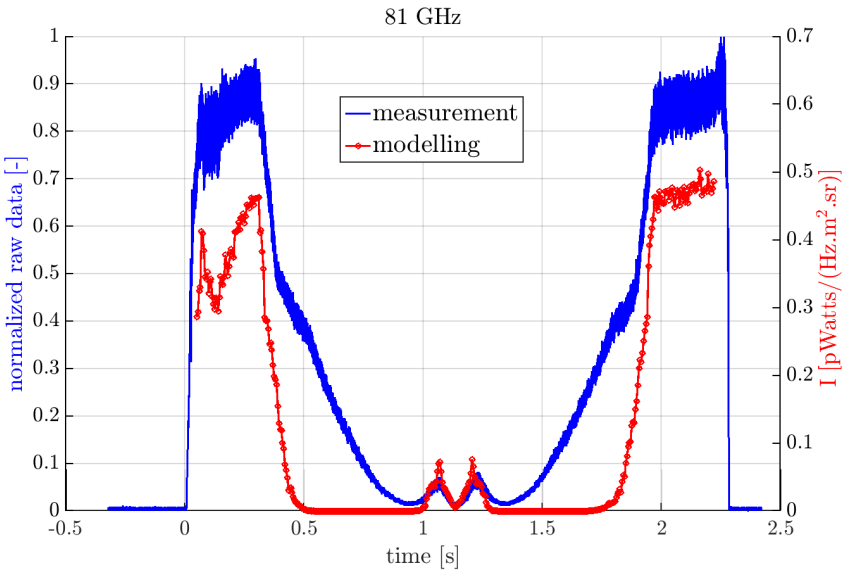

Figure 5.13: Modelling of the spectral intensity for the shot #75022 at frequency 81 GHz.

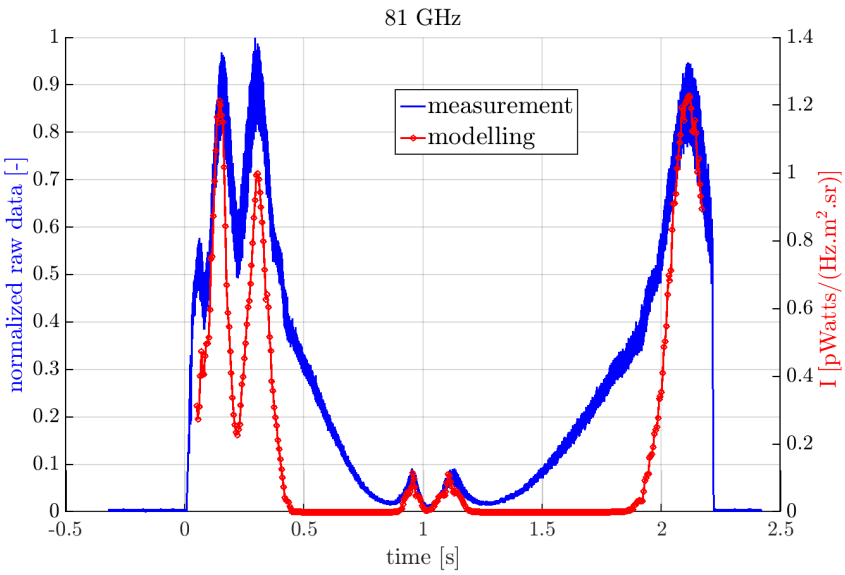

Figure 5.14: Modelling of the spectral intensity for the shot #75023 at frequency 81 GHz.

5.4.4 The calibration factors

The results from the modelling that have been shown so far are related to the calculation of the mean spectral intensity in the frequencies bandwidth. That was helpful to understand if the modelling qualitatively follows the signal trend observed during the measurement. To obtain the calibration factors, we should now have a more quantitative assessment of the peak power in the frequency bands. For that we start from the spectral intensity that has been computed. In reality, the spectral intensity is computed for the O- and X- polarizations. When the wire grid polarizer is oriented such that the radiometer measure only the X-mode, we use the spectral intensity computed for the X-mode only. In the absence of the wire grid polarizer, the radiometer detects the total intensity which is the sum of the X- and O- polarizations. In this case we consider, as well the sum of the calculated intensities at both polarizations.

Calculation of the peak power in a frequency band

We illustrate the calibration process using the same plasma discharge $\#67946$. The spectral intensities calculated for each channel of the radiometer $104 - 114$ GHz is shown in Figure 5.15. The spectral intensities at the peak are the values of interest for the calibration. The bandwidth power is obtained from the spectral intensities with an integration over the frequencies, solid angle and effective area of the antenna. Figure 5.15 shows the profile of the spectral intensity over the bandwidth frequencies at the peak of the single pass radiation. The shape of the intensity profile is parabolic for each channel, as can be seen on the Figure 5.16 for a given channel. This shape of the intensity profile explains the need for the optimization of the number of frequencies for the bandwidth discretization. Using only the two extreme frequencies would underestimate the integral over frequencies of the spectral intensity. The parabolic shape of the spectral intensity can be explained by the radial extent in the plasma of the channels bandwidth. The radial extent, Δ_R can be estimated via the relation

$$\Delta_R \approx R_0 \frac{\delta_f}{f} \approx 0.89 \times \frac{0.75}{100} \sim 0.67 \text{ cm}. \tag{5.19}$$

The radial extent of the bandwidth is smaller than the size of the emission layer ~ 2 cm. When the signal reaches its peak for a single pass emission, the crest of the emission layer probably coincides with the radial location of the central frequency of the bandwidth, explaining the parabolic shape. The shape is not an effect of the Gaussian distribution of the power in the antenna pattern. That is because the antenna beam is much wider than both the emission layer and the radial extent of the bandwidth. The spectral intensity integrated over the bandwidth frequencies need to be integrated as well over solid angle Ω_S and the effective antenna area A to obtain the bandwidth power P_{BW} via the formula:

$$P_{\mathrm{BW}} = 2\pi \int df dA d\Omega_S I(f). \tag{5.20}$$

From antenna theory, it can be shown that the product beam $dAd\Omega_{\mathrm{S}}$ is with some approximation, only a function of the wavelength of the considered radiation, $dAd\Omega_s \approx \lambda^2$. This simplifies Equation 5.20 as

$$P_{\mathrm{BW}} \approx 2\pi \int df \lambda^2 I(f) \approx 2\pi c^2 \int df \frac{I(f)}{f^2}. \tag{5.21}$$

The numerical integration of Equation 5.21, used to compute the synthetic bandwidth power thus reads

$$\begin{cases} P_{\mathrm{BW}} = 2\pi\delta_f \left[\frac{1}{2}(\frac{I(f_1)}{f_1^2} + \frac{I(f_N)}{f_N^2}) + \sum_{i=2}^{N-1} \frac{I(f_i)}{f_i^2}\right] c^2, \\ \delta_f = \Delta_{f,\mathrm{BW}}/\mathrm{nfreqs}, \\ f_1 = f_0 - \Delta_f/2 \; ; f_N = f_0 - \Delta_f/2, \\ \mathrm{nfreqs} = \text{number of frequencies in the synthetic bandwidth.} \end{cases}$$

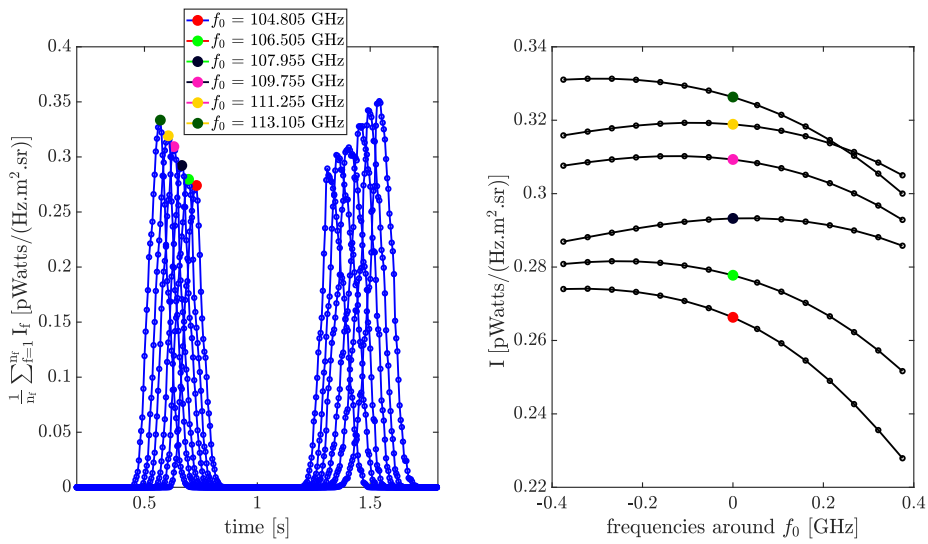

Figure 5.15: Modelled intensity in radiometer $104 - 114$ GHz during the shot #67946.

Finally, the calibration

Once the power in the bandwidth is calculated, it should be matched to the corresponding signal measured in volts. For that, the raw measurement (Figure 5.17) needs to be processed through filtering and scaling. The calculated bandwidth power during the peak is then compared to the measured radiation to obtain the calibration factors as illustrated in Figure 5.18. The obtained calibration factors are shown in Figure 5.20 and the calibrated signals in Figure 5.19.

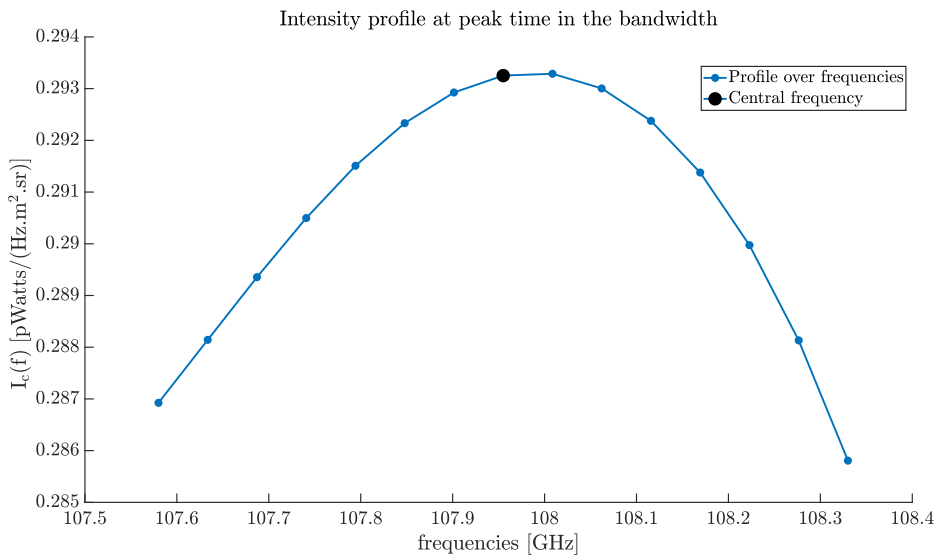

Figure 5.16: Profile of the modelled intensity in the bandwidth.

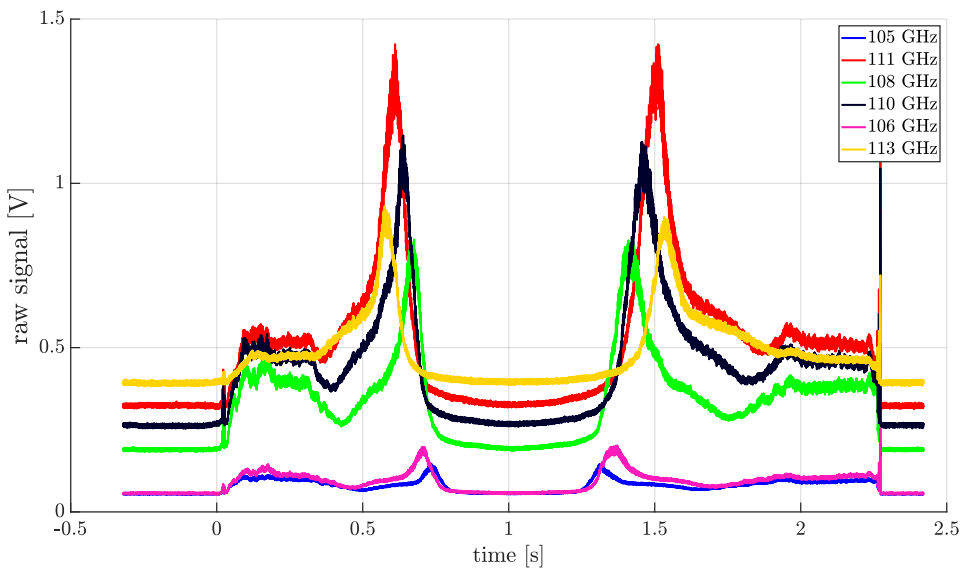

Figure 5.17: Raw signal from the radiometer $104 - 114$ GHz during the shot #67946

The validation of the calibration and the error bars in the calibration factors will be discussed in the next sessions.

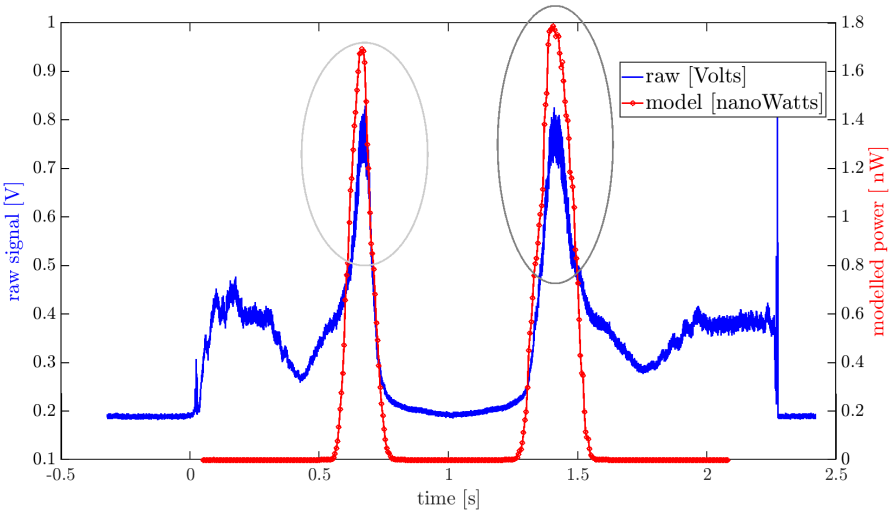

Figure 5.18: Calibrating the signals from the radiometer 104 – 114 GHz during the shot #67946.

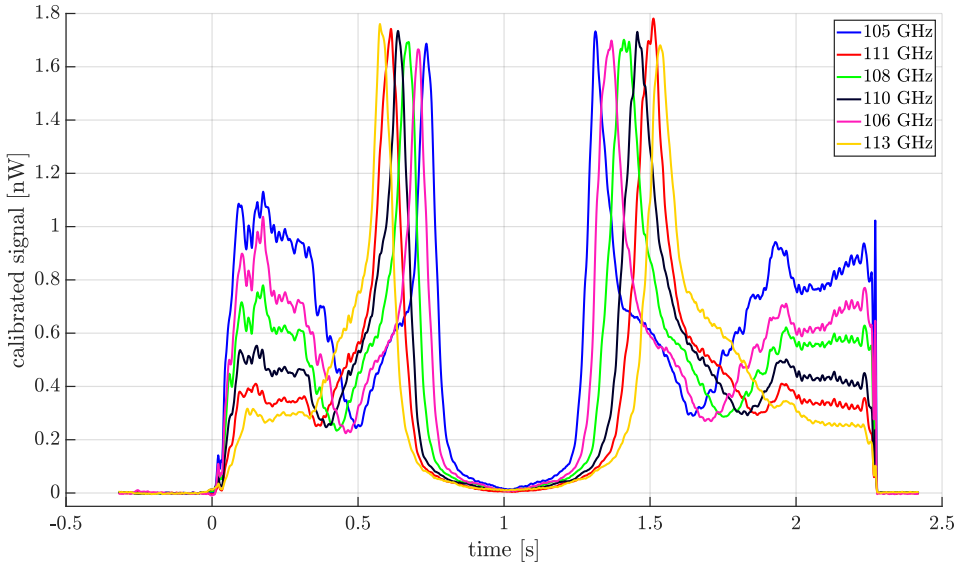

Figure 5.19: Calibrated signal of the radiometer 104 – 114 GHz during for shot #67946.

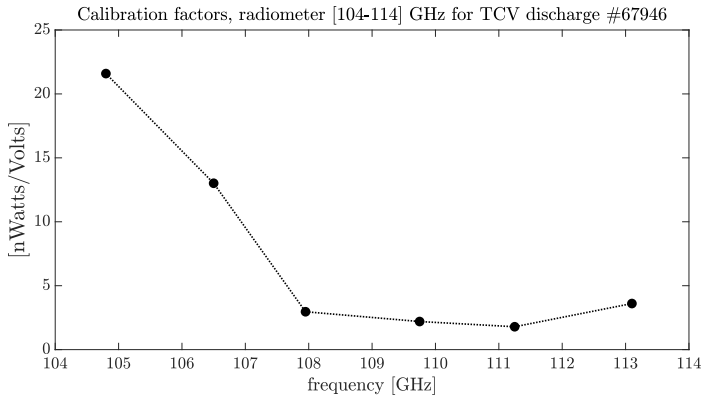

Figure 5.20: Calibration factors without error bar for the channels of the radiometer $104 - 114$ GHz obtained from the shot $\#67946$.

5.5 Validating the calibration

The calibration approach as presented, relies on the modelling of the bandwidth power for the calculation of the calibration factors. In this section, we discuss the attempts to validate the calibration. The validation of the calculated calibration factors means the validation of the modelling of the bandwidth power. The modelling presented in the previous sections relied on the calculation of the single X3 radiation. On TCV, the plasma is in general optically thin to this radiation and it could be judicious to find methods for validation of the modelling. The attempt to validate the calibration exploits the fact that the lowest frequencies of our detection system can measure the single pass radiation from both the second and the third harmonic. That is possible if the magnetic field is varied from its highest to its lowest value. The single pass radiation from the second harmonic reaches the black-body emission, which depends exclusively on a local electron temperature. That radiation can be used at those low frequencies to validate the modelling of the bandwidth power. The steps for this validation, for a channel centered at ~ 80 GHz, are summarized as follows:

- A plasma discharge is run such that the channel detects both the single pass X2 radiation and the single pass X3 radiation within the shot.
- The calibration factor is calculated as presented before exploiting the peaks corresponding to the single pass X3 radiation.
- The full discharge is calibrated using the calculated calibration factor.
- A black-body radiation power, P_{BB} is inferred from the calibrated signal, exploiting the measured peak of the single pass X2 radiation.
- An average electron temperature $\widetilde{T}_e$ is obtained from the inferred black-body radiation.
- That average electron temperature is compared to a measured electron temperature across a plasma area for validation.

5.5.1 Validation on the plasma black-body emission

On Figure 5.21, a time trace of a calibrated signal of a ~ 81 GHz channel from the radiometer $78 - 114$ GHz is shown. The raw signal for this channel has been calibrated using the modelling of the single pass X3 radiation. The single pass X3 radiation is observed in the form of the two peaks around 1 s in the time trace. The mean calibration factor obtained from the two peaks was about 82 [nWatts/Volts]. From the calibrated signal, the power associated with the black-body

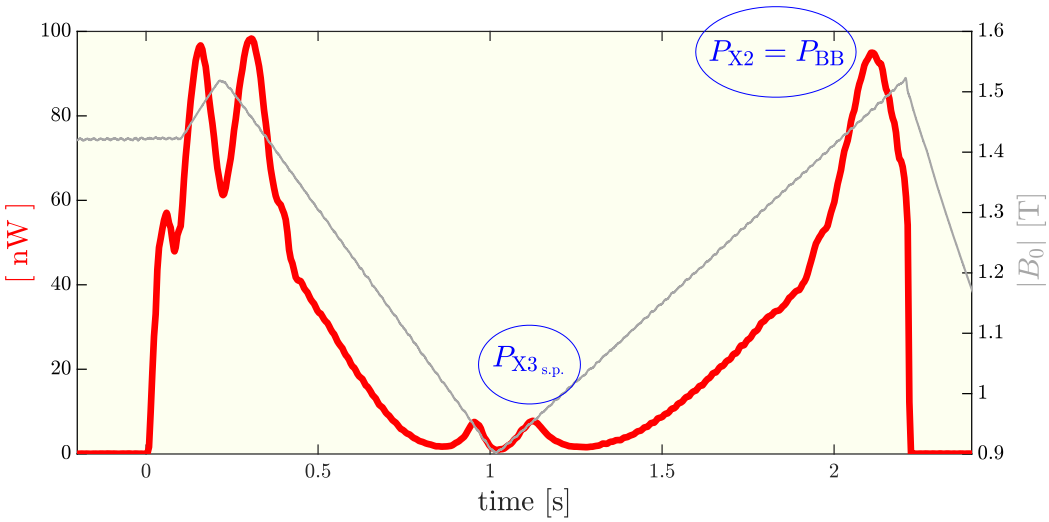

Figure 5.21: Calibrated signal from a channel centered at $\sim$ 81 GHz for the shot #75023.

radiation can the be inferred. That radiation corresponds to the measurements of the higher level peaks at the beginning of the discharge (at around ~ 0.16 s and ~ 0.3s) and at the end of the discharge near ~ 2.1s. The bandwidth power that can be associated to the black-body radiation is thus found to be close to $P_{\mathrm{BB}} = \sim 94$ nW.
Now, we can estimate an average temperature to associate to this black-body radiation power. For that we recall that The black-body radiation intensity, as discussed in Section 5.2 can be written as

$$I_{\mathrm{BB}} = \frac{\omega^2 T}{8\pi^3 c^2}. \tag{5.22}$$

The black-body intensity in Equation 5.22 is itself a spectral intensity in units of $\mathrm{Watts/Hz/sterad/m^2}$. The corresponding bandwidth power can be calculated using the integral from Equation 5.21

$$P_{\mathrm{BB}} = 2\pi c^2 \int df \frac{I_{\mathrm{BB}}}{f^2}. \tag{5.23}$$

We then define the quantity $\widetilde{T}_{\mathrm{e}}$ as the mean electron temperature seen in the bandwidth, such

that the black-body spectral intensity is independent of the bandwidth frequency and reads

$$I_{\mathrm{BB}} = \frac{\omega^2 \widetilde{T}_{\mathrm{e}}}{8\pi^3 c^2}. \tag{5.24}$$

The black-body radiation power expressed via the integral in Equation 5.23 can then drastically reduce to

$$P_{\mathrm{BB}} = \widetilde{T}_{\mathrm{e}} \Delta f_{\mathrm{BW}}. \tag{5.25}$$

The black-body radiation power P_{BB} is obtained from the calibrated signal to be approximately ~ 94 nW. We can then calculate the average temperature associated to the black-body radiation as

$$\widetilde{T}_{\mathrm{e}} = \frac{P_{\mathrm{BB}}}{\Delta f_{\mathrm{BW}}} = \frac{94 \times 10^{-9}[\mathrm{Watts}]}{750 \times 10^{6}[\mathrm{Hz}]} \sim 780\ [\mathrm{eV}]. \tag{5.26}$$

The value obtained for the mean temperature is close to ~ 0.8 keV. Result which is consistent with the expectations and which consolidates the reliability of the calibration approach. That is, $\widetilde{T}_{\mathrm{e}}$ represents the mean temperature of a plasma surface, where the maximum temperature (in the plasma center) is around 1 keV, as can be seen in Figure 5.22.

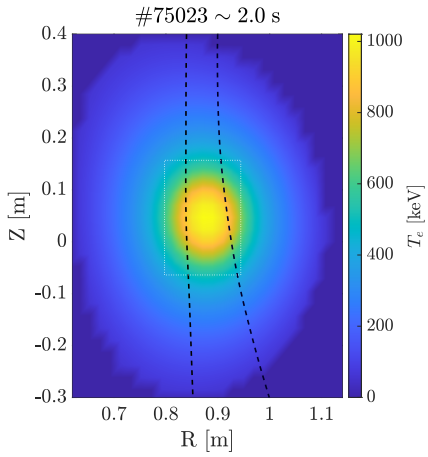

Figure 5.22: Map of the electron temperature in the plasma at the time of detection of the black-body radiation. The white square delimits the area $\Delta R_{\mathrm{Area}} \times \Delta Z_{\mathrm{Area}}$ from which the plasma black-body radiation essentially comes from.

The mean electron temperature deduced from the black-body radiation power agrees with the mean temperature measured across the plasma area from which the black-body radiation arises mainly. The area is surrounded in Figure 5.22. The mean temperature in that area being close to 0.8 keV. Without digging too much into the details, we can explain the determination of that plasma area with the following points. The radial extent of ΔR_{Area} of the area is extracted from

the convolution of the radial extent of the bandwidth frequency, ~ 1 cm and the antenna beam size, affected by refraction in the plasma. The height of the area ΔZ_{Area} is obtained by identifying the locations along the vertical direction where the radiation mainly comes from. That is done using optical depth calculation along the ray trajectories in the plasma. The mean temperature measured from the identified area validates the calibration performed with modelling of the X3 single pass radiation. In the future, higher frequencies than 81 GHz could also benefit from this validation by allowing them to observe the single pass second harmonic radiation. That can be done by shifting the antenna pattern towards the HFS such that the frequencies, which in a vertical configuration cannot detect the X2 single pass radiation, are able to do so with an inclined line of sight.
As a conclusion, it is interesting to note that the validation of the X3 calculation with the X2 radiation allows the validation of higher harmonics calibration with the X3 calibration in a sort of boots-trapping mechanism from the lower and (optically) thicker harmonics to the higher ones.

5.6 The Uncertainties in the calibration

This section discusses the assessment of the uncertainty in the calibration factors. The simplest way to present the assessment is by going through the actual process for a case example, the shot #67946 previously discussed. The uncertainty in the calculation can be estimated every time a discharge is calibrated and that is done for every channel being calibrated. The steps to be undertaken are summarized in the diagram of Figure 5.23. The steps are subdivided in two main branches. One branch is for the assessment of the uncertainty from the processing of the Vertical ECE raw signal. The other branch is for the assessment of the uncertainties in the estimation of the bandwidth power using the synthetic diagnostic.

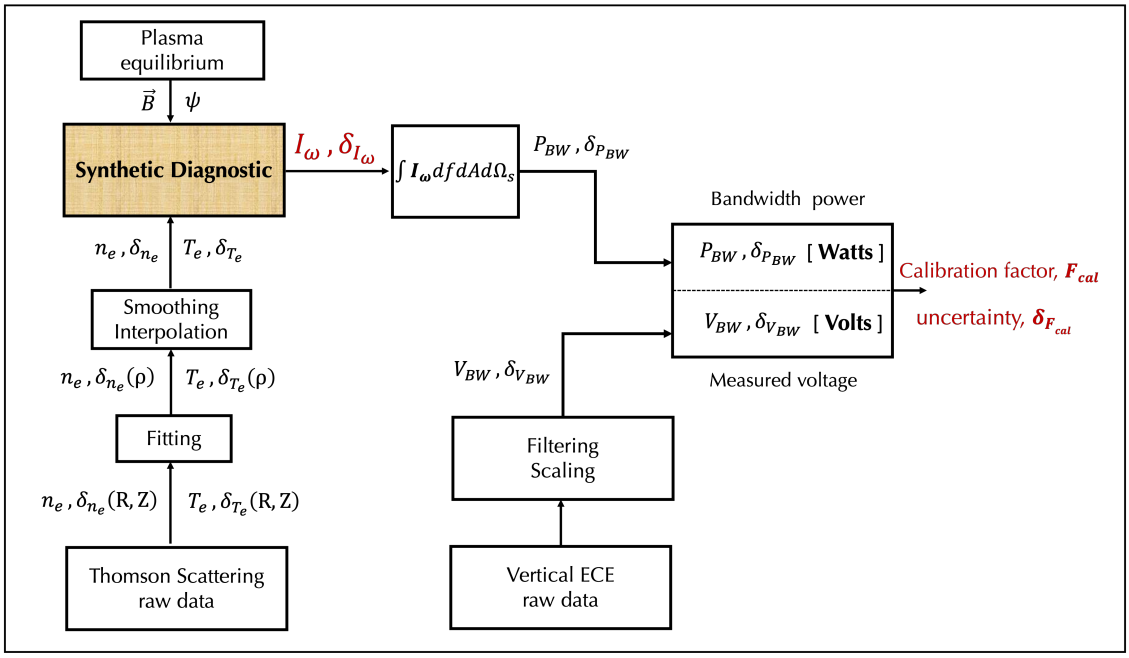

Figure 5.23: Block diagram illustrating the steps for the estimation of the uncertainty in the calibration procedure.

5.6.1 Uncertainties from the processing of the raw signal from the Vertical ECE

Each channel of the diagnostic is calibrated, as we have seen earlier, matching a measured voltage to a modelled bandwidth power. The uncertainty on the measured voltage comes essentially from the digital filtering of the raw data. The digital filter is a low pass Butterworth filter used to suppress thermal noises and fast MHD activities from the signal. Typically, in the calibration shots, the traces for raw and the filtered signals are similar. For the case of interest, shown in Figure 5.24, the relative uncertainty on the filtered value used for the calibration is

$$\frac{\delta_V}{V} < 5\%$$

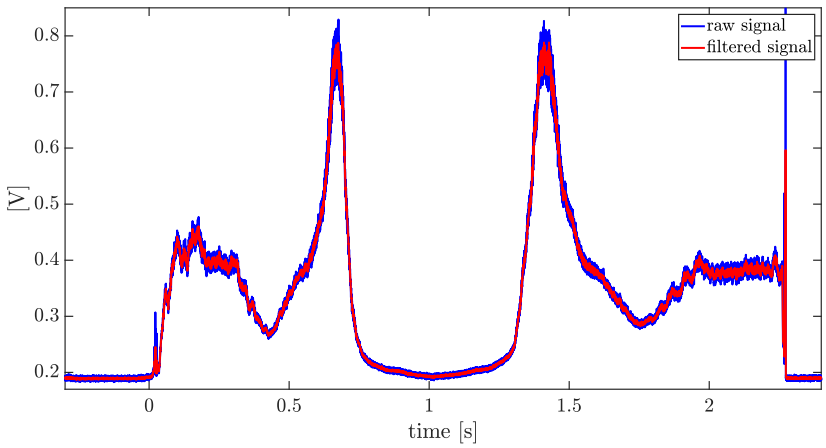

Figure 5.24: Raw signal and processed signal from the radiometer.

5.6.2 The uncertainty in the estimation of the bandwidth power with the synthetic diagnostic

The calibration of the diagnostic relies on measurements of plasma parameters that are given as input to the synthetic diagnostic. To assess the uncertainty in the modelled bandwidth power, the uncertainties in the parameters are propagated from the raw measurement to the calculated bandwidth power. It is not necessary to come up with an empirical formula relating the uncertainty in the calibration factor to the uncertainties on the measured plasma parameters. That is because this process can simply be applied together with the calculation of the calibration factors. As it can be seen in Figure 5.23, we do not account for the potential uncertainty on the measurement of the magnetic field. That is because the diagnostic is in general calibrated when the measurement reaches a peak, equivalent to a resonance within the line of sight. The frequencies in the channels and the orientation of the line of sight actually impose the value of the magnetic field needed to observe that peak. That is, the uncertainties that we propagate are the uncertainties from the measurement of the electron density, δ_{n_e} and electron temperature, δ_{T_e}. The Figure 5.25 shows values of $\delta_{n_\mathrm{e}}/n_\mathrm{e}$ and $\delta_{T_\mathrm{e}}/T_\mathrm{e}$ given as input to the synthetic diagnostic. The relative errors for both the density and the temperature are respectively below 5% and 10% at the plasma center. Both values increase significantly at the plasma edge, up to 25% and 40% respectively. It is important to note that the high uncertainties on the density and temperature profiles at the edge do not have in general a significant impact on the uncertainty in the modelled intensity. That is because the optical depth of the plasma drops at the edge in such a way that the uncertainty in the intensity depends mainly on the parameters in the core plasma, where the uncertainty is relatively low. The relative uncertainty, δ_I/I, on the spectral intensity, calculated for the frequency of 104 GHz roughly gives

$$\frac{\delta_I}{I} < 25\%.$$

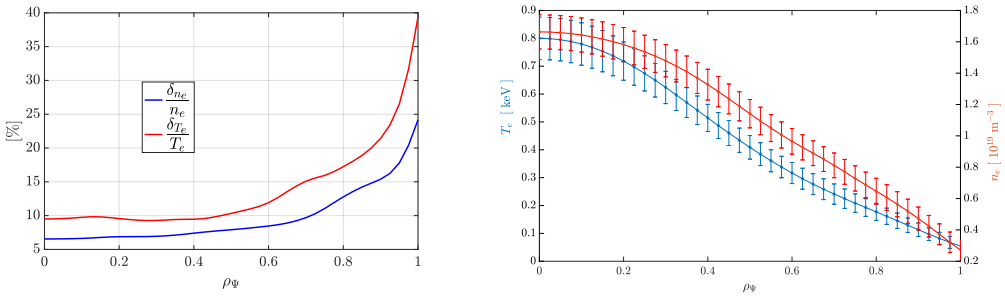

(a) Profiles of the relative uncertainty on the electron density and temperature.

(b) Density and temperature profiles with uncertainties

Figure 5.25: Uncertainty in the electron density and temperature profiles for the shot #67946 at ~ 0.6 s, near the resonance time.

Figure 5.26 shows the spectral intensities calculated with the synthetic diagnostic for different cases, with different uncertainties on the plasma parameters. From the figure, it is clear that the main contributor to the uncertainty on the spectral intensity is the uncertainty on the electron temperature. The uncertainty on the electron density plays a minor role. This can be explained by the fact that the radiation being modelled is the single pass, third harmonic intensity, which has a stronger dependence on the electron temperature. That is, a simplification of Equation 5.13 in case of a single pass radiation and low optical thickness yields

$$I_\omega \sim \frac{\omega^2}{8\pi^3 c^2} T \tau_0. \tag{5.27}$$

Since the plasma optical depth, τ_0, for the third harmonic scales as nT^2, the spectral intensity would then scale as $I_\omega \sim nT^3$, explaining the stronger dependence on the electron temperature. For the following, we assume that the relative uncertainties in the spectral intensity depends

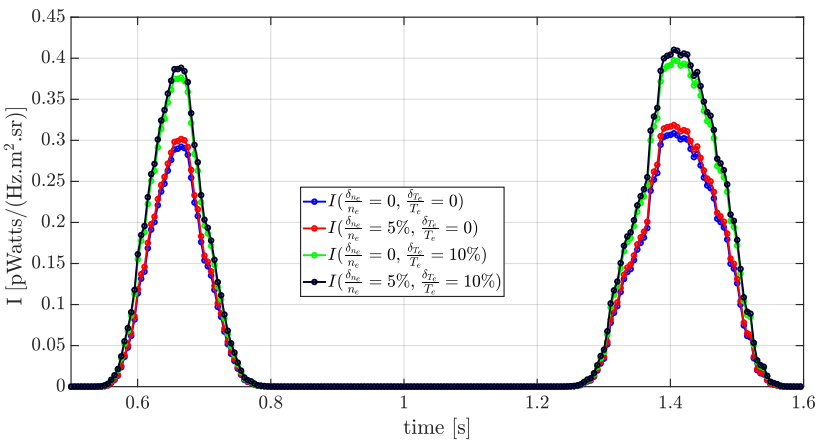

Figure 5.26: Spectral intensities calculated with plasma parameters affected by uncertainties.

only on the plasma parameters and not on the modelled frequencies. With that assumption, the uncertainties in the spectral intensity will propagate unaffected through the integral of Equation 5.21, giving an uncertainty on the modelled bandwidth power of

$$\frac{\delta_P}{P} < 25\%.$$

Finally, the uncertainties on the calibration factor for the illustrated case would be

$$\frac{\delta_{F_{\mathrm{cal}}}}{F_{\mathrm{cal}}} < 30\%,$$

accounting for both the uncertainties in the modelled power and the uncertainties from the raw Vertical ECE signal (see again the block diagram of Figure 5.23).
It is important, while concluding this section, to highlight that this uncertainty on the calibration factor is essentially due to the systematic uncertainty on the raw electron temperature measured by the Thomson scattering diagnostic.

5.7 Conclusions

On the refraction

The assessment of the uncertainty in the modelled intensity, as illustrated in the previous section, cannot fully account for the effects of δ_{n_e}/n_e, while the effects of δ_{T_e}/T_e are fully accounted in the estimation of δ_I/I . In reality, the uncertainty δ_{ne}/n_e could also introduce some effects related to the antenna beam refraction. Effects that are not captured by the modelling. The approach we have used for the estimation of the intensity at the antenna relies on a ray tracing approach. With that approach, we have modelled the antenna beam such that it would form a cylinder of radius equal to the waist size in vacuum. The missing effects of the beam diffraction in our approach are in general neglected. That is because the emission layer, as discussed already is much smaller than the beam size. However, if refraction is important, the effects introduced via δ_{ne}/n_e on the real antenna beam could indeed not be captured by the antenna pattern, modelled with rays. This consideration leads to the conclusion that calibration shots achieved with minimized refraction would be the most reliable. The experiment $\#67946$, discussed for the illustration, was achieved with a low enough electron density to minimized refraction effects.

On the frequency dependence

We have previously assumed that the uncertainty on the calibration factor $\delta_{F_{\rm cal}}/F_{\rm cal}$, does not have a dependence on the frequency and that the strongest dependencies are on the plasma parameters. In reality, when higher harmonics are measured, the signal to noise ratio for the higher frequencies is smaller than the signal to noise ratio of lower frequencies. That is because the ECE intensity decreases with the harmonic number. That is, the calibration of the radiometer $[133-148]$ GHz which measures radiation above the fourth harmonic, is less accurate than that of lower frequency radiometers. This point is important since the calibration method that has been developed applies only if thermal radiation can be measured by the radiometers. Higher frequencies, corresponding to higher harmonics, cannot be calibrated if their thermal resonances are not measured. This has not been a limitation for us since all our frequencies were able to detect thermal emission up to the fourth harmonic.

On the wave polarization

The calibration technique that we have developed exploits the measurement of the X-mode emission from a thermal plasma. This choice was motivated by the fact that in typical thermal plasmas at low temperatures, the single pass radiation intensity for the X-mode is typically two orders of magnitudes higher than that of the O-mode, and thus more prone for measurement. The ratio of the X-mode to the O-mode intensities decreases with increasing energy of the electrons, especially when the parallel energy is enhanced. During non-thermal measurements, the calibration factors obtained from the thermal X-mode calibration can be used to calibrate

the non-thermal O-mode signals. That is because we assume, with good reasons, considering the wave transmission line that the propagation of the both polarizations in the waveguide undergo similar power losses. For that, the calibration factors obtained from thermal X-mode measurement can be used in non-thermal measurement in either polarizations.

On the uncertainties in the absolute calibration due to Thomson scattering

It has been understood that the main uncertainties on the calibration factors come from the uncertainties in the electron and temperature profiles measured by the Thomson scattering diagnostic. It is worth mentioning that this affects the absolute calibration only, since the uncertainties on the plasma parameters are systematic, independent of the frequency. For the relative calibration between channels, the calibration factors can actually be freed from the previously estimated uncertainties. That is because we assume that δ_{T_e}/T_e and δ_{n_e}/n_e do not depend on frequency and so also $\delta_{F_{\mathrm{cal}}}/F_{\mathrm{cal}}$. For the absolute calibration, a reduction of the uncertainty can be obtained reducing the uncertainty on the measured electron temperature. In general measurement of higher temperature allows lower uncertainties on the Thomson scattering profiles. That uncertainty depends on the shot and can be improved, depending on the temperature that can be reached.

On the stability of the calibration

The stability of the calibration is a general issue in the calibration approaches that use substitutes to the plasma. We will now discuss the stability of our approach. For this work, more that 72 plasma discharges have been exploited for the calibration. The calibration factors, obtained from those discharges are indeed spread out and not peaked at a given value for a given channel. For a given channel, of a given radiometer, the spread in the values of the calibration factor can come from the calculation of the bandwidth power or from the measured voltage. At a fixed harmonic, the bandwidth power for a given frequency changes due to the changes in the electron temperature and density. The different plasma parameters from one shot to the other is responsible for the different calculated bandwidth power, which contribute to the spread of the calibration factors. The most important effect on the spread certainly comes from the measured signal for different discharges. The configuration of the transmission line and the radiometers can change by a lot from one shot to the other due to the flexible use of the detection system. Some components for power attenuation and power splitting are very often included in the transmission line for the fine tuning of the detected signal. This has the consequence of impacting significantly the detected voltage and certainly not the modelled power. This is the most important cause of spread in the calibration factors. This effect is much more important than that of the daily change in the radiometer internal parameters, which are due for example to the changes in the room temperature in the tokamak hall. For those reasons, the calibration approach we have developed is appropriate, given the conditions. The calibration can be performed directly with the detection system in the desired configuration by running a

calibration shot right after an experiment on fast electron measurement. Even better, one can have the calibration and the fast electron measurement within the same shot. In this latter case, the stability of the calibration factor would not be of question any longer. An example of this hybrid discharge will be presented in the next chapter.

Final remarks

The calibration approach we have developed offers the possibility for post calibration of the diagnostic. The Vertical ECE raw signals from the calibration discharges can be accessed for more accurate calculation of the calibration factors,if needed. That can be done for example in the future, if one needs to estimate the spectral intensity using more sophisticated approaches involving full wave calculation or beam tracing for the antenna pattern.

6 Experimental results

6.1 Introduction

We discuss in this chapter the measurement of non-thermal electron distributions. The non-thermal distributions of interest are generated during Electron Cyclotron Current drive and runaway electron discharges. In Section 6.2, we show a case example of a discharge with combined current drive and calibration. The calibration, as discussed in Chapter 5, is achieved exploiting the thermal radiation from the bulk electrons. For non-thermal measurements, the energies measured in the frequency bands of the system depends on the magnetic field value. Figure 6.1 shows the electron energies that can be measured with the radiometers frequencies,

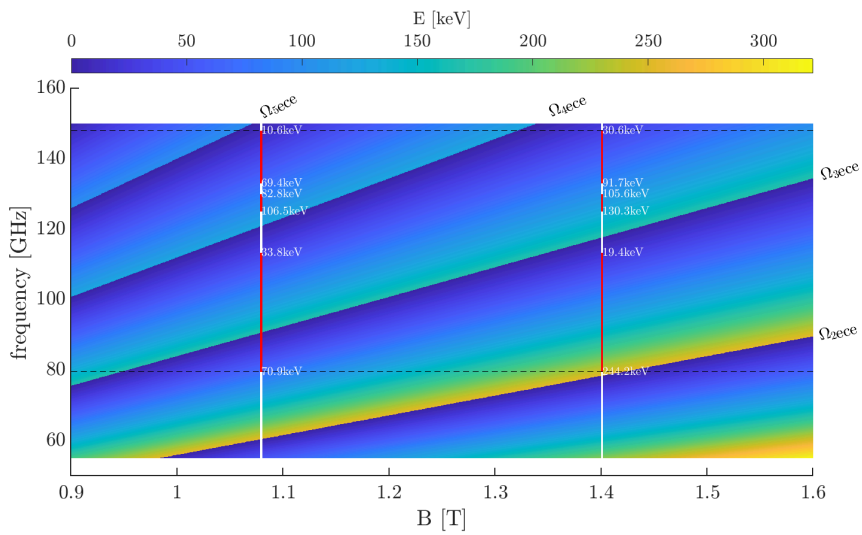

Figure 6.1: Energy map for the determination of the measured electron energy as a function of magnetic field and channel frequency.

at magnetic field values of ~ 1.4 T and ~ 1.09 T. The values of uncertainties on the calculated

energies, as found in Chapter 4 apply only in case the frequencies are well in between the harmonic frequencies (see again Figure 6.1). For frequencies close to the harmonic frequencies, the uncertainties on the energy values can be much higher. This is because the measured energy can vary from a high value, say ~ 200 keV, to the thermal energy, close to ~ 1 keV, just with a slight increase in the field value. The increase of the magnetic field value shifts upward the frequencies of the harmonics. That is why in general for the measurement, it is necessary to use magnetic reconstruction to determine, the most precisely, the values of the magnetic field components, for the estimation of the electron energies.
The non-thermal radiation which is measured for electron distribution studies is in general polarized linearly. The O- and X- polarizations are separated before the detection. The components of the magnetic field are taken into account in order to determine the orientation of the electric field vectors for the two polarizations. A high level of precision is needed in this procedure to avoid polarization scrambling at the wire grid polarizer.

6.2 The hybrid Current drive-Calibration scenario

The plasma discharge $\#73217$ on TCV has been designed to combine the calibration of the radiometer with the fast electron measurement. The time traces of the discharge parameters are shown in Figure 6.2. The heating phase occurs at constant magnetic field ~ 1.54 T, for about 1 s between 0.3 s and 1.3 s. When the heating is turned off, the value of magnetic field strength is kept unchanged for about 100 ms, until about 1.4 s. The field is then ramped down from 1.54 T to 0.9 T in the remaining part of the discharge. The heating phase occurs at a constant ECH power ~ 500 kW and constant launcher angle $\theta_L \sim 10°$. The launcher angle is used to control the direction of the ECH wave vector with respect to the toroidal magnetic field in the plasma. When that angle is close to 0, the ECH wave purely heats the plasma by increasing the perpendicular energy of the bulk electrons. Increasing the launcher angle allows the resonance of the ECH wave with higher energy electrons, as will be discussed in the next section. In this discharge, the plasma current is ramped down together with the magnetic field such that the equilibrium remains quasi frozen. That is done in order to preserve the same X-mode polarization from the current drive to the calibration phase. The measured intensity for X-mode radiation in the frequency range $96 - 114$ GHz is also shown on Figure 6.2. From the radiometer response, a clear distinction between the two phases can be made. The smooth ramp of the field allows the identification of the thermal peaks for each frequency. The higher frequencies, measuring the lower energies have their thermal resonances first, followed by the lower frequencies. The energies attributed to the frequencies are those corresponding to the constant field, current drive phase of the discharge.

One of the most interesting feature of the discharge $\#73217$ can be observed in the time interval between 1.3 s and 1.4 s, highlighted in Figure 6.3. That ~ 100 ms time interval corresponds to the period between the current drive and the field ramp. In that interval, the heating is turned off and the measured energies are kept equal by preserving the field value. The radiation intensity drops for all the measured energies as soon as the heating is turned off. The reduction in the

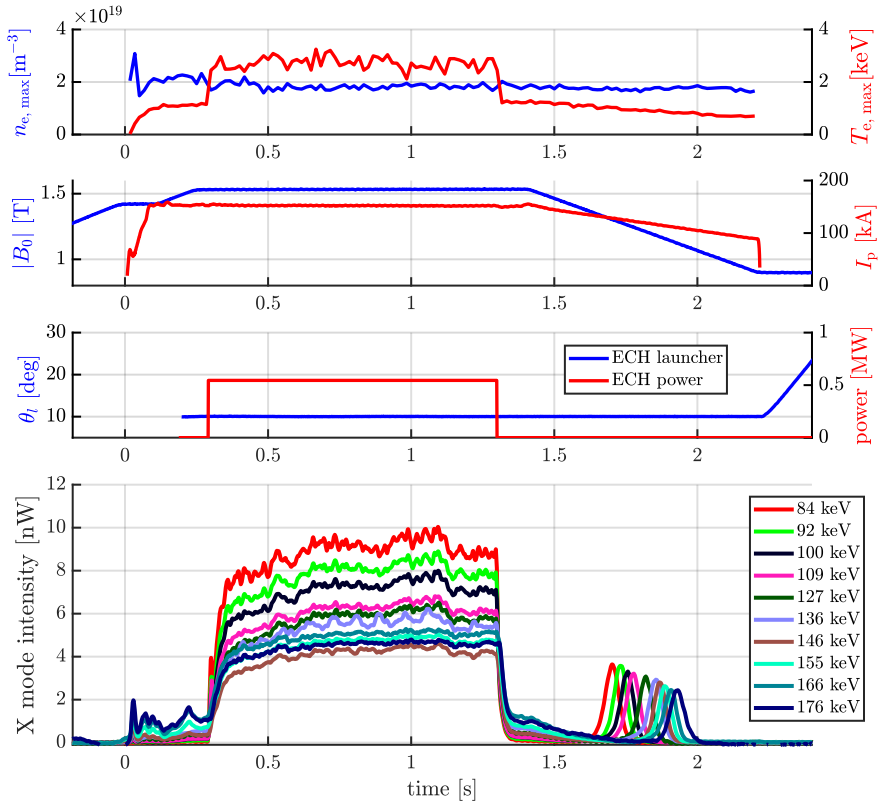

Figure 6.2: Time trace of the main parameters for the hybrid discharge #73217.

radiation intensity signifies that the radiation measured during current drive is essentially that of non-thermal electrons, with little or no thermal contribution, depending on the frequency. For illustration, we consider the relatively high frequency 112 GHz, measuring electrons at energy $\sim$ 84 keV. In general, the detected radiation during the current drive phase is the sum of both non-thermal radiation and thermal radiation from multiple wall reflections. The field value in the time interval between 1.3 s and 1.4 s keeps the X2 cold resonance of the frequency 112 GHz out of the plasma, with the consequence of a very low level of radiation measured when the heating is off. Since the X2 cold resonance in that interval is at the same location as it was during the heating phase, we can conclude that the radiation measured during current drive is essentially that of non-thermal electrons at $\sim$ 84 keV. This is actually an experimental verification of a prediction made in Chapter 4 on the conditions for non-thermal measurement. The clean measurement of non-thermal emission at 112 GHz is possible due to the absence of background radiation, whose origin is kept out of the plasma for that frequency. For the lowest frequencies, measuring the higher energies, the observation is consistent. The intensity that is measured at the highest energies during the transition phase can be attributed to the background radiation. The intensity level of the background radiation is higher for the lower frequencies. That is because the X2 cold resonances of the lower frequencies are located at smaller major radii in the plasma. For some of the frequencies, those having their thermal X2 in the plasma, the measured radiation during current drive is a combination of both thermal and non-thermal radiation at

the calculated energies. These observations consolidate the findings on the conditions for non-thermal electron measurement with the diagnostic. The discharge #73217, discussed in this

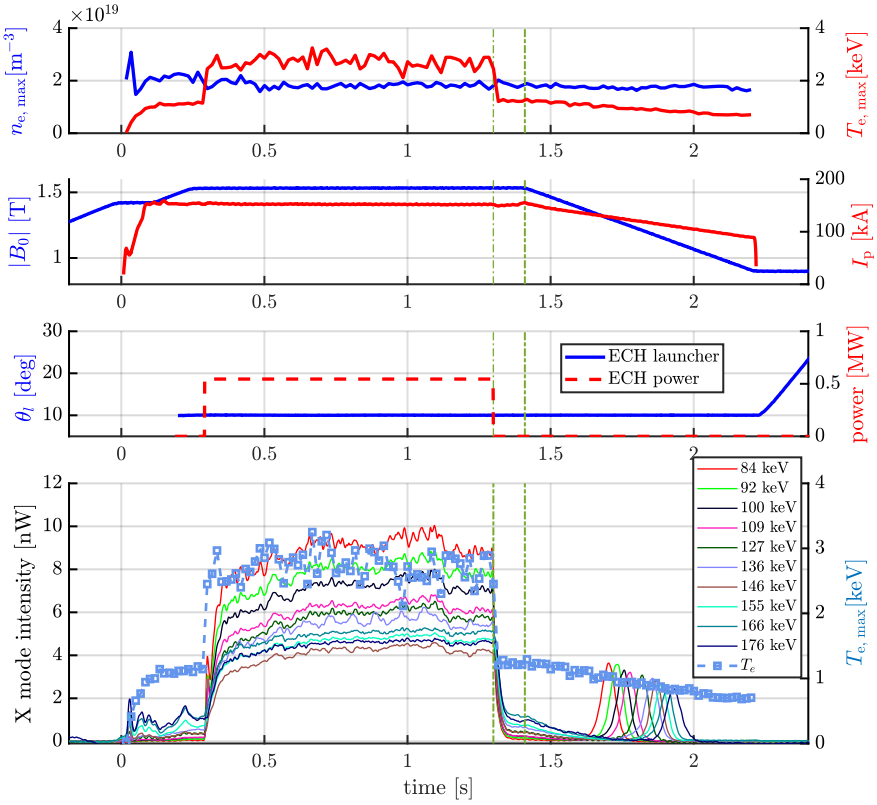

Figure 6.3: Time trace of the main parameters of the discharge #73217, with highlight of the time interval between 1.3 s and 1.4 s representing the transition between current drive and calibration at constant field.

section is also a good example of a self calibrated non-thermal experiment. The 3 dimensional plot on Figure 6.4 shows the two phases of the discharge with the transition interval marked by a reduction of the measured intensity in the direction of the lower energies. The thermal peak intensities on which the channels have been calibrated have lower intensities with increasing energies (decreasing frequencies). That is due to the drop in electron temperature with the field and current being ramp down. We note an additional feature regarding this discharge, on the relative intensities measured during the current drive phase. During that phase, the launcher angle, θ_L, constraints the region in the velocity space which resonates with the ECH wave. For this discharge, the launcher angle was low enough to excite the lower energy electrons. That explains the higher intensity observed at the lower energies. At the higher energies, the non-thermal contribution to the radiation adds up to the background radiation explaining the relatively high level of the measured intensity.

There is a region, observed in the energy space near $\sim$ 150 keV, which exhibits a feature similar to a "valley" in the measured intensity. That region, as can be seen in Figure 6.4, is the transition between two regions of interest. Those regions of interest are (1) the region where the thermal

background has a significant contribution to the measured intensity and (2) the region where it is a negligible fraction of the measured intensity. On Figure 6.4, the thermal background radiation can be observed over time, before and after the current drive and also in the energy space, with decreasing intensity level towards the lowest energies.

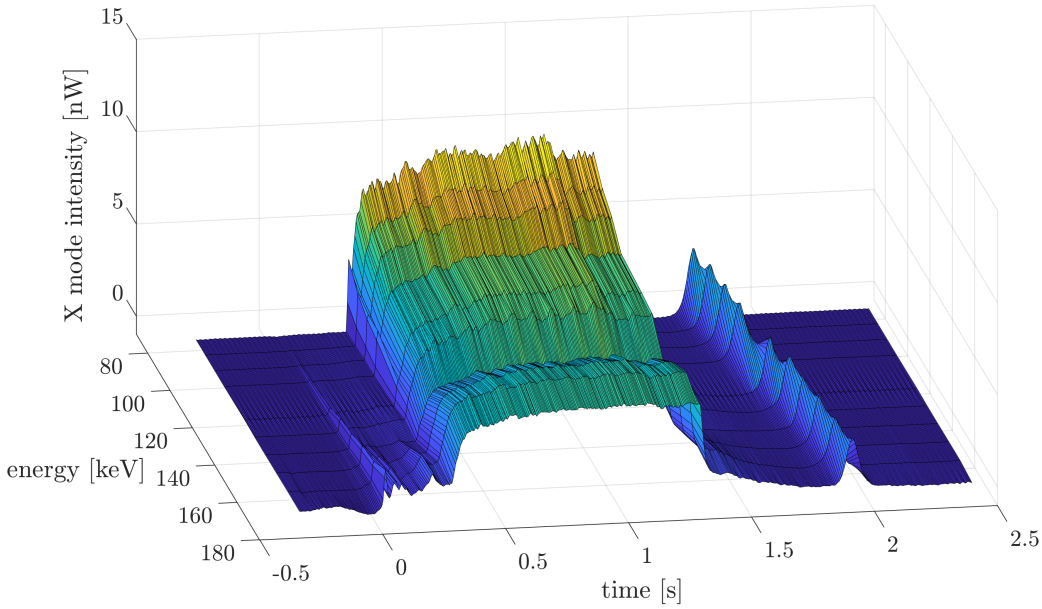

Figure 6.4: 3 dimensional plot of the measured intensity during the hybrid discharge #73217.

6.3 Measurements during electron cyclotron current drive

We present in this section an example of Vertical ECE measurement during a dedicated ECCD discharge on TCV. For that discharge, the #72644, the calibration of the diagnostic is achieved using a different plasma discharge. The ECH power had a value similar to that of the hybrid discharge #73217, while the launcher angle was varied in 5 stationary steps during the heating phase between 0.7 s and 1.9 s. Here as well the toroidal angle of the X2 launcher was kept constant at $\sim -90°$. The variation of the poloidal angle of the launcher from $\sim 10°$ to $\sim 26°$ in each stationary step allows the observation of stair-shape X-mode intensities. The Figure 6.5 shows the raw signal measured during the discharge #72644 and the previous discharge #73217 for comparison. When no heating power is applied in both plasma discharges, the measured intensities coincide and are in general close to the noise level of the radiometer since no background radiation pollutes the measurement. As soon as the heating is turned on in the discharge #73217 at ~ 0.3 s, all the channels immediately peak to reach a nearly stationary intensity level. It is interesting to note how the level of the intensity during the discharge #73217 is in general higher than the intensity level in the discharge #72644 when the launcher configurations are similar. That is certainly due to the more efficient current drive achieved in #73217. The maximum electron temperature measured in #73217 is twice that of #72644, as can be seen in Figure 6.5. The more efficient current drive achieved in #73217 is due in part to the lower density since the current drive efficiency is proportional, in general, to the ratio T_e/n_e [86].

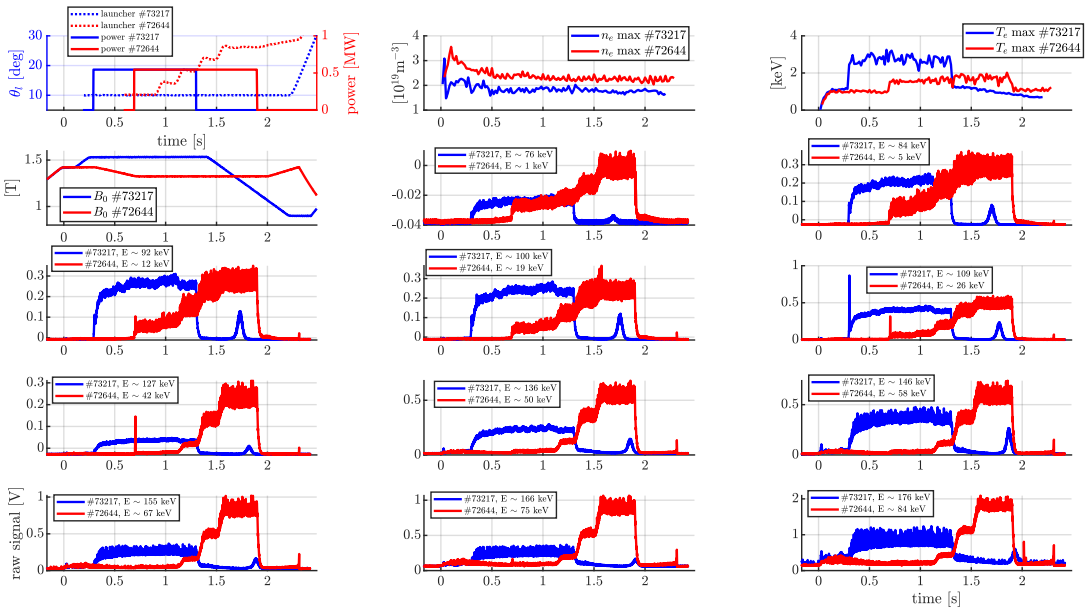

Figure 6.5: Raw measurements from the discharges #73217 and #72644 in the frequency range $96 - 114$ GHz.

We now focus on the discharge #72644, whose only calibrated signal is shown in Figure 6.6. An

assessment of the measured energy allows us to analyse the discharge following the dynamics in the phase space. When the heating is turned on during the discharge #72644, at ~ 0.7 s, only the low energies ($\sim 5 - 26$ keV) exhibit a sharp jump in the measured intensity. The intensity at the higher energies ($\sim 67 - 75$ keV) experiences a similar jump, with a delay of more than ~ 500 ms, when the launcher angle has been moved to its third stage. From that moment, the dynamics is inverted and the higher energies now experience the sharpest jump in intensity compared to the lower energies. Interestingly, the measurement at the middle energies, in our range, will then reach the highest value of intensity when the launcher angle reaches its last stage.

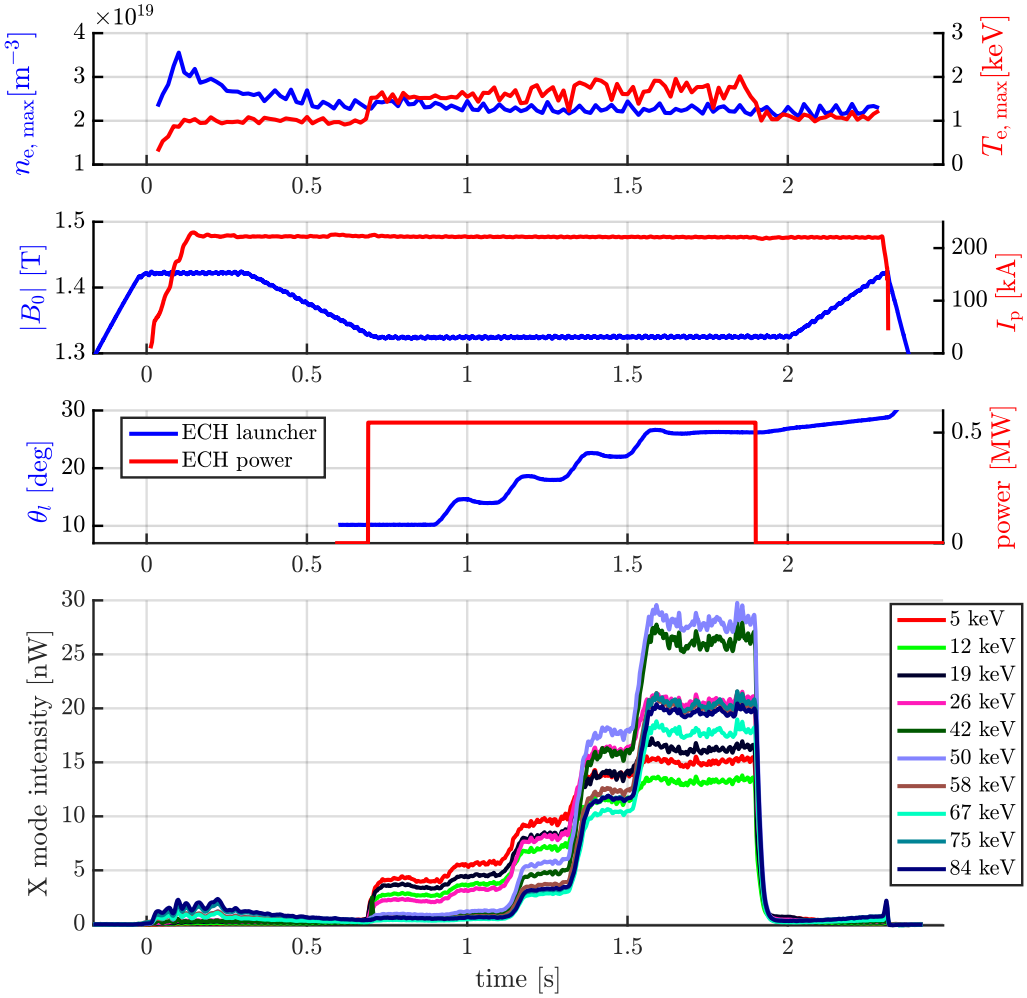

Figure 6.6: Calibrated signals for the discharge #72644. The increasing launcher angle allows the coupling of the wave with higher energy electrons.

Simulations of the ECH wave interaction with the plasma, for the discharge #72644 has been achieved using the code C3PO, for a better interpretation of the measurement. The profiles of the ECH power deposition in the plasma are shown on Figure 6.7.

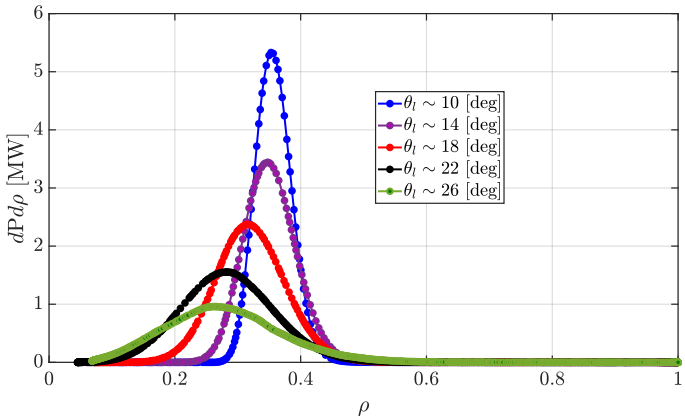

Figure 6.7: Profile of the power deposition in the plasma for the various launcher angles, swept during the discharge.

The profiles of the power deposition for the different launcher angle are useful for the calculation of the parallel refractive index in the region where the ECH power is mainly absorbed. The calculated refractive indices, as well as the ECH wave vector, for the various launcher angles are shown on Figure 6.8. As expected, the increase in the launcher poloidal angle allows to achieve higher values (in absolute term) of the parallel refractive index at the wave absorption location. Those values of refractive indices, used in the cyclotron resonance equation lead to the resonance curves shown of Figure 6.9. It can be seen from the figure how, higher parallel refractive indices allow the intersection between the resonant curves and the $v_{||}$ axis, to occur at higher (in absolute term) values of $v_{||}$ [87]. The physical mechanisms of the plasma-wave interaction is complex and can of course not be all revealed in the Figure 6.9. The mechanisms include, in general, momentum diffusion and pitch-angle scattering, which make the ECCD resonant interaction region complex to determine. What can be said for the interpretation of this experiment is that higher values θ_L and thus $N_{||}$ induce more energetic electrons in the plasma, explaining the different jumps in the measured intensities.

The dynamics of the jumps in intensity is studied exploiting the Figure 6.10. In the figure are plotted the jumps, with respect to the thermal phase, registered at each frequency in the different steady stages of the discharge. The jump is obtained by dividing the raw intensity in the steady, heated phase by the raw intensity in the thermal phase, before the heating power is turned on. By doing so, we ensure that the observed dynamics is not linked to potential errors in the calibration, since the Figure 6.10 is built directly from the raw measurement. On the figure it can be seen how at relatively low parallel refractive index ($N_{||} = -0.22$), the highest frequencies (lowest energies) jump is the most important. As $N_{||}$ increases, an intermediate frequency (intermediate energy as well), near 104 GHz experiences the sharpest jumps. It is important to recall that the X-mode intensity, measured with the Vertical ECE is the ideal conditions, is an intensity correlated essentially to the density of the non-thermal electrons in the given energy bands. That is, the highest jump observed around 104 GHz, with increasing $N_{||}$ may suggest

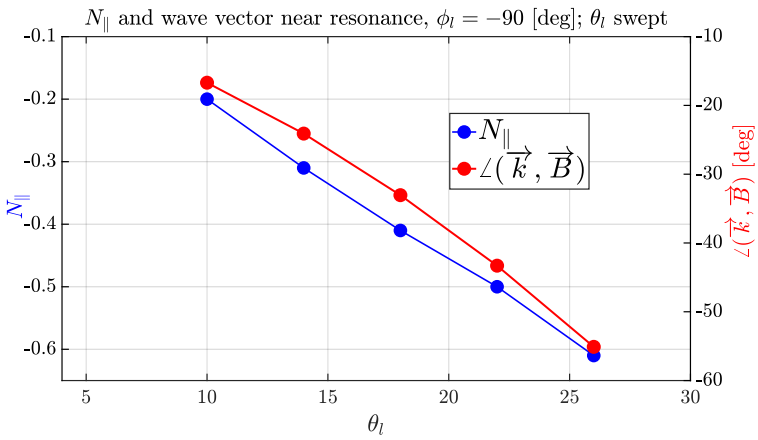

Figure 6.8: Parallel refractive index and ECH wave angle as a function of the launcher poloidal angle, swept during the discharge.

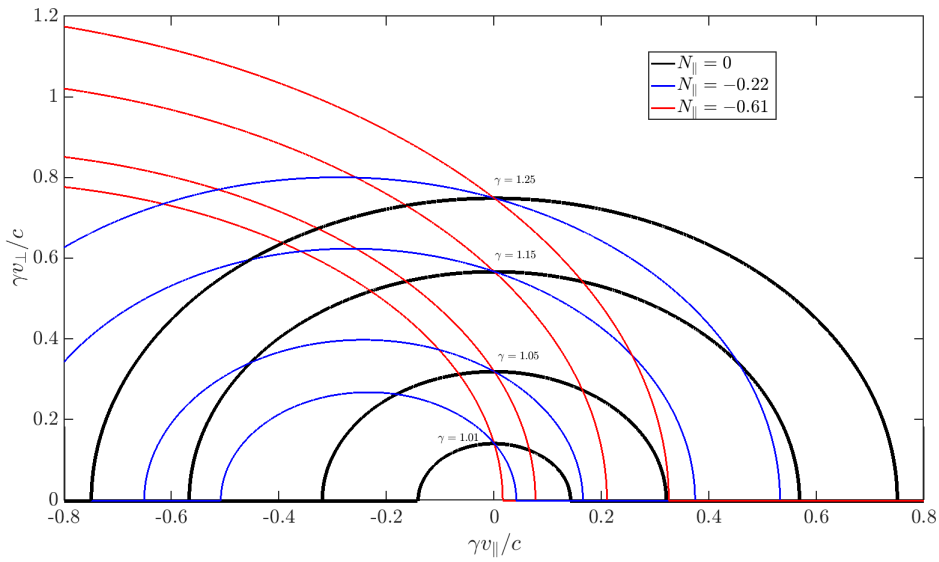

Figure 6.9: Electron Cyclotron Resonance curves for different values of parallel refractive index and energies.

an increase in the number density of non-thermal electrons at the corresponding energy. This does not necessarily mean that the ECH wave in damped on electrons energies measured at 104 GHz when the refractive index increases. The increase of the number density at the given energy, which explains the sharp jump, is a consequence of the overall dynamics in the electron energy space, originally caused by the ECH wave.
In order to observe the effects of the change in the parallel refractive index on the electron

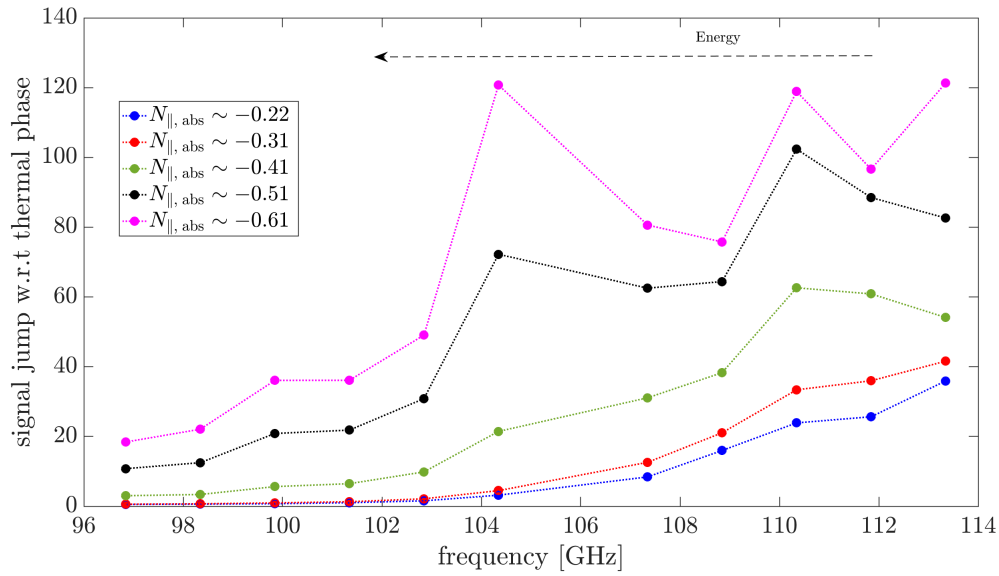

Figure 6.10: X-mode intensity as a function of energy at different values of parallel refractive index.

distribution, calculations have been performed at the different stages of the discharge #72644 using the code LUKE. The first calculation is shown in Figure 6.11. On that figure, the total number of electrons above a certain energy is plotted for a Maxwellian distribution and for the modelled distribution. As expected, this number is higher at all times for the modelled distribution. Furthermore, the total number of electrons above a certain energy increases with time intervals (with $N_{\|}$). This feature can also be seen in Figure 6.12 where is plotted the derivative with respect to energy. Figure 6.13 shows instead for all times the derivative of the number of electrons in the modelled distribution deducted from the density in the Maxwellian distribution. The discontinuity in the spectra is due to the logarithmic scale. It represents the regions where the density in the Maxwellian distribution is higher than that of the modelled distribution, which is the region in the phase space where the electrons are being pumped out by the ECH wave.
Measurement of the O-mode in the same range, $96 - 114$ GHz has also been achieved. The ratio of intensities between the two polarizations during the heating phase is shown in Figure 6.14. For the lower energies, The ratio decreases with θ_L, meaning that the parallel energy has been preferentially enhanced after the first stages of the discharge. This could mean that the interaction between the lower energy electrons and the ECH wave, which in principle enhances the parallel energy decreases with increasing $N_{\|}$. The low energy electrons then get their energy from collisions with the faster electrons, which enhances the parallel energy and reduces the ratio X-mode to O-mode intensities.

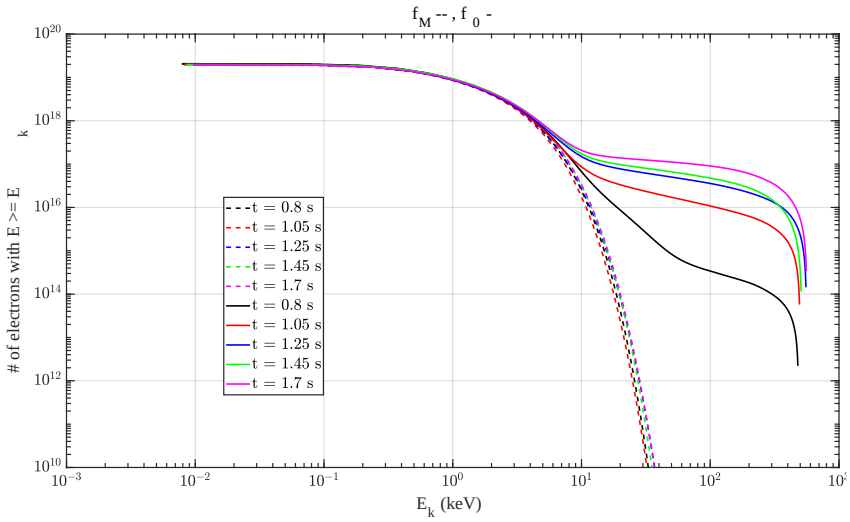

Figure 6.11: Calculation with the code LUKE of the total number of electrons above a certain energy. The dashed lines are relative to the Maxwellian distribution. The solid lines are the computed distribution for the discharge.

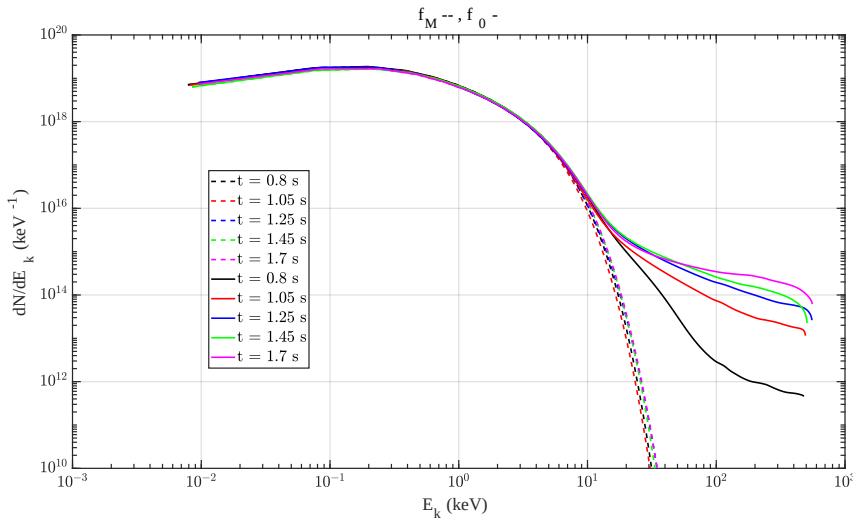

Figure 6.12: Calculation with the code LUKE of the derivative of number of electrons with respect to energy.

6.4 Measurement of Runaway electron emission

We present in this section examples of measurements achieved during runaway electron experiments on TCV. We consider the discharge #73002, where the radiometer $78 - 114$ GHz was used for measurement of the X-mode radiation. In typical runaway measurements, the

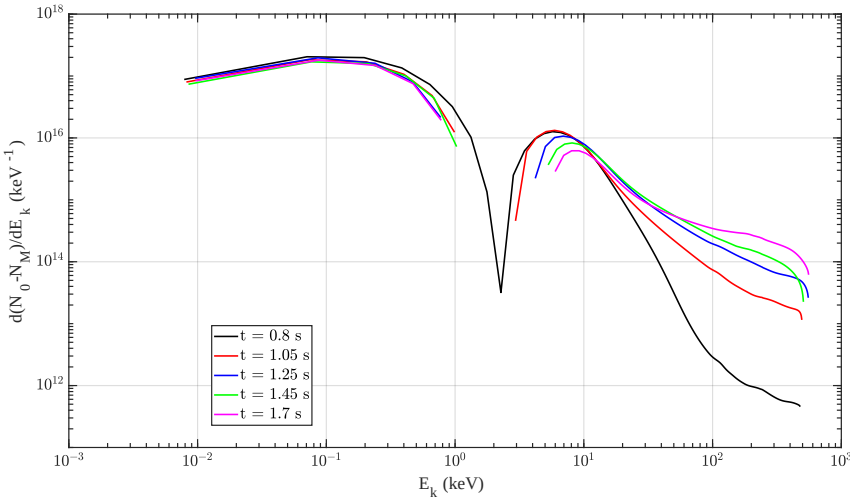

Figure 6.13: Calculation with the code LUKE of the derivative of number of electrons with respect to energy with respect to the Maxwellian distribution.

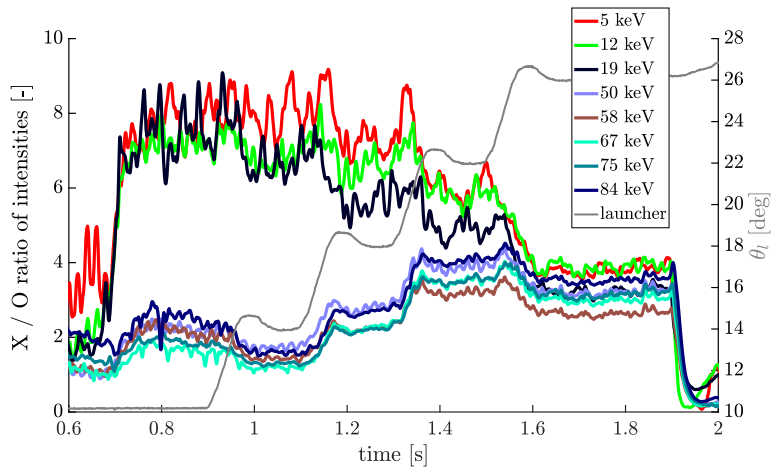

Figure 6.14: Ratio of Polarization during Current drive in TCV discharge #72644.

successful discharges are repeated, with the wire grid rotated $90°$, such that each radiometer sees both polarizations. A fine-tuning of the gains is usually needed to avoid the saturation in the detected signals. Once the gains at set, a calibration discharge in ran, keeping the same diagnostic configuration. In the discharge #73002, the generation of runaway electrons was achieved by reducing the electron density at a relatively high plasma current, $\sim$ 150 kA. The plasma parameters of the discharge and the measured radiation intensities are shown in Figure 6.15. The flat phase of the discharge, after ~ 0.5 s is not due to the saturation of the signal. The detected intensity is truly nearly constant in the presence of the runaway beam. The runaway beam was generated at around ~ 0.5 s. The measurement in the frequency range $78 - 96$ GHz,

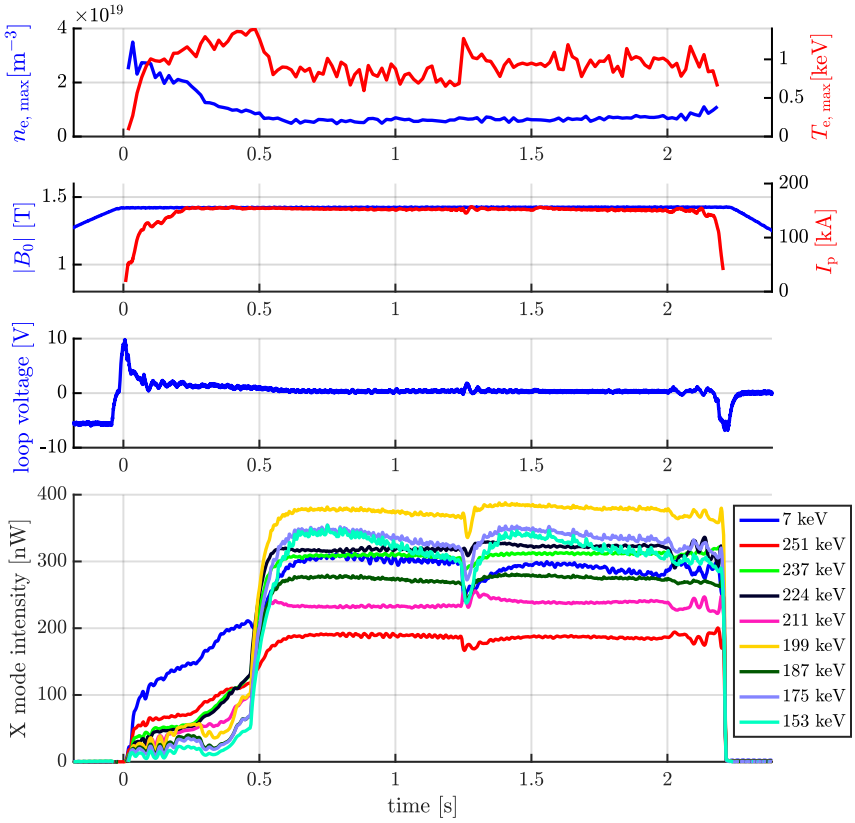

Figure 6.15: Measurement of the X-mode radiation during the discharge #73002 with the radiometer 78 − 96 GHz.

shown in the same Figure 6.15 features a thermal phase before ~ 0.5 s. The energies at which the thermal contribution is detected are associated to the lower frequencies, which have their X2 cold resonances within the line of sight. The higher frequencies, which correspond to energies ~ 153 keV in Figure 6.15, have a smaller thermal contribution since their X2 thermal resonances is not within the line of sight. That is, from ~ 0.5 s , the runaway electron radiation is measured by the diagnostic without thermal pollution from about ~ 0.5 s at some of the energies. Moreover, the drop in the plasma density and temperature should reduce the thermal emission from 0.5 s at all energies. The measurement is marked, at around ~ 1.2 s by a drop in intensity at all energies. The drop is perhaps the characteristic of the runaway beam interaction with some instabilities in the plasma. In fact the drop is also marked in Figure 6.16 on the loop voltage and the electric field. The ratio of the intensities of the X-mode to the O-mode radiation is shown in Figure 6.17 for a group of frequencies. The ratio decreases when the runaway beam is generated, confirming that it is the parallel energy of the electrons that is being enhanced. Moreover, the ratio is higher at some of the lower energies, meaning less enhancement of the parallel energy.

Another example of measurement of runaway electrons is shown in Figure 6.18. In this example, the ECH is used for current drive when the runaway electrons are generated. The runaway

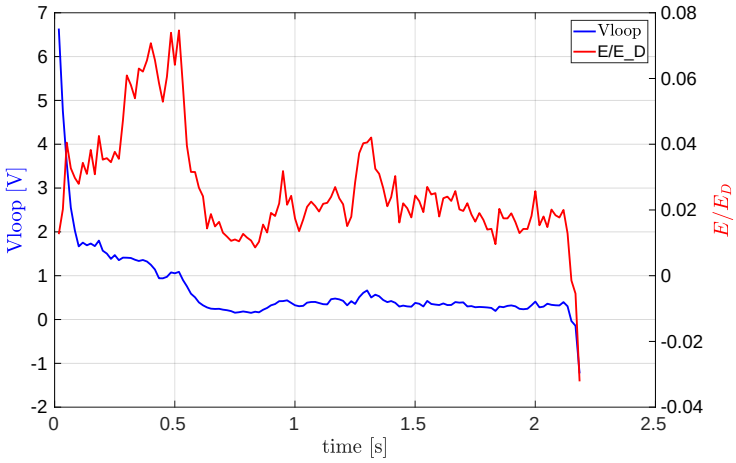

Figure 6.16: Loop voltage and ratio electric field to the Dreicer field.

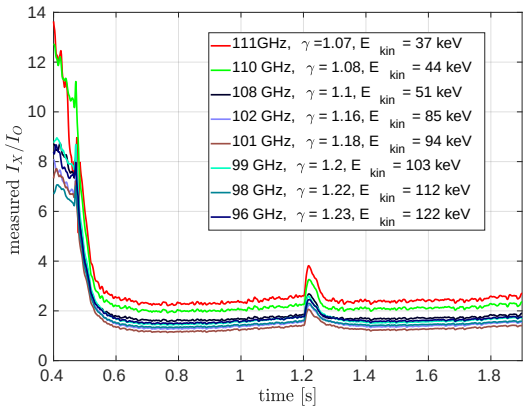

Figure 6.17: Ratio of the X-mode to the O-mode radiation intensity for a runaway electron discharge.

beam is generated as in the runaway discharge #73002, lowering the density at a relatively high plasma current. The current drive phase with ECH power is characterized by an increase of the temperature measured by the Thomson scattering, see Figure 6.18. The Vertical ECE signal in the other hand drops during the current drive phase, when the temperature increases, feature that is unusual for ECE diagnostics. This observation confirms the clear reduction of the runaway emission intensity during current drive. This can be due to transport of the runaway electrons in physical space or in the phase space. Investigations to determine the causes of the flushing are currently being carried out. A possible cause may be the interaction of the runaway electrons with MHD modes driven by the current drive.

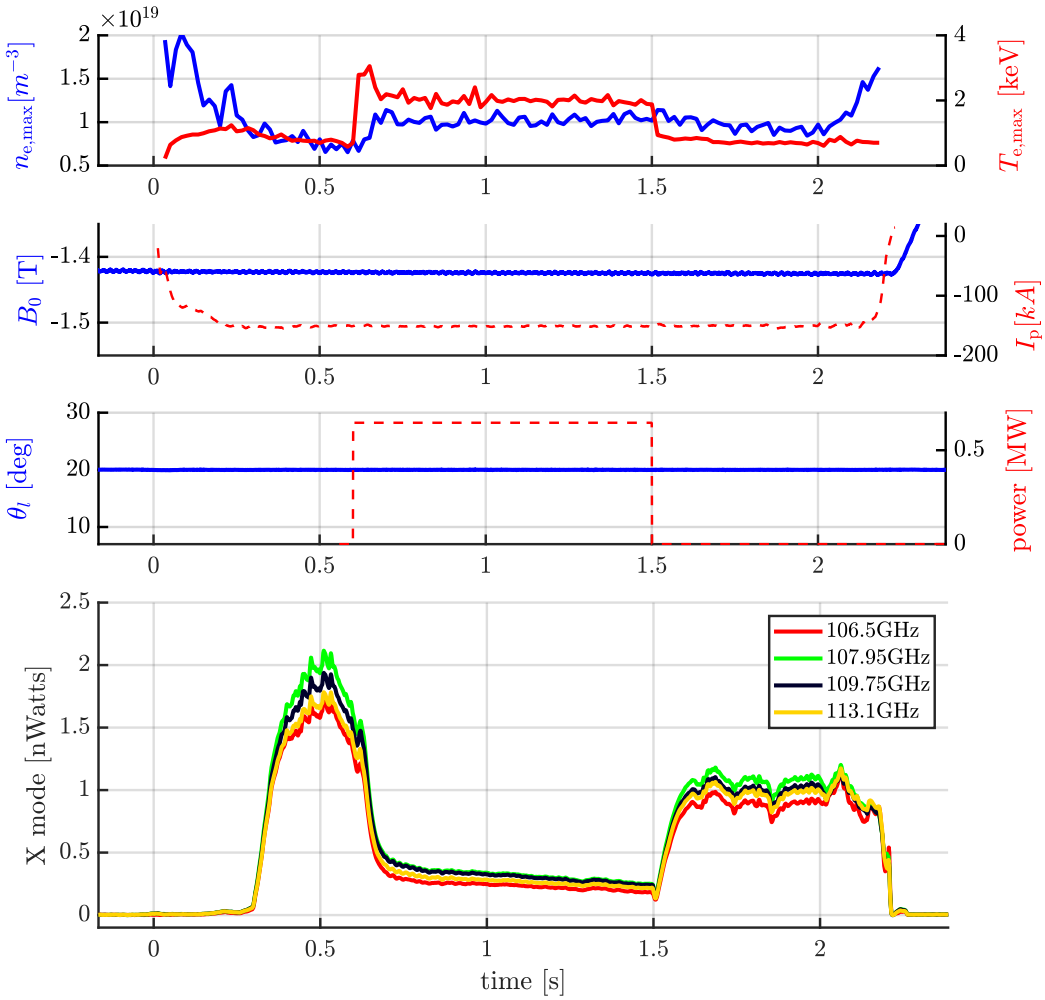

Figure 6.18: Flushing of runaway electrons using ECH.

6.5 Summary

This chapter has described examples of measurements achieved during ECCD and runaway electron scenarios on TCV. The discharges for both scenarios can be combined with a calibration phase, as shown with a ECCD case example. The impact of the change of the parallel refractive index on ECCD measurements has been observed. Modelling with LUKE helps to explain why higher values of refractive index allow the increase in the signal of higher energy channels of the diagnostic. That can be explained to be due to a higher number of energetic electrons present in the plasma, as $N_{||}$ increases. The emission from the runaway beam has been presented in a scenario at low density and high plasma current and in a scenario including ECCD. The combined ECCD and runaway electrons has shown an interesting decrease in the runaway electron emission intensity in the presence of current drive.

7 Reconstruction of the electron distribution

7.1 Summary of the method

We present in this chapter examples of the reconstruction of the electron energy distribution. The examples are selected from runaway electron and ECCD experiments performed on TCV, with measurements of the Vertical ECE. As discussed in Chapter 3, the main assumption for the reconstruction will be that of neglecting collective effects in the plasma. With that assumption, we will make an analytical derivation of the expression of the fast electron density at a given energy (frequency), as a function of the measured intensity. The expressions are derived with the assumption of a delta type distribution for the model of distribution function.
The reconstruction starts from the expressions of the single particle emissivities, which can be rewritten for the O-mode as

$$\eta_{\mathrm{O}} = \frac{e^2\omega^2}{8\pi^3\epsilon_0 c}\sum_{n=1}^{\infty}\left[\frac{p^2\cos^2\theta_{\mathrm{p}}}{1+p^2}J_n^2\left(\frac{\omega}{\omega_{\mathrm{ece}}}p\sin\theta_{\mathrm{p}}\right)\right] \tag{7.1}$$

and for the X-mode

$$\eta_{\mathrm{X}} = \frac{e^2\omega^2}{8\pi^3\epsilon_0 c}\sum_{n=1}^{\infty}\left[\frac{p^2\sin^2\theta_{\mathrm{p}}}{1+p^2}J_n'^2\left(\frac{\omega}{\omega_{\mathrm{ece}}}p\sin\theta_{\mathrm{p}}\right)\right]. \tag{7.2}$$

The single particles emissivities in Equations 7.1 and 7.2 have units of $\mathrm{Watts/Hz}$, since they represent the spectral power emitted by a single electron. The expressions have been rewritten as a function of the normalized momentum p and the pitch angle θ_{p}.
The emission coefficients of an uncorrelated ensemble of electrons is calculated in O-mode with the integral

$$j_{\mathrm{O}} = \int \eta_{\mathrm{O}} F(\overrightarrow{p})\mathrm{d}\overrightarrow{p} \tag{7.3}$$

and in X-mode with

$$j_{\mathrm{X}} = \int \eta_{\mathrm{X}} F(\overrightarrow{p}) \mathrm{d}\overrightarrow{p}. \tag{7.4}$$

The expressions of the emission coefficients in Equation 7.3 and 7.4 are in units of $\mathrm{Watts/Hz/m^3}$. To be able to use the calibrated measurements in each bandwidth, we need the spatial and spectral integrals of the emission coefficients. For the spectral integral, the integration is performed in the frequency bandwidth around a given central frequency, ω. The spatial integral is needed for the inclusion of the volume of plasma lying within the antenna pattern. The volume of plasma within the antenna pattern is found by the product of the effective area of the antenna A, in the radial direction, and the distance s, representing the vertical extent of the antenna. An integration over the solid angle Ω_{S} is also needed to obtain a quantitative match of the measurements in each bandwidth. The power in the bandwidth is thus found from the integrals

$$P_{\mathrm{O}}(\omega) = \int j_{\mathrm{O}} ds dA d\Omega_{\mathrm{S}} d\omega = \int \eta_{\mathrm{O}} F(\overrightarrow{p}) \mathrm{d}\overrightarrow{p} ds dA d\Omega_{\mathrm{S}} d\omega \tag{7.5}$$

and

$$P_{\mathrm{X}}(\omega) = \int j_{\mathrm{X}} ds dA d\Omega_{\mathrm{S}} d\omega = \int \eta_{\mathrm{X}} F(\overrightarrow{p}) \mathrm{d}\overrightarrow{p} ds dA d\Omega_{\mathrm{S}} d\omega \tag{7.6}$$

The expressions in Equations 7.5 and 7.6 represent the quantities that are measured by the diagnostic in units of Watts. They are measured independently in two polarizations and for the same electron distribution. Their simultaneous measurement allows the fitting of a $2-$parameters distribution function. In the case of a delta type distribution, the ratio of $j_{\mathrm{X}}/j_{\mathrm{O}}$ will be used to infer the weighted pitch angle. Since the weighted pitch angle is obtained from the ratio of the emission coefficients prior to the integration, it represents an average over the bandwidth and over the volume of intersection of the plasma and the antenna pattern.
The analytical expressions for the emission coefficients which will yield the weighted pitch angle are found calculating the integral of Equations 7.4 and 7.3 in a more appropriate coordinate system:

$$j(\omega) = \int \eta(\omega, p, \theta_{\mathrm{p}}) F(\overrightarrow{p}) \mathrm{d}\overrightarrow{p} \equiv \int_0^{2\pi} d\xi \int_0^{\pi} d\theta_{\mathrm{p}} \sin\theta_{\mathrm{p}} \int_0^{\infty} dp p^2 F(p, \cos\theta_{\mathrm{p}}) \eta(\omega, p, \theta_{\mathrm{p}}) \tag{7.7}$$

and using the form of the delta distribution[88] already introduced in Chapter 3:

$$F(p_0, y) = \frac{n_{\mathrm{fast}}}{2\pi p_0^2} \delta(p - p_0) \delta(y - y_0) \tag{7.8}$$

where $y = \cos\theta_{\mathrm{p}}$.

The integration over the delta distribution yields to the following expressions for the O-mode

emission coefficient

$$j_{\mathrm{O}}(\omega) = \frac{e^2\omega}{8\pi^2\epsilon_0 c} n_{\mathrm{fast}} p_0 y_0^2 J_n^2\left(\frac{\omega}{\omega_{\mathrm{ece}}} p_0 \sqrt{1-y_0^2}\right) \tag{7.9}$$

and for the X-mode,

$$j_{\mathrm{X}}(\omega) = \frac{e^2\omega}{8\pi^2\epsilon_0 c} n_{\mathrm{fast}} p_0 (1-y_0^2) J_n'^2\left(\frac{\omega}{\omega_{\mathrm{ece}}} p_0 \sqrt{1-y_0^2}\right). \tag{7.10}$$

The ratio of the intensities, which determines directly the weighted pitch angle, y_0, thus reads

$$\frac{j_{\mathrm{X}}(\omega)}{j_{\mathrm{O}}(\omega)} = \frac{1-y_0^2}{y_0^2} \times \frac{J_n'^2\left(\frac{\omega}{\omega_{\mathrm{ece}}} p_0 \sqrt{1-y_0^2}\right)}{J_n^2\left(\frac{\omega}{\omega_{\mathrm{ece}}} p_0 \sqrt{1-y_0^2}\right)}. \tag{7.11}$$

The normalized momentum p_0 is obtained directly from the measured frequency via the relation

$$p_0 = \sqrt{\left(\frac{n\omega_{\mathrm{ece}}}{\omega}\right)^2 - 1} = \sqrt{\left(\frac{n f_{\mathrm{ece}}}{f}\right)^2 - 1}. \tag{7.12}$$

Figure 7.1 shows the ratios of the X- to the O-mode intensities computed using Equation 7.11 for a range of energies (normalized momentum). The values of energies were found from the values of $\omega_{\mathrm{ece}} \sim 2\pi \times 40$ rad/s and selected frequencies ω in the range $\omega \sim 2\pi \times [96 - 114]$ rad/s, corresponding to a Vertical ECE operational range. We note that the higher is the energy, the lower is the polarization ratio than can be achieved. This means that there is a minimum energy required to achieved a given ratio. The form of the curves, near the high values of y_0^2, is relatively flat, meaning that an uncertainty in the ratio can yield a large uncertainty on the weighted pitch angle. The assessment of the enhancement in the reconstructed distributions, in one of the directions, parallel or perpendicular to the field, is done by comparing the theoretical ratios in Figure 7.1 to the measured ratio of intensities. Comparisons with an isotropic distribution can be made at each energy, in the different scenarios to determine the direction of the enhancement of the distribution . At a fixed energy, the lower ratios would suggest an enhancement in the parallel direction while the higher ratios would suggest an enhancement in the perpendicular direction. We recall that the approach to infer the weighted pitch angle is blind to any geometrical factors, since the expression of the polarization ratio has been obtained from the emission coefficients. For the density of the electrons, we need to use the calibrated intensity measured in one of the polarizations. Now we use the X-mode power in Equation 7.6, as the bandwidth power, for the estimation of density n_{fast}. We combine the Equations 7.6 and 7.10, to obtain the following expression of the bandwidth power

$$P_{\mathrm{BW}} = \frac{e^2 c \widetilde{H}_{\mathrm{p}} \Delta f}{2\epsilon_0 \widetilde{f}} n_{\mathrm{fast}} p_0 (1 - y_0^2) J_n'^2 \Big(\frac{\widetilde{f}}{f_{\mathrm{ece}}} p_0 \sqrt{1 - y_0^2} \Big) \tag{7.13}$$

The expression in Equation 7.13 is obtained by using the similar assumptions as in Chapter 5 for the estimation of the bandwidth power. The terms $\widetilde{f}$ and $\widetilde{H}_{\mathrm{p}}$ represent respectively the average frequency in the bandwidth (the bandwidth central frequency) and the mean plasma height within the antenna pattern. Finally, the number density of electrons at energy

$$E = (\frac{n f_{\mathrm{ece}}}{\widetilde{f}} - 1) m_{\mathrm{e0}} c^2, \tag{7.14}$$

measured from the nth harmonic, in the channel centered at the frequency $\widetilde{f}$ has the expression

$$n_{\mathrm{fast}}(\widetilde{f}) = \frac{2\epsilon_0 \widetilde{f} P_{\mathrm{BW}}(\widetilde{f})}{e^2 c \widetilde{H}_{\mathrm{p}} \Delta f p_0 (1 - y_0^2) J_n'^2 \Big(\frac{\widetilde{f}}{f_{\mathrm{ece}}} p_0 \sqrt{1 - y_0^2} \Big)}. \tag{7.15}$$

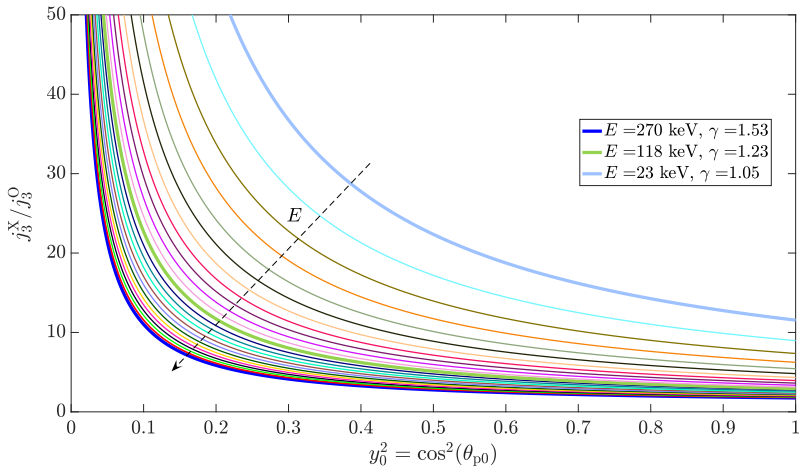

Figure 7.1: Ratio of X-mode to O-mode intensities as a function of pitch angle at various energies.

7.2 The reconstruction

The selected examples are the TCV ECCD discharges #72644 and #72648. The discharge #72648 is a repeat of #72644 with the wire grid rotated by 90° to invert the measured polarization in each line of the detection system. Similarly, for the runaway electron example, the considered discharges are the #73002 and the #73000. We use the data measured in the frequency range $96 - 114$ GHz. The ratio of the X-mode to the O-mode intensity for the ECCD example is shown in Figure 7.2. The intensities for the ECCD case are calculated at 5 stationary

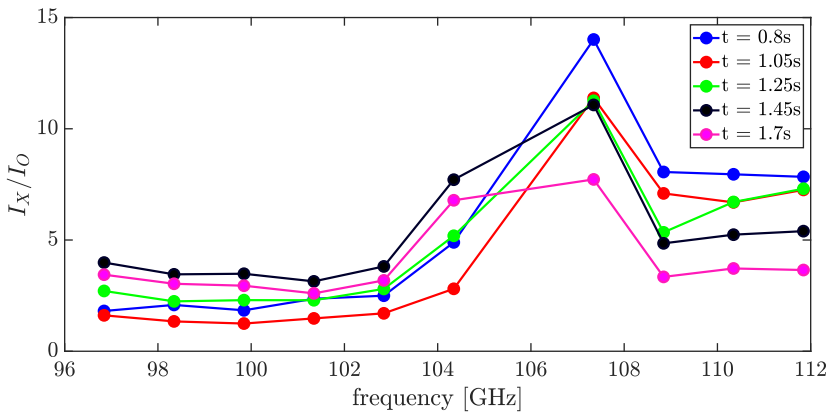

Figure 7.2: Measured ratio of the X mode to the O mode intensity with the radiometer $96 - 114$ GHz.

times, belonging to 5 stationary time intervals described in Chapter 6 for the TCV shot #72644. Each time corresponds to a launcher angle and thus to different parallel refractive index at the location of the power deposition. The ratio peaks at ~ 107 GHz at the selected times and is lower at the lower frequencies.

The energies associated with the frequencies in Figure 7.2 can be estimated, assuming harmonic overlap can be neglected, and that the non-thermal contribution to the radiation comes essentially from the third harmonic emission. The ratio as a function of the energy is shown in Figure 7.3. The peak in the ratio observed in the frequency space corresponds approximately to an energy of ~ 28 keV. We note that, at the lower energies, the ratio is higher for smaller times. This trend is inverted at the higher energies, where the polarization ratios have lower values in general. Based on single particle theory, it can be said that at smaller times, when the parallel refractive index is small, energies are more enhanced in the perpendicular direction, explaining the higher ratio of the X- to the O- mode intensities. At higher refractive index (higher times), the higher energies are more enhanced in the perpendicular direction, consistently with the expectations. In the same frequency range, the ratio of the two intensities for the runaway electron experiment

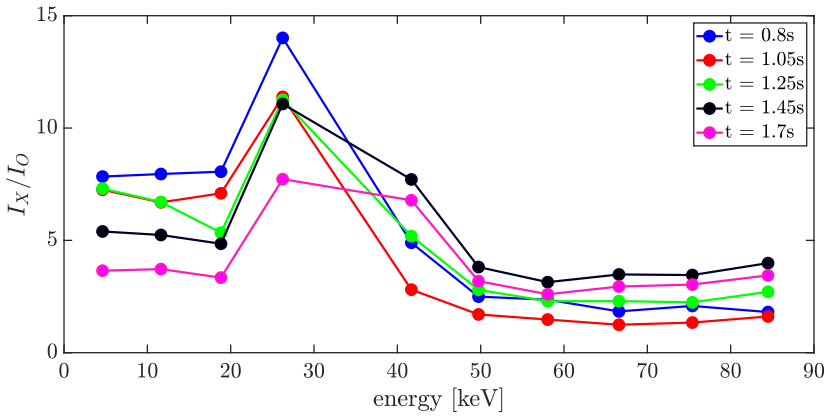

Figure 7.3: Ratio of X-mode to O-mode intensities as a function of pitch angle at various energies.

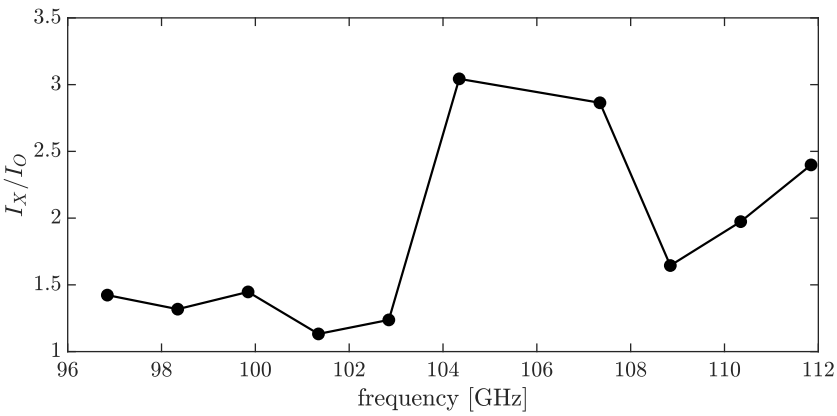

Figure 7.4: Ratio of X-mode to O-mode intensities as a function frequency.

is shown in Figure 7.4. In general the ratio is lower, at each frequency, compared to the ECCD case. We note that the plots of the polarization ratios do no have error bars as the ratio can be obtained from the raw data and are free from the uncertainties in the calibration. For the analysis of the distribution, it is suitable to focus on the runaway electron experiment. That is mainly for two reasons. The first reason is that the ECCD experiment is performed at a much higher density and necessitates the inclusion of the collective effects described in Chapter 3. The second reason is that the approach using the polarization ratio may not be appropriate in the high density case, due to possible contamination of the radiation by the multiply reflected radiation, which will lead to a ratio of polarization that cannot be trusted. The ratios shown in the ECCD case are useful to realize that perhaps in the phase space region of interaction of

the ECH wave and the electrons, the ratio increases as a consequence of an enhancement of the perpendicular energy. The absolute values of the ratio in ECCD should not however be compared to those of the runaway case. For the runaway case, we show the time traces of the vertical ECE signal and of the central density and temperature, in Figure 7.5. The analysis of the loop voltage and electric field helps to identify the time around ~ 0.5 s as the runaway beam formation time.

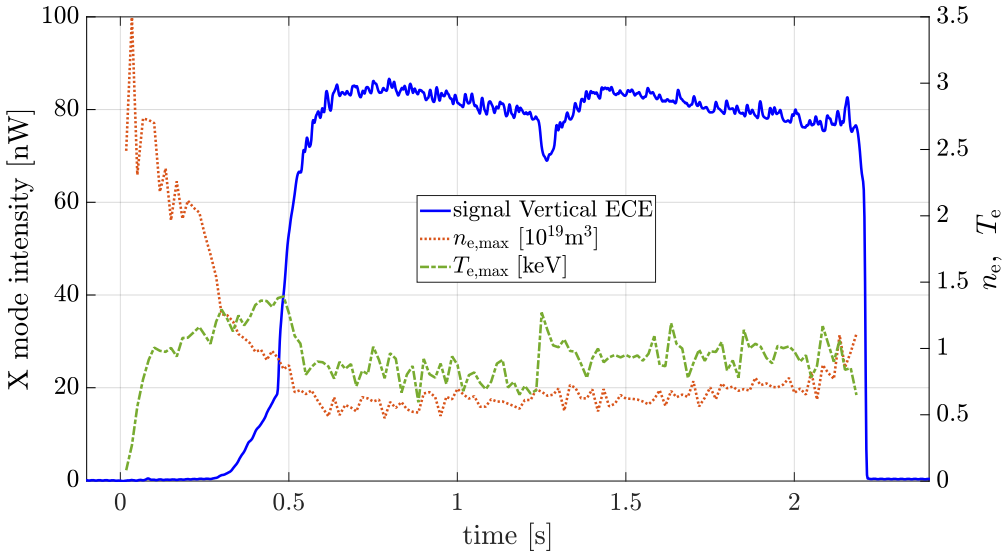

Figure 7.5: Runaway electron experiment used for the reconstruction of the non-thermal electron distribution.

The mean ratio of intensities at the two polarizations is obtained in the presence of the runaway electron beam. The ratio is shown for a single frequency in Figure 7.6. We have mentioned in Section 7.1 that a minimum energy is required to achieve a given ratio. Assuming that the polarization ratio obtained in the runaway case has not suffered any contamination, it is interesting to note that a much higher energy is needed in order match the measured ratio. That is why in this specific case, we allow the measured emission to be that of the emission from the 4th harmonic and not that from the above 3rd harmonic. With the emission coming from the 4th harmonic, as can be seen in Figure 7.6, the electron energy is sufficient to achieved the the measured ratio of the polarized intensities. We note that in reality, the emission that is detected comes from more than one harmonic. In the case of runaways, the expected distribution is flat, and in a case of a flat distribution, the higher energy emission can actually dominate the total radiation. From the figure, a clear enhancement in the parallel direction is observed, for the case of the runawway electron measurement. The obtained value of weighted pitch angle is close to about $y_0^2 \sim 0.68$.

The Equation 7.15 can then be finally used to compute the density at each of the energies. The calibrated intensity is needed for the estimation of the density at each energy. The intensity for

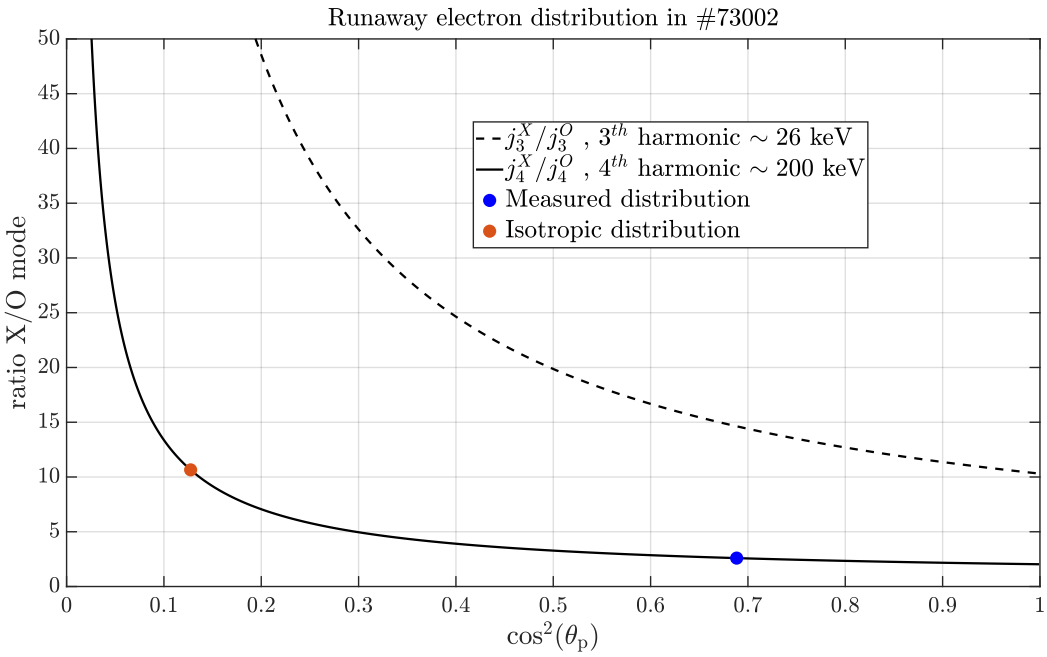

Figure 7.6: Polarization ratios of an isotropic distribution compared to the ratio from the runaway experiment.

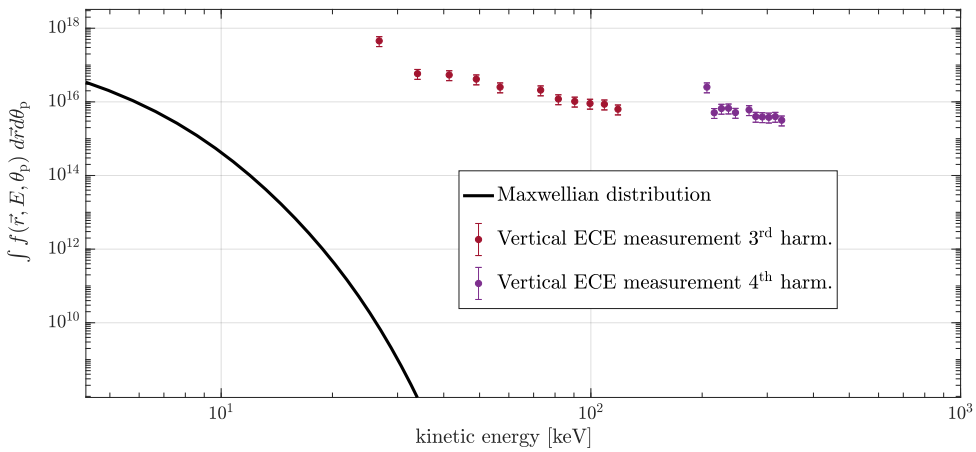

Figure 7.7: Example of reconstruction of the electron distribution in a runaway electron scenario

this case is the one shown in Figure 7.5. We note that this calculation would yield a value close to ~ 0, of the number density in the time period before about 0.5 s when the runaway beam is not formed yet and the bandwidth power is ~ 0. The mean number density of runaway electrons at some energies is reconstructed and shown in Figure 7.7. The densities are compared to those of a Maxwellian distribution. We note that the numbers shown in the figure are the fast electron

density found with Equation 7.15 and multiplied by a plasma volume, to obtain a total number of particle at a given energy. The reconstructed distribution shows a flat tail in both cases of the 3rd harmonic dominating the radiation or the 4th dominating. The flat tail, and the large number of electrons present at that energy, compared to a Maxwellian distribution, consolidates the possibility of using this approach for runaway electron distributions.

7.3 Conclusions

We have described in this chapter a method to reconstruct the energy distribution of electrons. The reconstruction needs independent measurements of the emission at the same energy. We have shown examples using independently measured X- and O-mode intensities. The reconstruction method assumes a weighted pitch angle at each energy, and calculates the density of the electrons needed at that energy, to match the measured intensities. This model of the distribution is known as a delta type distribution from previous studies. The experimental data from an ECCD and a runaway electron experiment have been used for the application of the method. The measured ratios of polarizations are consistent with the expectations. They are lower in the runaway case showing an enhancement in the parallel direction. The ratio of polarizations has not been used in ECCD for the estimation of density of the the non-thermal electrons because of the limitations. However, at some energies, in the ECCD case, the observed jump in the polarization ratio to values above 10 can be due to the perpendicular enhancement of the electrons energy by the ECH. The number density of runaway electrons, computed for the runaway case, shows a flat tail in the distribution whether the emission is dominated by the downshifted, 3rd or 4th harmonic.

8 Conclusions and outlook

The research goals at the beginning of this PhD adventure were

- to complete the design and construction of the Vertical ECE diagnostic on TCV,
- to calibrate and commission the diagnostic,
- and to exploit the diagnostic for measurements of non-thermal electron distributions for Electron Cyclotron Current Drive and runaway electron studies on TCV.

The research described in this thesis has contributed to the global effort toward fusion energy in the fields of both advanced diagnostic development and tokamak plasma physics. We review in this final chapter the main achievements, in the diagnostic development and in the original tokamak plasma physics contribution of the thesis.

8.1 Conclusions on the construction of the diagnostic system

Regarding the diagnostic system, TCV is equipped with a vertically viewing ECE antenna of maximum waist size ~ 3 cm. The designed waist size was validated against measurements achieved in laboratory. The line of sight produced by the antenna terminates, in vacuum, on a highly absorbing beam dump in MACOR. The beam dump, which has been characterized during this thesis, is compatible with the high temperature and high vacuum environment of the tokamak. For the measurements, a set of heterodyne radiometers has been installed, to provide highly resolved measurements of ECE spectra at multiple harmonics and polarizations.

8.2 Summary on the physics achievements of the thesis

The original contributions to tokamak physics, which emerged from this thesis can be summarized in the following points.

- **The optimal conditions for operating the Vertical ECE diagnostic on TCV have been identified.**
  Plasma refraction, which induces the background contamination of the measurements was considered to be a strong limitation for the diagnostic. In this thesis work, it has been discovered that the background radiation in TCV can be avoided straightforwardly by a suitable combination of magnetic field and measured frequency. An appropriate combination of field and frequency can keep the cold resonance location of the second harmonic of a measured frequency out of the plasma. This way of avoiding the background radiation has been very crucial as it relaxes the strong constraint on the plasma electron density imposed by plasma refraction. Moreover, this approach does not require a beam dump in the vessel and can be applied to other tokamaks as well.

- **A novel approach for the calibration of ECE diagnostics has been demonstrated and can be applied, generally, to magnetically confined plasmas for fusion.**
  The calibration of the Vertical ECE diagnostic has been achieved in this thesis relying on emission from the plasma itself. Original was the fact that the calibration did not require optical thick conditions, as in previous works. Calculation of the radiation power in optically thin conditions was achieved for the calibration by means of a synthetic ECE diagnostic. The calculation in optically thin conditions has been validated against the plasma black-body emission.

- **Highly resolved, polarized radiation from non-thermal electrons has been measured on TCV, for the first time, using the Vertical ECE.**
  The measurements were achieved in a variety of scenarios, including electron cyclotron current drive and runaway electron experiments, with a very clear identification of the non-thermal features in the measured signals.

- **The electron energy distribution has been reconstructed.**
  A line averaged energy distribution of electrons has been reconstructed from the measurement of non-thermal radiation. A number density of non-thermal electrons has been assigned to each measured energy, with the assumption of an averaged, weighted, pitch angle at those energy. The reconstructed distributions show parallel and perpendicular enhancement of the energy in electron cyclotron current drive experiments and a clear parallel enhancement in runaway electron experiments. Further, the reconstructed distribution for a selected runaway case, has allowed the observation of a flat tail in the energy distribution, as expected from theory.

The achievements of this thesis are the result of a successful collaboration between the author and other collaborators. The author has carried out the measurement of the dump properties, years after its installation, in order to assess its performance and compatibility with the tokamak environment. The author has achieved the measurement of the antenna beam size in vacuum to validate the designed size. The construction (assembly) of the radiometer $78 - 114$ GHz was undertaken by the author who also set up the hardware for the measurements at multiple

polarizations and multiple harmonics. The SPECE code, used for the thermal synthetic diagnostic was written by the collaborators at CNR-ISTP Milano. The author brought minor modifications to the code and set up the Matlab envelope for its use on TCV. The calibration of the diagnostic was achieved by the author in its conceptualisation, realisation, and validation. Most of the experimental scenarios presented in this work have been designed by the author who has also carried out the measurements. Some other scenarios, included in this thesis, were reproductions or piggybacking of scenarios from TCV collaborators. Finally, the electron distribution analysis from the Vertical ECE data was entirely carried on by the author.

8.3 Outlook

This research work will benefit TCV by complementing the diagnostic suite for non-thermal electrons studies. Vertical ECE measurements in current drive experiments will allow more precise characterization of the dynamics of non-thermal electrons, useful for an even better understanding of radio frequency current drive in tokamaks. For runaway studies, the Vertical ECE diagnostic brings several advantages compared to the existing diagnostics. A reconstruction of the electron distribution of the so-called startup runaway electrons can be achieved with the diagnostic, as it has been shown in this research work. It would be interesting, for future studies on TCV, to complete the Vertical ECE synthetic diagnostic. That can be achieved by simulating the Vertical ECE radiation intensity from arbitrary electron distribution. The new synthetic diagnostic can then be coupled to kinetic codes such as LUKE, for an even clearer interpretation of the Vertical ECE measurements, and for electron distribution reconstructions. Such a step would be greatly welcome, for the purpose of complementing our understanding of the physics of runaway electrons in tokamaks. All of this to guide the fusion community towards a better control of the dynamics of runaway electrons, in order to overcome one of the potential showstoppers on the path to a tokamak fusion reactor.
The final consideration is geared towards the Electron Cyclotron Emission community. Based on the findings of this thesis, we believe that it is valuable to reconsider the Vertical ECE diagnostic, as a non-thermal electron diagnostic. It may also be valuable to use the plasma itself for the calibration of the ECE instruments. As it has been demonstrated in this thesis, ECE diagnostics can now be calibrated in optically thin conditions using the radiation from the plasma. This calibration technique is of particular interest for the machines granting limited access to the vessel. It is a more modern approach, which leverages the decades of theoretical work on ECE to offer a solution to the stability issue in the calibrations.

A Characterization of the components for the radiometer

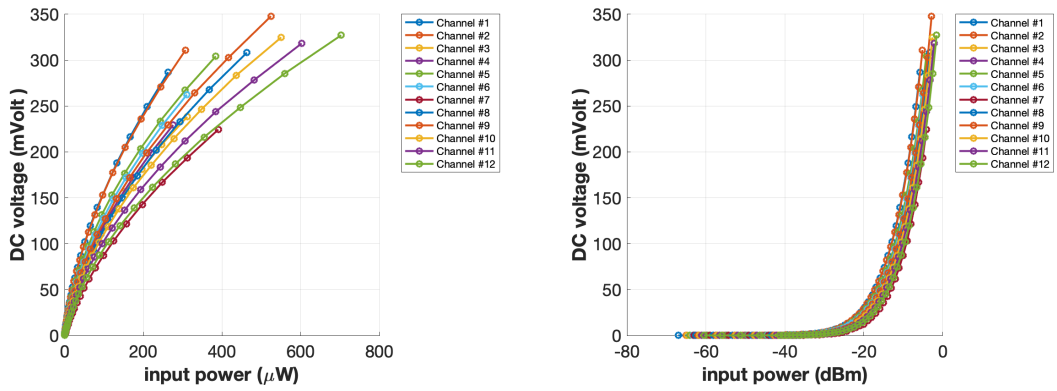

(a) input power in Watts (b) input power in dBm

Figure A.1: Curves of the diodes of the radiometer $78 - 114$ GHz for the channels 1 to 12.

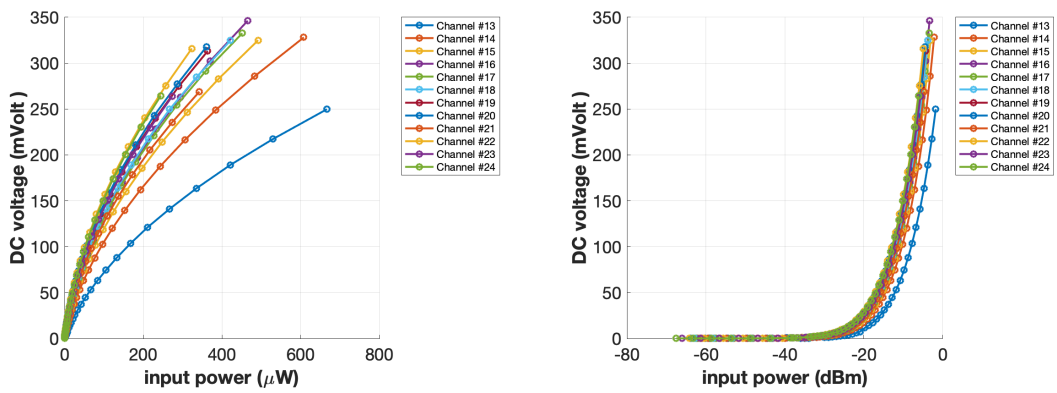

(a) input power in Watts (b) input power in dBm

Figure A.2: Curves of the diodes of the radiometer $78 - 114$ GHz for the channels 13 to 24.

The characterization of the the detector diodes in Figures A.1 and A.2 is useful for the identifica-

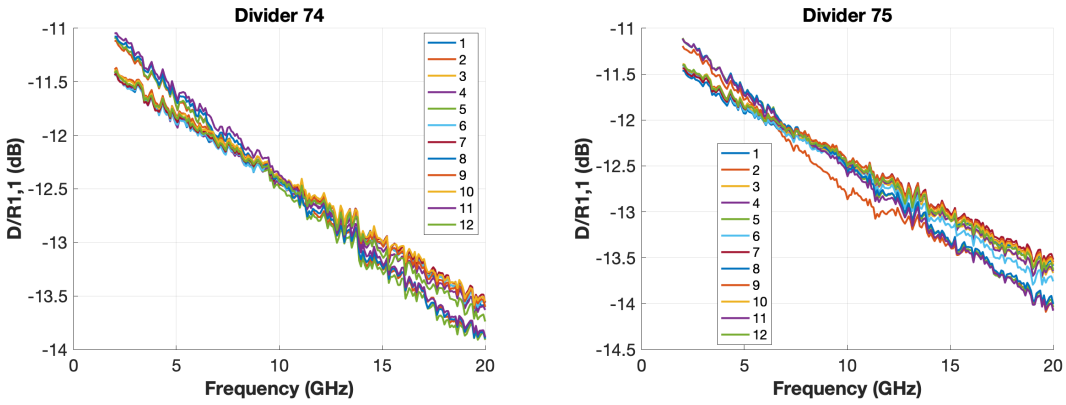

Figure A.3: Power transmission at the output of the 2, 12 ways power dividers.

tion of the linear and the non-linear power regime in the radiometer response. The characterization of the 12 ways power divider in Figure A.3 shows the difference in losses for each IF channel. The divider exhibits almost a 3 dB difference in the output power between the low frequency and the high frequency response. The degradation of the performance near 20 GHz is also seen in the characterization of the IF band pass filters in Figure A.5. That is the consequence of the technological constraints in the construction of microwave components in the IF range of frequencies. The technological constraints limit the IF bandwidth of the radiometer to around 20 GHz. When larger bandwidth are required, the idea is to split the incoming RF power into multiple, parallel, IF stages. The RF power can be split with microwave components or with quasi-optical mirrors. The latter solution can be more appropriate for high magnetic field machines.

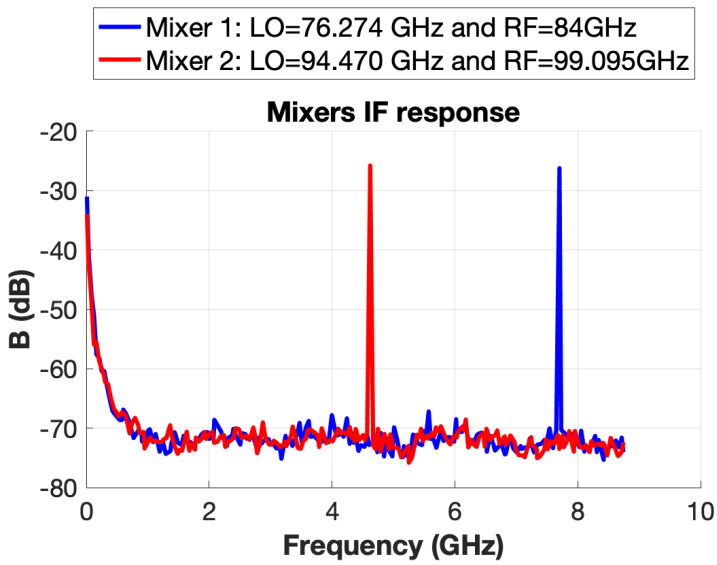

Figure A.4: Spectrum analysis of the mixers response. Each LO is fed with the appropriate voltage while a narrow band RF power feeds the RF input port of the mixers. The IF port of each mixer is connected to the PNA in Spectrum Analyser mode.

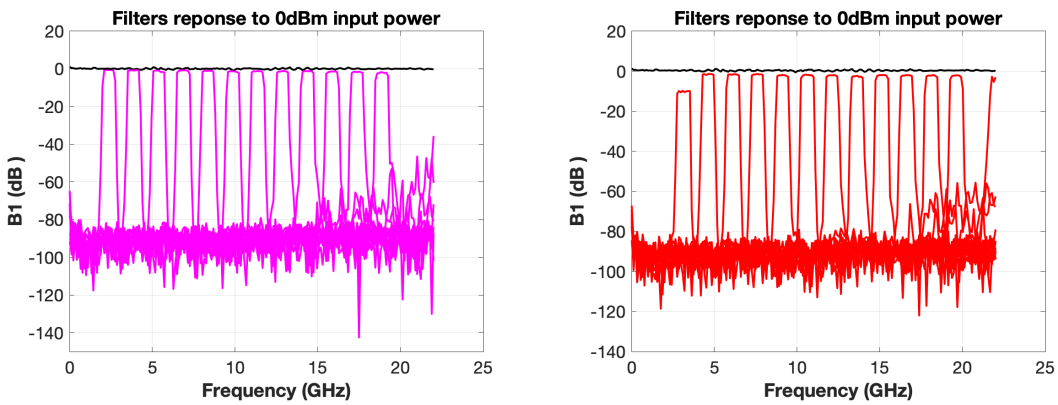

(a) channels 1 to 12 (b) channels 13 to 24

Figure A.5: Characterization of the band pass filters used for the radiometer 78 − 114 GHz.

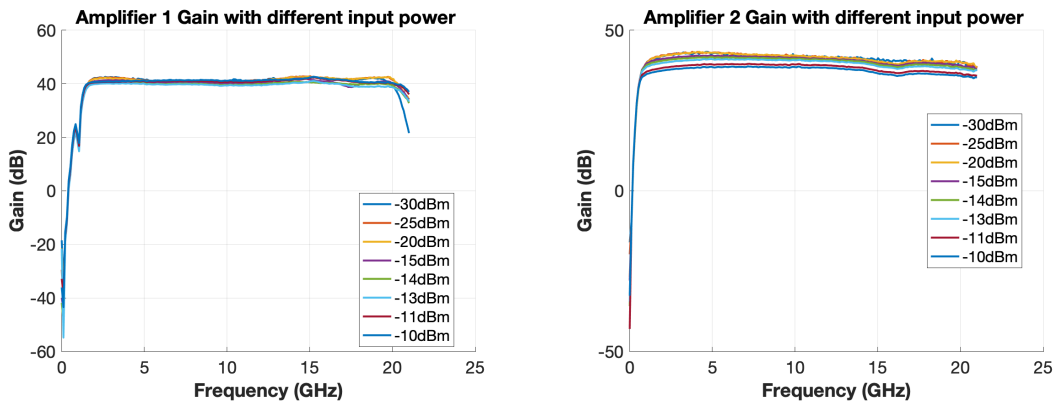

Figure A.6: Characterization of the IF power amplifiers used for the radiometer 78 − 114 GHz.

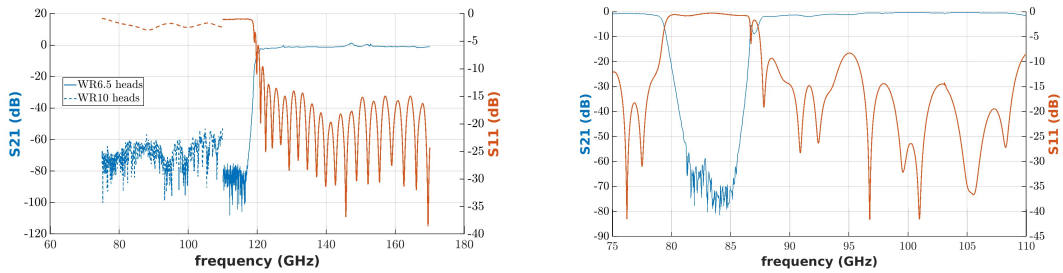

(a) RF stage (b) IF stage

Figure A.7: Characterization of band stop filters and high pass filters, part of the detection system.

B Symbols, acronyms and nomenclature

This chapter describes the symbols, the acronyms, and the nomenclature that has been used throughout the manuscript.

B.1 Nomenclature

The term frequency has been used throughout the thesis in a broad context. The term was used for the angular frequency in radians-per-second as well as for the temporal frequency in units of hertz. The angular frequency was favored in the equations while the temporal frequency was preferred for the numerical applications. The term microwave was used, as it is common, to indicate radiation including millimetres-waves radiation. The term was thus not referred to radiation with wavelength in the micrometer range. The term Radio-frequency generally refers to radiation of frequency between 3 kilohertz and 300 gigahertz. The term has been used in the thesis to refer to the radiation with frequency in the 10s and 100s GHz range, either emitted from the plasma or from a given source.

B.2 Acronyms

Tokamaks

- **TCV**: Tokamak à Configuration Variable, CH
- **JET**: Joint European Torus, EU
- **ITER**: International Thermonuclear Experimental Reactor aka *the way*
- **PLT**: Princeton Large Torus, US
- **ALCATOR**: Alto Campo Toro, US
- **TORE SUPRA**: Ancestor of the WEST tokamak, FR

- **DIII-D**: Doublet III tokamak upgrade, US

Tokamak systems

- **ECE**: Electron Cyclotron Emission
- **X- / O- mode**: eXtraordinary / Ordinary polarization of the ECE
- **X2 / X3**: Second / third harmonic of the X-mode emission.
- **EC(R)H**: Electron Cyclotron (Resonance) Heating
- **ECCD**: Electron Cyclotron Current Drive
- **LHCD**: Lower Hybrid Current Drive
- **MGI**: Massive Gas Injection
- **NBH**: Neutral Beam Heating
- **NBI**: Neutral Beam Injection
- **NTM**: Neoclassical Tearing Modes
- **HXRS**: Hard X-ray bremsstrahlung emission
- **PMTX**: Photo Multiplier Tube for Hard-X rays
- **MANTIS**: Multispectral Advanced Narrowband Tokamak Imaging System
- **DSS**: Divertor Spectroscopy System
- **IR**: Infrared Cameras
- **VUV / UV / NIR**: Vacuum ultraviolet / Ultraviolet / Near infrared Camera
- **HFS / LFS**: High Field Side / Low Field Side of the tokamak
- **LCFS**: Last Closed Flux Surface
- **MHD**: Magneto-Hydro-Dynamics

Simulation codes

- **SPECE**: Ray tracing code used for synthetic ECE
- **LUKE**: Fully relativistic 3D bounce-averaged Fokker-Planck solver, used for electron distribution modelling
- **SOFT**: Synchrotron-detecting Orbit Following Toolkit, used to simulate bremsstrahlung and cyclotron radiation.

Hardware

- **RF**: Radio Frequency wave
- **IF**: Intermediate Frequency wave
- **LO**: Local Oscillator
- **PNA**: Portable Network Analyzer, used as vector analyzer for the characterization of hardware components.
- **DUT**: Device Under Test
- **BW**: Bandwidth

B.3 Mathematical Symbols

- n_{e}: plasma electrons density in units of particles-per-cubic-metre
- B: magnetic field strength in tesla
- I_{p}: plasma current in amperes
- R: radial direction in the tokamak in metres
- Z: vertical direction in the tokamak in metres
- R_0: major radius in metres
- a: minor radius in metres
- B_0: magnetic field strength at the major radius R_0 in tesla
- $\theta_{\mathrm{L}}, \theta_{\mathrm{l}}$: poloidal angle of the ECH launcher in degrees
- $\phi_{\mathrm{L}}, \phi_{\mathrm{l}}$: toroidal angle of the launcher in degrees
- E_{kc}: critical beam energy in electron-volts
- m_{ion}: ion mass in kilograms
- m_{e}: electron mass in kilograms
- m_{e0}: rest electron mass in kilograms
- T_{e}: electron temperature in electron-volts
- E_{D}: Dreicer electric field in units of volts-per-metres
- E_{C}: critical electric field, in volts-per-metres

- e: electron charge in coulomb
- c: speed of light in metres-per-second
- ϵ_0: vacuum permittivity in farads-per-second
- $\log \Lambda$: coulomb logarithm, dimensionless
- T_{rad}: radiation temperature in electron-volts
- τ: optical depth, dimensionless
- ψ: poloidal magnetic flux in units of tesla-per-square-metres
- $\overrightarrow{u}$: fluid velocity of an ensemble of particles, in metres-per-second
- F: electron distribution function, in particles-per-cubic-metre
- γ: relativistic factor, dimensionless
- $\overrightarrow{v_{\mathrm{e}}}$: velocity of an electron in metres-per-second
- $\beta_{\perp}$: perpendicular component of the normalized particle velocity, dimensionless
- $\beta_{\parallel}$: parallel component of the normalized particle velocity, dimensionless
- ω_{ece}: angular frequency of the fundamental electron cyclotron emission in radians-per-second
- ω_{ecr}: realistically downshifted electron cyclotron angular frequency, in units of radians-per-second
- P: power in watts
- Ω_{S}: solid angle in steradian
- ω: angular frequency in units of radians-per-second
- Θ: angle between the magnetic field vector and the direction of observation of the ECE emission in degrees
- n: harmonic number, dimensionless
- η_{X} / η_{O} : single particle emissivity of the X-mode / O-mode in units of watts-per-hertz
- ϕ_{p}: pitch angle, angle between the particle velocity and the magnetic field vector, in degrees
- $\overrightarrow{p}$: vector of the normalized momentum, dimensionless
- j: emission coefficient of an ensemble of particles in watts-per-hertz-per-cubic-metres

- j_{X} / j_{O}: emission coefficient in X-mode / O-mode in units of watts-per-hertz-per-cubic-metres
- y: cosine of the pitch angle, dimensionless
- n_{fast}: fast electron density in unit of particles-per-cubic-metre
- ω_{pe}: electron plasma frequency in radians-per-second
- N_r: ray refractive index, dimensionless
- $N_{\mathrm{X}}/N_{\mathrm{O}}$: X/O mode refractive index, dimensionless
- Ω_{ece}: fundamental electron cyclotron frequency in hertz
- $\Omega_{\mathbf{q}\mathrm{ece}}$: frequency of the $\mathbf{q}^{\mathrm{th}}$ harmonic of the cyclotron frequency in hertz
- S_{21}, S_{11}: parameters of the scattering matrix, in decibels
- λ: wavelength in metres
- Δf: bandwidth in hertz
- P_{BW}: bandwidth power in watts
- α: absorption coefficient in units of per-metre
- k: wave number in cycle-per-metre
- I_ω: spectral intensity at a specific frequency, in watts-per-hertz-per-steradian-per-square-metre
- s: coordinate of the electromagnetic wave trajectory, in metres
- S_ω: source function in watts-per-hertz-per-square-metres
- r, p: reflection, depolarization coefficients of the vessel tiles, dimensionless parameters
- V: measured voltage in volts
- F_{cal}: calibration factor in watts-per-volts
- E: particle energy in kilo-electron-volts
- f: radiation frequency in hertz
- T: particle temperature in kilo-electron-volts
- P_{BB}: black-body radiation power in watts
- ϕ: toroidal direction in the tokamak
- $\|$: direction parallel-to-magnetic-field direction
- $\perp$: direction perpendicular-to-magnetic-field direction

List of Figures

List of Tables

Bibliography

[1] N. J. PEACOCK et al. "Measurement of the Electron Temperature by Thomson Scattering in Tokamak T3". In: *Nature* 224.5218 (Nov. 1969), pp. 488–490. DOI: 10.1038/224488a0 (cit. on p. 1).

[2] John Wesson. *Tokamaks*. OXFORD UNIV PR, Dec. 2011. 800 pp. ISBN: 0199592233. URL: https://www.ebook.de/de/product/14641403/john_wesson_tokamaks.html (cit. on p. 1).

[3] Kaname Ikeda. "ITER on the road to fusion energy". In: *Nuclear Fusion* 50.1 (Dec. 2009), p. 014002. DOI: 10.1088/0029-5515/50/1/014002 (cit. on p. 1).

[4] JET Team (prepared by M.L. Watkins). "Physics of high performance JET plasmas in DT". In: *Nuclear Fusion* 39.9Y (Sept. 1999), p. 1227. DOI: 10.1088/0029-5515/39/9Y/302. URL: https://dx.doi.org/10.1088/0029-5515/39/9Y/302 (cit. on p. 1).

[5] A. Costley. "ECE: THE STORY SO FAR". In: *Electron Cyclotron Emission and Electron Cyclotron Resonance Heating (EC-15)*. WORLD SCIENTIFIC, Apr. 2009. DOI: 10.1142/9789812814647_0001 (cit. on pp. 2, 81).

[6] J.R. Martin-Solis, A. Loarte, and M. Lehnen. "Formation and termination of runaway beams in ITER disruptions". In: *Nuclear Fusion* 57.6 (Apr. 2017), p. 066025. DOI: 10.1088/1741-4326/aa6939 (cit. on p. 2).

[7] T.C Hender et al. "Chapter 3: MHD stability, operational limits and disruptions". In: *Nuclear Fusion* 47.6 (June 2007), S128–S202. DOI: 10.1088/0029-5515/47/6/s03 (cit. on p. 2).

[8] Timothy C. Luce. "Superthermal electron distribution measurements with electron cyclotron emission". PhD thesis. Princeton University, 1987 (cit. on pp. 3, 16, 22, 27).

[9] P. W. Zheng et al. "Comparative study of Fisch-Boozer and Ohkawa current drive mechanisms for electron cyclotron waves". In: *Physics of Plasmas* 25.7 (July 2018), p. 072501. DOI: 10.1063/1.5027609 (cit. on p. 3).

[10] Pingwei Zheng et al. "On current drive by Ohkawa mechanism of electron cyclotron wave in large inverse aspect ratio tokamaks". In: *Nuclear Fusion* 58.3 (Jan. 2018), p. 036010. DOI: 10.1088/1741-4326/aaa338 (cit. on p. 3).

[11] Nathaniel J. Fisch. "Confining a Tokamak Plasma with rf-Driven Currents". In: *Physical Review Letters* 41.13 (Sept. 1978), pp. 873–876. DOI: 10.1103/physrevlett.41.873 (cit. on p. 3).

[12] H. Weisen et al. "Overview of TCV results". In: *Nuclear Fusion* 41.10 (Oct. 2001), pp. 1459–1472. DOI: 10.1088/0029-5515/41/10/313 (cit. on p. 5).

[13] S. Coda et al. "Physics research on the TCV tokamak facility: from conventional to alternative scenarios and beyond". In: *Nuclear Fusion* 59.11 (Aug. 2019), p. 112023. DOI: 10.1088/1741-4326/ab25cb (cit. on p. 5).

[14] H. Reimerdes et al. "Overview of the TCV tokamak experimental programme". In: *Nuclear Fusion* 62.4 (Mar. 2022), p. 042018. DOI: 10.1088/1741-4326/ac369b (cit. on p. 5).

[15] T.P Goodman et al. "An overview of results from the TCV tokamak". In: *Nuclear Fusion* 43.12 (Dec. 2003), pp. 1619–1631. DOI: 10.1088/0029-5515/43/12/008 (cit. on p. 5).

[16] J. M. Moret. "Progress in the Understanding and the Performance of Electron Cyclotron-Heating and Plasma Shaping on TCV". In: *20th IAEA FEC, Vilamoura, Portugal*. 2004. URL: http://www-naweb.iaea.org/napc/physics/fec/fec2004/datasets/OV_4-5.html (cit. on p. 5).

[17] A. Fasoli and. "Overview of TCV results". In: *Nuclear Fusion* 48.3 (Jan. 2008), p. 034001. DOI: 10.1088/0029-5515/48/3/034001 (cit. on p. 5).

[18] A. Fasoli. "Overview of physics research on the TCV tokamak". In: *Nuclear Fusion* 49.10 (Sept. 2009), p. 104005. DOI: 10.1088/0029-5515/49/10/104005 (cit. on p. 5).

[19] S. Coda. "Progress and scientific results in the TCV tokamak". In: *Nuclear Fusion* 51.9 (Aug. 2011), p. 094017. DOI: 10.1088/0029-5515/51/9/094017 (cit. on p. 5).

[20] S. Coda for the TCV Team. "Overview of recent and current research on the TCV tokamak". In: *Nuclear Fusion* 53.10 (Sept. 2013), p. 104011. DOI: 10.1088/0029-5515/53/10/104011 (cit. on p. 5).

[21] S. Coda and. "The science program of the TCV tokamak: exploring fusion reactor and power plant concepts". In: *Nuclear Fusion* 55.10 (Mar. 2015), p. 104004. DOI: 10.1088/0029-5515/55/10/104004 (cit. on p. 5).

[22] S. Coda et al. "Overview of the TCV tokamak program: scientific progress and facility upgrades". In: *Nuclear Fusion* 57.10 (June 2017), p. 102011. DOI: 10.1088/1741-4326/aa6412 (cit. on p. 5).

[23] F Hofmann et al. "Stability and energy confinement of highly elongated plasmas in TCV". In: *Plasma Physics and Controlled Fusion* 43.12A (Nov. 2001), A161–A173. DOI: 10.1088/0741-3335/43/12a/312 (cit. on p. 6).

[24] G. Merlo et al. "Turbulent transport in TCV plasmas with positive and negative triangularity". In: *Physics of Plasmas* 26.10 (Oct. 2019), p. 102302. DOI: 10.1063/1.5115390 (cit. on p. 6).

[25] G Merlo et al. "Nonlocal effects in negative triangularity TCV plasmas". In: *Plasma Physics and Controlled Fusion* 63.4 (Mar. 2021), p. 044001. DOI: 10.1088/1361-6587/abe39d (cit. on p. 6).

[26] J. Decker et al. "Full conversion from ohmic to runaway electron driven current via massive gas injection in the TCV tokamak". In: *Nuclear Fusion* 62.7 (May 2022), p. 076038. DOI: 10.1088/1741-4326/ac544e (cit. on pp. 6, 9).

[27] C. Theiler et al. "Results from recent detachment experiments in alternative divertor configurations on TCV". In: *Nuclear Fusion* 57.7 (Mar. 2017), p. 072008. DOI: 10.1088/1741-4326/aa5fb7 (cit. on p. 6).

[28] Jonas Degrave et al. "Magnetic control of tokamak plasmas through deep reinforcement learning". In: *Nature* 602.7897 (Feb. 2022), pp. 414–419. DOI: 10.1038/s41586-021-04301-9 (cit. on p. 6).

[29] J.I. Paley et al. "Real time control of plasmas and ECRH systems on TCV". In: *Nuclear Fusion* 49.8 (July 2009), p. 085017. DOI: 10.1088/0029-5515/49/8/085017 (cit. on p. 6).

[30] R. Prater. "Heating and current drive by electron cyclotron waves". In: *Physics of Plasmas* 11.5 (May 2004), pp. 2349–2376. DOI: 10.1063/1.1690762 (cit. on p. 6).

[31] Katsumichi HOSHINO. "Electron Cyclotron Heating (ECH) of Tokamak Plasmas". In: *Journal of Nuclear Science and Technology* 27.5 (May 1990), pp. 391–405. DOI: 10.1080/18811248.1990.9731201 (cit. on p. 6).

[32] M. Vallar et al. "Status, scientific results and technical improvements of the NBH on TCV tokamak". In: *Fusion Engineering and Design* 146 (Sept. 2019), pp. 773–777. DOI: 10.1016/j.fusengdes.2019.01.077 (cit. on p. 8).

[33] Alexander N. Karpushov et al. "Upgrade of the neutral beam heating system on the TCV tokamak – second high energy neutral beam". In: *Fusion Engineering and Design* 187 (Feb. 2023), p. 113384. DOI: 10.1016/j.fusengdes.2022.113384 (cit. on p. 8).

[34] Joaquin Galdon-Quiroga. "Velocity-space resolved measurements of fast-ion losses due to magnetohydrodynamic instabiltities in the ASDEX Upgrade tokamak". PhD thesis. University of Seville, 2018 (cit. on p. 8).

[35] Mathias Hoppe. "Runaway-electron model development and validation in tokamaks". PhD thesis. Chalmers University of Technology, 2021 (cit. on p. 8).

[36] S. Gnesin et al. "Suprathermal electron studies in the TCV tokamak: Design of a tomographic hard-x-ray spectrometer". In: *Review of Scientific Instruments* 79.10 (Oct. 2008), 10F504. DOI: 10.1063/1.2957843 (cit. on p. 9).

[37] A. Perek et al. "MANTIS: A real-time quantitative multispectral imaging system for fusion plasmas". In: *Review of Scientific Instruments* 90.12 (Dec. 2019), p. 123514. DOI: 10.1063/1.5115569 (cit. on p. 9).

[38] T.A. Wijkamp et al. "Tomographic reconstruction of the runaway distribution function in TCV using multispectral synchrotron images". In: *Nuclear Fusion* 61.4 (Mar. 2021), p. 046044. DOI: 10.1088/1741-4326/abe8af (cit. on p. 9).

[39] M. Hoppe et al. "Runaway electron synchrotron radiation in a vertically translated plasma". In: *Nuclear Fusion* 60.9 (Aug. 2020), p. 094002. DOI: 10.1088/1741-4326/aba371. URL: https://dx.doi.org/10.1088/1741-4326/aba371 (cit. on p. 9).

[40] K. Verhaegh et al. "Spectroscopic investigations of divertor detachment in TCV". In: *Nuclear Materials and Energy* 12 (Aug. 2017), pp. 1112–1117. DOI: 10.1016/j.nme.2017.01.004 (cit. on p. 10).

[41] V. S. Udintsev et al. "Recent Electron Cyclotron Emission Results on TCV". In: *Fusion Science and Technology* 52.2 (Aug. 2007), pp. 161–168. DOI: 10.13182/fst07-a1495 (cit. on p. 10).

[42] P Blanchard et al. "High field side measurements of non-thermal electron cyclotron emission on TCV plasmas with ECH and ECCD". In: *Plasma Physics and Controlled Fusion* 44.10 (Sept. 2002), pp. 2231–2249. DOI: 10.1088/0741-3335/44/10/310 (cit. on pp. 10, 82).

[43] D. Farina et al. "SPECE: a code for Electron Cyclotron Emission in tokamaks". In: *AIP Conference Proceedings*. AIP, 2008. DOI: 10.1063/1.2905053 (cit. on pp. 11, 63).

[44] Daniela Farina. "A Quasi-Optical Beam-Tracing Code for Electron Cyclotron Absorption and Current Drive: GRAY". In: *Fusion Science and Technology* 52.2 (Aug. 2007), pp. 154–160. DOI: 10.13182/fst07-a1494 (cit. on p. 11).

[45] Lorenzo Figini. "Electron cyclotron in tokamaks: development of a new modeling tool for data validation, analysis and predictions". PhD thesis. Università degli Studi di Milano, 2008 (cit. on p. 11).

[46] A. E. Costley et al. "Electron Cyclotron Emission from a Tokamak Plasma: Experiment and Theory". In: *Physical Review Letters* 33.13 (Sept. 1974), pp. 758–761. DOI: 10.1103/physrevlett.33.758 (cit. on pp. 11, 71, 81).

[47] M. Brusati. "A proposal for measuring the local ion distribution function and the neutral-density profile in toroidal plasmas". In: *Nuclear Fusion* 17.1 (Feb. 1977), pp. 144–147. DOI: 10.1088/0029-5515/17/1/016 (cit. on p. 12).

[48] J. Decker and Y. Peysson. *DKE: a fast numerical solver for the 3-D relativistic bounce-averaged electron Drift Kinetic Equation*. Report EUR-CEA-FC-1736. Association EURATOM-CEA, 2004 (cit. on p. 12).

[49] M. Hoppe et al. "SOFT: a synthetic synchrotron diagnostic for runaway electrons". In: *Nuclear Fusion* 58.2 (Jan. 2018), p. 026032. DOI: 10.1088/1741-4326/aa9abb (cit. on p. 12).

[50] Kosuke Kato. "Diagnosis of Mildly Relativistic Electron Velocity Distributions by Electron Cyclotron Emission in the Alcator C Tokamak". PhD thesis. Massachusetts Institute of Technology, 1986 (cit. on pp. 16, 18, 23, 27).

[51] G. Giruzzi et al. "Observation of the m = 1 mode by microwave transmission measurements in TORE SUPRA". In: *Nuclear Fusion* 31.11 (Nov. 1991), pp. 2158–2162. DOI: 10.1088/0029-5515/31/11/013 (cit. on p. 16).

[52] G. Giruzzi et al. "Measurement of the Time Constants of Fast Electron Distributions in the Tore Supra Tokamak". In: *Physical Review Letters* 74.4 (Jan. 1995), pp. 550–553. DOI: 10.1103/physrevlett.74.550 (cit. on p. 16).

[53] D. R. Roberts et al. "Vertical viewing of electron-cyclotron emissions for diagnosing fast-electron dynamics in TEXT-U". In: *Review of Scientific Instruments* 66.1 (Jan. 1995), pp. 427–429. DOI: 10.1063/1.1146368 (cit. on p. 16).

[54] Scott J. Janz. "Analysis of Nonthermal Electron Cyclotron Emission During Electron Cyclotron CurrentDrive Experiments on the DIII-D Tokamak". PhD thesis. 1992 (cit. on pp. 16, 27).

[55] H. J. Hartfuss and T. Geist. "Passive Diagnostics, chap 4". In: *Fusion Plasma Diagnostics with mm-Waves*. John Wiley and Sons, Ltd, 2013. Chap. 4, pp. 117–150. ISBN: 9783527676279. DOI: https://doi.org/10.1002/9783527676279.ch4. eprint: https://onlinelibrary.wiley.com/doi/pdf/10.1002/9783527676279.ch4. URL: https://onlinelibrary.wiley.com/doi/abs/10.1002/9783527676279.ch4 (cit. on pp. 16, 17).

[56] I. H. Hutchinson. *Principles of Plasma Diagnostics*. Cambridge University Press, July 2002. DOI: 10.1017/cbo9780511613630 (cit. on pp. 16, 17).

[57] B. A. Trubnikov. "Radiation of plasma in magnetic field". In: *Dokl. Akad. Nauk SSSR* 118.5 (May 1958), pp. 913–916 (cit. on p. 17).

[58] G. Bekefi. *Radiation Processes in Plasmas*. John Wiley and Sons, New York, 1966 (cit. on pp. 24, 83, 84).

[59] Thomas Howard Stix and F. R. Scott. "The Theory of Plasma Waves". In: *American Journal of Physics* 31.10 (Oct. 1963), pp. 816–816. DOI: 10.1119/1.1969127 (cit. on p. 24).

[60] A. Tema Biwole et al. "Performance of a high vacuum, high temperature compatible millimeter-range viewing dump for the vertical ECE experiment on TCV". In: *Fusion Engineering and Design* 162 (Jan. 2021), p. 112079. DOI: 10.1016/j.fusengdes.2020.112079 (cit. on p. 27).

[61] Patrick Blanchard. "Etudes du rayonnement suprathermnique emis lors du chauffage cyclotronique electronique du plasma du tokamak TCV". PhD thesis. ECOLE POLYTECHNIQUE FEDERALE DE LAUSANNE, 2002 (cit. on pp. 28, 39).

[62] Igor Klimanov. "Reconstruction of the electron distribution function during ecrh/eccd and magnetic reconnection eventsin a tokamak plasma". PhD thesis. ÉCOLE POLYTECHNIQUE FÉDÉRALE DE LAUSANNE, 2005 (cit. on p. 28).

[63] A. Tema Biwole. *Characterization of components for the HFS ECE radiometer on TCV*. Tech. rep. Swiss Plasma Center, Oct. 2018 (cit. on p. 30).

[64] H. J. Hartfuss and T. Geist. "Radiation Generation and Detection, chap 6". In: *Fusion Plasma Diagnostics with mm-Waves*. John Wiley and Sons, Ltd, 2013. Chap. 6, pp. 201–274. ISBN: 9783527676279. DOI: https://doi.org/10.1002/9783527676279.ch6. eprint: https://onlinelibrary.wiley.com/doi/pdf/10.1002/9783527676279.ch6. URL: https://onlinelibrary.wiley.com/doi/abs/10.1002/9783527676279.ch6 (cit. on p. 37).

[65] F. Felici. *ECPOL: equations and MATLAB tools for EC wave reflection and polarization calculations*. Tech. rep. Centre des Recherches en Physique des Plasmas, Ecole Polytechnique Fédérale de Lausanne, Feb. 2012 (cit. on p. 48).

[66] Jean-Marie Haussonne. *Céramiques et verres: principes et techniques d'élaboration*. Vol. 16. PPUR presses polytechniques, 2005 (cit. on p. 49).

[67] M.N. Afsar and K.J. Button. "Precise Millimeter-Wave Measurements of Complex Refractive Index, Complex Dielectric Permittivity and Loss Tangent of GaAs, Si, SiO/sub 2/, A1/sub 2/O/sub 3/, BeO, Macor, and Glass". In: *IEEE Transactions on Microwave Theory and Techniques* 31.2 (Feb. 1983), pp. 217–223. DOI: 10.1109/tmtt.1983.1131460 (cit. on p. 49).

[68] SAS Corning. *Macor® machinable glass ceramic for industrial applications*. 2012 (cit. on p. 49).

[69] JP Coad et al. "Deposition results from rotating collector diagnostics in JET". In: *Physica Scripta* 2009.T138 (2009), p. 014023 (cit. on p. 51).

[70] O D'Arcangelo et al. *Performance of a macor beam dump for vertical ece diagnostic by EPFL lausanne in the 75-110 GHz*. Tech. rep. Istituto di fisica del plasna-CNR, 2007 (cit. on p. 54).

[71] Paul F. Goldsmith. *Quasioptical Systems*. IEEE, 1998, p. 83. DOI: 10.1109/9780470546291 (cit. on p. 55).

[72] P.F. Goldsmith. "Quasi-optical techniques". In: *Proceedings of the IEEE* 80.11 (1992), pp. 1729–1747. DOI: 10.1109/5.175252 (cit. on p. 55).

[73] I. Rolfes and B. Schiek. "Calibration methods for microwave free space measurements". In: *Advances in Radio Science - Kleinheubacher Berichte* 2 (Jan. 2004). DOI: 10.5194/ars-2-19-2004 (cit. on p. 59).

[74] A. Murk, A. Duric, and F. Patt. "Characterization of ALMA Calibration Targets". In: *19th International Symposium on Space Terahertz Technology, Groningen (NL)*. Apr. 2008 (cit. on p. 59).

[75] A. Murk and A. Duric. *ALMA Calibration Device Prototype Calibration Load Test Report FEND-40.06.04.00-005-A-REP*. Tech. rep. June 2007. URL: https://safe.nrao.edu/wiki/pub/ALMA/CalAmp/FEND-40.06.04.00-005-A-REP.pdf (cit. on p. 59).

[76] M. Bornatici et al. "Electron cyclotron emission and absorption in fusion plasmas". In: *Nuclear Fusion* 23.9 (Sept. 1983), pp. 1153–1257. DOI: 10.1088/0029-5515/23/9/005 (cit. on pp. 62, 86).

[77] H. J. Hartfuss and T. Geist. "Millimeter-Waves in Plasmas, chap 2". In: *Fusion Plasma Diagnostics with mm-Waves*. John Wiley and Sons, Ltd, 2013. Chap. 2, pp. 19–63. ISBN: 9783527676279. DOI: https://doi.org/10.1002/9783527676279.ch2. eprint: https://onlinelibrary.wiley.com/doi/pdf/10.1002/9783527676279.ch2. URL: https://onlinelibrary.wiley.com/doi/abs/10.1002/9783527676279.ch2 (cit. on p. 62).

[78] L. Friedland and I. B. Bernstein. "Comparison of geometric and wave optics in an absorbing spherical plasma". In: *Physical Review A* 21.2 (Feb. 1980), pp. 666–671. DOI: 10.1103/physreva.21.666 (cit. on p. 64).

[79] Oulfa Chellaï. "Millimeter-Wave Beam Scattering by Edge Turbulence in Magnetically-Confined Plasmas". PhD thesis. ECOLE POLYTECHNIQUE FEDERALE DE LAUSANNE, 2019 (cit. on p. 66).

[80] Lorenzo Figini. "Electron cyclotron emission in Tokamaks: Development of a new modelling tool for data validation, analysis and predictions". PhD thesis. Università degli studi di Milano, 2009 (cit. on p. 71).

[81] S. Schmuck et al. "Electron cyclotron emission measurements on JET: Michelson interferometer, new absolute calibration, and determination of electron temperature". In: *Review of Scientific Instruments* 83.12 (Dec. 2012), p. 125101. DOI: 10.1063/1.4768246 (cit. on p. 81).

[82] I. Klimanov et al. "Electron cyclotron emission spectrometry on the Tokamak à Configuration Variable". In: *Review of Scientific Instruments* 76.9 (Sept. 2005), p. 093504. DOI: 10.1063/1.2042667 (cit. on p. 82).

[83] M. Fontana et al. "The effect of triangularity on fluctuations in a tokamak plasma". In: *Nuclear Fusion* 58.2 (Dec. 2017), p. 024002. DOI: 10.1088/1741-4326/aa98f4. URL: https://doi.org/10.1088/1741-4326/aa98f4 (cit. on p. 82).

[84] M Bornatici. "Theory of electron cyclotron absorption of magnetized plasmas". In: *Plasma Physics* 24.6 (June 1982), pp. 629–638. DOI: 10.1088/0032-1028/24/6/005 (cit. on pp. 86, 93).

[85] H. Bindslev and D.V. Bartlett. *A Technique for Improving the Relative Accuracy of Jet ECE Temperature Profiles*. Tech. rep. JET, 1988 (cit. on p. 87).

[86] Y. R. Lin-Liu, V. S. Chan, and R. Prater. "Electron cyclotron current drive efficiency in general tokamak geometry". In: *Physics of Plasmas* 10.10 (Oct. 2003), pp. 4064–4071. DOI: 10.1063/1.1610472 (cit. on p. 122).

[87] Emanuele Poli et al. "Fast evaluation of the current drive efficiency by electron cyclotron waves for reactor studies". In: *EPJ Web of Conferences* 203 (2019). Ed. by E. Poli, H. Laqua, and J. Oosterbeek, p. 01008. DOI: 10.1051/epjconf/201920301008 (cit. on p. 124).

[88] T. C. Luce, P. C. Efthimion, and N. J. Fisch. "Superthermal electron distribution measurements from polarized electron cyclotron emission (invited)". In: *Review of Scientific Instruments* 59.8 (Aug. 1988), pp. 1593–1598. DOI: 10.1063/1.1140158 (cit. on p. 134).

Acknowledgements

The scientific achievements of this PhD thesis are the result of 4 years of research at the Swiss Plasma Center, but also, and most importantly, they are the culmination of a much longer human adventure. My adventure towards this accomplishment has in fact started many years ago, in Bafoussam, my hometown. As a child in Bafoussam, I dreamt to be able to contribute to a human endeavor which will help mankind. Holding onto my childhood dream was itself a challenge, considering our living conditions. That is why I thank my family, above all my mother and my brothers, who did not stop me from dreaming, but instead, closed their eyes to dream with me.

My adventure, thanks to the Italian government, took a giant leap when I was selected to study in Torino, at the Politecnico. The excellent teachers, in the energy department of the Politecnico, transmitted to me their passion for nuclear energy, particularly for fusion energy. The training in Torino consolidated my willingness to use science to solve some of the problems that our world is facing. I would like to thank Italy and my teachers in Italy, for the great education that I have received. Education which has also led to a wonderful research opportunity overseas at General Atomics, in San Diego. There, I definitely embarked, with great pride, into the global efforts for fusion energy. I feel privileged to have worked with the great scientists and great fellows at General Atomics. My sincere gratitude is geared towards the United States Department of Energy for the sponsorship, which allowed me, on my way, to also achieve my American dream.

It is in that spirit that I tried, with all my heart and brain, to join the Swiss Plasma Center in 2018. The reception of my acceptance e-mail was a great moment in my life. I very well remember when I used to come to the lab in Lausanne, well before the start date of my appointment, in order to feel the awesome work atmosphere. It is in that atmosphere that I started my PhD, feeling like a duck to water. I quickly developed friendship with my office mates, with my colleagues from the services. I was blessed to also benefit from the wisdom of my extremely competent advisors and staff colleagues. However, since the beginning, I always felt an extra pressure, while remembering all my way to EPFL and trying not to fail, so close to my objective. It did not help to bring the pressure down when, after a month of promoting science in my home country, I was cited as an example by the President of the Republic in front of 28 million Cameroonians.

The pressure on my shoulders was then at the highest. My goal being that of keeping up the good work and realize my dream, to continue to inspire my fellow countrymen. The situation with the thesis was however not the easiest due to the complicated topics, the tight deadlines, the frustrations when the results were slow in coming, and the tiredness which had also come into play. To overcome the difficult time, I could draw strength from the smile of my little child who was born right at the beginning of my last year. I could also count on the unconditional and priceless support from my wife when I was stressed. At the lab, I was touched, deeply, by the prompt reaction of my office mates and thesis advisors, my friends, who understood my difficulties and provided me with invaluable help. Without their help, I would not have been able to write this PhD thesis.

It was a childhood dream to hold a PhD in physics and to work to change the world. It was definitely beyond my dreams that I would have been able to write my thesis at the Swiss Plasma Center of EPFL. The Swiss Plasma Center, from my experience, is the best place in the world for work. That is due, not only to the very nearby lake and mountains, but foremost to its exceptionally nice people to whom I will always be grateful for having had me among them.

My last thought is for my family, to whom I dedicate this PhD thesis. To my wife, my little one, my mother and my brothers, I would like to say: " Perhaps you have felt sometimes left out when I was focused on my scientific objectives. Perhaps you have thought sometimes that you were insignificant, compared to size of the Sun which fascinates me, compared to the billions of people whom I hope our research will help. I would like to say that you are what matters the most in my life, and I hope above all, that I have made you proud. "

Lausanne, le 31 Décembre 2022

ATB

Dear colleagues, dear friends,
I very much appreciate the time we have shared together. I did not manage to insert all your names previously, here they are. Many thanks for your contribution to my thesis ! If you do not find your name, please try again.
I have found the names of my advisors so that they waste no more time on my thesis.

```
P A T R I C K C P I E R R E R O X A N E K T F G K
Z B N Y J E A N - M A R C O W N J W O Z H K U G G
I E C C E N K D A S T E F A N O E R S I M O N E B
I N E H K T W J E A N P G T T P A M B R O G I O K
V J F R A N C E S C O B F R E D N A O L I V I E R
O A F I L I P P O E D I T H F G - P A O L A K V Y
C M S S V Q N C R T S V O U U V P J B I A U Z S S
J I D T B D U I T K Q D L Y P W H O A Y R K D F T
J N N I C O S E V E R I N O O G I M S S N A M Y E
C L L N P E D R O C M S J K L L L A I C A F H O P
J T Q E M J C L H H A T L U I A I R L T U E O L H
O H Z V W U M A R N C T Y G V U P P H H D D L I A
A T I N A T L X I A K K A O I R P S C U E E U V N
N D Y M N J B Q O Q W R N A E I E T J S R R K I T
F Z F A A U I Z D R U H I S R E T E N H J I Q E S
S G K T N S K I C H R I S T I A N V T I C C V R H
T U I H M T G F R W D P K Z X I N E R R H O E I D
E I W I A I F H P L P W W R F S I O V L G V S D J
F L F A T N E A A Z B M I G U E L O C O U L R D D
A L M S T T C B S T E F A N O V U R X R J V O T L
N A B Y H D I G U I L L E R M O K D I E G O B V D
O U A O I S X S Q K J E S U S N E Z A N U M E S H
S M G N E A Y L W I N V L A U R E N T Z C U R F B
W E A A U C H R I S T I A N T D E J U O P Y T R V
P C L A U D I A M I K E Z S O P H I E C U R D I N
```

Thanks B.V. for the inspiration.

Tema Biwole, Arsène Stéphane
Weissensteinstrasse 18
3008 Bern
Switzerland

arsene.temabiwole@epfl.ch
people.epfl.ch/arsene.temabiwole

Born in Bafoussam, Cameroon
June 15, 1992
Cameroonian

Education

Dec. 06, 2022 **PhD defense**

2018 - 2022 **PhD in Physics**
Swiss Federal Institute of Technology in Lausanne (EPFL)
Thesis: From the electron cyclotron emission to the electron energy distribution in tokamak plasmas.
Advisors: Prof. Ambrogio Fasoli, Dr. Laurie Porte.

2015 - 2018 **Master of Science (MSc) in Energy and Nuclear Engineering**
Politecnico di Torino (PoliTo)
Master thesis: Neural network calculation of the neoclassical bootstrap current

2011 - 2015 **Bachelor of Science (BSc) in Energy Engineering**
Politecnico di Torino (PoliTo)
Bachelor work: Nuclear proliferation

Professional experience

2018 - 2021 **Teaching assistant in Physics**
EPFL, Lausanne, Switzerland

2017 - 2018 **Research Scholar in fusion and high temperature physics**
General Atomics, San Diego, United States of America

2015 - 2017 **Teaching assistant in Energy engineering**
PoliTo, Torino, Italy

Publications

First author

A. **Tema Biwolé,** L. Figini, L. Porte and A. Fasoli : "The plasma itself as a calibration source for ECE diagnostics". To be published in ***Nuclear Fusion***.

A. Tema Biwolé, L. Porte, S. Coda, A. Fasoli and the TCV team : "The Vertical ECE of TCV". To be published in ***Review of Scientific Instruments***.

A. Tema Biwolé, L. Porte, S. Coda, A. Fasoli and the TCV team: **"**Non-thermal electron distribution measurement from polarized electron cyclotron radiation in the TCV tokamak". Submitted to ***EPJ Web of conference.***

A. Tema Biwolé, L. Porte, A. Fasoli, A. Simonetto and O. D'Arcangelo : **"**Performance of a high vacuum, high temperature compatible millimeter-range viewing dump for the vertical ECE experiment on TCV". Published in ***Fusion Engineering and Design,*** *DOI 10.1016/j.fusengdes.2020.112079*.

Co-author

J. Cazabonne *et al* including **A. Tema Biwolé:** "Experimental and numerical investigations of electron transport enhancement by Electron-Cyclotron plasma-wave interaction in tokamaks". Submitted to ***Plasma Physics and Controlled Fusion.***

O. meneghini *et al* including **A. Tema Biwolé:** "Neural-network accelerated coupled core-pedestal simulations with self-consistent transport of impurities and compatible with ITER IMAS". Published in ***Nuclear Fusion,*** *DOI 10.1088/1741-4326/abb918***.**

D. Choi *et al* including **A. Tema Biwolé:** "Suprathermal electron driven fishbone instability in the TCV tokamak"**.** Published in ***Plasma Physics and Controlled Fusion,*** *DOI 10.1088/1361-6587/ab5147*.

Conferences

Invited speaker

- 21st workshop on electron cyclotron emission and electron cyclotron resonance heating. June 2022, ITER Organization.

Oral

- 9th Runaway electron meeting. May 2022, Garching, Germany.
- Joint Annual meeting of the Swiss Physical Society and the Austrian physical Society. August 2019, Zurich, Switzerland.
- 57th Annual meeting of the American Physical Society Division of Plasma Physics. October 2017, Milwaukee, Wisconsin, USA.

Honors and awards

- Knight of the order of merit of the Republic of Cameroon
- EPFL *EXAF* ambassador for scientific excellence in Africa

Expertise in

- Fusion plasma diagnosis with millimeter-waves
- Electron Cyclotron Emission in tokamak plasmas
- Modelling of fusion plasma emission for synthetic diagnostics
- Data analysis of fusion plasmas experiments
- Design and construction of microwave diagnostic systems